

Cover Page



Universiteit Leiden



The handle <http://hdl.handle.net/1887/19776> holds various files of this Leiden University dissertation.

Author: Runtuwene, Vincent Jimmy

Title: Functional characterization of protein-tyrosine phosphatases in zebrafish development using image analysis

Date: 2012-09-12



Functional Characterization of Protein -Tyrosine Phosphatases in Zebrafish Development using Image Analysis
Vincent J. Runtuwene 2012

**Functional Characterization of Protein
-Tyrosine Phosphatases in Zebrafish
Development using Image Analysis**

Vincent J. Runtuwene

Functional Characterization of Protein-Tyrosine Phosphatases in Zebrafish Development using Image Analysis

Vincent Jimmy Runtuwene

ISBN: 978-94-6190-134-7

Cover: Vincent Runtuwene, 'Infinite stitched repeat of confocal image of zebrafish pre-somitic mesoderm tagged with mCherry-H2B and YFP-CAAX'

Printing: AB Copie, Sint-Genesius-Rode

Copyright © 2012 by Vincent Runtuwene. All rights reserved. No part of this book may be reproduced, stored in a retrieval system or transmitted in any form or by any means, without prior permission of the author.

To Elise Johanna, Ade and my parents

Functional Characterization of Protein-Tyrosine Phosphatases in Zebrafish Development using Image Analysis

Functionele Karakterisering van Proteïne-Tyrosine Fosfatasen in Zebraavis Ontwikkeling gebruik makend van Beeldanalyse
(met samenvatting in het Nederlands)

PROEFSCHRIFT
ter verkrijging van
de graad van Doctor aan de Universiteit Leiden,
op gezag van Rector Magnificus Prof. mr. dr. Paul F. van der Heijden
volgens besluit van het College voor Promoties
te verdedigen op woensdag 12 september 2012
klokke 16u15

door
Vincent Jimmy Runtuwene
Geboren te Leuven (België)
in 1982

Promotiecommissie

Promotor:

Prof. Dr. Jeroen den Hertog

Overige leden:

Prof. Dr. Herman P. Spaink (lid manuscriptcommissie, secretaris) verbonden aan FWN, Leiden

Prof. Dr. Michael K. Richardson (lid manuscriptcommissie) verbonden aan FWN, Leiden

Prof. Dr. Johan Memelink (lid manuscriptcommissie) verbonden aan FWN, Leiden

Dr. Wiljan Hendriks (lid manuscriptcommissie) verbonden aan Radboud Universiteit, Nijmegen

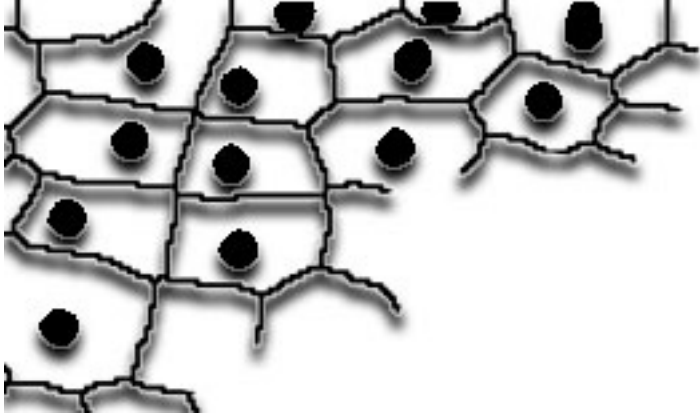
Dr. Ewa Snaar-Jagalska verbonden aan FWN, Leiden

Dr. Erik Danen verbonden aan FWN, Leiden

The research described in this thesis was performed at the Hubrecht Institute for developmental biology and Stem Cell Research, part of the Royal Dutch Academy of the Arts and Sciences (KNAW), within the framework of the Graduate School of Cancer, Genomics and Developmental Biology (CGDB) in Utrecht, the Netherlands and Leiden University Graduate School of Science in Leiden, the Netherlands. This work was in part supported by a Marie Curie Research Training Network Grant (PTPNET/MRTN-CT-2006-035830).

Table of contents

CHAPTER 1	Introduction	9
CHAPTER 2	RPTP α and PTP ϵ Signaling via Fyn/Yes and RhoA is essential for Zebrafish Convergence and Extension Cell Movements during Gastrulation	31
CHAPTER 3	Pair-Wise Regulation of Convergence and Extension Cell Movements by Four Phosphatases via RhoA	65
CHAPTER 4	Noonan Syndrome Gain-of-Function Mutations in NRAS cause Zebrafish Gastrulation Defects	99
CHAPTER 5	Cell Outliner and Cell Roses: New tools for Automated Cell Membrane Detection and Determination of Cell Polarity	119
CHAPTER 6	The Protein-Tyrosine Phosphatase Family in Gastrulation Cell Movements in Zebrafish	139
CHAPTER 7	Summarizing Discussion	161
Addendum	Samenvatting in het Nederlands	171
	Summary	173
	List of Publications	175
	Curriculum vitae	176



1

Introduction

1 Zebrafish

The zebrafish model system has proven to be invaluable to the study of vertebrate embryogenesis, as human disease models, cancer models and epigenetic research [1-3]. Many features inherent to zebrafish make the system an extraordinarily useful and versatile framework for addressing molecular biological issues. First, zebrafish are relatively easy to maintain, including a comparatively low housing cost [2, 4]. Second, there is a very high fecundity, producing a high number of translucent embryos, which develop rapidly and *ex utero*. As a result, collection of the embryos is straightforward, as is their manipulation. Third, they have a short generation time (3 months), which is evidently advantageous to genetic studies [4]. Additional benefits go hand in hand with the ongoing innovation in parallel fields of research, adding remarkable techniques to the zebrafish genetics toolkit. The advent of morpholino (MO) knockdown technology provided the first method of reverse genetics [5]. This method allowed for direct, albeit transient, interference with the translation of a target gene in embryos by morpholino micro-injection, in contrast to forward genetic techniques, which require multiple rounds of incrossing to perform functional gene studies. TILLING (targeted induced local lesions in genome) provided another reverse genetics method for generating zebrafish knockouts [6, 7] Recently, the use of designed zinc-finger nucleases has proven to be an even more efficient reverse genetics approach [8]. Reverse genetics applications, in their turn, benefit greatly from the assembly of the zebrafish genome [9]. Progressions in the field of transgenesis have developed methods for generating specific zebrafish lines, which have now become standard protocols, available in many laboratories [10, 11]. Further, extraordinary advances in the development of new fluorescent markers (for a review [12]), and groundbreaking steps in imaging technology (for a review [13]), continue to allow for a higher resolution analysis of cellular structure, dynamics, and signaling. In this thesis we utilized the zebrafish system to study the role of protein-tyrosine phosphatases (PTPs) in early development.

2 Gastrulation in zebrafish

Early morphogenesis is very similar in all vertebrates. Variations found between classes of animals are most likely due to differences in the structure of the egg, more exactly the amount of yolk present [14]. As in all vertebrates, fertilization of the zebrafish oocyte, results in a one cell stage zygote. The zygote consists of a large cell on top of a bigger yolk. This stage is followed by the morula stage throughout which six rounds of cell division occur, resulting in a mass of cells on top of the yolk with a combined volume roughly equal to that of the first cell. During the blastula stage, which starts



at the 128-cell stage, cell division continues, the enveloping layer (a single cell layer of larger cells which surrounds the entire embryo) is created and at 4 hours post fertilization the yolk domes into the cells at the animal pole in a process called epiboly. This process, during which the cells radially intercalate, results in a thinning layer of cells gradually spreading vegetally over the yolk. When the cells have covered 50% of the yolk, internalization of cells at the margin starts and marks the onset of gastrulation [15].

During gastrulation, the embryo is reshaped from an evidently undiversified blastula stage embryo to a multi-layered elongated framework consisting of three germ layers containing clearly defined structures. During this impressive remodeling the cells, and consequently the anlagen, are repositioned according to their future arrangement along the antero- posterior axis (Fig. 1 A-E) [14]. At 50% epiboly some anlagen, like the precursor cells of forebrain, midbrain and hindbrain, are already positioned in accordance with the later conformation. However, the extent of reorganization is perhaps best exemplified by the change in proximity of the forebrain and the prechordal plate. These organs are, at the start of gastrulation, at opposing poles of the embryo, the former at the animal and the latter at the vegetal pole (Fig. 1 A). Ultimately, adjacent to each other, they will constitute the most anterior structure of the embryo by the end of gastrulation (Fig. 1 D).

The reshaping of the embryo is coordinated by 4 morphogenetic cell movements: internalization, epiboly, convergence and extension (Fig. 1 F-I). Internalization (Fig. 1 F, purple arrow) describes the migration of the mesendodermal precursor cells through the blastoderm margin, which is the position where the enveloping layer makes contact with the yolk syncytial layer (a layer consisting of nuclei situated at the margin, lying directly beneath the blastomeres, within the yolk). The mesendodermal precursors form the hypoblast layer underneath an overlying epiblast (Fig. 1 F). The hypoblast cells at the dorsal side will accumulate, thereby breaking the embryo's radial symmetry, and result in a bulging structure at the dorsal side called the shield, the zebrafish equivalent of the *Xenopus* Spemann-Mangold organizer (Fig. 1 G) [16-18]. While the epiblast continues epiboly, the hypoblast cells at the shield position migrate anteriorly, moving separately from the overlying layer (Fig. 1 G, dashed turquoise arrow). Epiblast and hypoblast are physically separated by Brachet's cleft. The convergence and extension (CE) movements describe the movement of the lateral cells towards the midline (convergence) and dorsal cell populations in the anterior direction (extension) (Fig. 1 G-I; convergence, blue arrows; extension, turquoise arrows). Medio-lateral cell intercalation at the dorsal side causes the anterior-posterior axis of the embryo to extend. The ventral mesodermal cells however do not converge toward the midline and migrate vegetally, engaging solely in epiboly movements (Fig. 1 G, H; red arrows) [19]. Cell behaviours are variable

depending on the position within the embryo. This difference in behaviour is also reflected in the differences at the cellular level of these populations. During late gastrulation, a large proportion of the mesodermal and ectodermal cells at the dorsal side are more medio-laterally elongated than the ventral mesodermal cells [20-22]. Active medio-lateral polarization, and intercalation of the migrating cells are critical for proper CE movements. Moreover, analysis of cellular morphology of the dorsal ectoderm and mesoderm in CE defected phenotypes often reveal a loss of cell polarization.

3 Genetic regulation of CE movements

In order to choreograph simultaneous cell movements resulting in a net displacement of an entire cell population, the cells are required to collectively polarize in a common direction, as the sum of random singular cell movements would sum up to a zero total displacement. This alignment of the orientations of cells is called planar cell polarity (PCP), and it represents a basic requirement for the establishment of the bilaterally symmetrical body axis during zebrafish gastrulation.

Non-canonical Wnt/PCP pathway

The PCP pathway has been studied to great extent in *Drosophila melanogaster*. Mutations in the components of this pathway have been shown to result in randomization/disorganization in the surface bristles on the thorax, the hairs on the wings, and the photoreceptors in the eye [23-28]. The core components of this pathway identified in *Drosophila* are *strabismus (stbm)/van Gogh (vang)*, *frizzled (fz)*, *disheveled (dsh or dvl)*, *starry night (stan) / flamingo (fmi)*, *prickle (pk)*, and *diego (dgo)* [29, 30]. More downstream components are small GTPases RhoA and Rac, and the RhoA effector dRok [31-33]. The mechanism for the establishment of *Drosophila* wing hair cell polarity is a well-studied system utilizing the PCP pathway (Fig. 2A). In wildtype flies every cell produces a single hair, which is aligned along the proximal-distal axis of the wing at the distal membrane of the cell. The PCP pathway controls the number of hairs produced by the cells as well as their subcellular position and the global alignment of the hairs within the wing epithelium. While the mutation of the core components results in defects of the global alignment and subcellular position, the disruption of downstream components results in an increase in the number of hairs produced from a single cell [31-34]. In concordance with a role in cell polarity, several core components of the PCP pathway have a preferential subcellular localization on either the proximal or distal membranes. *Stbm* and *pk* are mostly detected on the proximal membrane and *fz*, *dvl*, and *dgo* on the distal membrane (Fig. 2B). *Fmi* on the other hand is located on both membranes. Other PCP elements like *dachsous (ds)* and *four-jointed (fj)* have been identified, which show expression gradients

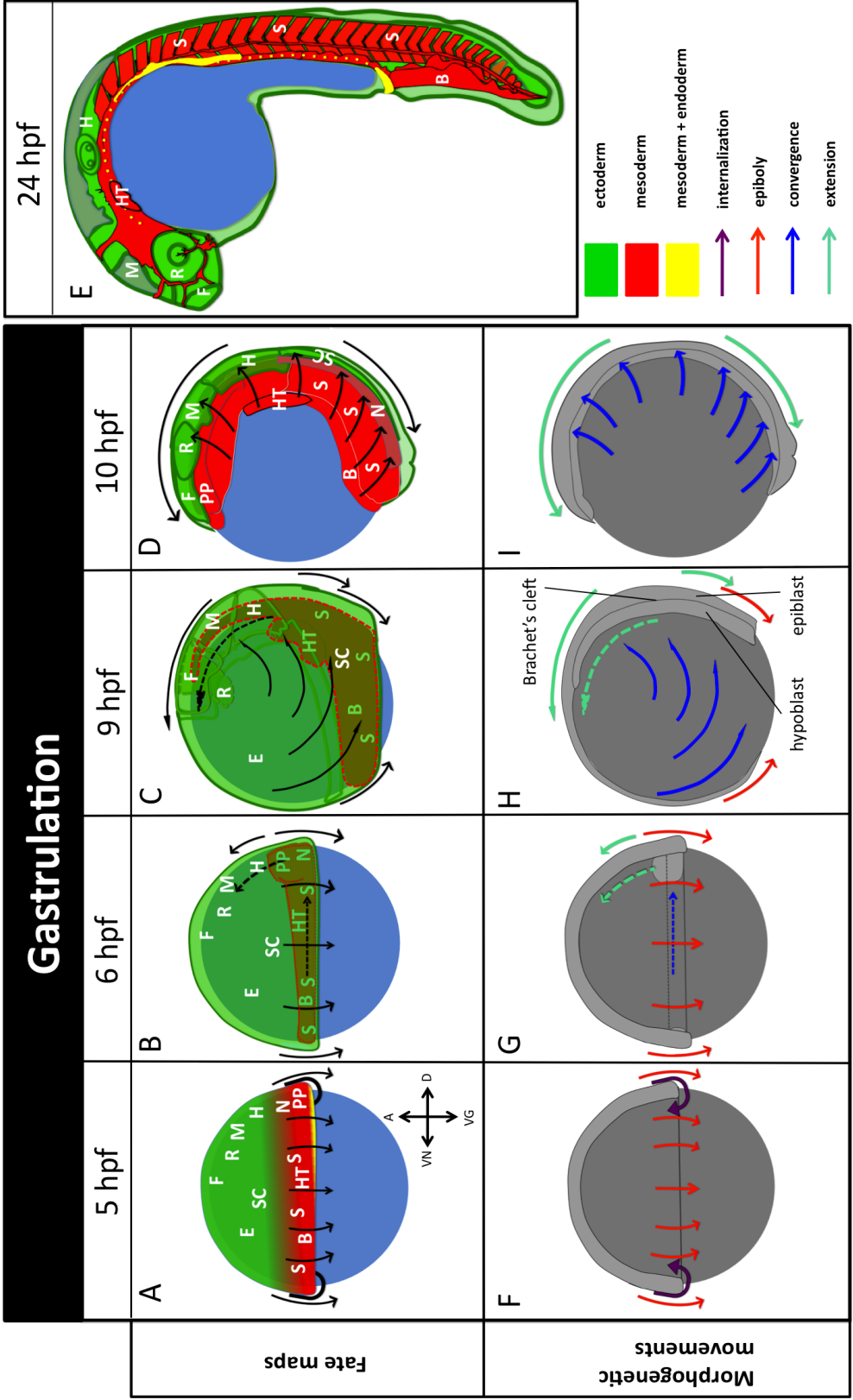


Figure 1: Gastrulation stage fate maps and morphogenetic movements. animal (A), vegetal (VG), dorsal (D), and ventral (VN) directions are indicated in A. The morphogenetic movements are shown using black arrows in A-D. A: Lateral view of a fate map at 50 % epiboly stage (5 hpf). Precursors of the germ layers are arranged along the animal-vegetal axis. The layers are shown with gradient borders since the precursor cells are interspersed at the boundaries rather than showing clear separation. Several ectodermal and mesodermal anlagen are indicated [105-110]. Yellow indicates both mesodermal and endodermal precursors, modified from [111]. B: Lateral view of a fate map at shield stage (6 hpf), showing the positions of the mesodermal precursors after internalization, inferred from [111]. Cell fates lying within the underlying hypoblast are indicated by a green font. C: Lateral view of a fate map at 90% epiboly (9 hpf). Cell fates lying within the underlying hypoblast are indicated by a green font. Position of the spinal cord is inferred from [112], modified from [111]. D: Lateral view of a fate map at bud stage (10 hpf). Regions shown are approximations derived from the expression of marker genes (ZFIN.org). Modified from [111]. E: Lateral view of a fate map at 24 hpf. The rearrangement of the structures (forebrain, mid-brain, hindbrain, heart, retina, somites and vascular system) derived from the anlagen in previous stages is shown (A-D) [15, 107, 110]. Yellow indicates endoderm. F: Cross section of 50 % epiboly stage embryo. Arrows indicate epiboly (red) and internalization (purple) cell movements. G: Cross section of shield stage embryo. Epiboly (red), convergence (blue) and extension (turquoise) movements are indicated. H: Cross section of 90% epiboly stage embryo. Epiboly (red), convergence (blue) and extension (turquoise) movements are indicated. I: Cross section of bud stage embryo. Convergence (blue) and extension (turquoise) movements are indicated. Abbreviations: F, forebrain; R, retina; M, midbrain; H, hindbrain; E, epidermis; SC, spinal cord; N, notochord; PP, prechordal plate; S, somites; B, blood; HT, heart.

along the proximal–distal axis. *Ds* shows a high expression in the distal region, which gradually declines towards the proximal region and the situation has been shown to be inverted for the expression of *ff* (Fig. 2B). A third gradient is formed by the inhibitory activity of *Ds* on *fat* (*ft*), which shows an even expression along the tissue. The interaction results in an activity gradient with the highest activity in the distal region (Fig. 2B) [35, 36]. It has been hypothesized that Ft and Ds form asymmetric heterodimers, which interact with the PCP core components resulting in the observed asymmetric distribution [35, 37]. Another hypothesis suggests that Fj is a Golgi kinase which regulates Ft and Ds by phosphorylation [38].

In vertebrates, homologs of the core components of the *Drosophila* PCP pathway, are required for the generation of the highly organized structure of the auditory and vestibular epithelia. Structurally reminiscent of the *Drosophila* wing epithelium, these epithelia consist of hair cells with clear planar polarization of an asymmetrically located kinocilium and adjacent stereocilia. The hair cells in the semicircular canals of the vestibular labyrinth are unidirectionally oriented along the long axis of each canal. The cochlear hair cells within the auditory system are organized in V-shaped patterns, which point to the periphery of the cochlea (Fig. 2C). The characteristic orientation of the hair cells in these tissues showed a disrupted phenotype in mice harboring core PCP component mutations [25,



39-43]. The parallels of these tissues with the *Drosophila* wing epithelium are even clear at the subcellular level, where components of the mammalian systems mimic the *Drosophila* subcellular organization to a very high degree: Pk and Vangl on the medial side and Fz, Dvl and Dgo on the lateral (Fig. 2D). Due to duplication events in vertebrates, not all single mutations in core PCP components result in a PCP-related phenotype [44]. The existence of redundant gene duplicates of several PCP core components like *fz3* and *fz6* [41], and *dvl1* and *dvl2* [45] make it necessary to interfere with the expression of both genes to generate a PCP-related phenotype.

Non-canonical Wnt signaling, which shares many components with the PCP pathway, is activated by Wnt5 and Wnt11 and is distinguished from canonical Wnt signaling in the fact that it transduces its signals independent from β -catenin [46, 47]. Upon binding of Wnt5 or Wnt11 to Fz, Dsh is recruited to the plasma membrane where it interacts with Daam1 [48, 49]. This activation of Daam1 results, through interaction with RhoGEFs like WGEF, in the activation of the small GTPase RhoA, which propagates the signal to Rok2 [50-52]. Non-canonical Wnt signaling, through direct interaction with the Fz-Dsh complex, also activates the small GTPase Rac1, which transduces the signal to C-Jun N-terminal kinase (JNK) (Fig. 3) [53, 54]. This signaling ultimately results in the remodeling of the cell cytoskeleton and, as a consequence, the establishment of polarization. Non-canonical Wnt signaling regulates CE movements by establishing the necessary polarization of the ectodermal and mesodermal cells during gastrulation [19]. Mutants, which harbor mutations in components of the non-canonical Wnt pathway, display defects in CE movements, and a loss of cell polarization in dorsal neurectoderm, and paraxial and axial mesoderm (Fig. 2E) [19, 22, 55-57]. Very similar to the situation in PCP signaling, several components are subcellularly localized in the migrating cells, with Fz and Dsh at the distal membrane and Pk and Vangl at the proximal membrane [58-60]. While the subcellular localization of these components is reminiscent of PCP signaling as it is found in epithelial tissues, it remains to be shown whether these elements perform a functionally similar role within these embryonic tissues.

Other pathways

Stat3 signaling has been implied to regulate CE movements. It has been suggested that Stat3 non-autonomously activates non-canonical Wnt signaling in neighbouring cells by enabling the expression of an as of yet unknown downstream target in the shield region, which forms an extracellular gradient. This gradient is required for lateral mesendodermal cells to sense the direction of convergence movements via the activation of RhoA downstream of Dsh [61].

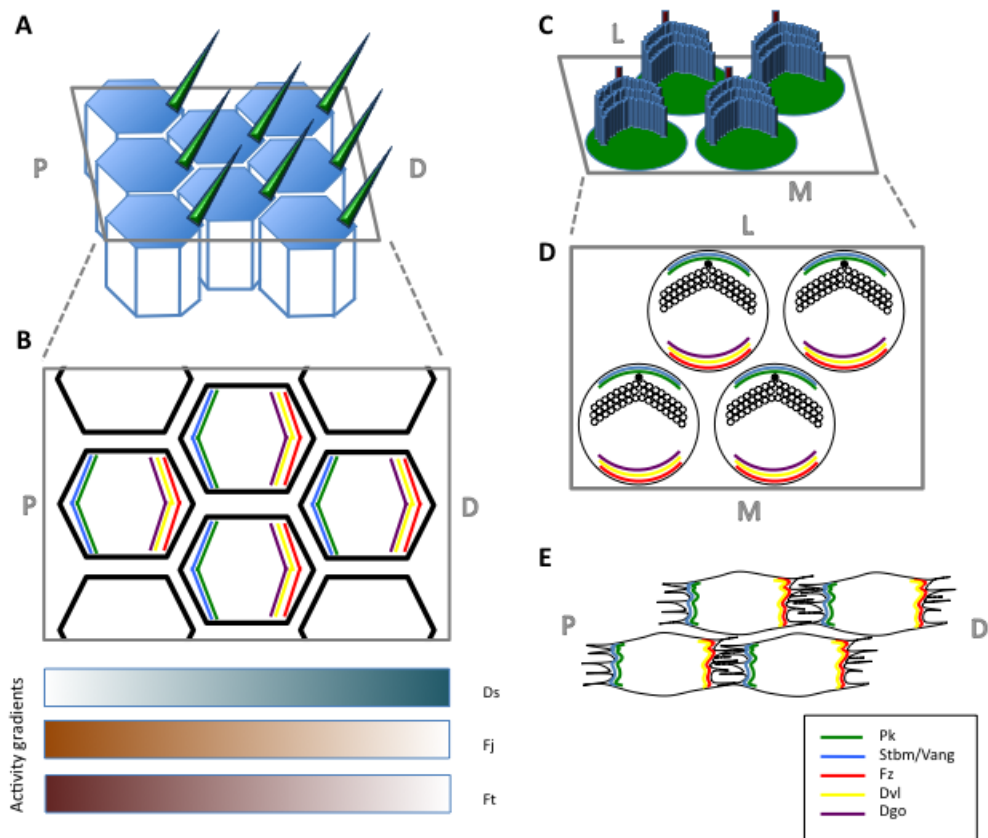


Figure 2. Planar cell polarity pathway. A: Schematic representation of *Drosophila* wing epithelial cells producing one hair each (presented in green). Proximal (P) and distal (D) directions are indicated. B: Schematic representation showing the subcellular distribution of PCP proteins Prickle (Pk), Strabismus (Stbm), Frizzled (Fz), Dishevelled (Dvl), and Diego (Dgo) and activity gradients over the wing epithelium of *Dachsous* (Ds), *Four-jointed* (Fj), and *Fat* (Ft). Proximal (P) and distal (D) directions are indicated. C: Schematic representation of cochlea hair cells with a big kinocilium (indicated in red), and stereocilia (indicated in blue) organized in a V-shape. Lateral (L) and medial (M) directions are indicated. D: Schematic representation of intracellular distribution of PCP components Pk, Stbm, Fz, Dvl, and Dgo in cochlea hair cells. E: Schematic representation of the distribution of PCP components Pk, Stbm, Fz, and Dvl in polarized mesodermal migrating cells in CE movements. Proximal (P) and distal (D) directions are indicated.

Bmp signaling has also been proposed to contribute to CE movements. It is expressed as a gradient, which is high at the ventral side and low at the dorsal. As Bmp signaling negatively regulates Ca^{2+} /cadherin-dependent cell-cell adhesiveness, the gastrula is subdivided in different migratory regions. The resulting lower cell-cell adhesion at the ventral side and higher adhesiveness at the dorsal side contributes to cell migration towards the dorsal side [62].

Csk, Fyn and Yes have been shown to activate RhoA in parallel to non-

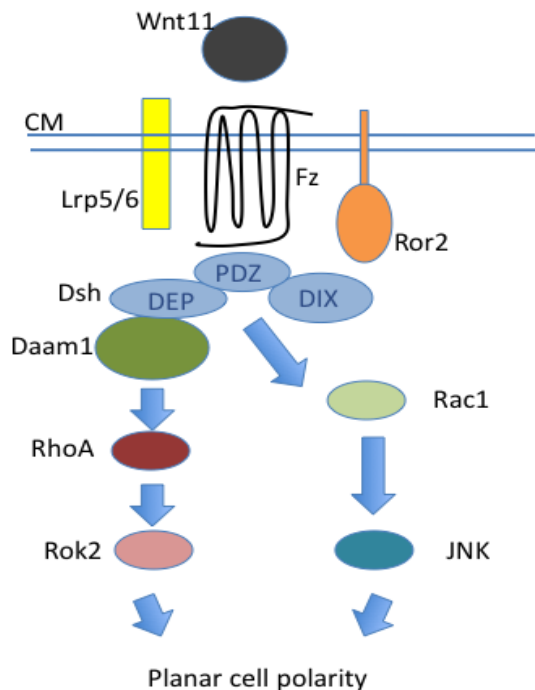


Figure 3. Non-canonical Wnt signaling pathway. Dishevelled (Dsh/Dvl) is recruited by Frizzled upon Wnt11 (ligand) binding. The Wnt-Frizzled complex interacts with Ror2 and Lrp5/6. Rac1 is activated through Dsh and RhoA through Daam1, which binds the DEP domain of Dishevelled. RhoA activates Rok2 and Rac1 activates JNK, both leading to planar cell polarity signaling.

canonical Wnt signaling [63, 64]. Other factors which have been implicated to have a role in CE are ephrins [65], Slit/Robo [66], Scribble-1 [67], Widerborst [68], Cyclooxygenase [69], and Has2 [70].

4 Ptps in zebrafish development

Reversible tyrosine phosphorylation of proteins is a key mechanism for transducing inter- and intracellular stimuli, and acts as a highly dynamic molecular switch between different activation states of signaling molecules, and consequently plays an important role in cellular processes like migration, proliferation, and differentiation [71-74]. Given its elemental role, it is not surprising that disruption of the synergy between protein-tyrosine kinases (PTKs) and phosphatases (PTPs) underlies many human diseases and developmental defects [75-80]. While great advances have been made in the field of research of PTKs, our understanding of the function of PTPs is lagging behind. This discrepancy is largely attributable to the wrongful assumption that PTPs are mere household enzymes with low substrate specificities, which plainly counter the effects of the PTKs by continuous dephosphorylation [75]. By now, many studies have acknowledged PTPs to be a very diverse family of proteins with highly specific roles in both development and disease [81]. For example, following the demonstration of direct interaction between the insulin receptor and PTP1B [82], the first PTP purified and sequenced [83], PTP1B knockout mice were shown to have enhanced insulin sensitivity, specifically in liver and muscle tissues [84]. Furthermore, the PTP1B locus maps to

a chromosomal region, 20q13.1-q13.2 [85], identified as a quantitative trait locus linked to diabetes and obesity [86]. PTPRO, a type III transmembrane PTP, plays an essential role in the development and function of the sensory nervous system [87]. This PTP is expressed in mouse dorsal root ganglion neurons. Ablation results in both a significant decrease in the number of peptidergic nociceptive neurons, and concomitant aberrations in their spinal pathfinding. Adult PTPRO knockout mice showed defects in nociception and sensorimotor coordination [87]. Mouse knockout models have contributed greatly to the elucidation of PTP functions. However, their *in utero* development constitutes an obvious complication when investigating events during early embryogenesis.

Given the many advantages of using zebrafish for studies of early vertebrate development, enumerated earlier, we used the zebrafish model to elucidate functions of PTPs in CE cell movements during gastrulation. Previously, we have identified all members of the family of classical PTPs in the zebrafish genome by blasting human PTP domains against the zebrafish Ensembl genome sequence (Zv8). With the exception of three PTP genes, homologs of the entire family of classical PTPs has been identified (Fig. 4). Fourteen genes have been found to have undergone duplication, which is not uncommon in zebrafish [88]. These duplicates have been hypothesized to result from a genome duplication event during teleost evolution [89]. Comparative sequence analysis of the human and zebrafish PTPs demonstrated that both protein families are closely related and highly comparable. Furthermore, detailed analysis of the spatio-temporal expression patterns of the 48 PTPs during early embryonic development revealed that most zebrafish PTPs are maternally contributed and are broadly expressed during early development, supporting the view of a potential role for PTPs during these stages [88]. A study using very potent generic PTP inhibitors, like peroxivanadate, already indicated that many aspects of egg activation require PTP activity [90]. Here we will review earlier work, which demonstrated that specific zebrafish PTPs are indeed essential for normal development.

The first zebrafish PTP to be cloned was PTP1B. Functional analysis *in vivo* using ectopic expression of wild type and dominant negative PTP1B C213S mutant, demonstrated that expression of wild type PTP1B, but not the catalytically inactive form, resulted in defects in somite formation [91].

It is unclear whether Pez, a FERM domain containing cytosolic PTP, encoded by *Ptpn14* in the zebrafish genome, contains a PTP domain [88]. This protein is transiently expressed at multiple sites, in developing brain, heart, pharyngeal arches, and somites during development. Knockdown by injection of ATG MOs, produces defects in these organsystems. Additionally, overexpression of Pez in epithelial MDCK cells causes epithelial-mesenchymal transition (EMT). Ectopic expression of Pez induces TGF β signaling in MDCK cells, and, in zebrafish

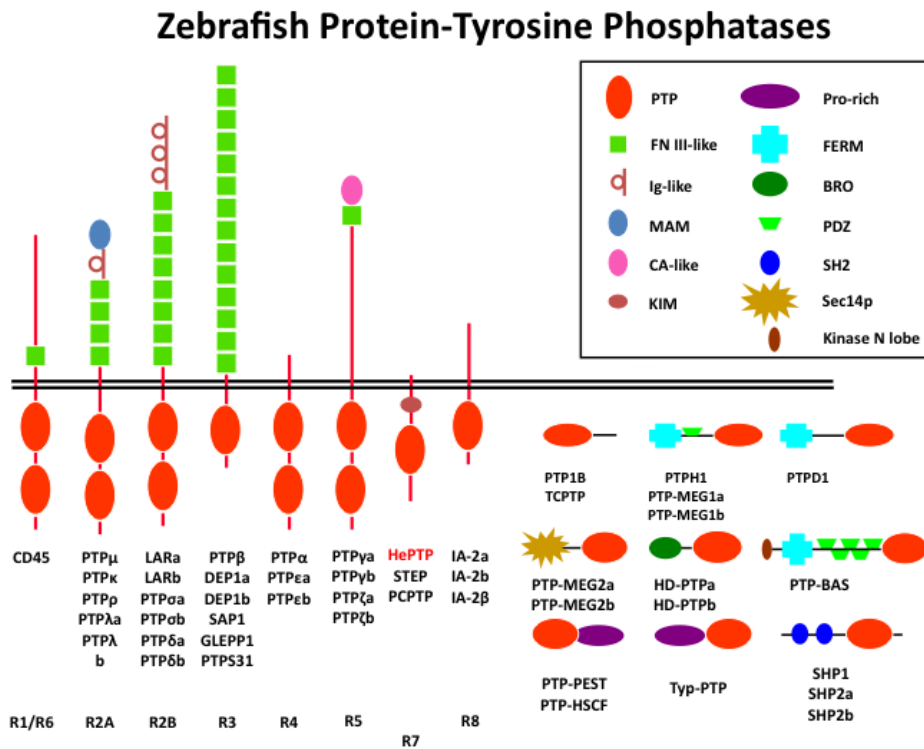


Figure 4. Zebrafish protein tyrosine phosphatases. Schematic representation of PTPs as they are found in the zebrafish genome. Human orthologs not identified in the zebrafish genome are indicated in red. Duplicated gene names were appended with “a” or “b”.

embryos, TGFβ3, which is coexpressed with *Pez*, is lost upon knockdown of *Pez*. These results indicate a critical role for *Pez* in organogenesis by induction of TGFβ signaling and EMT [92].

Knockdown of *ptpra*, which is maternally contributed and broadly expressed during early development [93], using ATG MOs resulted in specific defects in eye development, which were visible at 3 days post fertilization (dpf). The eyes were smaller and the layered structure of the retina were absent. Interestingly, at 5 dpf concomitant with the loss of knockdown efficiency of the MOs, the lamination of the retina was restored, although significant gaps in the amacrin layer were still observed [94]. In Chapter 2, we demonstrate that *ptpra* $^{-/-}$ mutants and morphants display, next to eye defects, CE defects.

Ptprua, which encodes the protein PTPψ and has an ohnolog *ptprub* [88] is shown to be critical for the normal functioning of the somitogenesis clock. Injection of ATG MOs in one cell stage embryos resulted in a disruption of the segmental pattern of the embryo. Analysis of the cyclic genes in *ptprua* morphant embryos indicates regulation of the somitogenesis clock upstream or in parallel

with Delta/Notch signaling. Moreover, *in situ* analysis of several markers revealed that *ptprua* morphants display CE defects [95]. In chapter 6, by confocal imaging of the presomitic mesoderm during gastrulation and subsequent polarization analysis, we provide direct evidence of the loss of cell polarization during CE movements in *ptprua* morphants.

Zebrafish Shp2a, encoded by the gene *ptpn11a*, is broadly expressed in early development [96]. A potential ohnolog, *ptpn11b*, has been identified [88], however its expression and function are still undetermined. MO mediated Shp2a knockdown causes CE defects, demonstrated by *in situ* analysis of well-established markers for CE and cell tracking experiments using caged fluorescein dextran. Successful rescue experiments wherein Shp2 MOs were coinjected with mRNA of constitutively active variants of the Src family kinases Fyn and Yes, and the small GTPase RhoA, provided evidence that Shp2a signals upstream of these signaling molecules [96], in concordance with the mouse knockout model. Shp2 null mice die at mid-gestation, displaying defects in the node, notochord and posterior elongation, indicating severe gastrulation defects [97]. Shp2 mutations underlie human Noonan and LEOPARD syndrome [98, 99]. These two conditions have a set of overlapping symptoms, including short stature, craniofacial abnormalities, and cardiac defects. Intriguingly, embryos injected with Shp2a mRNA harboring Noonan or LEOPARD mutations display CE defects during gastrulation and at later stages, defects reminiscent of the symptoms of human patients [96]. These results indicate that zebrafish can be used to model human diseases.

5 Image processing approaches for autosegmentation

Remarkable advances are being made in the field of biomedical imaging. New lightsheet technology is pushing the envelope regarding speed, sensitivity, spectral and depth resolution [100]. This is being complemented by the development of a veritable rainbow of brighter and more sensitive fluorescent probes. Nowadays, most standard laboratories have access to confocal and multiphoton microscopes, able to generate 3-D and 4-D (timelapse) data sets. A vast amount of morphological information at cellular resolution can be extracted from these huge data sets. This situation echoes a similar problem, which posed itself with the enhancements in sequencing technology in the post-genomic era. The massive availability of genomic information, found in online databases, warranted the development of data mining, which was facilitated by the advent of fast and accurate search algorithms. While complex formulas and sophisticated hardware and software have been developed for detecting cellular features in images [100-104], these technologies are usually not available in standard biological/biomedical laboratories.

Critical parameters in determining CE defects on a cellular level



are migration patterns and cell shape/polarization [19]. However, since the gastrulation cell movements involve the migration of entire layers of cells, individual cell readings are less relevant than the determination of the net movement of a group of cells. For a similar reason, a relatively high number of cells needs to be analyzed for polarization, to be able to determine whether a randomization of polarization has occurred. Manual collection of these types of data from confocal data sets is tedious, time-consuming, error-prone, and subjective.

6 *Outline of this thesis*

In this thesis we use the zebrafish system to identify members of the PTP family, having a role in CE movements during gastrulation. The aim is not only to identify, characterize the function and interactions of these genes, but also to generate fast and reliable methods to quantify morphological parameters of CE movements like tissue migration and polarization.

Tail length is a simple but effective morphological measurement used to identify CE phenotypes. While it is not a conclusive parameter to identify CE defects, we argue that it can be used to identify proteins involved in the same biochemical pathway by combining partial gene knockdown. Applying varying MO concentrations, this method is used to identify molecules regulating RhoA activity independent of non-canonical Wnt signaling in Chapter 2 and 3. In these chapters we also introduce an algorithm for automated detection of cell migration and a new method for more efficient detection of cell polarization.

In chapter 4, we identify a novel Noonan-associated gain-of-function *NRAS* mutation. Using mRNA- injections, we go on to show that this mutation and other Noonan-associated mutations can also be used to model Noonan syndrome in zebrafish. Moreover, we demonstrate the relative ease-of-use (addition to the water) of chemical compounds in zebrafish to modify aberrant RAS-MAPK signaling.

In chapter 5, we introduce an automated algorithm for detection of mesodermal cell membranes, and a novel method for presenting polarization data, providing a more straightforward representation of orientation and elongation of cells within a layer.

In chapter 6, we perform a screen of the entire PTP family. Candidate genes are analyzed in detail for convergence and extension defects, by tail length measurements, *in situ* hybridization and confocal microscopy-based cell shape analysis, yielding one *bona fide* novel PTP with a role in convergence and extension cell movements. We also provide direct proof of the cell polarization defects underlying the CE defects in *ptpn11a* and *ptprua* morphants.

References

1. Lieschke, G.J. and P.D. Currie, Animal models of human disease: zebrafish swim into view. *Nat Rev Genet*, 2007. 8(5): p. 353-67.
2. Ali, S., et al., Zebrafish embryos and larvae: a new generation of disease models and drug screens. *Birth Defects Res C Embryo Today*, 2011. 93(2): p. 115-33.
3. Mudbhary, R. and K.C. Sadler, Epigenetics, development, and cancer: zebrafish make their ARK. *Birth Defects Res C Embryo Today*, 2011. 93(2): p. 194-203.
4. Wixon, J., Featured organism: *Danio rerio*, the zebrafish. *Yeast*, 2000. 17(3): p. 225-31.
5. Nasevicius, A. and S.C. Ekker, Effective targeted gene 'knockdown' in zebrafish. *Nat Genet*, 2000. 26(2): p. 216-20.
6. Wienholds, E., et al., Target-selected inactivation of the zebrafish *rag1* gene. *Science*, 2002. 297(5578): p. 99-102.
7. Wienholds, E., et al., Efficient target-selected mutagenesis in zebrafish. *Genome Res*, 2003. 13(12): p. 2700-7.
8. Doyon, Y., et al., Heritable targeted gene disruption in zebrafish using designed zinc-finger nucleases. *Nat Biotechnol*, 2008. 26(6): p. 702-8.
9. Flicek, P., et al., Ensembl 2011. *Nucleic Acids Res*, 2011. 39(Database issue): p. D800-6.
10. Grabher, C. and J. Wittbrodt, Recent advances in meganuclease- and transposon-mediated transgenesis of medaka and zebrafish. *Methods Mol Biol*, 2008. 461: p. 521-39.
11. Udvardia, A.J. and E. Linney, Windows into development: historic, current, and future perspectives on transgenic zebrafish. *Dev Biol*, 2003. 256(1): p. 1-17.
12. Tsien, R.Y., Nobel lecture: constructing and exploiting the fluorescent protein paintbox. *Integr Biol (Camb)*, 2010. 2(2-3): p. 77-93.
13. Megason, S.G. and S.E. Fraser, Imaging in systems biology. *Cell*, 2007. 130(5): p. 784-95.
14. Schoenwolf, G.C. and J.L. Smith, Gastrulation and early mesodermal patterning in vertebrates. *Methods Mol Biol*, 2000. 135: p. 113-25.
15. Kimmel, C.B., et al., Stages of embryonic development of the zebrafish. *Dev Dyn*, 1995. 203(3): p. 253-310.
16. Warga, R.M. and C.B. Kimmel, Cell movements during epiboly and gastrulation in zebrafish. *Development*, 1990. 108(4): p. 569-80.
17. Montero, J.A., et al., Shield formation at the onset of zebrafish gastrulation. *Development*, 2005. 132(6): p. 1187-98.



18. Montero, J.A. and C.P. Heisenberg, Gastrulation dynamics: cells move into focus. *Trends Cell Biol*, 2004. 14(11): p. 620-7.
19. Myers, D.C., D.S. Sepich, and L. Solnica-Krezel, Convergence and extension in vertebrate gastrulae: cell movements according to or in search of identity? *Trends Genet*, 2002. 18(9): p. 447-55.
20. Concha, M.L. and R.J. Adams, Oriented cell divisions and cellular morphogenesis in the zebrafish gastrula and neurula: a time-lapse analysis. *Development*, 1998. 125(6): p. 983-94.
21. Myers, D.C., D.S. Sepich, and L. Solnica-Krezel, Bmp activity gradient regulates convergent extension during zebrafish gastrulation. *Dev Biol*, 2002. 243(1): p. 81-98.
22. Topczewski, J., et al., The zebrafish glypican knypek controls cell polarity during gastrulation movements of convergent extension. *Dev Cell*, 2001. 1(2): p. 251-64.
23. Shimada, Y., et al., Asymmetric colocalization of Flamingo, a seven-pass transmembrane cadherin, and Dishevelled in planar cell polarization. *Curr Biol*, 2001. 11(11): p. 859-63.
24. Veeman, M.T., J.D. Axelrod, and R.T. Moon, A second canon. Functions and mechanisms of beta-catenin-independent Wnt signaling. *Dev Cell*, 2003. 5(3): p. 367-77.
25. McNeill, H., Planar cell polarity: keeping hairs straight is not so simple. *Cold Spring Harb Perspect Biol*, 2010. 2(2): p. a003376.
26. Gubb, D. and A. Garcia-Bellido, A genetic analysis of the determination of cuticular polarity during development in *Drosophila melanogaster*. *J Embryol Exp Morphol*, 1982. 68: p. 37-57.
27. Chae, J., et al., The *Drosophila* tissue polarity gene *starry night* encodes a member of the protocadherin family. *Development*, 1999. 126(23): p. 5421-9.
28. Taylor, J., et al., Van Gogh: a new *Drosophila* tissue polarity gene. *Genetics*, 1998. 150(1): p. 199-210.
29. Fanto, M. and H. McNeill, Planar polarity from flies to vertebrates. *J Cell Sci*, 2004. 117(Pt 4): p. 527-33.
30. Feiguin, F., et al., The ankyrin repeat protein Diego mediates Frizzled-dependent planar polarization. *Dev Cell*, 2001. 1(1): p. 93-101.
31. Eaton, S., R. Wepf, and K. Simons, Roles for Rac1 and Cdc42 in planar polarization and hair outgrowth in the wing of *Drosophila*. *J Cell Biol*, 1996. 135(5): p. 1277-89.
32. Strutt, D.I., U. Weber, and M. Mlodzik, The role of RhoA in tissue polarity and Frizzled signalling. *Nature*, 1997. 387(6630): p. 292-5.
33. Winter, C.G., et al., *Drosophila* Rho-associated kinase (Drok) links Frizzled-mediated planar cell polarity signaling to the actin cytoskeleton. *Cell*, 2001. 105(1): p. 81-91.

34. Wong, L.L. and P.N. Adler, Tissue polarity genes of *Drosophila* regulate the subcellular location for prehair initiation in pupal wing cells. *J Cell Biol*, 1993. 123(1): p. 209-21.
35. Ma, D., et al., Fidelity in planar cell polarity signalling. *Nature*, 2003. 421(6922): p. 543-7.
36. Yang, C.H., M.A. Simon, and H. McNeill, mirror controls planar polarity and equator formation through repression of fringe expression and through control of cell affinities. *Development*, 1999. 126(24): p. 5857-66.
37. Yang, C.H., J.D. Axelrod, and M.A. Simon, Regulation of Frizzled by fat-like cadherins during planar polarity signaling in the *Drosophila* compound eye. *Cell*, 2002. 108(5): p. 675-88.
38. Ishikawa, H.O., et al., Four-jointed is a Golgi kinase that phosphorylates a subset of cadherin domains. *Science*, 2008. 321(5887): p. 401-4.
39. Vladar, E.K., D. Antic, and J.D. Axelrod, Planar cell polarity signaling: the developing cell's compass. *Cold Spring Harb Perspect Biol*, 2009. 1(3): p. a002964.
40. Kelly, M. and P. Chen, Shaping the mammalian auditory sensory organ by the planar cell polarity pathway. *Int J Dev Biol*, 2007. 51(6-7): p. 535-47.
41. Wang, Y., N. Guo, and J. Nathans, The role of Frizzled3 and Frizzled6 in neural tube closure and in the planar polarity of inner-ear sensory hair cells. *J Neurosci*, 2006. 26(8): p. 2147-56.
42. Wang, J., et al., Dishevelled genes mediate a conserved mammalian PCP pathway to regulate convergent extension during neurulation. *Development*, 2006. 133(9): p. 1767-78.
43. Etheridge, S.L., et al., Murine dishevelled 3 functions in redundant pathways with dishevelled 1 and 2 in normal cardiac outflow tract, cochlea, and neural tube development. *PLoS Genet*, 2008. 4(11): p. e1000259.
44. Wansleben, C. and F. Meijlink, The planar cell polarity pathway in vertebrate development. *Dev Dyn*, 2011. 240(3): p. 616-26.
45. Wang, J., et al., Regulation of polarized extension and planar cell polarity in the cochlea by the vertebrate PCP pathway. *Nat Genet*, 2005. 37(9): p. 980-5.
46. Boutros, M., et al., Dishevelled activates JNK and discriminates between JNK pathways in planar polarity and wingless signaling. *Cell*, 1998. 94(1): p. 109-18.
47. Moon, R.T., et al., Xwnt-5A: a maternal Wnt that affects morphogenetic movements after overexpression in embryos of *Xenopus laevis*. *Development*, 1993. 119(1): p. 97-111.
48. Wong, H.C., et al., Direct binding of the PDZ domain of Dishevelled to a conserved internal sequence in the C-terminal region of Frizzled. *Mol Cell*, 2003. 12(5): p. 1251-60.
49. Punchedewa, C., et al., Sequence requirement and subtype specificity



- in the high-affinity interaction between human frizzled and dishevelled proteins. *Protein Sci*, 2009. 18(5): p. 994-1002.
50. Alberts, A.S., Diaphanous-related Formin homology proteins. *Curr Biol*, 2002. 12(23): p. R796.
 51. Higgs, H.N., Formin proteins: a domain-based approach. *Trends Biochem Sci*, 2005. 30(6): p. 342-53.
 52. Liu, W., et al., Mechanism of activation of the Formin protein Daam1. *Proc Natl Acad Sci U S A*, 2008. 105(1): p. 210-5.
 53. Rosso, S.B., et al., Wnt signaling through Dishevelled, Rac and JNK regulates dendritic development. *Nat Neurosci*, 2005. 8(1): p. 34-42.
 54. Habas, R., I.B. Dawid, and X. He, Coactivation of Rac and Rho by Wnt/ Frizzled signaling is required for vertebrate gastrulation. *Genes Dev*, 2003. 17(2): p. 295-309.
 55. Wallingford, J.B., S.E. Fraser, and R.M. Harland, Convergent extension: the molecular control of polarized cell movement during embryonic development. *Dev Cell*, 2002. 2(6): p. 695-706.
 56. Jessen, J.R., et al., Zebrafish trilobite identifies new roles for Strabismus in gastrulation and neuronal movements. *Nat Cell Biol*, 2002. 4(8): p. 610-5.
 57. Wallingford, J.B., et al., Dishevelled controls cell polarity during *Xenopus* gastrulation. *Nature*, 2000. 405(6782): p. 81-5.
 58. Adler, P.N., Planar signaling and morphogenesis in *Drosophila*. *Dev Cell*, 2002. 2(5): p. 525-35.
 59. Tree, D.R., et al., Prickle mediates feedback amplification to generate asymmetric planar cell polarity signaling. *Cell*, 2002. 109(3): p. 371-81.
 60. Jenny, A., et al., Prickle and Strabismus form a functional complex to generate a correct axis during planar cell polarity signaling. *EMBO J*, 2003. 22(17): p. 4409-20.
 61. Miyagi, C., et al., STAT3 noncell-autonomously controls planar cell polarity during zebrafish convergence and extension. *J Cell Biol*, 2004. 166(7): p. 975-81.
 62. von der Hardt, S., et al., The Bmp gradient of the zebrafish gastrula guides migrating lateral cells by regulating cell-cell adhesion. *Curr Biol*, 2007. 17(6): p. 475-87.
 63. Jopling, C. and J. Hertog, Essential role for Csk upstream of Fyn and Yes in zebrafish gastrulation. *Mech Dev*, 2007. 124(2): p. 129-36.
 64. Jopling, C. and J. den Hertog, Fyn/Yes and non-canonical Wnt signaling converge on RhoA in vertebrate gastrulation cell movements. *EMBO Rep*, 2005. 6(5): p. 426-31.
 65. Oates, A.C., et al., An early developmental role for eph-ephrin interaction during vertebrate gastrulation. *Mech Dev*, 1999. 83(1-2): p. 77-94.
 66. Yeo, S.Y., et al., Overexpression of a slit homologue impairs convergent

- extension of the mesoderm and causes cyclopia in embryonic zebrafish. *Dev Biol*, 2001. 230(1): p. 1-17.
67. Wada, H., et al., Dual roles of zygotic and maternal Scribble1 in neural migration and convergent extension movements in zebrafish embryos. *Development*, 2005. 132(10): p. 2273-85.
68. Hannus, M., et al., Planar cell polarization requires Widerborst, a B' regulatory subunit of protein phosphatase 2A. *Development*, 2002. 129(14): p. 3493-503.
69. Cha, Y.I., et al., Cyclooxygenase-1 signaling is required for vascular tube formation during development. *Dev Biol*, 2005. 282(1): p. 274-83.
70. Bakkers, J., et al., Has2 is required upstream of Rac1 to govern dorsal migration of lateral cells during zebrafish gastrulation. *Development*, 2004. 131(3): p. 525-37.
71. Hunter, T., Protein kinases and phosphatases: the yin and yang of protein phosphorylation and signaling. *Cell*, 1995. 80(2): p. 225-36.
72. van der Geer, P., T. Hunter, and R.A. Lindberg, Receptor protein-tyrosine kinases and their signal transduction pathways. *Annu Rev Cell Biol*, 1994. 10: p. 251-337.
73. Van Vactor, D., A.M. O'Reilly, and B.G. Neel, Genetic analysis of protein tyrosine phosphatases. *Curr Opin Genet Dev*, 1998. 8(1): p. 112-26.
74. Clark, E.A. and J.S. Brugge, Integrins and signal transduction pathways: the road taken. *Science*, 1995. 268(5208): p. 233-9.
75. den Hertog, J., Protein-tyrosine phosphatases in development. *Mech Dev*, 1999. 85(1-2): p. 3-14.
76. Alonso, A., et al., Protein tyrosine phosphatases in the human genome. *Cell*, 2004. 117(6): p. 699-711.
77. Hendriks, W.J., et al., Protein tyrosine phosphatases: functional inferences from mouse models and human diseases. *FEBS J*, 2008. 275(5): p. 816-30.
78. LaForgia, S., et al., Receptor protein-tyrosine phosphatase gamma is a candidate tumor suppressor gene at human chromosome region 3p21. *Proc Natl Acad Sci U S A*, 1991. 88(11): p. 5036-40.
79. Tartaglia, M., et al., Mutations in PTPN11, encoding the protein tyrosine phosphatase SHP-2, cause Noonan syndrome. *Nat Genet*, 2001. 29(4): p. 465-8.
80. Wang, Z., et al., Mutational analysis of the tyrosine phosphatome in colorectal cancers. *Science*, 2004. 304(5674): p. 1164-6.
81. Tonks, N.K., Protein tyrosine phosphatases: from genes, to function, to disease. *Nat Rev Mol Cell Biol*, 2006. 7(11): p. 833-46.
82. Seely, B.L., et al., Protein tyrosine phosphatase 1B interacts with the activated insulin receptor. *Diabetes*, 1996. 45(10): p. 1379-85.
83. Tonks, N.K., C.D. Diltz, and E.H. Fischer, Purification of the major pro-

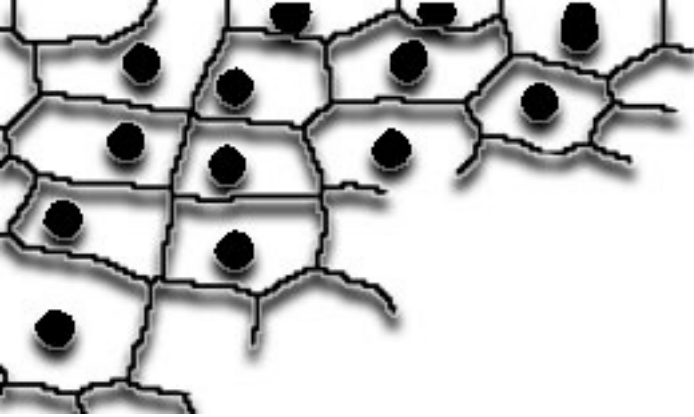


- tein-tyrosine-phosphatases of human placenta. *J Biol Chem*, 1988. 263(14): p. 6722-30.
84. Elchebly, M., et al., Increased insulin sensitivity and obesity resistance in mice lacking the protein tyrosine phosphatase-1B gene. *Science*, 1999. 283(5407): p. 1544-8.
85. Brown-Shimer, S., et al., Molecular cloning and chromosome mapping of the human gene encoding protein phosphotyrosyl phosphatase 1B. *Proc Natl Acad Sci U S A*, 1990. 87(13): p. 5148-52.
86. Lumbert, A.V., et al., Identification of an obesity quantitative trait locus on mouse chromosome 2 and evidence of linkage to body fat and insulin on the human homologous region 20q. *J Clin Invest*, 1997. 100(5): p. 1240-7.
87. Gonzalez-Brito, M.R. and J.L. Bixby, Protein tyrosine phosphatase receptor type O regulates development and function of the sensory nervous system. *Mol Cell Neurosci*, 2009. 42(4): p. 458-65.
88. van Eekelen, M., et al., Identification and expression of the family of classical protein-tyrosine phosphatases in zebrafish. *PLoS One*, 2010. 5(9): p. e12573.
89. Postlethwait, J.H., The zebrafish genome in context: ohnologs gone missing. *J Exp Zool B Mol Dev Evol*, 2007. 308(5): p. 563-77.
90. Wu, W. and W.H. Kinsey, Role of PTPase(s) in regulating Fyn kinase at fertilization of the zebrafish egg. *Dev Biol*, 2002. 247(2): p. 286-94.
91. van der Sar, A.M., et al., Pleiotropic effects of zebrafish protein-tyrosine phosphatase-1B on early embryonic development. *Int J Dev Biol*, 1999. 43(8): p. 785-94.
92. Wyatt, L., et al., The protein tyrosine phosphatase Pez regulates TGF-beta, epithelial-mesenchymal transition, and organ development. *J Cell Biol*, 2007. 178(7): p. 1223-35.
93. van der Sar, A., et al., Expression of receptor protein-tyrosine phosphatase alpha, sigma and LAR during development of the zebrafish embryo. *Mech Dev*, 2001. 109(2): p. 423-6.
94. van der Sar, A.M., D. Zivkovic, and J. den Hertog, Eye defects in receptor protein-tyrosine phosphatase alpha knock-down zebrafish. *Dev Dyn*, 2002. 223(2): p. 292-7.
95. Aerne, B. and D. Ish-Horowicz, Receptor tyrosine phosphatase psi is required for Delta/Notch signalling and cyclic gene expression in the presomitic mesoderm. *Development*, 2004. 131(14): p. 3391-9.
96. Jopling, C., D. van Geemen, and J. den Hertog, Shp2 knockdown and Noonan/LEOPARD mutant Shp2-induced gastrulation defects. *PLoS Genet*, 2007. 3(12): p. e225.
97. Saxton, T.M., et al., Abnormal mesoderm patterning in mouse embryos mutant for the SH2 tyrosine phosphatase Shp-2. *EMBO J*, 1997. 16(9): p.

2352-64.

98. Allanson, J.E., Noonan syndrome. *J Med Genet*, 1987. 24(1): p. 9-13.
99. Gorlin, R.J., R.C. Anderson, and J.H. Moller, The leopard (multiple lentiginos) syndrome revisited. *Laryngoscope*, 1971. 81(10): p. 1674-81.
100. Keller, P.J., et al., Reconstruction of zebrafish early embryonic development by scanned light sheet microscopy. *Science*, 2008. 322(5904): p. 1065-9.
101. Megason, S.G., In toto imaging of embryogenesis with confocal time-lapse microscopy. *Methods Mol Biol*, 2009. 546: p. 317-32.
102. Mosaliganti, K., et al., Anisotropic Plate Diffusion Filtering for Detection of Cell Membranes in 3d Microscopy Images. *Proc IEEE Int Symp Biomed Imaging*, 2010: p. 588-591.
103. Jurrus, E., et al., Detection of neuron membranes in electron microscopy images using a serial neural network architecture. *Med Image Anal*, 2010. 14(6): p. 770-83.
104. M.A.Luengo-Oroz, L.D., C.Castrorfi, T.Savyk E.Faure, B.Lombardo, and N.P.a.A.S. P.Bourgine, Can voronoi diagram model cell geometries in early sea urchin embryogenesis? *ISBI*, 2008: p. 504-507.
105. Dougan, S.T., et al., The role of the zebrafish nodal-related genes *squint* and *cyclops* in patterning of mesendoderm. *Development*, 2003. 130(9): p. 1837-51.
106. Gritsman, K., W.S. Talbot, and A.F. Schier, Nodal signaling patterns the organizer. *Development*, 2000. 127(5): p. 921-32.
107. Keegan, B.R., D. Meyer, and D. Yelon, Organization of cardiac chamber progenitors in the zebrafish blastula. *Development*, 2004. 131(13): p. 3081-91.
108. Kimmel, C.B., R.M. Warga, and T.F. Schilling, Origin and organization of the zebrafish fate map. *Development*, 1990. 108(4): p. 581-94.
109. Woo, K. and S.E. Fraser, Specification of the hindbrain fate in the zebrafish. *Dev Biol*, 1998. 197(2): p. 283-96.
110. Woo, K. and S.E. Fraser, Order and coherence in the fate map of the zebrafish nervous system. *Development*, 1995. 121(8): p. 2595-609.
111. Schier, A.F. and W.S. Talbot, Molecular genetics of axis formation in zebrafish. *Annu Rev Genet*, 2005. 39: p. 561-613.
112. Kudoh, T., S.W. Wilson, and I.B. Dawid, Distinct roles for *Fgf*, *Wnt* and retinoic acid in posteriorizing the neural ectoderm. *Development*, 2002. 129(18): p. 4335-46.





2

RPTP α and PTP ϵ Signaling via Fyn/Yes and RhoA is Essential for Zebrafish Convergence and Extension Cell Movements during Gastrulation

Mark van Eekelen*, Vincent Runtuwene*, John Overvoorde, Jeroen den Hertog

Dev Biol. 2010 Apr 15;340(2):626-39

*=equal contribution

Abstract

Convergence and extension (C&E) cell movements are essential to shape the body axis during vertebrate gastrulation. We have used the zebrafish to assess the role of the receptor protein-tyrosine phosphatases, RPTP α and PTP ϵ , in gastrulation cell movements. Both RPTP α and PTP ϵ knockdown and *ptpra*^{-/-} embryos show defects in C&E movements. A method was developed to track gastrulation cell movements using confocal microscopy in a quantitative manner and *ptpra*^{-/-} embryos displayed reduced convergence as well as extension speeds. RPTP α and PTP ϵ knockdowns cooperated with knockdown of a well known factor in C&E cell movement, non-canonical Wnt11. RPTP α and PTP ϵ dephosphorylate and activate Src family kinases in various cell types *in vitro* and *in vivo*. We found that Src family kinase phosphorylation was enhanced in *ptpra*^{-/-} embryos, consistent with reduced Src family kinase activity. Importantly, both *ptpra*^{-/-} and RPTP α and PTP ϵ knockdown induced C&E defects were rescued by active Fyn and Yes. Moreover, active RhoA rescued the RPTP α and PTP ϵ knockdown and *ptpra*^{-/-} induced gastrulation cell movement defects as well. Our results demonstrate that RPTP α and PTP ϵ are essential for C&E movements in a signaling pathway parallel to non-canonical Wnts and upstream of Fyn, Yes and RhoA.

Introduction

RPTP α (*ptpra*) and PTP ϵ (*ptpre*) are two highly similar receptor-like protein-tyrosine phosphatases consisting of a short highly glycosylated extracellular domain and two cytoplasmically localized phosphatase domains. RPTP α and PTP ϵ are involved in several processes, including cell polarization (Chiusaroli et al., 2004; Herrera Abreu et al., 2008), migration (Zeng et al., 2003) and cell cycle control (Ardini et al., 2000). The function of RPTP α and PTP ϵ is often ascribed to direct activation of Src family kinases (SFKs) through dephosphorylation of the inhibitory pTyr527 residue in the C-terminus (Courtneidge, 1985; den Hertog et al., 1993; Peretz et al., 2000; Zheng et al., 1992). Src and SFKs are known to be activated by different stimuli, including cell adhesion to ECM proteins and growth factors (Hsia et al., 2005; Roche et al., 1995). Many of these actions require actin cytoskeleton remodeling through activation of Rho GTPase family members (Ridley and Hall, 1992; Ridley et al., 1992).

During vertebrate gastrulation a series of cellular movements result in the formation of the three germ layers, endoderm, mesoderm and ectoderm that create the basic body plan of the developing embryo (Warga and Kimmel, 1990). Convergence and extension (C&E) represent two of these essential cell movements that have been well characterized in zebrafish. Cells converge towards the midline, forming the medial/lateral axis, where they intercalate with one another

and extend around the yolk, giving rise to the anterior/posterior axis (Griffin et al., 1995; Keller et al., 1992; Solnica-Krezel et al., 1996). C&E cell movements are regulated by the non-canonical Wnt signaling pathway which is similar to the planar cell polarity (PCP) pathway identified in *Drosophila* (Matsui et al., 2005; Medina et al., 2000; Solnica-Krezel and Eaton, 2003).

In vertebrates, the non-canonical Wnt pathway becomes activated when Wnt11 or Wnt5 binds to Frizzled receptors resulting in the downstream activation of RhoA and Rac. RhoA and Rac subsequently propagate the signal to their respective downstream effectors, including Rok2 and JNK (Habas et al., 2003, 2001; Veeman et al., 2003). In *C. elegans*, this cascade will remodel the cell, establishing polarity and allowing it to mount a proper chemotactic response through remodeling of the actin cytoskeleton (Goldstein et al., 2006). It is assumed that non-canonical Wnt signaling induced cell polarization is at the basis of vertebrate C&E cell movements as well. A number of mutants have been described in zebrafish that harbor mutations in genes regulating this process (Heisenberg et al., 2000; Jessen et al., 2002; Kilian et al., 2003; Topczewski et al., 2001). The phenotype that all of these mutants have in common is that the embryos are shorter and broader as one might expect if C&E are disrupted.

More recently a number of studies have come to light that show that C&E is not solely governed by the non-canonical Wnt pathway. The list of other factors that modulate non-canonical Wnt signaling directly (Wada et al., 2005) or function independently (Hannus et al., 2002) is ever growing. Recently, we have shown that signaling through the Src family kinases Fyn and Yes converges with non-canonical Wnt signaling and serves to modulate the activity of the small GTPase RhoA during C&E cell movements (Jopling and den Hertog, 2005). Csk, a negative regulator of SFKs also has a role in C&E cell movements (Jopling and den Hertog, 2007). Moreover, we have shown that the protein-tyrosine phosphatase Shp2, an indirect activator of SFKs (Zhang et al., 2004), regulates C&E during gastrulation via Fyn/Yes and RhoA (Jopling et al., 2007).

Here we show that knockdown of RPTP α or PTP ϵ induced C&E defects using *in situ* hybridization of C&E specific markers. Coinjection of ptp α -MO and ptp ϵ -MO induced various degrees of cyclopia in fish, indicating that RPTP α and PTP ϵ are at least partially redundant. Ptp α mutant zebrafish were isolated by target selected gene inactivation and we established that ptp α -/- embryos displayed C&E defects, similar to the ptp α -MO injected embryos. Time-lapse confocal microscopy was used to track cell movements during gastrulation and this technology was adapted to allow quantification of cell movements during gastrulation. Ptp α -/- embryos displayed reduced C&E cell movement speed as compared to wildtype siblings. Co-injection of low amounts of ptp α -MO or ptp ϵ -MO together with low amounts of Wnt11-MO phenocopied the silberblick phenotype,

suggesting that RPTP α and PTP ϵ have a genetic interaction with Wnt11. In search of an underlying mechanism, we found enhanced SFK phosphorylation on the inhibitory site and reduced SFK autophosphorylation, indicating that SFK activity was reduced in mutant embryos compared to siblings. C&E defects in *ptpra*^{-/-} embryos were rescued by active Fyn and Yes, which is consistent with RPTP α being upstream of SFKs. Moreover, active RhoA rescued the *ptpra*^{-/-} phenotype as well. Based on our data, we propose a model in which RPTP α and PTP ϵ act in parallel to non-canonical Wnt signaling upstream of the SFKs, Fyn and Yes and upstream of RhoA.

Materials and methods

Zebrafish and in situ hybridization

Zebrafish were kept and the embryos were staged as described before (Westerfield, 1995). *In situ* hybridizations were done essentially as described (Thisse et al., 1993) using probes specific for *bmp2b*, *chd*, *gsc*, *ntla*, *dlx3*, *hgg1* (currently known as *ctsl1b*), *myod* and *krox20* as described (Jopling and Hertog, 2007; Jopling et al., 2007). *In situ* probes for *ptpra*, *ptprea* and *ptpreb* were generated by performing an RT reaction on isolated RNA from zebrafish embryos (48 hpf). We designed oligos to perform PCR on the cDNA constructs of *ptpra*, *ptprea* and *ptpreb* spanning approximately 800 bp, and a nested oligo pair with a T7 sequence in the reverse oligo. We used the T7 tag to generate DIG labeled antisense RNA for *in situ* hybridization and the nested oligo pair to verify the sequences. A premature stop *ptpra* mutant was identified using target selected gene inactivation as described in Wienholds et al. (2002). The *ptpra*^{hu3334} allele changes a TTG to a TAG codon resulting in a L133STOP coding change.

Constructs

Mouse *ptpra* constructs were used as described earlier (den Hertog and Hunter, 1996). For zebrafish *ptpra* constructs 1 dpf zebrafish were lysed and mRNA was isolated. Reverse transcription was done with oligo dT and *ptpra* cDNA was amplified and cloned into a pSG5-13 vector and sequenced.

MOs, RNA and injections

Antisense splice site donor MOs were designed one or two exons upstream of the catalytic site of the respective cDNAs and ordered from GeneTools (Philomath,OR): *ptpra*, 5'-TTGCGGCGTTTACCTCTTTCCGCTC; *ptprea*, 5'-AAGGGATGCTAACCTCTTTTCTCTC; *ptpreb*, 5' TATCTTATCTCACCTCTTTTCTCTC; *wnt11* as described in: Lele et al. (2001). 5' capped sense RNAs were synthesized using mMessage mMachine kit (Ambion). The amount of RNA that was injected at the one cell stage was optimized for each synthetic RNA. For the rescue experi-



ments, we used mutant, constitutively active forms of human Fyn, Yes (Jopling and denHertog, 2007), and active human RhoA and Rac1 (Jopling and den Hertog, 2005) as described previously. Phenotypes were assessed at indicated stages, based on morphology or based on *dlx3/hgg1* markers at 10 hpf.

Western blot

Embryos were grown until 52 hpf and were deyolked with deyolking buffer (1/2 Ginzburg Fish Ringer) without calcium (Link et al., 2006; Westerfield, 1995). Subsequently embryos were grinded in buffer containing 50 mM Tris, pH 7.5, 150 mM NaCl, 1 mM EDTA, 1 mM sodium orthovanadate, 1% Nonidet P-40, 0.1% sodium deoxycholate, and protease inhibitor mixture (Complete Mini, Roche Diagnostics) and lysed using a syringe. Lysates were centrifuged at 14,000 g to pellet cellular debris. Lysates were subjected to SDS-PAGE and blotted (amount loaded per lane corresponds to 15 embryos). After transfer the membrane was stained with Coomassie Blue stain to verify equal loading of the lysates. Subsequently the PVDF membrane was blocked with 1% BSA or 5% Milk and then incubated with the corresponding antibodies against pSrc418 (1:1000, BioSource Technologies), actin (1:5000, kindly provided by MP Peppelenbosch, University Medical Center Groningen, the Netherlands) and antiserum against RPTP α #5478 (1:1000; den Hertog et al., 1994) followed by the horseradish peroxidase conjugated secondary antibody. The membranes were subjected to detection by enhanced chemiluminescence.

Confocal microscopy

Histone 1 injection

The embryos were injected at the 1-cell stage with Histone 1 tagged with Alexa fluor 488 from Molecular Probes (H1).

Image acquisition

For time-lapse imaging the embryos were dechorionated (at 30% epiboly) and mounted at shield stage in 1% low melting point agarose in E3 embryo rearing medium and covered with E3 in a culture dish with a glass coverslip replacing the bottom. A Leica SP2 confocal microscope with a 40x objective was used for live imaging of the Alexa 488 signal using a 488 nm laser line for excitation. Temperature was maintained at approximately 28.5 °C on a heated stage. Time points were recorded every 2 min from shield stage until 1-somite stage.

Positioning

The H1-injected embryos are positioned with the dorsal side against the coverslip approximately 100 μ m anterior to shield position. At this position the

C&E cell movements of the epiblast can be clearly visualized.

Analysis

Time-lapse images were analyzed using ImageJ (<http://rsbweb.nih.gov/ij/>). The nuclear labeling is used to determine the position of the individual cells in a single optical slice for each time point. In the images the embryo is positioned with the anterior side towards the top of the image. The Cartesian coordinates of cell tracks generated in this way will represent the contribution of cell migration to convergence (X-axis) and extension (Y-axis).

Detection and tracing of cell positions

Due to the innate changes in intensity, size and shape of H1 signal of the nuclei additional image processing is needed for efficient tracing of the cells. Making the images binary solves the problem of variable fluorescent intensities. The occasionally occurring of fused objects is handled by a watershedding process which is able to re-separate most fused objects. These objects still change during the time-lapse run in size and shape. Eroding every object to a single pixel generates an image with single point markings representing the individual positions of each object. For tracing purposes these single pixels need to be dilated. When the resulting image is re-projected onto the original it shows that the generated objects represent cell positions with a very high accuracy. The objects generated are readily traced with an algorithm plugin which implements the feature point detection and tracking algorithm as described in Sbalzarini and Koumoutsakos (2005). The algorithm generates a report with the Cartesian coordinates for all traced objects at each time point.

Quantification

During mid-gastrulation the general cell movements visualized with this method are in the extension direction. The Y-coordinates of the cell tracks are used as a measurement for the contribution of these cell tracks to extension of the embryo. The individual movements between time frames in the Y-direction of the traced cells are quantified. During late gastrulation the general cell movements visualized with this method are in the convergence direction. The X-coordinates of the cell tracks are used as a measurement for the contribution of these cell tracks to convergence of the embryo. The individual movements between time frames in the X-direction of the traced cells are quantified. The statistical analysis has been performed by the Microsoft Excel Student t-test assuming unequal variances with $\alpha=0.05$.

Cell shape analysis

To achieve ubiquitous fluorescent membrane labeling, the embryos were

injected at 1 cell stage with 20 pg of mRNA encoding membrane-citrine (a YFP variant with a C-terminal fusion of the Ras membrane localization sequence [CAAX]). To visualize the cell shape in the presomitic mesoderm, membrane-citrine expressing live embryos were mounted in 0.75% soft agarose at the dorsal side in glass bottomed Petri dishes. Using a SP2 Leica confocal microscope the presomitic mesoderm was imaged using a 40x oil objective. Images were processed in ImageJ and, analysis of cell length-to-width ratio and angular deviation was performed by the Shape_Descriptor1u plugin (Syverud et al., 2007).

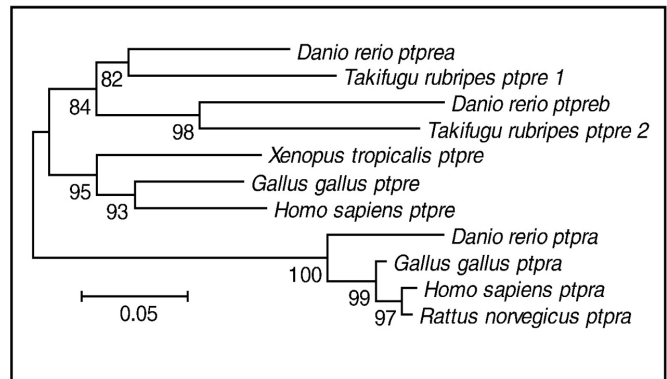
Results

Identification and expression of zebrafish *ptpra*, *ptprea* and *ptpreb*

To assess the function of *ptpra* and *ptpre* in early vertebrate development we set out to identify these genes in the zebrafish genome. We blasted the PTP domain of human RPTP α and PTP ϵ respectively against the zebrafish genome Zv7 in the Ensembl database. Candidate gene hits were found based on homology of the PTP domain and similarity of the overall protein structure. They were blasted back against the human genome and aligned with RPTP α and PTP ϵ of several species to validate these hits (Fig. 1), using Mega4 software (Tamura et al., 2007). Upon aligning it became apparent that the zebrafish genome contains one ortholog for RPTP α and two for PTP ϵ , named PTP ϵ a (*ptprea*) and PTP ϵ b

Fig. 1. RPTP α and PTP ϵ are conserved in the zebrafish genome.

Protein sequences were obtained from Ensembl database of RPTP α and PTP ϵ from *fugu*, *Xenopus*, chicken and human. The N-terminal phosphatase domains were used to align with the zebrafish RPTP α and two PTP ϵ (N-terminal phosphatase) protein sequences using the MEGA4 program. The evolutionary history was inferred using the Neighbor-Joining method.



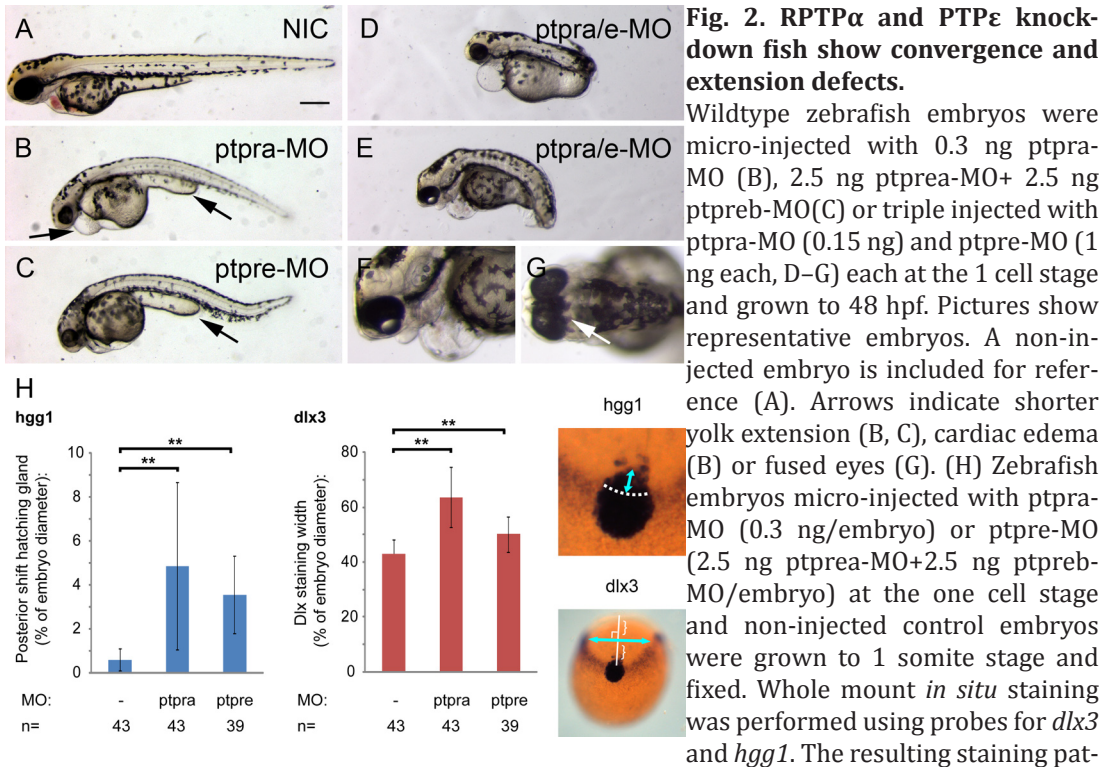
The optimal tree with the sum of branch length = 0.96066757 is shown. The percentage of replicate trees in which the associated taxa clustered together in the bootstrap test (500 replicates) is shown next to the branches. The tree is drawn to scale, with branch lengths in the same units as those of the evolutionary distances used to infer the phylogenetic tree. The evolutionary distances were computed using the Dayhoff matrix based method and are in the units of the number of amino acid substitutions per site. All positions containing alignment gaps and missing data were eliminated only in pairwise sequence comparisons (pairwise deletion option). There were a total of 264 positions in the final dataset.

(*ptpreb*) henceforth. Zebrafish *ptpra* was found on chromosome 21 and annotated as *ptpra* (ENSDARG00000001769) and the coding sequence is consistent with the cDNA that we cloned previously (accession number Y15874) (van der Sar et al., 2002). *Ptprea* was found on chromosome 3, annotated as LOC567443 (ENSDARG00000015891); *ptpreb* was found on chromosome 17, annotated as NP_001038642.1 (ENSDARG00000021151). The zebrafish orthologs are highly homologous to human and mouse RPTP α and PTP ϵ , showing 77%, 68% and 72% protein sequence identity to human and 75%, 71% and 72% protein sequence identity to mouse, respectively.

In order to reveal the expression patterns of *ptpra*, *ptprea* and *ptpreb* respectively, we generated *in situ* probes as described in the Materials and methods section. In short: a nested PCR was performed on a cDNA library to generate PCR products spanning approximately 800 bp of the *ptpra*, *ptprea* and *ptpreb* cDNAs and introducing a T7 tag for antisense RNA transcription on the 3' end. The probes were verified by sequencing. *In situ* hybridization experiments show that *ptpra*, *ptprea* and *ptpreb* are ubiquitously expressed during early stages of zebrafish development (Fig. S1). At later stages (24 hpf, 36 hpf and 72 hpf) *ptpra*, *ptprea* and *ptpreb* are broadly expressed with enhanced levels of expression in the anterior parts of the embryo. The PCR products were verified by sequencing and since we detected mRNA expression of all three genes, we conclude that they all are functional genes.

RPTP α and PTP ϵ knockdown induced C&E defects during gastrulation

In order to knockdown expression of RPTP α and PTP ϵ , we designed splice donor MOs targeting the exon immediately upstream of the catalytic site of these genes and injected them at the one cell stage. We found that 0.3 ng *ptpra*-MO consistently produced specific defects in embryonic development. *ptprea*-MO or *ptpreb*-MO by themselves did not induce phenotypes, even at high concentrations. However, 2.5 ng *ptprea*-MO together with 2.5 ng *ptpreb*-MO induced specific defects, suggesting redundancy between the two *ptpre* genes. Henceforth, *ptprea*-MO and *ptpreb*-MO were co-injected and referred to as “*ptpre*-MOs”. The earliest visible defect for both *ptpra*-MO and *ptpre*-MOs was at 10 hpf when the embryo fails to extend properly around the yolk. At later stages (2 dpf) the RPTP α knockdown and PTP ϵ knockdown embryos were shorter and *ptpra*-MO injected embryos developed edemas around the heart and yolk (Figs. 2B, C). When co-injected, *ptpra*-MO and *ptpre*-MOs induced an increasingly severe phenotype even when lower amounts of morpholino were used. Occasionally, we observed a phenotype resembling the *silberblick* mutant phenotype (Heisenberg et al., 2000) and the Fyn/Yes knockdown phenotype (Jopling and den Hertog, 2005), with a subset of fish showing severe cyclopia (Figs. 2D–G). The phenotype was reminiscent of C&E defects and to verify that knockdown of RPTP α and PTP ϵ affected



C&E, morpholino injected embryos were fixed at the 1 somite stage and stained for *dlx3* (edges of the neural plate) and *ctsl1b* (referred to in this article as *hgg1*; precursor of the hatching gland) by whole mount *in situ* hybridization (Fig. 2H). C&E phenotypes were assessed by measuring the posterior shift of the hatching gland and the widening of the *dlx3* staining in injected and control embryos as indicated in the inset of Fig. 2H. The average lengths were plotted as a percentage of the embryo diameter and compared to control embryos by Student t-test. We found that knockdown of RPTP α or PTP ϵ severely affected C&E movements (Fig. 2H).

In order to establish the effectiveness of the RPTP α knockdown, we analyzed RPTP α protein levels in zebrafish lysates by immunoblotting with an immunoserum against mouse RPTP α . We found that *ptpra*-MO reduced RPTP α protein expression in a dose-dependent manner (Fig. 3A). We proceeded to co-inject

morpholinos with varying amounts of RNA encoding mouse RPTP α or PTP ϵ , which are not recognized by their respective morpholinos. RPTP α or PTP ϵ RNA rescued the observed phenotypes when co-injected with *ptpra*-MO or *ptpre*-MO, respectively (Figs. 3B–D). Injection of RPTP α or PTP ϵ RNA at these concentrations by itself did not affect early zebrafish development morphologically (data not shown). As a control, we co-injected similar amounts of GFP RNA, which did not rescue these phenotypes (Fig. S2). We conclude that the RPTP α and PTP ϵ knockdowns were specific and induced phenotypes that were consistent with defects in C&E cell movements.

C&E defects in ptpra^{-/-} zebrafish embryos

In search of genetic mutants that lack functional RPTP α , we used targeted gene inactivation (Wienholds et al., 2002) and identified a nonsense mutation in exon 3 of *ptpra*. The identified *ptpra^{hu3334}* allele has a TTG–TAG codon change resulting in a L133X premature stop in the extracellular region of RPTP α , likely rendering the protein non-functional and henceforward referred to as *ptpra^{+/-}* for heterozygous and *ptpra^{-/-}* for homozygous mutant alleles (Fig. 4A). Incrosses of heterozygous *ptpra^{+/-}* fish led to morphological defects in a Mendelian ratio. These defects were detectable from 24 hpf onwards. In order to verify that RPTP α protein expression was affected, heterozygous *ptpra^{+/-}* fish were incrossed and the offspring was sorted based on phenotype. At 52 hpf embryos were lysed and analyzed by immunoblotting with an anti-RPTP α antibody (Fig. 4B). RPTP α expression was readily detectable in morphologically wildtype embryos (siblings), whereas RPTP α protein was hardly detectable in mutant embryos. Expression of actin was monitored to control for equal protein loading. The genotype of the embryos that were used for immunoblotting could not be determined because lysis for immunoblotting is not compatible with genotyping procedures. Nevertheless, these results demonstrate that RPTP α protein expression is abolished in roughly a quarter of the offspring of an incross of heterozygous *ptpra^{+/-}* fish, which are likely homozygous mutant embryos.

Incrosses of *ptpra^{+/-}* fish were separated based on morphology and development was followed over time. Finally, the genotype of these embryos was determined by sequencing of *ptpra* exon 3. Homozygous mutant embryos can be identified as early as 24 hpf, having shorter yolk extensions and a shorter body axis (Figs. 4C, F, arrow). Starting from around 48 hpf these embryos developed cardiac edemas (Figs. 4D, G). The phenotype of *ptpra^{-/-}* embryos was very similar to *ptpra*-MO injected embryos, as *ptpra*-MO injected embryos generally had shorter yolk extensions and also developed cardiac edemas (*cf.* Figs. 4D and 2B). At later stages these edemas grew bigger and caused blood circulation to stop. Homozygous mutant embryos died around 5–6 dpf with massive cardiac edemas.

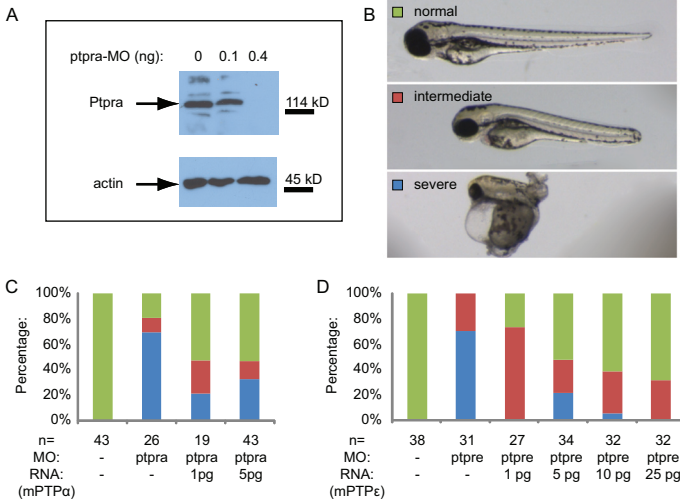


Fig. 3. RPTP α knockdown abolished protein expression and both RPTP α and PTP ϵ knockdowns were rescued by co-injection of RNA.

(A) Zebrafish embryos were micro-injected at the 1 cell stage with *ptpra*-MO (0.1 ng/embryo or 0.4 ng/embryo) and grown to 52 hpf. Embryos were dechorionated, deyolked and lysed using sodium orthovanadate and protease inhibitors. Samples of non-injected control and MO injected embryos were loaded on SDS-PAGE in such a way that all samples contain equal amounts of protein. Immunoblots were analyzed for expression of

RPTP α and actin as a loading control. (B–D) Zebrafish embryos were micro-injected with *ptpra*-MO (C) or *ptpre*-MO (D) with or without mRNA encoding mouse RPTP α (C) or PTP ϵ (D). Embryos were grown to 2 dpf and phenotypes were assigned as indicated in panel B, where embryos scored as normal resemble non-injected control, embryos with overall normal looking phenotype and body plan but shortened body axis were labeled as intermediate, and embryos with severely disrupted morphology were labeled severe.

The morphological defects from 24 hpf onwards were consistent with defects in C&E cell movements during gastrulation that are known to result in reduced embryonic axis extension. To verify that *ptpra*^{-/-} mutants have defective C&E movements, embryos from *ptpra*^{+/-} incrosses were fixed at the 1 somite stage and stained for *dlx3* and *hgg1* using whole mount *in situ* hybridization (Fig. 4I). The embryos were scored in a similar fashion as described above. After individual staining and scoring, the embryos were genotyped. Whereas the phenotype was not fully penetrant, homozygous *ptpra* mutants displayed a significant increase in posterior shift of the hatching gland and widening of the neural plate, which was consistent with the RPTP α knockdown phenotype. Although no differences between wildtype siblings and heterozygous embryos were observed at later stages, heterozygous embryos sometimes appeared to show an intermediate phenotype when looking at *dlx3/hgg1* staining at the 1 somite stage. This might be due to a dosage effect but because the effect was not consistently observed, we did not investigate this any further. To verify that the observed phenotype was indeed caused by lack of RPTP α we injected embryos from a *ptpra*^{+/-} incross at the 1 cell stage with 10 pg *zf-ptpra* mRNA. Injection of RNA reduced the number of mutant embryos showing defective C&E as assessed by analyzing *dlx3* and *hgg1* expression to levels observed in siblings (Fig. 4I). We conclude that homozygous *ptpra*^{-/-} embryos display C&E defects that were rescued by microinjection of *ptpra* RNA.

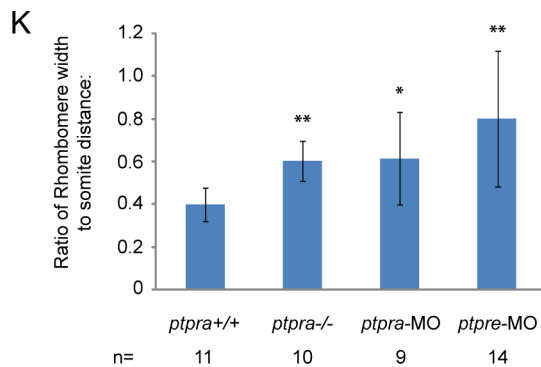
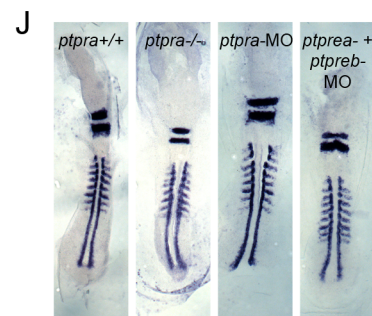
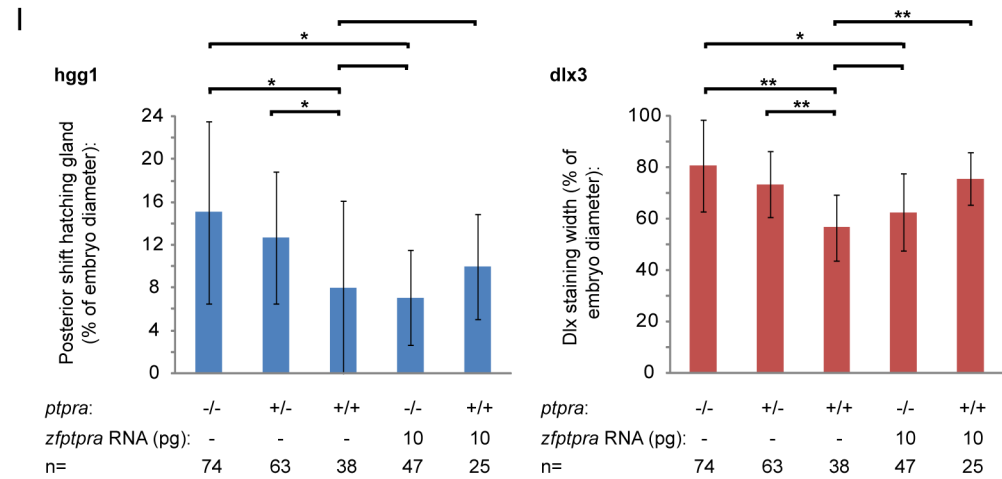
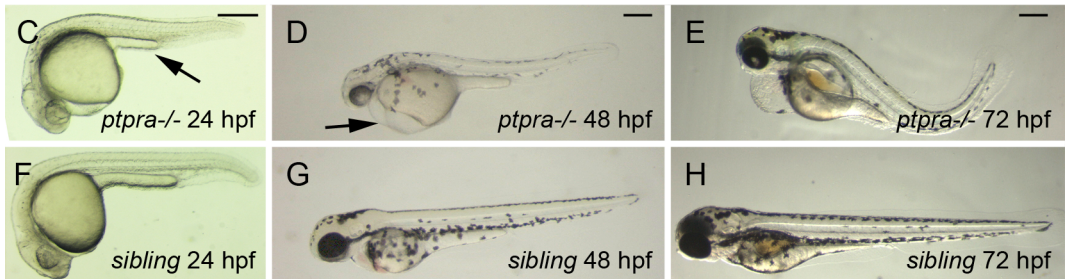
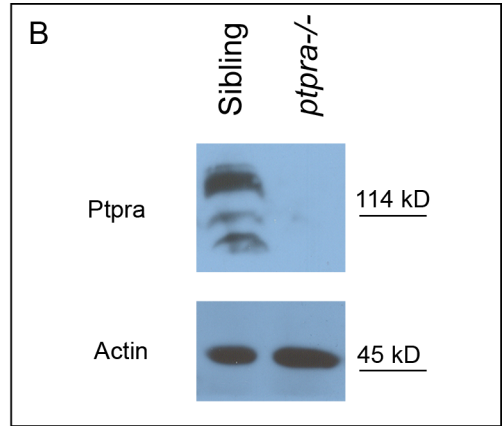
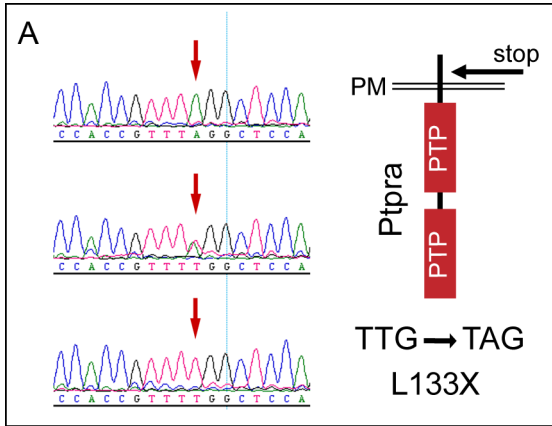


Fig. 4. A *ptpra* stop mutation phenocopied the *ptpra* knockdown and can be rescued by *zf-ptpra* mRNA.

(A) A *ptpra* mutant (hu3334) was identified by target selected gene inactivation. Homozygous mutant (top), heterozygous (middle) and wildtype (bottom) sequences are depicted here and the TTG to TAG codon change resulting in a L133X stop in the extracellular domain is indicated. (B) Heterozygous *ptpra*^{+/-} fish were in-crossed and their offspring was grown to 52 hpf. Embryos were characterized as mutant or sibling based on observed phenotype, dechorionated, deyolked and lysed using sodium orthovanadate and protease inhibitors. The resulting lysates were analyzed for RPTP α expression. Actin expression was monitored as a loading control. Heterozygous *ptpra*^{+/-} fish were in-crossed and offspring embryos were photographed and genotyped at 24 hpf (C, F), 48 hpf (D, G) and 72 hpf (E, H). Mutants (A–C) and siblings (D–F) are shown. (I) Heterozygous *ptpra*^{+/-} fish were in-crossed and embryos were either grown to 1 somite stage and fixed without injection, or micro-injected at the one cell stage with 10 pg/embryo *zf-ptpra* mRNA and then grown to 1 somite stage and fixed. Whole mount *in situ* staining was performed using probes for *dlx3* and *hgg1*. The resulting staining patterns were analyzed by measuring the posterior shift of the hatching gland and the width of the *dlx3* staining as described in Fig. 2H. After pictures were taken embryos were lysed and genotyped. The average posterior shift of the hatching gland (*hgg1*) or width of the *dlx3* staining is plotted as a percentage of the embryo (yolk) diameter. (J) Heterozygous *ptpra*^{+/-} fish were in-crossed and embryos were grown to 8 somite stage and fixed, or wildtype embryos were micro-injected at the one cell stage with 0.3 ng/embryo *ptpra*-MO or *ptpre*-MO and then grown to 8 somite stage and fixed. Whole mount *in situ* staining was performed using probes for *krox20* and *myod*. The resulting staining patterns were analyzed by measuring the rhombomere width and the distance from the 1st to the 8th somite. *Ptpra* in-cross embryos were subsequently genotyped. For each group a representative embryo is shown. The rhombomere width and the distance from the 1st to the 8th somite were measured. The resulting ratio was plotted (K). Mutant and knockdown embryos were compared to wildtype embryos. Error bars in all graphs indicate standard deviations, Student t-tests were performed (2 tailed, assuming unequal variance) between indicated groups where ** indicates a P-value<0.001, * a P-value<0.05 and no asterisk indicates no significant difference, P-value<0.05. Scalebars=250 μ m.

To further characterize the C&E defect phenotype in mutant and knockdown embryos we performed *in situ* hybridization experiments with *krox20* and *myod* probes at the 8 somite stage (Li et al., 2008) (Fig. 4J). We analyzed mutant and knockdown embryos and compared them to wildtype siblings by determining the ratio of rhombomere width and distance from the 1st to the 8th somite (Fig. 4K). We found a significant increase in rhombomere width to somite distance ratio, indicating shorter and wider embryos. These results are consistent with the conclusion that the loss of RPTP α or PTP ϵ by knockdown or mutation led to C&E defects.

RPTP α and PTP ϵ do not affect cell specification

RPTP α and PTP ϵ have been reported to affect several distinct signaling pathways (Gil-Henn and Elson, 2003; Lacasa et al., 2005; Maksumova et al., 2005; von Wichert et al., 2003). These pathways may affect cell specification, which may hamper interpretation of the results from the *dlx3/hgg1* staining, in that defects

in cell specification may be mistaken for C&E defects. To ensure that cell specification is not affected and the defects we observed in the experiments described above are due to C&E cell movements, we performed *in situ* hybridization with 6 hpf old MO injected embryos, mutant embryos and siblings using a panel of markers that are all known to be involved in cell specification (Fig. 5): *bone morphogenetic protein 2b* (*bmp2b*) specifies cells with ventral fates, *chordin* (*chd*) and *goosecoid* (*gsc*) are dorsalizing factors in the zebrafish organizer and *notail* (*ntla*) is a mesodermal marker. None of these markers displayed any major differences when RPTP α or PTP ϵ knockdown or mutant embryos were compared to sibling embryos. *Goosecoid* expression in *ptpra*^{-/-} embryos appeared to be located more towards the leading edge and was not properly localized towards the animal pole, which might reflect C&E cell migration defect. Taken together, these results show that dorsal-ventral specification was not affected in homozygous *ptpra* mutant, RPTP α or PTP ϵ knockdown embryos, suggesting that the observed defects were due to defective morphogenetic cell movements, not to defects in cell specification during gastrulation.

Visualizing C&E cell migration patterns and intercalation

In order to visualize C&E cell movements, we proceeded to track epiblast cells during zebrafish gastrulation using confocal fluorescent microscopy. Zebrafish embryos were injected at the 1 cell stage with fluorescently labeled Histone 1 (H1) protein, labeling all nuclei. For time-lapse imaging the embryos were dechorionated at 30% epiboly and mounted at shield stage in 1% low melting point agarose. The H1-injected embryos were positioned with the dorsal side against the coverslip approximately 100 μ m anterior to shield position and im-

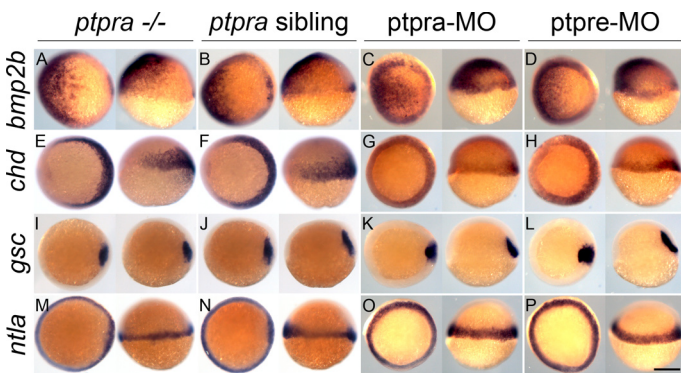


Fig. 5. No cell specification defects in *ptpra* mutant or RPTP α and PTP ϵ knockdown embryos. Embryos were fixed at 6 hpf and whole mount *in situ* hybridization was performed using probes for *bmp2b*, *chordin* (*chd*), *goosecoid* (*gsc*) or *no tail* (*ntla*). Embryos from *ptpra*^{+/-} incrosses were processed and genotyped after *in situ* hybridization. Alternatively, embryos injected at the 1-cell stage with *ptpra*-MO (0.3 ng/embryo) or

ptpre-MO (2.5 ng *ptprea*-MO+2.5 ng *ptpreb*-MO/embryo) were used. Each panel depicts on the left: animal pole view with dorsal to the right; on the right: lateral view with dorsal to the right. Scale bar=250 μ m.

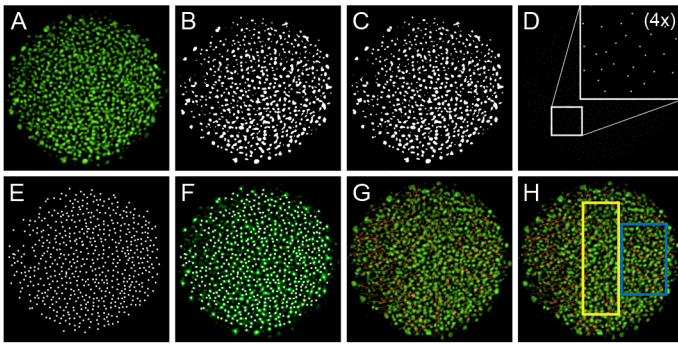
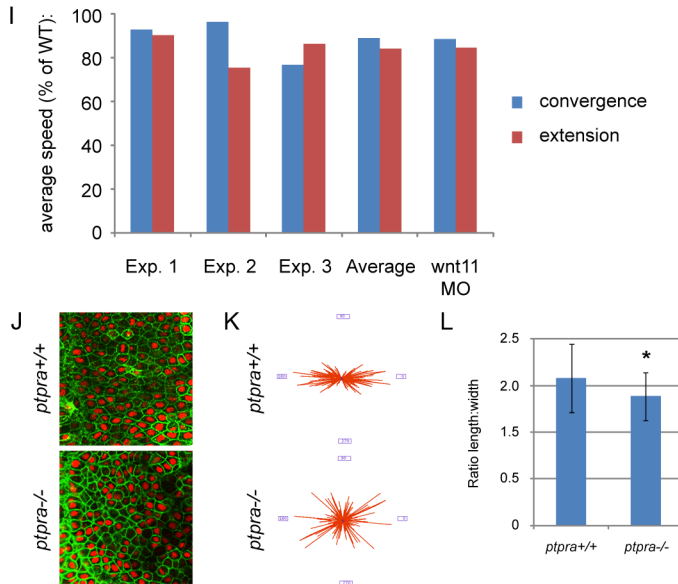


Fig. 6. Decreased convergence and extension cell migration speed and cell intercalation in *ptpra*^{-/-} mutant.

Image processing used for cell tracking in order to quantify migration speeds: (A) original single Z-slice image acquired by confocal imaging of a wildtype embryo micro-injected with fluorescently labeled Histone 1 protein, (B) binary image, (C) binary image processed by watershed segmentation, (D) all objects are eroded to a single pixel (inset shows 4× magnification for clarity), (E) every pixel is dilated, (F) projection of the resulting objects used for tracing onto the original image, (G) tracks generated by tracking algorithm projected onto the original image, (H) tracks generated by tracking algorithm projected onto the original image; the yellow rectangle indicates the area where tracks for extension speeds are collected, the blue rectangle represents the area where tracks for convergence speeds are collected. (I) *Ptpra*^{+/-} fish were in-crossed and embryos were in-



jected with Alexa Histone 1. Subsequently, 4–6 embryos were imaged in parallel using confocal microscopy starting from shield stage. Images were processed as described above and average cell migration speed was calculated by dividing the track length by the number of frames. For every experiment the average speed was calculated in either the convergence or the extension direction for typically more than 1000 cells per embryo. The embryos were subsequently genotyped and the average convergence and extension speeds in *ptpra*^{-/-} mutant embryos were plotted as a percentage of the average speeds in wildtype siblings for every experiment individually. The average of the 3 experiments is indicated as well. As a positive control, convergence and extension speed was determined in *wnt11* knockdown embryos, that are well known to have convergence and extension cell movement defects. The average reduction determined in 3 independent experiments is shown. (J) *Ptpra*^{+/-} fish were in-crossed and embryos were injected with YFP-CAAX and H2A-mCherry RNA. Embryos were mounted and imaged at late gastrulation stage posterior of the future site of the first somite in the region next to the notochord. After imaging embryos were genotyped. Shown are mutant and wildtype embryos. Obtained images were processed and the angles of cells were determined using ImageJ software and Shape_Descriptor1u plugin (Syverud et al., 2007). Resulting angles are from 2 mutant embryos and 2 wildtype embryos and are plotted in a rose diagram (K). Length and width of the cells were determined in a similar fashion and the ratios were plotted (L). Mutants were compared to wildtype data using Student t-test, error bars represent standard deviation, asterisk indicates a P-value<0.001.

aged at 40x magnification. At this position the C&E movements of the epiblast can be clearly visualized. We recorded from shield stage until 1-somite stage with 2 minute intervals. Time-lapse images were analyzed using ImageJ. The nuclear labeling was used to determine the position of individual cells in a single optical slice for each time point (Fig. 6A). To account for z-drift the imaged volume region included the enveloping layer (EVL), epiblast, hypoblast, and the yolk syncytial layer with 4 μm spacing between the z-positions. The difference between the epiblast and EVL was straightforward since the EVL nuclei were larger and clearly distinguishable from epiblast nuclei. The difference between hypoblast and epiblast was evident because of the difference in dynamics of the axial mesendoderm cells to the overlying epiblast. From shield stage to 65%–70% epiboly the axial mesendoderm cells migrated anteriorly while the overlying epiblast cells were slightly moving towards the vegetal pole undergoing the early gastrulation epiboly movement. The layers were also clearly separated by Brachet's cleft. Using these parameters the z-position of the epiblast cells was readily determined in the data. 2D cell tracing for the epiblast was performed at this z-position. In case of z-drift the position of tracing was adjusted accordingly to a lower or higher position at the time point of the drift.

Cell tracing, C&E analysis and image processing

Time-lapse images were analyzed using ImageJ. This 2D image analysis program was amenable at this magnification in this region because the imaged region used for analysis was approximately flat and the region got even more flattened because of the positioning against the coverslip. The slight tissue curvature which was still apparent was both present in the mutant and wt control embryos and as such accounted for when calculating the relative differences of the cell migrations (data not shown). In the images the embryo was positioned with the anterior side towards the top of the image. The Cartesian coordinates of cell tracks generated in this way represented the contribution of cell migration to convergence (X-axis) and extension (Y-axis). The cells were readily traced after some image processing (see below) with an algorithm that implemented feature point detection and tracking (Sbalzarini and Koumoutsakos, 2005). The algorithm generated a report with the Cartesian coordinates for all traced objects at each time point. Using the coordinates we were able to calculate >1000 cell movements per analyzed embryo, which were used to determine the average contribution of the individual cell tracks to convergence (Y-direction) or extension (X-direction, Fig. 6H). Tracks used for the analysis of extension were calculated from cells at the axial epiblast region at time points between 70% and 90% epiboly. Tracks used for the analysis of convergence were calculated from cells at the paraxial region at time points between 90% epiboly and 1-somite stage from the same dataset.

Due to the innate changes in intensity, size and shape of H1 signal of the

nuclei, we developed additional image processing for efficient tracing of the cells. Making the images binary solves the problem of variable fluorescent intensities (Fig. 6B). The occasional occurrence of fused objects was handled by a watershed process which re-separated most fused objects (Fig. 6C). These objects still changed during the time-lapse run in size and shape. Eroding every object to a single pixel generated an image with single point markings representing the individual positions of each object (Fig. 6D). For tracing purposes these single pixels were dilated (Fig. 6E). When the resulting image was re-projected onto the original it was evident that the generated objects represented cell positions with a very high accuracy (>99%, Fig. 6F).

*Reduced C&E movements in *ptpra*^{-/-} embryos*

We used the tracking method described above to quantify C&E cell movements in *ptpra*^{-/-} embryos and to compare with wildtype siblings. To this end, heterozygous *ptpra*^{+/-} fish were in-crossed and four to six embryos were mounted and imaged as described above. When comparing *ptpra*^{-/-} mutants with wildtype embryos great precaution was taken to position the embryos in a similar way. The exact imaging position was determined retrospectively using embryonic features, including otoliths and somites that had developed at the end of the run as coordinates. Data from embryos that were not positioned correctly or that moved slightly during imaging were discarded. Following imaging, the embryos were genotyped by sequencing. The relative speed of cells in *ptpra*^{-/-} embryos compared to wildtype siblings from 3 independent experiments is plotted in Fig. 6I. We consistently found a reduction in migration speed in both X-direction (convergence) and Y-direction (extension) for mutant embryos. The statistical analysis has been performed by Student t-test assuming unequal variances with alpha=0.05. Since the data for every experiment consisted of over 1000 data-points for every experiment, *P*-values were much lower than 0.0001. We still detected a fluctuation between values of the relative speed for mutants between experiments, which could be accounted for by small differences from experiment to experiment in temperature inside the imaging chamber or slight differences in positioning of the embryo. In order to validate our method we used a well known regulator of C&E to assess its effect on cell migration speed in our setup. We used *wnt11*-MO injected embryos and found a reduction in migration speed compared to non-injected siblings in convergence (12%) and extension (15%), which was comparable to the measured reduction of migration speed in *ptpra*^{-/-} embryos compared to siblings (Fig. 6I). In conclusion, we have developed a method to reliably quantify C&E cell movements using time-lapse confocal microscopy. Using this method, we found that the average relative speed of C&E cell movements during gastrulation was significantly reduced in *ptpra*^{-/-} mutant embryos compared to wildtype siblings.

Mutant embryos have cell intercalation defects

One of the underlying mechanisms of C&E is cell intercalation and medio-lateral elongation (Concha and Adams, 1998; Myers et al., 2002). We used membrane labeling by YFP-CAAX to determine the cell shape of intercalating cells in late gastrulation. Injected embryos were mounted and the presomitic mesoderm was imaged posterior to the site of the future first somite in the region neighboring the notochord as described (Jessen et al., 2002). We used ImageJ software and the Shape_Descriptor1u plugin (Syverud et al., 2007) to analyze the angle of the cells towards the notochord and the ratio of length to width of the cells. We found that indeed in *ptpra*^{-/-} mutants the ratio of length:width is significantly reduced (Student t-test, $P < 0.001$) and angles towards the notochord are distributed more randomly (Figs. 6J–L). This further reinforces the role of RPTP α in C&E.

*Simultaneous knockdown of RPTP α and PTP ϵ phenocopied *silberblick**

C&E movements are regulated by the non-canonical Wnt signaling pathway. The main players in this pathway are Wnt5 and Wnt11, which activate downstream Rho-like GTPases instead of β -catenin as is the case in canonical Wnt signaling (Veeman et al., 2003). Mutation or knockdown of Wnt11 results in defects in embryonic axis extension in the anterior regions of the embryo (Heisenberg et al., 2000), whereas mutation or knockdown of *wnt5* results in defects in the posterior regions of the embryo (Kilian et al., 2003), reflecting the expression patterns of Wnt11 and Wnt5, respectively. As shown above, co-injection of *ptpra*-MO and *ptpre*-MO caused a phenotype resembling the *wnt11* mutant/*silberblick* phenotype. Co-injection of *ptpra*-MO and *ptpre*-MO resulted in severe defects and early embryonic lethality. At lower concentrations, co-injection resulted in cyclopia in ~10% of the embryos (data not shown). Injection of *ptpre*-MO in *ptpra*^{-/-} fish resulted in cyclopic fish as well (data not shown). We proceeded to quantify the number of cyclopic fish upon co-injection of *ptpra*-MO and *ptpre*-MO with Wnt11-MO (Fig. 7). Low amounts of *ptpre*-MO together with low concentrations of Wnt11-MO induced a high percentage of cyclopic fish (>60%), whereas *ptpra*-MO together with Wnt11-MO induced a high percentage of fish with a severe phenotype (>60%). Injection of single morpholinos at these reduced concentrations resulted in hardly any phenotype (Fig. 7). Together, these results suggest that RPTP α and PTP ϵ function either in the same pathway as Wnt11, or they have a common downstream target with Wnt11.

RPTP α and PTP ϵ signal upstream of RhoA and Fyn/Yes

The major downstream targets of the non-canonical Wnt signaling pathway are the small GTPases, Rac and RhoA. To test if these might be common downstream targets for both Wnt11 signaling and RPTP α and PTP ϵ , we investigated whether co-injection of mRNA coding for constitutively active Rac or RhoA res-

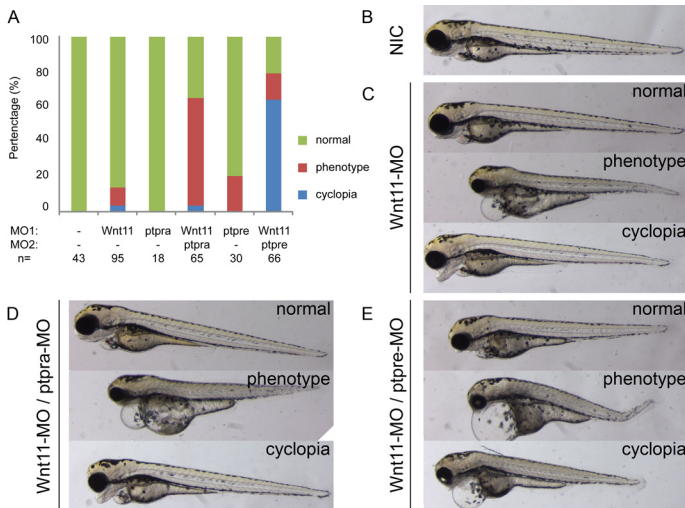


Fig. 7. RPTP α and PTP ϵ knockdown phenotypes were enhanced by *wnt11* knockdown and induced cyclopia.

(A) Zebrafish embryos were injected with low amounts of morpholino targeting RPTP α (0.15 ng/embryo), PTP ϵ (1 ng each/embryo) and Wnt11 (2 ng/embryo) and grown to 3 dpf. Embryos were scored based on morphology “cyclopia” when eyes were fused, as “phenotype” when shorter, showing abnormal morphology and/or edemas, or as “normal”. The percentages of embryos with phenotypes were plotted. Representative embryos from

each (co-)injection are depicted in panels B–E.

cued the observed C&E phenotypes. We found that both caRac and caRhoA mRNA produced severe phenotypes when injected at high doses (data not shown), and titrated to find concentration ranges that might be suitable for rescue experiments. We found that injection of 2 pg caRhoA RNA per embryo or less did not induce any phenotypes by itself. Injection of 0.5 pg caRac RNA per embryo still induced truncated or shorter embryos. We co-injected ptpra-MO or ptpre-MO with either 1 pg caRhoA RNA or 0.5 pg caRac RNA and found that the penetrance and severity of the phenotype was reduced by co-injection of caRho RNA, but not caRac RNA (Figs. 8A, B). As read-out for the phenotype we measured body axis extension, i.e. the length of the tail, a hallmark of C&E defects (as indicated in Fig. 8B). Co-injection of caRhoA RNA led to a significant increase in body length compared to ptpra-MO or ptpre-MO alone, but caRac RNA did not alleviate the body axis extension defect (Fig. 8B). These results indicate that caRhoA, but not caRac, rescued the RPTP α and PTP ϵ knockdown phenotypes.

CaRac or caRhoA RNA was injected in *ptpra*^{+/-} incross embryos and C&E defects were determined by *dlx3/hgg1* whole mount in situ hybridization at the 1 somite stage. It is noteworthy that the phenotypes were assigned and afterwards, embryos were genotyped. We found that caRhoA significantly rescued C&E defects in *ptpra*^{-/-} embryos (Fig. 8C). CaRac improved the extension phenotype slightly as assessed by *hgg1* staining, but convergence, measured by *dlx3* staining was not rescued significantly. We generally observed that injection of caRac RNA induced poor overall morphology in mutant as well as wildtype embryos at later stages and hence we cannot conclude that caRac rescued the *ptpra*^{-/-} pheno-

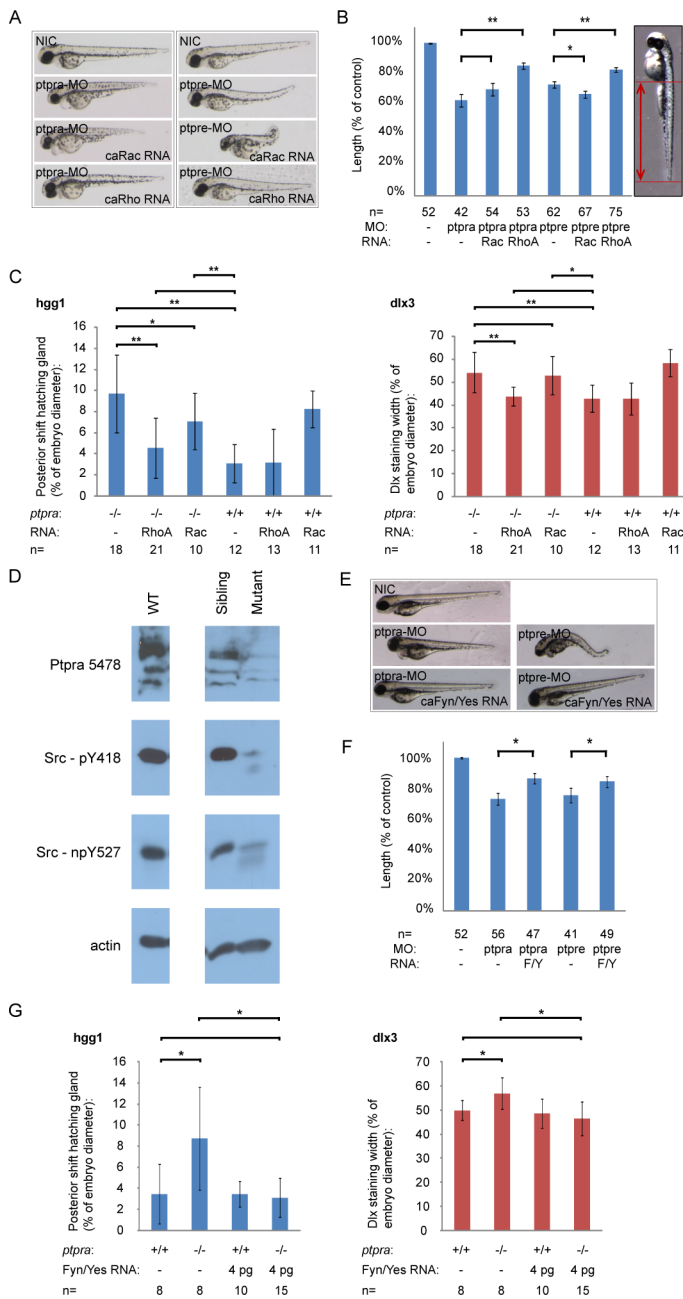


Fig. 8. RPTP α and PTP ϵ knock-down rescued by active RhoA or active Fyn and Yes.

(A) Zebrafish embryos were micro-injected at the 1-cell stage with *ptpra*-MO (0.3 ng/embryo) or *ptpre*-MO (2.5 ng *ptprea*-MO+2.5 ng *ptpreb*-MO/embryo) alone or co-injected with active Rac (1 pg/embryo) or RhoA (1 pg/embryo) mRNA. Embryos were grown to 2 dpf. Morpholino knockdown and RNA co-injection rescue experiments were done in the same clutch of embryos. The figure depicts representative embryos for every group from two independent experiments. (B) The phenotypes of all individual fish depicted in (A) were assessed by measuring tail lengths using ImageJ software. Tail lengths were depicted as a percentage of the length of non-injected control embryos. The figure represents the results of two independent experiments, where morpholino knockdown and RNA co-injection rescue experiments were performed in the same clutches of embryos. RNA co-injections were compared to their respective morpholino injections and Student t-tests were applied.* represents a P-value<0.05, ** represents a P-value<0.001, no asterisk represents no significant difference (P>0.05). (C) Heterozygous *ptpra*^{+/-} fish were in-crossed and offspring embryos were micro-injected at the 1-cell stage with either active Rac or active RhoA mRNA. Non-injected embryos were taken as a control. Embryos were grown

to 1 somite stage and fixed. Whole mount *in situ* staining was performed using probes for *dlx3* and *hgg1*. The resulting staining patterns were analyzed as described in Fig. 2H, by measuring the posterior shift of the hatching gland and the width of the *dlx3* staining. After pictures were taken and phenotypes were assigned, embryos were lysed and genotyped. The average posterior shift or width of the *dlx3* is plotted as a percentage of the embryo (yolk) diameter. (D) Heterozygous *ptpra*^{+/-} or wildtype (WT) fish were in-crossed and their offspring was grown to 52 hpf. Embryos were characterized as mutant or sibling based on observed phenotype, dechorionated, deyolked and lysed using sodium orthovanadate and protease inhibitors. Western blots were run and probed using 5478-anti RPTP α serum, Src-pY418 antibody, Src-npY527 antibody and actin

antibody as a loading control. (E) Embryos were injected with *ptpra*-MO (0.3 ng/embryo) or *ptpre*-MO (2.5 ng *ptprea*-MO+2.5 ng *ptpreb*-MO/embryo) like in figure (A) and co-injections were done with active Fyn and Yes (4 pg each/embryo) RNA. Figure represents two separate experiments; morpholino injection and RNA co-injections were done in the same clutches of embryos. A representative embryo for each injected group is shown. (F) The lengths of the embryos' tails were measured and the average was plotted. (G) Heterozygous *ptpra*^{+/-} fish were in-crossed and embryos were micro-injected in a similar fashion as in (C) with 4 pg/embryo of both active Fyn and Yes mRNA. The embryos were stained for *dlx3* and *hgg1*, analyzed and genotyped and the posterior shift of the hatching gland and the width of the *dlx3* staining were plotted for each group. Error bars in all graphs represent standard deviations. Student t-tests were performed between indicated groups, where ** indicates a P-value<0.001, * a P-value<0.05 and no asterisk no significant difference (P-value>0.05).

type. Our results indicate that caRhoA rescued the *ptpra*^{-/-} induced C&E defects, consistent with the caRhoA rescue of the *ptpra*-MO knockdown.

We recently described how Fyn and Yes play a role in C&E in zebrafish by activating RhoA in parallel with the non-canonical Wnt signaling pathway (Jopling and den Hertog, 2005). RPTP α dephosphorylates the inhibitory tyrosine phosphorylation site in the C-terminus of Src family kinases (Tyr 527 in chicken Src) thus resulting in activation of the Src family kinases (den Hertog et al., 1993; Zheng et al., 1992). Therefore we wondered whether Src family kinase phosphorylation was affected in *ptpra*^{-/-} zebrafish embryos. At 24 hpf, embryos from a *ptpra*^{+/-} incross were divided in two groups based on morphology: mutants and siblings. The embryos were lysed at 52 hpf and lysates were immunoblotted. As a control, RPTP α expression was monitored in these lysates (Fig. 8D). RPTP α protein was not detected in the mutants. The Src nonphospho (np)Tyr527 antibody is specific for non-phosphorylated Tyr527. The signal is clearly reduced in *ptpra*^{-/-} mutants, indicating that phosphorylation of this site is enhanced in mutant embryos that do not express RPTP α . Phosphorylation of Tyr416, the autophosphorylation site of Src family kinases is directly proportional to its activation state. Tyr416 phosphorylation is reduced dramatically in mutants, reflecting reduced activity of Src family kinases as a result of enhanced phosphorylation of the inhibitory Tyr527. These results demonstrate that phosphorylation of the inhibitory C-terminal Tyr527 in Src is enhanced resulting in reduced Src activity which is reflected by reduced autophosphorylation of Tyr416.

To investigate directly whether the observed defects upon knockdown of RPTP α and PTP ϵ were linked to Src family kinases, we co-injected RNA encoding active Fyn and Yes with *ptpra*-MO or *ptpre*-MO and assessed body axis extension. It is evident that Fyn and Yes significantly rescued both RPTP α knockdown as well as PTP ϵ knockdown (Figs. 8E, F). Moreover when we injected active Fyn and Yes mRNA in *ptpra*^{+/-} incross embryos and assessed the phenotype in a similar fashion as in Fig. 8C, we observed a clear reduction of the posterior shift of the

hatching gland and reduction of the width of *dlx3* staining in mutant embryos to the level of wildtype sibling (Fig. 8G), indicating that activation of the SFKs Fyn and Yes rescued the *ptpra*^{-/-} induced C&E phenotype. Our results demonstrate that Src family kinase activity was reduced in *ptpra*^{-/-} fish and that Src family kinases rescued RPTP α and PTP ϵ knockdown induced defects, firmly placing Src family kinases downstream of RPTP α and PTP ϵ in C&E cell movements.

Discussion

C&E cell movements during gastrulation are tightly regulated by several signaling pathways, including non-canonical Wnt signaling and signaling by Src family kinases. Here, we provide evidence that RPTP α and PTP ϵ are essential for C&E cell movements during gastrulation as well. RPTP α and PTP ϵ knockdown embryos as well as *ptpra*^{-/-} embryos displayed C&E defects, which were rescued by co-injection of synthetic RNAs encoding the respective proteins. We developed a cell tracking method using confocal time-lapse microscopy, which allowed us to quantify cell movements of all cells in the developing embryo. We have used this method to demonstrate that both convergence and extension cell movements were reduced in *ptpra*^{-/-} embryos. RPTP α and PTP ϵ signal upstream of Src family kinases and the small GTPase RhoA to regulate C&E cell movements.

RPTP α and PTP ϵ function in C&E movements

During axis formation in vertebrate gastrulation, dorsal mesendodermal cells become highly motile and polarized, a process regulated in part by rearrangements of actin cytoskeleton. These cells move to the midline where they intercalate, which results in extension of the embryonic body axis. We demonstrate here that RPTP α and PTP ϵ are involved in these processes and we propose that the underlying mechanism involves controlling the activity of downstream targets of the non-canonical Wnt signaling pathway. Whether the C&E defects result from reduced polarization of the cells, reduced cell adhesion or an impaired chemotactic response remains to be determined. However, these data do not simply reflect a delay in development since mutant embryos reached the 1 somite stage at the same time as sibling or wildtype embryos (data not shown). Cell specification was not affected in RPTP α or PTP ϵ knockdown embryos or *ptpra*^{-/-} embryos, ruling out that defective cell specification was at the basis of the observed defects.

Cell tracking

We adapted and employed a method to efficiently track cells in the developing embryo using time-lapse confocal microscopy. Recently, *in toto* imaging was described for zebrafish embryos in which all cells were visualized and tracked over a period of 24 h (Keller et al., 2008). Scanned light sheet microscopy was employed to allow for rapid scanning through the entire embryo. We were

interested particularly in C&E cell movements during gastrulation and we used conventional time-lapse confocal microscopy to image cell movements in an area anterior to the shield, where C&E cell movements take place during gastrulation. We improved ImageJ software, allowing us to automatically track large numbers of cells in the area of interest and to quantify cell movements in this area. Whereas we imaged the cells in 3D, we employed the data analysis in 2D, because the distortion resulting from the curvature of the embryo was minimal (up to 6% at the edges of the image, data not shown). Using this method, we reliably calculated the velocities of many individual cells and we compared C&E movements of more than 1000 cells in three independent *ptpra*^{-/-} embryos with those of cells in wildtype siblings in three independent experiments. We detected significant differences in cell movements in all three experiments with on average 11% reduced convergence and 16% reduced extension (Fig. 6). In principle this method can be used to detect changes in all kinds of cell movements and only requires time-lapse imaging using a conventional (confocal) microscope.

Signaling driving C&E cell movements

The β -Catenin independent wnt-PCP signaling pathway has been shown to control C&E movements (Wallingford et al., 2002). Key events in the regulation of C&E movements are the activation of RhoA and Rac1 (Habas et al., 2001; Tahinci and Symes, 2003). We have identified several other proteins that modulate this pathway, including Shp2, Csk, Fyn and Yes (Jopling and den Hertog, 2005; Jopling and den Hertog, 2007; Jopling et al., 2007). Moreover, Has2, PAPC and STAT3 have a role in the pathway as well (Bakkers et al., 2004; Miyagi et al., 2004; Unterseher et al., 2004). All of these proteins act in C&E movements by changing the activity of RhoA and/or Rac1 in dorsally migrating cells during gastrulation.

Several lines of evidence suggest a role for RPTP α and PTP ϵ in non-canonical Wnt signaling. Co-injection of *ptpra*-MO and *ptpre*-MO or injection of *ptpre*-MO in *ptpra*^{-/-} embryos resulted in cyclopia (Fig. 7), a phenotype also observed in *wnt11* mutant fish (Heisenberg et al., 1996). Co-injection of low amounts of Wnt11-MO together with low amounts of *ptpra*-MO or *ptpre*-MO specifically caused cyclopia and severe phenotypes in fish, suggesting that Wnt11 and RPTP α and PTP ϵ interact genetically. We attempted to rescue the Wnt11 knockdown phenotype by co-injection of *ptpra* or *ptpre* RNA. Coinjection of these synthetic RNAs at concentrations that rescued the respective *ptpra*- and *ptpre*-MO injections (Fig. 3) did not rescue the Wnt11-MO phenotype in a significant way (data not shown). This is consistent with our previous finding that the Src family kinases, Fyn and Yes, act in a signaling pathway parallel to non-canonical Wnt signaling, converging on RhoA. RPTP α and PTP ϵ have been shown to dephosphorylate and activate Src family kinases in cell-based assays. Here, we demonstrate that Src family kinase phosphorylation on the inhibitory C-terminal residue (Tyr527)

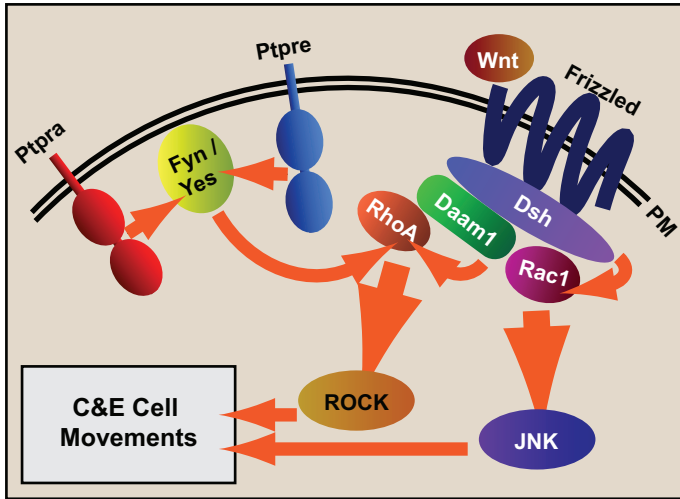


Fig. 9. RPTP α and PTP ϵ act in parallel to non-canonical Wnt signaling in C&E cell movements.

In non-canonical Wnt signaling, Frizzled is activated by binding of Wnt which results in Dishevelled (Dsh) and Daam1-mediated activation of RhoA and Rac1. In turn, Rac1 and RhoA activate Jun N-terminal Kinase (JNK) and ROCK, respectively, leading to cell polarization, actin cytoskeleton rearrangements and cell movements. RPTP α and PTP ϵ dephosphorylate and activate the Src family kinases, Fyn and Yes, leading to downstream activation of RhoA through an unknown inter-

mediate, thereby mediating convergence and extension cell movements.

was enhanced in *ptpra*^{-/-} zebrafish embryos. Autophosphorylation (on Tyr416) was reduced, indicating that Src family kinase activity was reduced in zebrafish embryos lacking functional RPTP α . Interestingly, mutant *ptpra*^{-/-} embryos and RPTP α and PTP ϵ knockdowns were rescued by active Fyn and Yes, demonstrating that these Src family kinases indeed acted downstream of RPTP α and PTP ϵ in the control of C&E cell movements (Fig. 8). Finally, we demonstrated that active RhoA, but not Rac1, rescued the RPTP α and PTP ϵ knockdown and *ptpra*^{-/-} mutant phenotype, similar to RhoA-mediated rescue of Wnt11 and Fyn/Yes knockdown (Jopling and den Hertog, 2005). These results led us to propose a model where RPTP α and PTP ϵ act in C&E cell movements in a SFK dependent pathway parallel to non-canonical Wnt signaling, modulating downstream RhoA activity (Fig. 9).

RPTP α and PTP ϵ knock out mice

Interestingly, RPTP α and PTP ϵ and even RPTP α /PTP ϵ double knock out (DKO) mice are viable (Tiran et al., 2006), whereas *ptpra*^{-/-} zebrafish were embryonic lethal. Co-injection of *ptpra*-MO or *ptpre*-MO, resulting in transient knockdown of RPTP α or PTP ϵ already caused lethality. DKO mice are shorter but retain a normal growth rate, which is consistent with a mild C&E defect phenotype. Detailed analysis of gastrulation in RPTP α and PTP ϵ knock out mice may lead to identification of subtle or transient defects in gastrulation in these mice. Moreover, analysis of the orientation of stereociliary bundles in cochleae is one of the best read-outs for planar polarity in the mouse and several knock outs of factors from the non-canonical Wnt signaling pathway display defective bundle orientation (Montcouquiol et al., 2003). It will be interesting to analyze stereocili-

ary bundle orientation in RPTP α and PTP ϵ knock out mice to establish whether these mice display subtle defects resembling the PCP signaling defects. It remains to be determined why there is a difference between mice and fish. Perhaps C&E movements are more easily affected by changes in activity of RPTP α and PTP ϵ in zebrafish embryos, or perhaps zebrafish embryos lack factors that compensate for the absence of RPTP α and PTP ϵ in mouse embryos. It will be interesting to see if DKO mice are shorter because of defects in Src family kinase signaling and/or RhoA activity. It is noteworthy that cell movements of pyramidal neurons in RPTP α knock out mice are defective (Petroni et al., 2003), and it will be interesting to see if defective RhoA signaling is at the basis of these cell movement defects in a similar manner as in C&E cell movements in zebrafish embryos.

Conclusion

In conclusion, we demonstrate here that RPTP α and PTP ϵ have an essential role in C&E cell movements during gastrulation. Moreover, RPTP α and PTP ϵ act in a signaling pathway upstream of Src family kinases and the small GTPase RhoA. It will be interesting to see what is upstream of RPTP α and PTP ϵ . Our results demonstrate that the RPTP-SFK-RhoA signaling pathway is an important regulator of C&E cell movements next to the well known non-canonical Wnt/PCP signaling pathway.

Acknowledgments

This work was supported in part by a Marie Curie Research Training Network (PTPNET/MRTN-CT-2006-035830) and a grant from the Research Council for Earth and Life Sciences (ALW 815.02.007) with financial aid from the Netherlands Organisation for Scientific Research (NWO).

References

Ardini, E., Agresti, R., Tagliabue, E., Greco, M., Aiello, P., Yang, L.T., Menard, S., Sap, J., 2000. Expression of protein tyrosine phosphatase alpha (RPTPalph) in human breast cancer correlates with low tumor grade, and inhibits tumor cell growth in vitro and in vivo. *Oncogene* 19, 4979–4987.

Bakkers, J., Kramer, C., Pothof, J., Quaedvlieg, N.E., Spaink, H.P., Hamerschmidt, M., 2004. Has2 is required upstream of Rac1 to govern dorsal migration of lateral cells during zebrafish gastrulation. *Development* 131, 525–537.

Chiusaroli, R., Knobler, H., Luxenburg, C., Sanjay, A., Granot-Attas, S., Tiran, Z., Miyazaki, T., Harmelin, A., Baron, R., Elson, A., 2004. Tyrosine phosphatase epsilon is a positive regulator of osteoclast function in vitro and in vivo. *Mol. Biol. Cell* 15, 234–244.

Concha, M.L., Adams, R.J., 1998. Oriented cell divisions and cellular morphogenesis in the zebrafish gastrula and neurula: a time-lapse analysis. *Development* 125, 983–994.

Courtneidge, S.A., 1985. Activation of the pp 60c-src kinase by middle T antigen binding or by dephosphorylation. *EMBO J.* 4, 1471–1477.

den Hertog, J., Hunter, T., 1996. Tight association of GRB2 with receptor protein tyrosine phosphatase alpha is mediated by the SH2 and C-terminal SH3 domains. *EMBO J.* 15, 3016–3027.

den Hertog, J., Pals, C.E., Peppelenbosch, M.P., Tertoolen, L.G., de Laat, S.W., Kruijer, W., 1993. Receptor protein tyrosine phosphatase alpha activates pp 60c-src and is involved in neuronal differentiation. *EMBO J.* 12, 3789–3798.

den Hertog, J., Tracy, S., Hunter, T., 1994. Phosphorylation of receptor protein-tyrosine phosphatase alpha on Tyr789, a binding site for the SH3–SH2–SH3 adaptor protein GRB-2 in vivo. *EMBO J.* 13, 3020–3032.

Gil-Henn, H., Elson, A., 2003. Tyrosine phosphatase-epsilon activates Src and supports the transformed phenotype of Neu-induced mammary tumor cells. *J. Biol. Chem.* 278, 15579–15586.

Goldstein, B., Takeshita, H., Mizumoto, K., Sawa, H., 2006. Wnt signals can function as positional cues in establishing cell polarity. *Dev. Cell* 10, 391–

Griffin, K., Patient, R., Holder, N., 1995. Analysis of FGF function in normal and no tail zebrafish embryos reveals separate mechanisms for formation of the trunk and the tail. *Development* 121, 2983–2994.

Habas, R., Kato, Y., He, X., 2001. Wnt/Frizzled activation of Rho regulates vertebrate gastrulation and requires a novel Formin homology protein Daam1. *Cell* 107, 843–854.

Habas, R., Dawid, I.B., He, X., 2003. Coactivation of Rac and Rho by Wnt/Frizzled signaling is required for vertebrate gastrulation. *Genes Dev.* 17, 295–309.

Hannus, M., Feiguin, F., Heisenberg, C.P., Eaton, S., 2002. Planar cell polarization requires *Widerborst*, a B' regulatory subunit of protein phosphatase 2A. *Development* 129, 3493–3503.

Heisenberg, C.P., Brand, M., Jiang, Y.J., Warga, R.M., Beuchle, D., van Eeden, F.J., Furutani-Seiki, M., Granato, M., Haffter, P., Hammerschmidt, M., Kane, D.A., Kelsh, R.N.,

Mullins, M.C., Odenthal, J., Nusslein-Volhard, C., 1996. Genes involved in forebrain development in the zebrafish, *Danio rerio*. *Development* 123, 191–203.

Heisenberg, C.P., Tada, M., Rauch, G.J., Saude, L., Concha, M.L., Geisler, R., Stemple, D.L., Smith, J.C., Wilson, S.W., 2000. *Silberblick/Wnt11* mediates convergent extension movements during zebrafish gastrulation. *Nature* 405, 76–81.

Herrera Abreu, M.T., Penton, P.C., Kwok, V., Vachon, E., Shalloway, D., Vidali, L., Lee, W., McCulloch, C.A., Downey, G.P., 2008. Tyrosine phosphatase PTPalpha regulates focal adhesion remodeling through Rac1 activation. *Am. J. Physiol. Cell Physiol.* 294, C931–C944.

Hsia, D.A., Lim, S.T., Bernard-Trifilo, J.A., Mitra, S.K., Tanaka, S., denHertog, J., Streblo, D.N., Ilic, D., Ginsberg, M.H., Schlaepfer, D.D., 2005. Integrin alpha4-beta1 promotes focal adhesion kinase-independent cell motility via alpha4 cytoplasmic domain-specific activation of c-Src. *Mol. Cell. Biol.* 25, 9700–9712.

Jessen, J.R., Topczewski, J., Bingham, S., Sepich, D.S., Marlow, F., Chandrasekhar, A., Solnica-Krezel, L., 2002. Zebrafish trilobite identifies new roles for *Strabismus* in



gastrulation and neuronal movements. *Nat. Cell Biol.* 4, 610–615.

Jopling, C., den Hertog, J., 2005. Fyn/Yes and non-canonical Wnt signalling converge on

RhoA in vertebrate gastrulation cell movements. *EMBO Rep.* 6, 426–431.

Jopling, C., den Hertog, J., 2007. Essential role for Csk upstream of Fyn and Yes in

zebrafish gastrulation. *Mech. Dev.* 124, 129–136.

Jopling, C., van Geemen, D., den Hertog, J., 2007. Shp2 knockdown and Noonan/

LEOPARD mutant Shp2-induced gastrulation defects. *PLoS Genet.* 3, e225.

Keller, R., Shih, J., Domingo, C., 1992. The patterning and functioning of protrusive activity

during convergence and extension of the *Xenopus* organiser. *Dev. Suppl.* 81–91.

Keller, P.J., Schmidt, A.D., Wittbrodt, J., Stelzer, E.H., 2008. Reconstruction of zebrafish early

embryonic development by scanned light sheet microscopy. *Science* 322, 1065–1069.

Kilian, B., Mansukoski, H., Barbosa, F.C., Ulrich, F., Tada, M., Heisenberg, C.P., 2003. The

role of Ppt/Wnt5 in regulating cell shape and movement during zebrafish gastrulation. *Mech. Dev.* 120, 467–476.

Lacasa, D., Boute, N., Issad, T., 2005. Interaction of the insulin receptor with the

receptor-like protein tyrosine phosphatases PTPalpha and PTPepsilon in living

cells. *Mol. Pharmacol.* 67, 1206–1213.

Lele, Z., Bakkers, J., Hammerschmidt, M., 2001. Morpholino phenocopies of the swirl,

snailhouse, somitabun, minifin, silberblick, and pipetail mutations. *Genesis*

30, 190–194.

Li, C., Inglis, P.N., Leitch, C.C., Efimenko, E., Zaghloul, N.A., Mok, C.A., Davis, E.E., Bialas, N.J., Healy, M.P., Heon, E., Zhen, M., Swoboda, P., Katsanis, N., Leroux, M.R., 2008. An essential role for DYF-11/MIP-T3 in assembling functional intraflagellar transport complexes. *PLoS Genet* 4, e1000044.

Link, V., Shevchenko, A., Heisenberg, C.P., 2006. Proteomics of early zebrafish embryos. *BMC Dev. Biol.* 6, 1.

Maksumova, L., Le, H.T., Muratkhodjaev, F., Davidson, D., Veillette, A., Pallen, C.J., 2005. Protein tyrosine phosphatase alpha regulates Fyn activity and Cbp/PAG phosphorylation in thymocyte lipid rafts. *J. Immunol.* 175, 7947–7956

Matsui, T., Raya, A., Kawakami, Y., Callol-Massot, C., Capdevila, J., Rodriguez-Esteban, C., Izpisua Belmonte, J.C., 2005. Noncanonical Wnt signaling regulates midline convergence of organ primordia during zebrafish development. *Genes Dev.* 19, 164–175.

Medina, A., Reintsch, W., Steinbeisser, H., 2000. *Xenopus* frizzled 7 can act in canonical and non-canonical Wnt signaling pathways: implications on early patterning and morphogenesis. *Mech. Dev.* 92, 227–237.

Myers, D.C., Sepich, D.S., Solnica-Krezel, L., 2002. Bmp activity gradient regulates convergent extension during zebrafish gastrulation. *Dev. Biol.* 243, 81–98.

Miyagi, C., Yamashita, S., Ohba, Y., Yoshizaki, H., Matsuda, M., Hirano, T., 2004. STAT3 noncell-autonomously controls planar cell polarity during zebrafish convergence and extension. *J. Cell Biol.* 166, 975–981.

Montcouquiol, M., Rachel, R.A., Lanford, P.J., Copeland, N.G., Jenkins, N.A., Kelley, M.W., 2003. Identification of *Vangl2* and *Scrb1* as planar polarity genes in mammals. *Nature* 423, 173–177.

Peretz, A., Gil-Henn, H., Sobko, A., Shinder, V., Attali, B., Elson, A., 2000. Hypomyelination and increased activity of voltage-gated K(+) channels in mice lacking protein tyrosine phosphatase epsilon. *EMBO J.* 19, 4036–4045.

Petrone, A., Battaglia, F., Wang, C., Dusa, A., Su, J., Zagzag, D., Bianchi, R., Casaccia-Bonnel, P., Arancio, O., Sap, J., 2003. Receptor protein tyrosine phosphatase alpha is essential for hippocampal neuronal migration and long-term potentiation. *EMBO J.* 22, 4121–4131.



- Ridley, A.J., Hall, A., 1992. The small GTP-binding protein rho regulates the assembly of focal adhesions and actin stress fibers in response to growth factors. *Cell* 70, 389–399.
- Ridley, A.J., Paterson, H.F., Johnston, C.L., Diekmann, D., Hall, A., 1992. The small GTP-binding protein rac regulates growth factor-induced membrane ruffling. *Cell* 70, 401–410.
- Roche, S., Koegl, M., Barone, M.V., Roussel, M.F., Courtneidge, S.A., 1995. DNA synthesis induced by some but not all growth factors requires Src family protein tyrosine kinases. *Mol. Cell. Biol.* 15, 1102–1109.
- Sbalzarini, I.F., Koumoutsakos, P., 2005. Feature point tracking and trajectory analysis for video imaging in cell biology. *J. Struct. Biol.* 151, 182–195.
- Solnica-Krezel, L., Eaton, S., 2003. Embryo morphogenesis: getting down to cells and molecules. *Development* 130, 4229–4233.
- Solnica-Krezel, L., Stemple, D.L., Mountcastle-Shah, E., Rangini, Z., Neuhaus, S.C., Malicki, J., Schier, A.F., Stainier, D.Y., Zwartkruis, F., Abdelilah, S., Driever, W., 1996. Mutations affecting cell fates and cellular rearrangements during gastrulation in zebrafish. *Development* 123, 67–80.
- Syverud, K., Chinga, G., Johnsen, P.O., Leirset, I., Wiik, K., 2007. Analysis of lint particles from full-scale printing trials. *Appita J.* 60, 286–290.
- Tahinci, E., Symes, K., 2003. Distinct functions of Rho and Rac are required for convergent extension during *Xenopus* gastrulation. *Dev. Biol.* 259, 318–335.
- Tamura, K., Dudley, J., Nei, M., Kumar, S., 2007. MEGA4: Molecular Evolutionary Genetics Analysis (MEGA) software version 4.0. *Mol. Biol. Evol.* 24, 1596–1599.
- Thisse, C., Thisse, B., Schilling, T.F., Postlethwait, J.H., 1993. Structure of the zebrafish *snail1* gene and its expression in wild-type, spadetail and no tail mutant embryos. *Development* 119, 1203–1215.
- Tiran, Z., Peretz, A., Sines, T., Shinder, V., Sap, J., Attali, B., Elson, A., 2006. Tyrosine phosphatases epsilon and alpha perform specific and overlapping functions in regulation of voltage-gated potassium channels in Schwann cells. *Mol. Biol. Cell.*
- Topczewski, J., Sepich, D.S., Myers, D.C., Walker, C., Amores, A., Lele, Z., Hammerschmidt, M., Postlethwait, J., Solnica-Krezel, L., 2001. The zebrafish

glypican knypek controls cell polarity during gastrulation movements of convergent extension. *Dev. Cell* 1, 251–264.

Unterseher, F., Hefele, J.A., Giehl, K., De Robertis, E.M., Wedlich, D., Schambony, A., 2004. Paraxial protocadherin coordinates cell polarity during convergent extension via Rho A and JNK. *EMBO J.* 23, 3259–3269.

van der Sar, A.M., Zivkovic, D., den Hertog, J., 2002. Eye defects in receptor proteintyrosine phosphatase alpha knock-down zebrafish. *Dev. Dyn.* 223, 292–297.

Veeman, M.T., Axelrod, J.D., Moon, R.T., 2003. A second canon. Functions and mechanisms of beta-catenin-independent Wnt signaling. *Dev. Cell* 5, 367–377.

von Wichert, G., Jiang, G., Kostic, A., De Vos, K., Sap, J., Sheetz, M.P., 2003. RPTP-alpha acts as a transducer of mechanical force on alpha5/beta3-integrin-cytoskeleton linkages. *J. Cell Biol.* 161, 143–153.

Wada, H., Iwasaki, M., Sato, T., Masai, I., Nishiwaki, Y., Tanaka, H., Sato, A., Nojima, Y., Okamoto, H., 2005. Dual roles of zygotic and maternal Scribble1 in neural migration and convergent extension movements in zebrafish embryos. *Development* 132, 2273–2285.

Wallingford, J.B., Fraser, S.E., Harland, R.M., 2002. Convergent extension: the molecular control of polarized cell movement during embryonic development. *Dev. Cell* 2, 695–706.

Warga, R.M., Kimmel, C.B., 1990. Cell movements during epiboly and gastrulation in zebrafish. *Development* 108, 569–580.

Westerfield, M., 1995. *The Zebrafish Book*. University of Oregon Press, Eugene, Oregon.

Wienholds, E., Schulte-Merker, S., Walderich, B., Plasterk, R.H., 2002. Target-selected inactivation of the zebrafish rag1 gene. *Science* 297, 99–102.

Zeng, L., Si, X., Yu, W.P., Le, H.T., Ng, K.P., Teng, R.M., Ryan, K., Wang, D.Z., Ponniah, S., Pallen, C.J., 2003. PTP alpha regulates integrin-stimulated FAK autophosphorylation and cytoskeletal rearrangement in cell spreading and migration. *J. Cell Biol.* 160, 137–146.

Zhang, S.Q., Yang, W., Kontaridis, M.I., Bivona, T.G., Wen, G., Araki, T., Luo, J., Thompson, J.A., Schraven, B.L., Philips, M.R., Neel, B.G., 2004. Shp2 regulates SRC family kinase activity and Ras/Erk activation by controlling Csk recruit-

ment. *Mol. Cell* 13, 341–355.

Zheng, X.M., Wang, Y., Pallen, C.J., 1992. Cell transformation and activation of pp 60c-src by overexpression of a protein tyrosine phosphatase. *Nature* 359, 336–339.

Appendix. Supplementary Figures

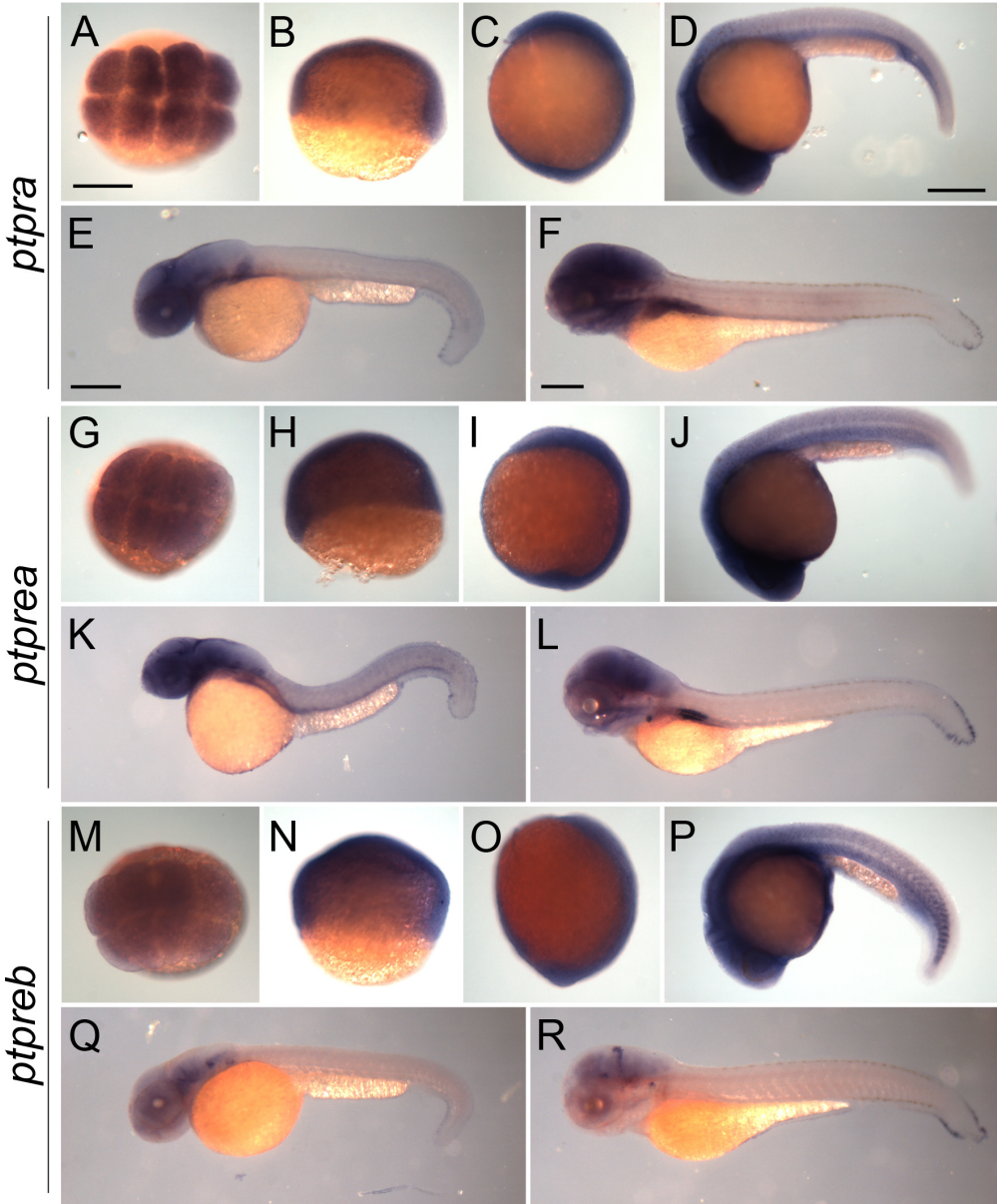


Fig. S1. *ptpra*, *ptprea* and *ptpreb* are ubiquitously expressed during early zebrafish development.

Wildtype zebrafish embryos were collected and fixed at 8 cell stage (A, G, M), 6 hpf (B, H, N), 1 somite stage (C, I, O), 24 hpf (D, J, P), 36 hpf (E, K, Q) and 72 hpf (F, L, R). Whole mount *in situ* hybridization was performed using probes targeting *ptpra* (A-F), *ptprea* (G-L) or *ptpreb* (M-R). Scale bars = 250 μm.

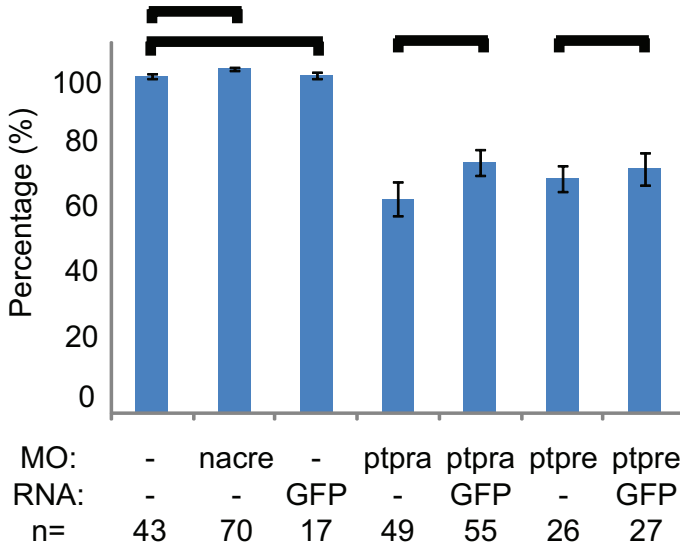
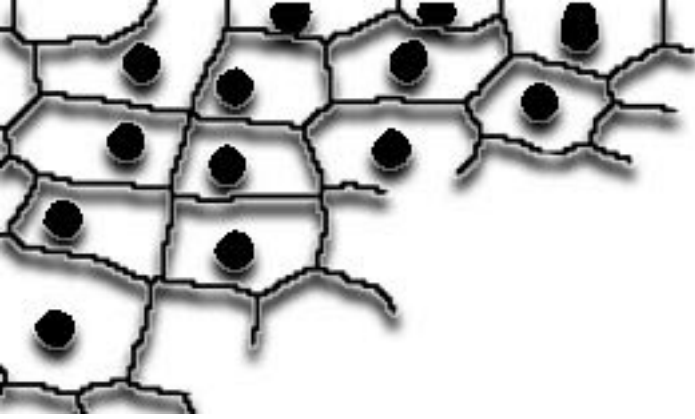


Fig. S2. Mock morpholino or RNA (co-) injections do not alter phenotype or length.

(A) Embryos were micro-injected at the 1-cell stage with either nacre morpholino, ptptra-MO, ptptra-MO and GFP RNA, ptpre-MO or ptpre-MO and GFP RNA. Non-injected embryos were taken as control. Embryos were grown to 2 dpf and pictures were taken. Tail lengths were determined using ImageJ software and compared to non-injected control. The tail lengths of the embryos are plotted as the average relative to non-injected control embryos. A Student t-test was performed between the non-injected control

and nacre MO groups, the ptptra-MO and ptptra-MO/GFP RNA groups and the ptpre-MO and ptpre-MO/GFP RNA groups. No significant differences were found in response to GFP RNA co-injection ($P > 0.05$).



3

Pair-Wise Regulation of Convergence and Extension Cell Movements by Four Phosphatases via RhoA

Mark van Eekelen, Vincent Runtuwene, Wouter Masselink and Jeroen den Hertog

PLoS One. 2012; 7(4): e35913

Abstract

Various signaling pathways regulate shaping of the main body axis during early vertebrate development. Here, we focused on the role of protein-tyrosine phosphatase signaling in convergence and extension cell movements. We identified Ptpn20 as a structural paralogue of PTP-BL and both phosphatases were required for normal gastrulation cell movements. Interestingly, knockdowns of PTP-BL and Ptpn20 evoked similar developmental defects as knockdown of RPTP α and PTP ϵ . Co-knockdown of RPTP α and PTP-BL, but not Ptpn20, had synergistic effects and conversely, PTP ϵ and Ptpn20, but not PTP-BL, cooperated, demonstrating the specificity of our approach. RPTP α and PTP ϵ knockdowns were rescued by constitutively active RhoA, whereas PTP-BL and Ptpn20 knockdowns were rescued by dominant negative RhoA. Consistently, RPTP α and PTP-BL had opposite effects on RhoA activation, both in a PTP-dependent manner. Downstream of the PTPs, we identified NGEF and Arhgap29, regulating RhoA activation and inactivation, respectively, in convergence and extension cell movements. We propose a model in which two phosphatases activate RhoA and two phosphatases inhibit RhoA, resulting in proper cell polarization and normal convergence and extension cell movements.

Introduction

Early vertebrate embryonic development is characterized by three processes, cell proliferation, differentiation and migration. In order to form the basic body plan and - at a later time-point - organs, cells will not only need to differentiate to become the proper cell type, but they will need to be at the right place at the right time. In vertebrates the earliest two processes conducted by cell migration are the formation of the three germ layers during gastrulation by epiboly and internalization (or ingression/emboly, depending on the organism), and the formation of the medio-lateral body axis by convergence and extension (C/E) cell movements [1], [2]. C/E cell movements require cells of the axial and paraxial mesoderm and neurectoderm to polarize and elongate in their direction of movement. These cells migrate towards the dorsal midline and participate in a process called intercalation in order to extend the body axis. C/E cell movements are highly coordinated, using lateral lamellipodia to actively and directionally crawl between neighboring cells towards the midline to align there. Impaired C/E cell movements result in shorter and wider embryos, which can be accounted for by fewer cells reaching the dorsal midline and decreased intercalation. Additional phenotypes of C/E defects constitute neural tube defects and cyclopia [1], [3], [4], [5], [6], [7], [8], [9].



Although the mechanisms of gastrulation cell movements have been well described, the underlying molecular regulation remains elusive. Over the past years many proteins have been reported to contribute to C/E cell movements. C/E cell movements are expected to be affected by proteins involved in cell polarity, migration, adhesion and more, explaining why many mutant/knockdown phenotypes give rise to C/E defects. Several signaling pathways are known to participate in proper C/E cell movements, like Bmp signaling [10], [11], PDGF-PI3K signaling [12], [13], [14], Jak-Stat signaling [15], [16] and Eph-ephrin signaling [17], [18], [19], but the most extensively described is the non-canonical Wnt/Planar Cell Polarity (PCP) signaling pathway [3], [20], [21], [22], [23], [24], [25], [26], [27]. The PCP pathway was first identified in *Drosophila* where organization of wing epithelial hairs is regulated by this pathway. The term PCP is used to describe the organization of cells and their components within a plane, usually an epithelial layer. In flies, the PCP pathway regulates the asymmetric localization of several core PCP proteins like Vangl, Pk, Fz, Dsh and Dgo [28], [29], [30], [31], [32], [33], which in turn regulates the morphology of the wing epithelium with a wing-hair at the distal tip of each cell. Other epithelial structures organized by PCP signaling are the drosophila eye and vertebrate hair cells in the cochlea [34], [35]. Although the function of all the core PCP components is not completely understood, the main function seems to be regulating cell-cell communication in order to organize structure. In vertebrates, a major part of this pathway consists of the non-canonical wnt signaling pathway. Non-canonical Wnt signaling is β -catenin independent and involves Wnt4/5a/7a/11, Fz3/6/7, Dvl1/2/3 and Pk1/2 to activate the two main downstream components, RhoA and Rac1 [36], [37], [38].

PTPs play an important role in signal transduction in concert with their enzymatic counterparts, the protein-tyrosine kinases (PTKs). RPTP σ and LAR for example have an important role in neuronal development [39], [40], [41], while CD45 has a critical function in immune cell regulation [42]. The role of Shp2 has been extensively studied in mouse and zebrafish, as activating and inactivating mutations lead to Noonan and LEOPARD syndrome in humans [43]. We have shown previously that Noonan and LEOPARD associated mutations in Shp2 confer C/E cell movement defects in zebrafish [44]. We also reported two other PTPs in C/E cell movements, RPTP α and PTP ϵ [45], that mediate their effects by activation of RhoA through the Src family kinases (SFKs) Fyn and Yes.

Here, we show that four PTPs are involved in regulating cell polarity and C/E cell movements. RPTP α and PTP ϵ activate RhoA through the Fyn and Yes SFKs, and PTP-BL and Ptpn20 inhibit RhoA activity. Co-knockdown experiments indicate that these four PTPs work in pairs. The Rho-GEF, NGEF, acts downstream of RPTP α and PTP ϵ , and the Rho-GAP, Arhgap29 (Parg1), downstream of PTP-BL

and Ptpn20. We suggest a model where RhoA is activated following recruitment of NGEF upon RPTP α /PTP ϵ and Fyn/Yes mediated stimulation and RhoA activity is inhibited following recruitment of Arhgap29 upon PTP-BL/Ptpn20 mediated repression. Based on these results, we conclude that normal activation and inhibition of RhoA is required for proper cell polarization and normal C/E cell movements.

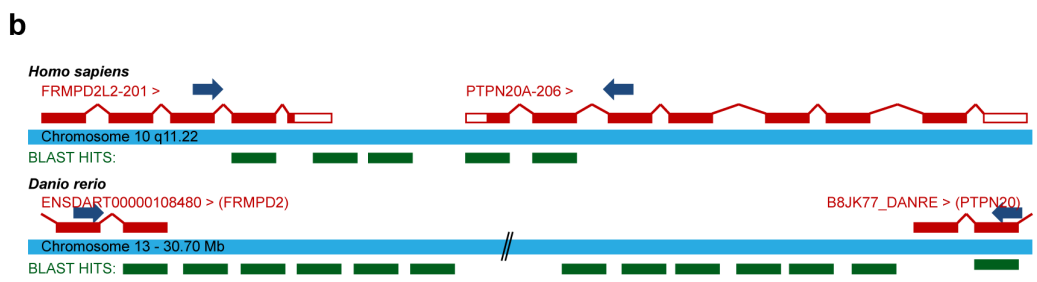
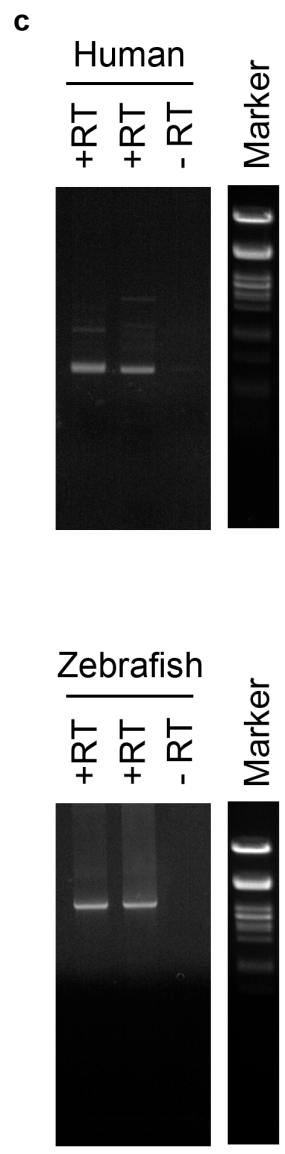
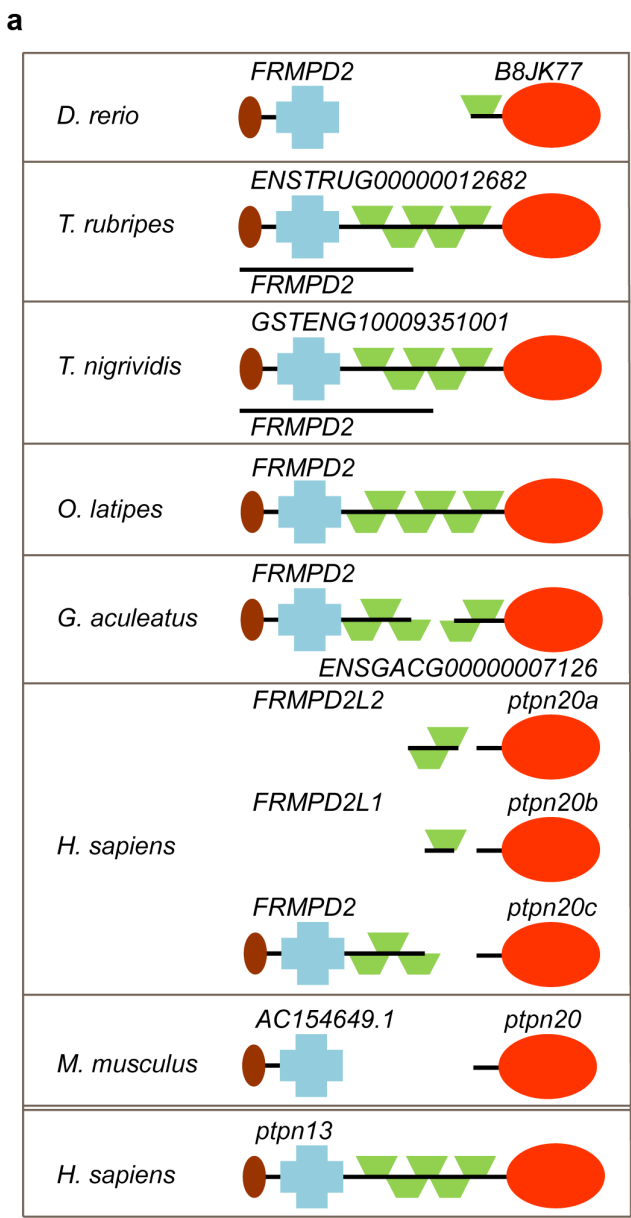
Results

Identification of Ptpn20 as a homologue of PTP-BL

We recently identified all protein tyrosine phosphatase (PTP) genes in the zebrafish genome by blasting the individual PTP domains of human genes against the zebrafish genome (Zv8, Ensembl) [46]. We compared the genes we identified with four other fish genomes available (medaka, fugu, stickleback and tetraodon) to evaluate our findings (Fig. S1 and Table S1). Although these fish genomes were not completely annotated, in general they were more complete than the zebrafish genome, and missing PTP encoding genes could easily be identified by blasting. When aligning several candidate genes for *ptpn20* we noticed that some fish genes were annotated with different names and protein structures (Fig. 1a). Having a closer look at the *ptpn20* candidate genes, we found that in *Oryzia latipes* this gene was annotated as *frmpd2* and in *Tetraodon nigrivindis* as *GSTENG10009351001*, both bearing remarkable resemblance to the structure of the human *PTPN13* gene encoding PTP-BL (also known as PTP-BAS, PTP-L1 or FAP1). Interestingly, the PTP domain of *ptpn13* has the highest sequence homology to the PTP domain of *ptpn20*. Upon further investigation we found a gene named *frmpd2* or a gene with similar structure to the 5' side of *ptpn20* in all species, including the human genome which according to the Ensembl database contains 3 copies of *ptpn20*; *ptpn20a*, *ptpn20b* and *ptpn20c*, all accompanied with their own *frmpd2*-(like) gene. We hypothesized that *frmpd2* and *ptpn20* might in fact be a single gene with

Figure 1. Identification of *ptpn20* as a homologue of *ptpn13*.

(a) Protein structures are shown encoded by *ptpn20* homologue and the immediately 5' upstream *FRMPD2*, as currently annotated in five fish genomes, the human genome and the mouse genome. In some cases like Fugu and Tetraodon a single known coding transcript exists besides separate transcripts encoding the PTP domain and the "FRMPD" part. For comparison the protein structure encoded by human *ptpn13* (PTPBL) is added below. (b) Primers were designed as indicated, leaving approximately 100 bp known coding sequence for the purpose of alignment of generated sequences. PCR products with forward primers on the second to last known exon of human and zebrafish *FRMPD2* and reverse oligos on the second exon of *PTPN20*. A schematic representation of retrieved sequences blasted to the genome are indicated in green (not to scale). (c) Generated PCR products on human (top) and zebrafish (bottom) cDNA libraries using the described primer sets. Generated band sizes are consistent with expected values based on homology with the *ptpn13* gene.



structural resemblance to *ptpn13*, like *frmpd2* in *O. latipes*. In order to test this hypothesis, we generated cDNA from zebrafish embryos and HEK293 cells using reverse transcription (RT) and designed forward primers on the second to last known coding exon of *frmpd2* and reverse primers on the second known coding exon of *ptpn20* (Fig. 1b). We performed PCR using these primer sets and generated PCR products indicating that single transcripts containing *frmpd2* and *ptpn20* coding sequence exist (Fig. 1c). These PCR products were sequenced and these were blasted back to the zebrafish and human genome, resulting in identification of the missing exons connecting the two transcripts, confirming the existence of a single *ptpn13*-like *ptpn20* transcript (Fig. 1b). Full length *ptpn20* transcript encodes a protein with a FERM domain, KIND domain, 5 PDZ domains and a PTP domain, similar to PTP-BL. We conclude - based on their structural resemblance - that Ptpn20 and PTP-BL are paralogues, which is reflected by the high sequence similarity between the PTP domains of PTP-BL and Ptpn20.

Ptpn13, ptpn20, ptpra or ptpre knockdown results in defective C/E cell movements and cell polarization

PTP-BL is a large multi-domain protein containing a FERM, KIND, 5 PDZ and a PTP domain, suggesting a role as a scaffold protein since all except the PTP domain play a role in protein-protein interactions. Indeed many binding partners have been described, suggesting an inhibiting role in Fas-mediated apoptosis [47], [48] and a role in SFK dependent phosphorylation of ephrin-B [49], [50]. We designed splice donor morpholinos targeting the active site of the PTP domain and demonstrated that *ptpn13* induced C/E defects. We performed *in situ* hybridization with probes staining *dlx3*, *hgg1*, *krox20* and *myod*, all well-established markers for C/E cell movements [51], [52]. *Dlx3* stains the edge of the neural plate which in the case of impaired convergence will be wider, while *hgg1* stains the precursors of the hatching gland, which in the case of defective extension movements will be shifted posteriorly. We fixed embryos at the one somite stage and performed whole mount *in situ* hybridization. By quantifying the angle of *dlx3* staining and the length of the anterior shift of *hgg1* staining as indicated (Fig. 2a, inset), we found that knockdown of *ptpn13* significantly affects C/E cell movements (Fig. 2a-c). The phenotype observed in *ptpn13* knockdown embryos was fully rescued by co-injection of mouse *ptpn13* RNA (Fig. S2). Interestingly, *ptpn20* knockdown induced similar C/E cell movement defects (Fig. 2a-c). Moreover, *ptpra* and *ptpre* knockdowns also induced C/E defects (Fig. 2a-c). To assess C/E defects in an independent manner, we performed *in situ* hybridization experiments with probes for *krox20*, which stains rhombomeres 3 and 5, and *myod*, which stains the somites. In case of defective C/E movements the rhombomeres will be wider (reduced convergence) and the length of 8 somites will be shorter (reduced extension). Defects can be quantified by calculating the ratio of the

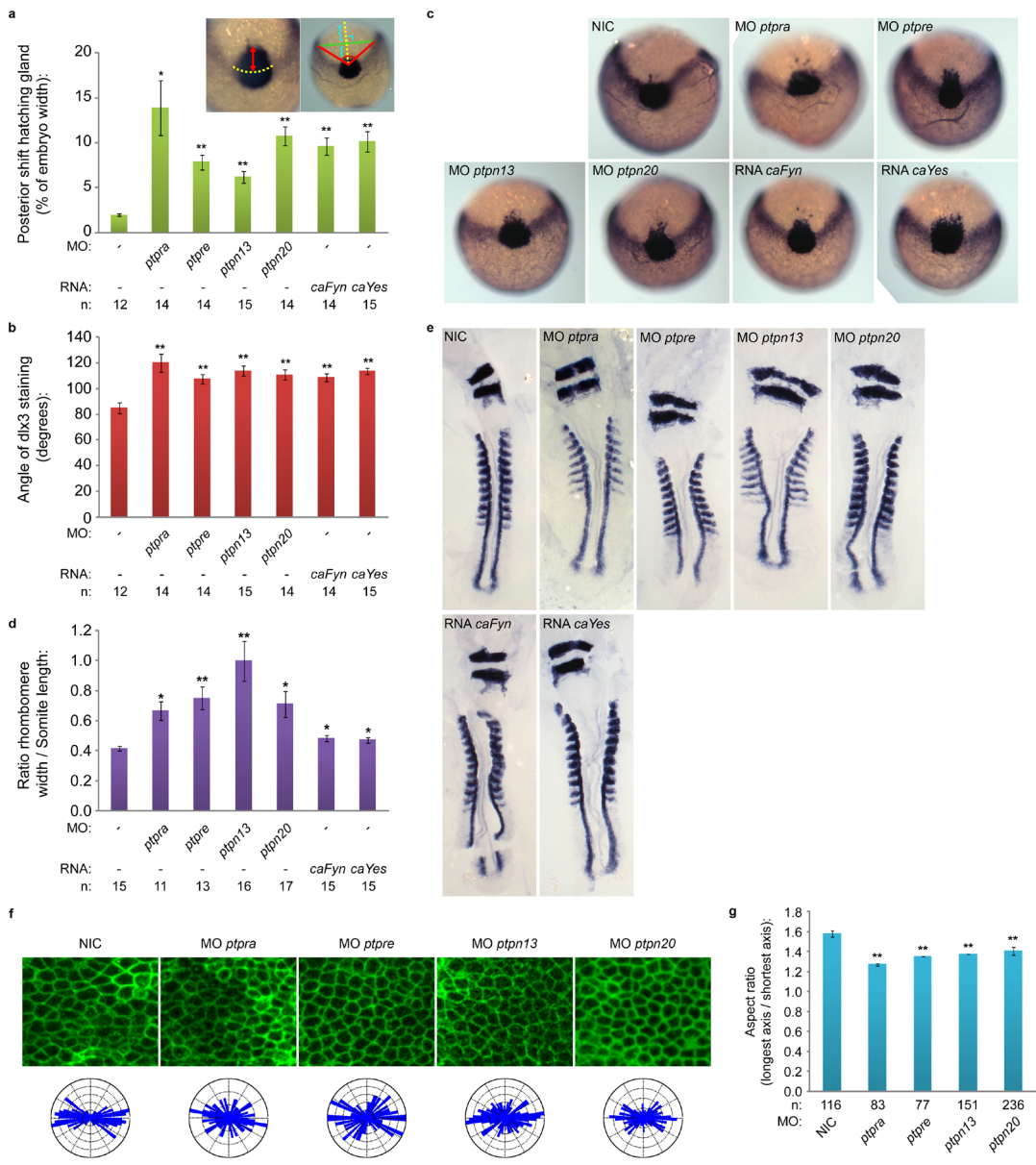


Figure 2. PTP knockdowns affect C/E and cell polarization.

(a) Zebrafish embryos were microinjected with morpholinos (high concentration) targeting the different phosphatase genes or RNA constructs encoding constitutively active forms of Fyn or Yes at the one cell stage and grown to 1 somite stage. Embryos were fixed and stained for *dlx3* and *hgg1* expression using whole mount *in situ* hybridization, staining the precursors of the hatching gland (*hgg1*) and the edge of the neural plate (*dlx3*). Posterior shift of the hatching gland and angle of *dlx3* staining are measured as shown in inset, the results are plotted in (a) and (b). Pictures of representative embryos used in the quantifications in (a) and (b) are shown in (c). Embryos were microinjected using the same conditions as described above and grown to 8–9 somite stage. Embryos were fixed and stained for *krox20* and *myod* using whole mount *in situ* hybridization. *Krox20* stains rhombomere 3 and 5, while *myod* stains the somites. Resulting stain-

ing patterns were used to quantify width to ratio by measuring rhombomere width (*krox20*) and somite length (8 somites, *myod*). Ratios are plotted in (d), representative embryos are depicted in (e). (f) Zebrafish embryos were micro-injected using the constructs described above, co-injected with RNA encoding YFP-caax and RNA encoding mCherry-H2B at the one cell stage and mounted at shield stage. Embryos were imaged over time at the presomitic mesoderm, representative areas of presomitic mesoderm for each condition are shown. Resulting images were analyzed for cell shape (aspect ratio) by dividing the length of the longest axis by the length of the shortest axis for each cell, average aspect ratios are plotted in (g). The distribution of angles of the longest axis towards the dorsal midline were plotted in rose-plots and shown in (f; bottom). All error bars are standard error of the mean. Student t-tests were performed with non-injected control; no asterisk indicates $P > 0.05$, * indicates $0.05 > P > 0.001$ and ** indicates $P < 0.001$.

width of rhombomere 3/the length of 8 somites. Using this read-out, we again established that knockdown of *ptpn13*, *ptpn20*, *ptpra* and *ptpre* induced significant C/E cell migration defects (Fig. 2d,e)

We previously showed that RPTP α and PTP ϵ function in C/E cell movements by activation of the SFKs, Fyn and Yes [45], [46]. We assessed the effects of expression of constitutively active mutants of Fyn and Yes that harbor point mutations (Tyr to Phe) in their inhibitory C-terminal phosphorylation sites on C/E cell movements. As expected, injection of constitutively active variants of *fyn* and *yes* mRNA (*caFyn* and *caYes*) also induced C/E cell movement defects as assessed using the *dlx3/hgg1* and *krox20/myod* markers (Fig. 2a–e).

C/E cell movement defects can result from defective cell polarization, resulting in less elongated cells with reduced polarization towards the dorsal midline. In order to investigate if cell polarization is causing the observed phenotypes, we determined the shapes of dorsally migrating presomitic cells as described before [45]. Wildtype or knockdown embryos were (co-)injected with YFP-caax mRNA and mCherry-H2B to label the cell membrane and nuclei, respectively. We imaged cell shapes in the presomitic mesoderm (Fig. 2f) and determined the cell elongation by analyzing the membrane marker YFP-caax and calculated the aspect ratio (the longest axis divided by the shortest axis). This aspect ratio is directly proportional to cell polarization and is significantly reduced upon knockdown of *ptpn13*, *ptpn20*, *ptpra* and *ptpre* (Fig. 2g). Imaging of presomitic mesoderm cells also provided us with a means to assess the angle that single cells make towards the dorsal midline. These angles were plotted in rose diagrams, and indicate that *ptpn13*, *ptpn20*, *ptpra* and *ptpre* knockdown results in more random distribution of the cell axis and less elongated presomitic cells, compared to wildtype embryos (Fig. 2f). Taken together, we show that RPTP α , PTP ϵ , PTP-BL and Ptpn20 are involved in C/E cell movements by regulating cell polarity.



Ptpn20 and ptpn13 show redundancy, and function together with ptppra and ptpre

Knockdown of all four PTPs induced C/E cell movement defects (Fig. 2). One of the hallmarks of C/E cell migration defects during gastrulation is the severely shortened embryo body axis at 3 days post fertilization (dpf) (Fig. 3a). The tail length at 3 dpf directly correlates to the severity of C/E related phenotypes [45]. We measured the tail length as an easy and unbiased method to quantify C/E defects. Given the similarity in phenotypes and the structural similarity between PTP-BL and *Ptpn20*, we proceeded to investigate whether combined knockdowns act synergistically. To this end, we titrated morpholinos down until no obvious phenotype was observed and these low doses of morpholinos were combined. Genes functioning in the same pathway will reconstitute the original (full dosage) phenotype, in this case shorter fish embryos, like we have shown previously in combined *ptpra* and *ptpre* knockdown [45]. Although tail length by itself does not discriminate between different possible processes that could underlie defects in body axis extension, we believe that - combined with detailed analysis of C/E cell movement defects in the full knockdowns - this method accurately identifies components of the same pathway and is suitable for screening purposes. For convenience, low dosage morpholino concentrations will be indicated in green whereas full dosage morpholino concentrations are indicated in red. Using this method, we found that knockdown of either *ptpn13* or *ptpn20* induced shortened embryo body axes (Fig. 3a,b). Low doses of these morpholinos did not induce phenotypes by themselves. Combined low dose *ptpn13* and *ptpn20* knockdown induced a similar phenotype as high dose knockdown of either *ptpn13* or *ptpn20*, suggesting that *ptpn13* and *ptpn20* knockdowns acted synergistically.

We have previously described a similar phenotype in *ptpra* and *ptpre* knockdown zebrafish, as well as in *ptpra*^{-/-} fish lines. Therefore we decided to investigate if these four PTPs might function in the same pathway by using low dose combined knockdown of *ptpn13* or *ptpn20* with either *ptpra* or *ptpre*. As a readout, we investigated if these combinations resulted in reconstitution of the shorter phenotype. We found that combining *ptpn13* and *ptpra* or *ptpn20* and *ptpre* knockdown specifically reconstituted shorter tail length phenotypes. Interestingly combining *ptpn13* and *ptpre* or *ptpn20* and *ptpra* did not induce shorter fish (Fig. 3c-e). These results indicate that these PTPs acted in pairs and illustrate that our analyses were specific in that not just any pair of PTP morpholinos induced tail defects.

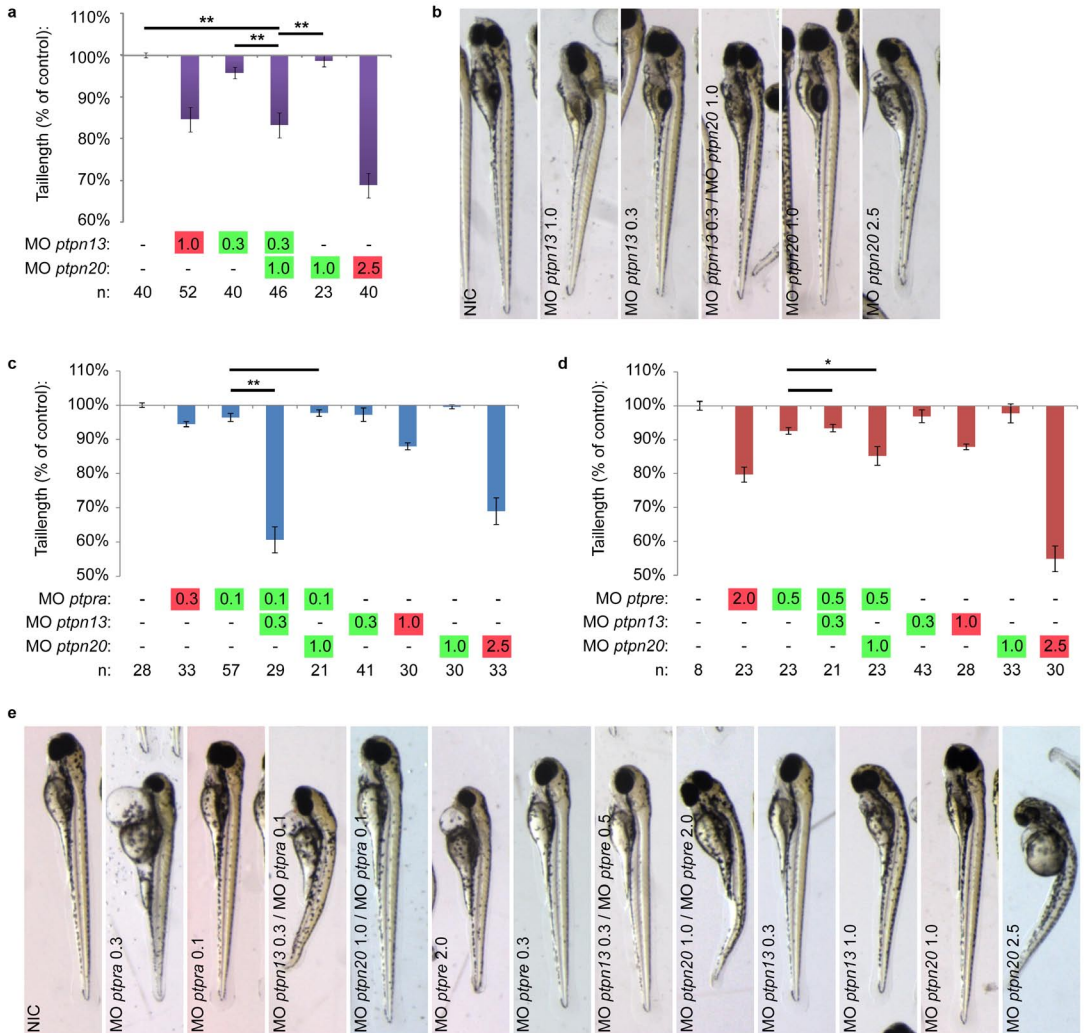


Figure 3. *Ptpn13* and *ptpn20* cooperate with each other and with *ptpra* and *ptpre*.

Morpholinos targeting *ptpn13* and *ptpn20* were injected in the zebrafish at the one cell stage, and concentrations were titrated down until no phenotype was observed. Normal (red), low (green) concentrations and combined low concentrations of *ptpn13* and *ptpn20* morpholino were microinjected and embryos were grown to 3 dpf under normal conditions. Pictures were taken from all embryos and tails were measured using ImageJ imaging software, from the yolk to the tip of the tail, and compared to non-injected control. Average tail length compared to non-injected control is plotted as a percentage deviating from 100% in (a) and representative fish are shown for each condition in (b). Zebrafish embryos were microinjected as described above, using low concentration combined knockdown of *ptpra* with either *ptpn13* or *ptpn20*, or *ptpre* with either *ptpn13* or *ptpn20* and tail lengths are plotted in (c) and (d). (e) Shown are representative fish from the experiments depicted in (c) and (d). All error bars are standard error of the mean. Student t-test was performed where indicated; no asterisk indicates $P > 0.05$, * indicates $0.05 > P > 0.001$ and ** indicates $P < 0.001$. Morpholino concentrations are color coded: red for “full” knockdown, giving full phenotype without being toxic and green for “low” concentration, giving no observable phenotype.

C/E cell movement defects are caused by defective RhoA regulation

RhoA has been shown to play a major role in cell polarization [5], [6] and RhoA is activated during cell movements in response to Wnt11 and Wnt5a. Shp2, RPTP α , PTP ϵ , Fyn and Yes also signal to RhoA in C/E [45], [53], [54]. In order to test whether defective RhoA regulation is at the basis of the cell polarization defects observed here, we co-injected *ptpra*, *ptpre*, *ptpn13* and *ptpn20* morpholinos with either RNA encoding constitutively active *rhoa* (*caRhoA*) or dominant negative *rhoa* (*dnRhoA*). We used tail length at 3 dpf as readout to see if co-injections were able to rescue or further increase the knockdown phenotypes. As described before [45] *caRhoA* mRNA can rescue *ptpra* and *ptpre* knockdown. As expected, co-injection of *dnRhoA* mRNA in *ptpra* and *ptpre* knockdown embryos increased the phenotype. Surprisingly, co-injection of *ptpn13* and *ptpn20* morpholinos with *caRhoA* mRNA worsened the phenotype and co-injection of *dnRhoA* mRNA with *ptpn13* and *ptpn20* morpholinos rescued the phenotype (Fig. 4, Fig. S3). Our results suggest that RPTP α and PTP ϵ have an activating effect on RhoA, whereas PTP-BL and Ptpn20 inhibit RhoA activity. To assess the effects of RPTP α and PTP-BL on RhoA activation directly, we expressed RPTP α or PTP-BL in HEK293T cells and selectively precipitated GTP-bound Rho using the Rhotekin Rho-binding domain. A higher proportion of RhoA was precipitated upon expression of RPTP α , compared to mock-transfected cells (Fig. 4b). In contrast, a lower proportion of GTP-bound RhoA was precipitated upon expression of PTP-BL. As controls, we expressed catalytically inactive RPTP α or PTP-BL with Cys to Ser mutations in their catalytic sites to a similar extent as their wild type counterparts as assessed by immunoblotting or fluorescence microscopy (Fig. 4b,c). Expression of either catalytically inactive PTP did not affect the proportion of GTP-bound RhoA that was precipitated in these assays (Fig. 4b). These results indicate that RPTP α activates RhoA, whereas PTP-BL inhibits RhoA, which is consistent with the observed effects in zebrafish embryos.

RhoA is activated by NGEF and inactivated by Arhgap29

RhoA is a member of the Rho family GTPases that is activated by Rho guanine nucleotide exchange factors (Rho-GEFs) and inactivated by Rho GTPase-activating proteins (Rho-GAPs). Of the many Rho-GEFs and Rho-GAPs described in the literature it is not known which have a role in C/E cell movements. We decided to investigate Arhgap29, which is also known as Parg1 (PTP-BL associated Rho-GAP1), that has previously been shown to bind directly to PTP-BL [55]. We used a non-related Rho-GAP, Arhgap5 (also known as Gap5) as a control. Knockdown of *arhgap29b* induced C/E cell movement defects as assessed by whole mount *in situ* hybridization using *dlx3/hgg1* and *krox20/myod* as markers (Fig. 5a-e). *Arhgap5* knockdown did not induce C/E cell movement defects, indicating that



Figure 4. PTPs affect RhoA activation.

(a) PTP knockdowns are rescued by active or dominant negative RhoA. Embryos were micro-injected at the one cell stage using morpholinos (high concentration) targeting the indicated genes together with no RNA, RNA encoding constitutively active RhoA (3 pg/embryo) or RNA encoding dominant negative RhoA (20 pg/embryo). Fish were grown to 3dpf and tail lengths were measured. Average tail length compared to non-injected control is plotted. All error bars are standard error of the mean. Student t-tests were performed between morpholino knock-down and RNA co-injections with the same morpholino; no asterisk indicates $P > 0.05$, * indicates $0.05 > P > 0.001$ and ** indicates $P < 0.001$. (b) Direct effects of PTPs on RhoA activation. HEK293T cells were either mock transfected or transfected with HA-RPTP α -WT, HA-RPTP α -C433S/C723S, EGFP-PTPBL-WT or EGFP-PTPBL-C/S. Cells were lysed and GTP-bound RhoA was selectively precipitated using Rhotekin RBD-beads. The beads were washed and precipitated RhoA was detected using a RhoA-specific antibody (top panel). Total RhoA (middle panel) and transfected HA-RPTP α (bottom panel) was monitored in lysate by immunoblotting. (c) Expression of EGFP-PTPBL-WT or EGFP-PTPBL-C/S was monitored by fluorescence microscopy. Representative images are depicted here.

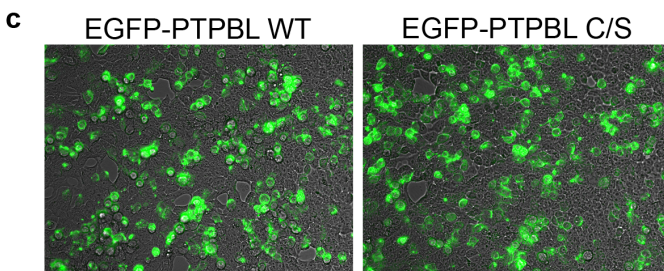
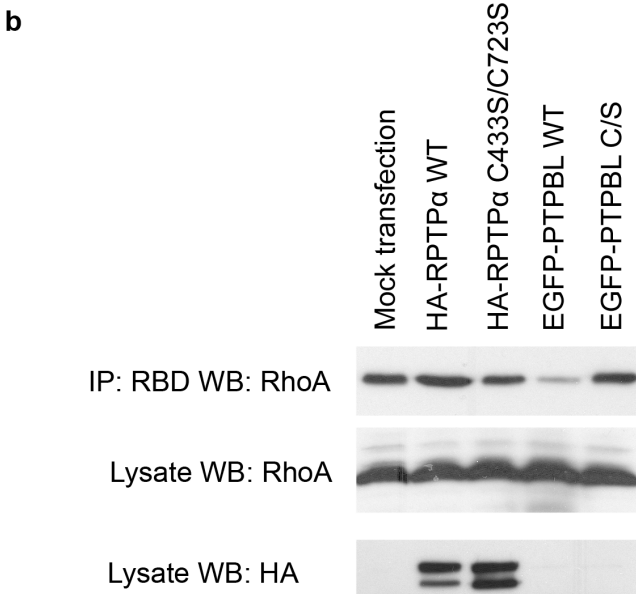
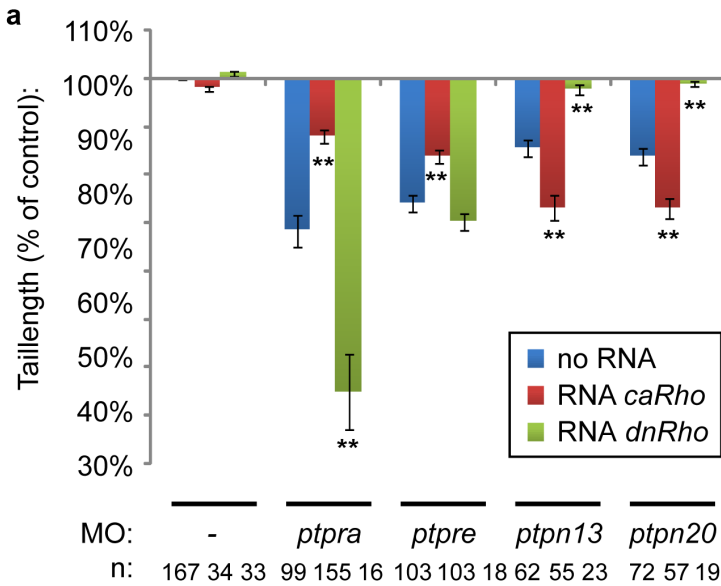
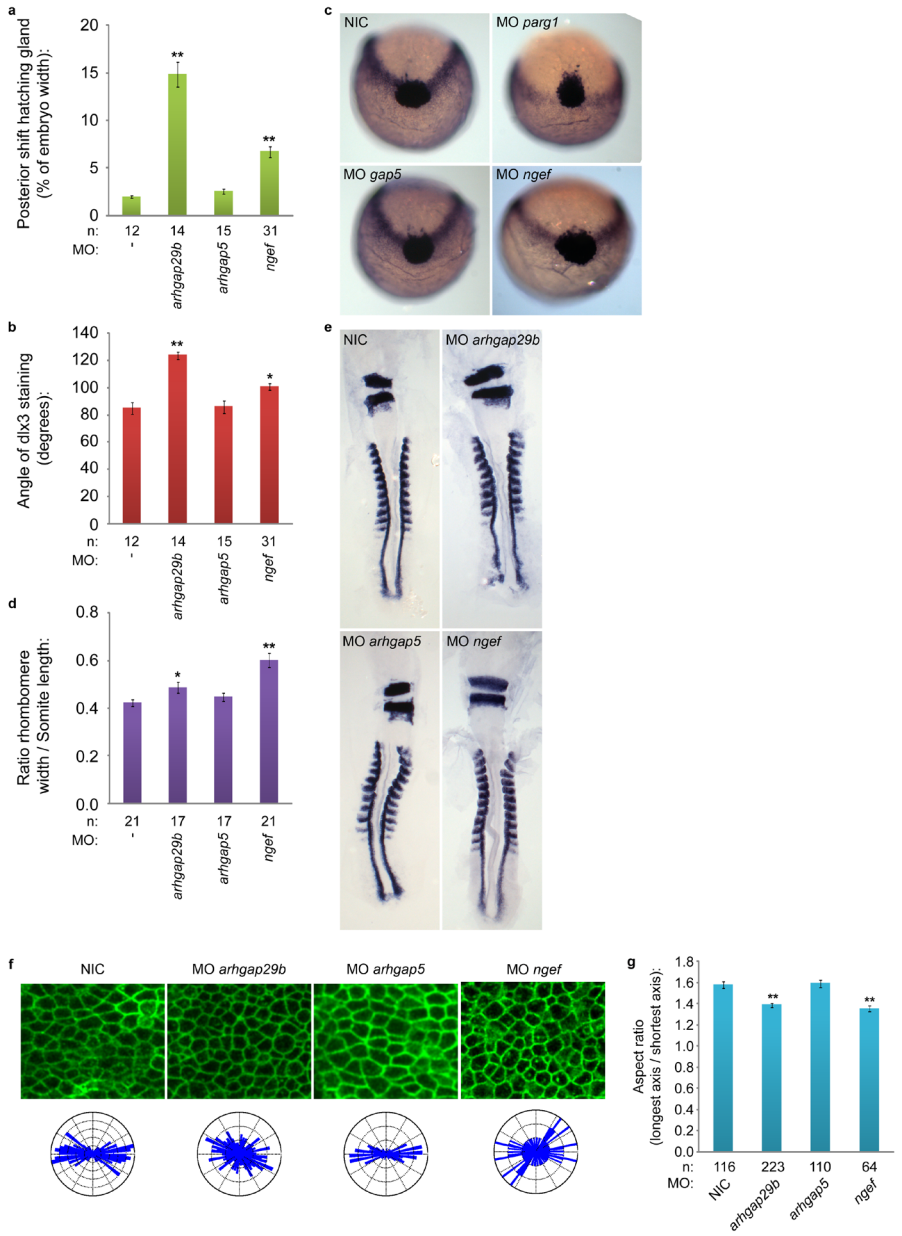


Figure 5. Knockdown of *ngef* or *arhgap29b* induces C/E cell movement and cell polarization defects.

Zebrafish embryos were microinjected with morpholinos (high concentration) targeting *arhgap29b*, *arhgap5* or *ngef* at the one cell stage and grown to 1 somite stage. Embryos were fixed and stained for *dlx3* and *hgg1* expression using whole mount *in situ* hybridization. Posterior shift of the hatching gland and angle of *dlx3* staining are measured as in Fig. 3. (a,b). Representative embryos are shown in (c). Embryos were grown to 8–9 somite stage, fixed and stained for *krox20* and *myod*. Rhombomere width (*krox20*) and somite length (8 somites, *myod*) ratios are plotted in (d); representative embryos are depicted in (e). (f) Representative areas of presomitic mesoderm for the indicated conditions were analyzed for cell shape and the distribution of angles of the longest axis towards the dorsal midline was plotted in rose-plots (f; bottom); aspect ratio plotted in (g). All error bars are standard error of the mean. Student t-tests were performed with non-injected control; no asterisk indicates $P > 0.05$, * indicates $0.05 > P > 0.001$ and ** indicates $P < 0.001$.



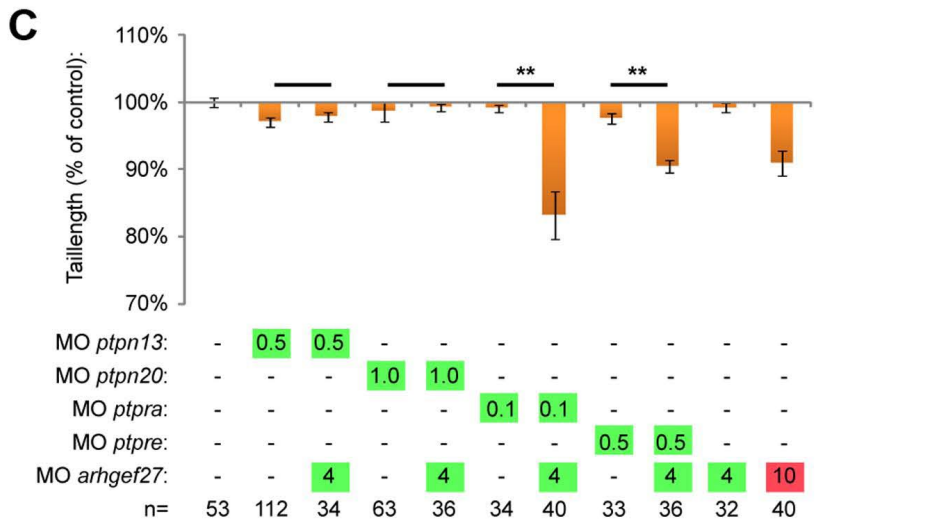
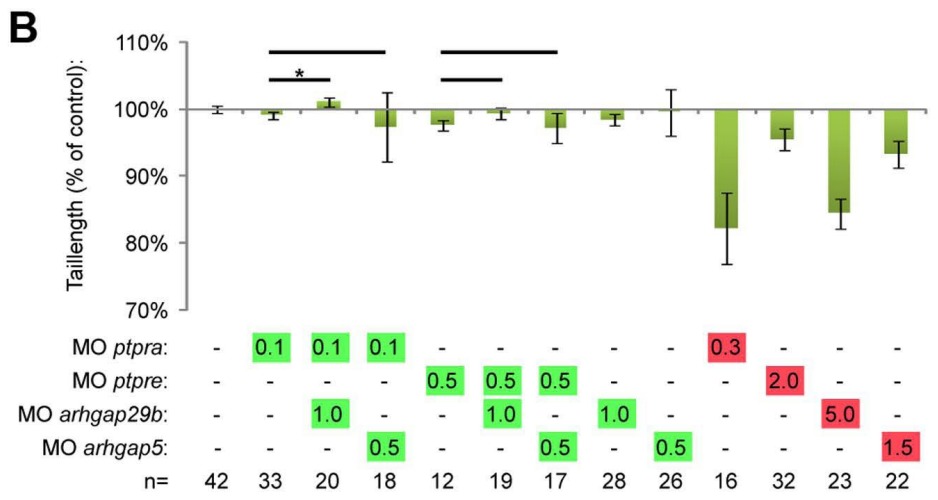
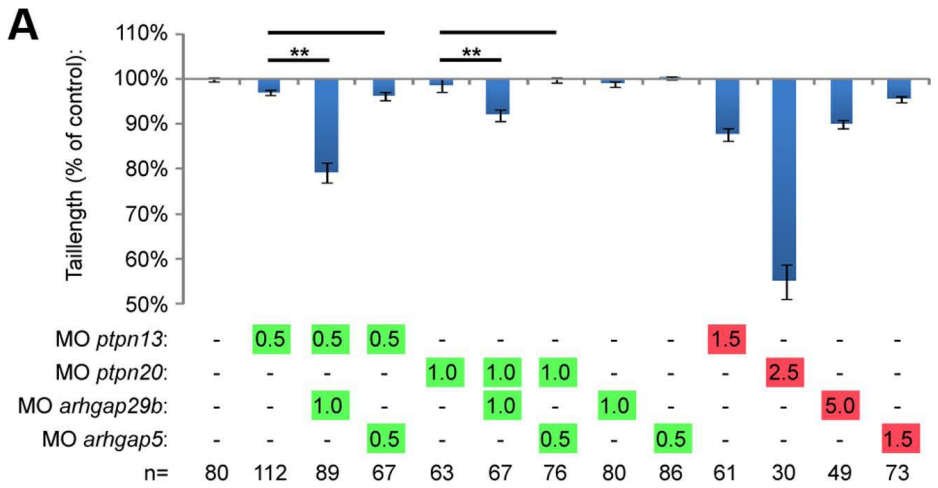
the *arhgap29* knockdown phenotype was specific (Fig. 5a–e). NGEF, also known as Ephexin/Arhgef27, is tightly regulated by tyrosine (de)phosphorylation [56] and hence it is a good candidate Rho-GEF to mediate the effects of PTPs. Knockdown of *arhgef27* induced C/E cell movement defects in zebrafish embryos (Fig. 5a–e). We analyzed cell polarization in Rho-GAP and Rho-GEF knockdown embryos and observed decreased cell elongation specifically in *ngef* and *arhgap29b* knockdown embryos, but not in *arhgap5* knockdown embryos (Fig. 5f–g). These data are consistent with NGEF and Arhgap29 acting in cell polarization and C/E cell movements.

To investigate whether PTP-BL and Ptpn20 interacted genetically with Arhgap29, we used combined low-dose knockdown of either *ptpn13* or *ptpn20* and *arhgap29b*. When we co-injected morpholinos targeting these genes, we were able to demonstrate that only combined low-dose knockdown of *ptpn13* or *ptpn20* with *arhgap29b* decreased tail length (Fig 6a, Fig. S4). Combined knockdown with *arhgap5* did not induce a phenotype, suggesting that the Arhgap29b – PTP phenotype was specific and not a mere generic effect of combined knockdown with any Rho-GAP. Interestingly, when we performed combined low dose knockdown of *ptpra* or *ptpre* with *arhgap29b*, we did not see reconstitution of the shorter phenotype (Fig 6b, Fig. S4).

To investigate functional interactions of the four PTPs with NGEF, we performed partial knockdowns of *ngef* and the different phosphatases. Analysis of the tail length at 3 dpf revealed that RPTP α and PTP ϵ , but not PTP-BL and Ptpn20, interacted with NGEF (Fig.6c, Fig S4). These results are consistent with our hypothesis that RPTP α and PTP ϵ are upstream activators of RhoA while PTP-BL and Ptpn20 inactivate RhoA. Combining low dose knockdown of either two activators (*ptpra/ptpre* and *ngef*) or in-activators (*ptpn13/ptpn20* and *arhgap29b*) results in a phenotype, whereas combined co-knockdown of an activator with an inacti-

Figure 6. Arhgap29 and NGEF act downstream of distinct PTPs.

(a) Low dose combined knockdowns of *ptpn13* or *ptpn20* and *arhgap29b* were performed by injecting indicated amounts of morpholino at the one cell stage. Tail lengths were measured at 3dpf and plotted. Co-knockdowns with *arhgap5* were included as a control. (b) Similar co-knockdowns as in (a) but with *ptpra* and *ptpre* knockdown instead of *ptpn13* and *ptpn20* knockdown. (c) Zebrafish embryos were micro-injected with morpholinos targeting the different phosphatases in low concentrations together with low dose *arhgef27* (*ngef*) morpholino. Embryos were grown to 3 dpf and tail lengths were determined and plotted as a percentage of non-injected control. All error bars are standard error of the mean. Student t-test was performed where indicated; no asterisk indicates $P > 0.05$, * indicates $0.05 > P > 0.001$ and ** indicates $P < 0.001$.



vator does not affect development.

Discussion

Here, we describe four PTPs involved in regulating cell polarity in zebrafish C/E cell movements, RPTP α , PTP ϵ , PTP-BL and Ptpn20 (Fig. 2 and 3). These phosphatases function in pairs, and have opposing effects on RhoA activation (Fig. 4, Fig. S3). Our data suggest a role for NGEF (ephexin1) and Arhgap29 (Parg1) as activators and inhibitors of RhoA activity in C/E movements downstream of PTP signaling. We propose a model (Fig. 7a), where RPTP α and PTP ϵ dephosphorylate and activate the SFKs Fyn and Yes, which then leads to downstream activation of NGEF perhaps by direct phosphorylation of Tyr-87, resulting in RhoA activation. PTP-BL and Ptpn20 recruit and activate Arhgap29, leading to decreased RhoA activity downstream. Positive and negative effects of the PTPs on RhoA activation act in concert to mediate cell polarization which is at the basis of C/E cell movements.

Ptpn20 and Frmpd2 have been studied very little. In the Tiganis lab studies have been done on different isoforms of *PTPN20* using 5' RACE [57]. They describe the identification of several isoforms, all consisting of the PTP domain only. Stenzel *et al.* report the basolateral targeting of Frmpd2 in epithelial cells and searched for different *FRMPD2* isoforms *in silico* [58]. No coding transcripts have been described so far spanning both the *FRMPD2* gene and the *PTPN20* gene. Our data clearly show that *frmpd2* and *ptpn20* sequences belong to the same gene (Fig. 1), but do not exclude the existence of the *ptpn20* isoforms described so far. We provide evidence that at least one additional *ptpn20* isoform exists, which is a paralogue of *ptpn13*. It would be interesting to investigate if indeed *frmpd2*, the PTP domain of *ptpn20* and the whole *ptpn20* as described here are separately expressed and have unique functions. Our results indicating that *ptpn13* and *ptpn20* are paralogues are not surprising, considering the high degree of conservation between their PTP domains. Their remarkable homology in sequence and structure clearly suggests a common ancestor. PTP-BL is a well-studied protein, and the identification of a paralogue brings a scala of interesting possibilities. Like PTP-BL, Ptpn20 is to be expected to act as an adaptor protein and participate in protein-protein interactions. *Ptpn13*^($\Delta P/\Delta P$) mice have a surprisingly mild phenotype [59], which could possibly be explained by partially redundant functions with *ptpn20*.

We demonstrate here the requirement of four phosphatases in normal C/E cell movements through their ability to regulate RhoA. Although RhoA is a well-known target of non-canonical Wnt signaling, an important signaling pathway in C/E cell movements, as well as other pathways controlling C/E, not much is known presently about the GEFs and GAPs controlling RhoA activity. Here we identified Arhgap29 (Parg1) and NGEF as Rho-GAP and Rho-GEF, respectively, for

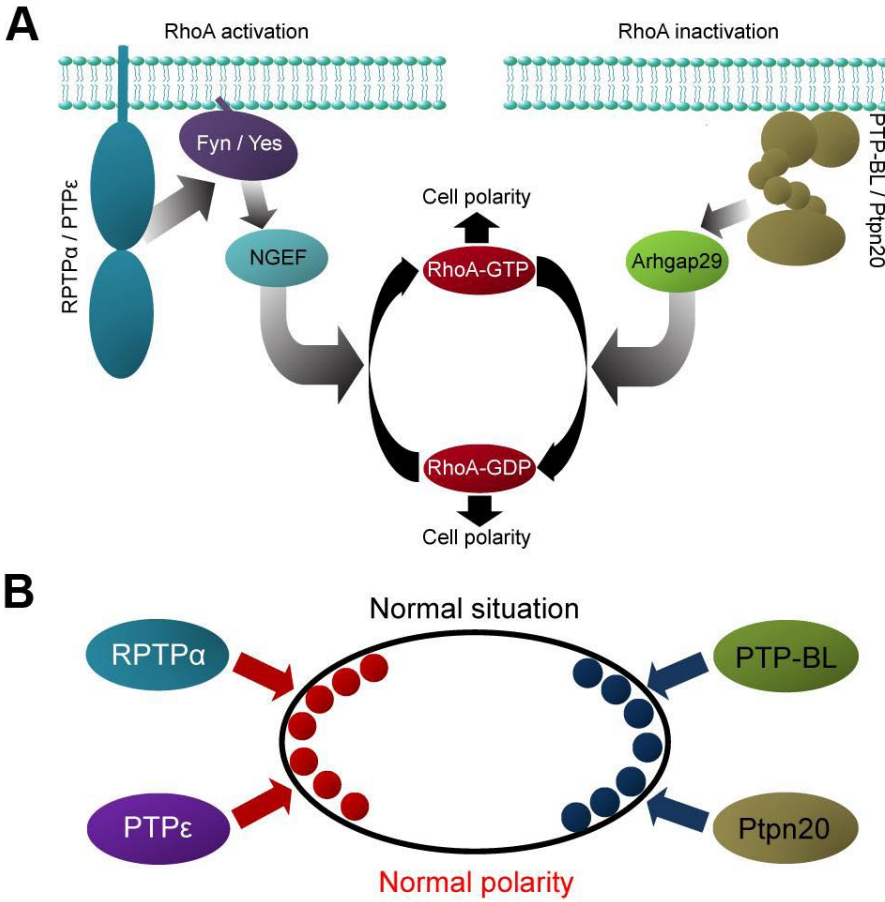


Figure 7. Model for PTP signaling in RhoA (in)activation and cell polarization.

(a) RPTP α and PTP ϵ are known activators of the SFKs, Fyn and Yes. Fyn and Yes either directly or indirectly activate NGEF by phosphorylation of Tyr-87 residue, increasing the specificity and activity of NGEF towards RhoA. PTP-BL and Ptpn20 likely indirectly activate Arhgap29 by either ensuring its recruitment or activation in order to inhibit RhoA activity. (b) Model for how enhanced and decreased RhoA activation may induce similar phenotypes. Assuming polarized distribution of RhoA-GTP (red dots) and RhoA-GDP (blue dots), either loss or increase of RhoA activation will result in loss of cell polarity (see text and Fig. S5 for further details).

RhoA in C/E cell movements. Genetic interactions were established between *arhgap29* and *ptpn13/ptpn20*, two inhibitors of RhoA activity and between *ngef* and *ptpra/ptpre*, two activators of RhoA (Fig. 6). Knockdown of *ngef* or *arhgap29b* led to C/E cell movement defects mediated by impaired cell polarization (Fig. 5). Arhgap29 was originally identified as Parg1, PTP-BL interacting Rho-GAP [55] NGEF (ephexin1) is a well-established downstream component of Eph/ephrin signaling, and has been shown to play a role in axon pathfinding [60], [61], [62], [63].

Several lines of evidence presented here suggest a pathway controlled by tyrosine phosphatases regulating RhoA activity independently of the non-canonical Wnt signaling pathway. First we show that RPTP α , PTP ϵ , PTP-BL and Ptpn20 have opposing effects on RhoA activation as RPTP α and PTP ϵ knockdown induced defects can be rescued by co-injection of constitutively active RhoA, while PTP-BL and Ptpn20 knockdown induced defects can be rescued by co-injection of dominant negative RhoA in zebrafish embryos. Consistent with these data is the observation that RhoA is activated in HEK293T cells over-expressing RPTP α and inactivated in cells expressing PTP-BL (Fig. 4). Next we show genetic interactions of the Rho-GEF NGEF with RPTP α and PTP ϵ , and the Rho-GAP Arhgap29b with PTP-BL and Ptpn20, resulting in a plausible explanation how RhoA activity can be altered downstream of these phosphatases (Fig. 6). Lastly we demonstrate by means of markers at the 1 somite and 7/8 somite stage as well as analysis of the cell shape and polarity during C/E cell movements that all genes involved indeed show defective C/E cell movements upon knockdown (Fig. 2, 5).

We present here the use of morpholino knockdown as a powerful tool for screening for components functioning within a single pathway, by co-injecting different morpholinos in suboptimal concentrations. The phenotypes demonstrated by knockdown of a single gene were reproduced by a second morpholino and/or rescued by co-injection of mRNA encoding the target gene, demonstrating specificity. Full knockdown of all the genes involved results in a phenotype. Full co-knockdowns of combinations of these genes often resulted in embryonic lethality, like co-knockdown of *ptpra* and *ptpre*, *ptpn13* and *ptpn20* or *ptpra* and *ptpn13* (data not shown). Suboptimal co-knockdowns allowed us to assess epigenetic interactions. Not all combinations of low dose morpholinos induced developmental defects, which enhanced confidence in our approach. Moreover, the inclusion of a control, *gap5*, that is not involved in C/E cell movements and does not result in an increased phenotype when co-injected at sub optimal doses, as opposed to *ngef* or *arhgap29b*, demonstrates the specificity of our approach. We use tail length at 3dpf as an easily quantifiable initial readout for the extent that the embryos are affected by combined low dose knockdowns. All genes described here were confirmed to be involved in C/E cell movements by analysis of their full knockdown phenotype using the appropriate markers at 1 somite and 7/8 somite stage, and analyzing cell polarity and cell shape in the presomitic mesoderm during C/E cell movements.

PTP-BL has previously been shown to be able to interact through its PDZ domains with PDZ binding proteins such as ephrin-B. Ephrin-B ligands have a PDZ binding motif at their C-terminus. Binding of PTP-BL has been suggested to regulate the dephosphorylation of the ephrin-B tyrosine 298 residue [50]. This



residue was shown to be phosphorylated by SFKs, which has been verified *in vitro* by mass spectrometry analysis [64], and has been suggested to mediate the recruitment of Disheveled and RhoA. We have shown [45] that Fyn and Yes act downstream of RPTP α and PTP ϵ , and mediate activation of RhoA, thus opposing the effect of PTP-BL and Ptpn20. It will be interesting to find out if Eph/ephrin-B signaling indeed link phosphatase signaling to downstream RhoA activation, which is also suggested by the involvement of NGEF, a downstream component of ephrin-B reverse signaling.

We propose a model for PTP regulated activation and inhibition of RhoA activity in C/E cell movements through NGEF and Arhgap29 (Fig. 7a). Activation of the SFKs Fyn and Yes by RPTP α and PTP ϵ may directly lead to phosphorylation of NGEF on Tyr87 and conversion of RhoA-GDP to RhoA-GTP. PTP-BL and Ptpn20 recruit Arhgap29, leading to conversion of RhoA-GTP to RhoA-GDP. The two pairs of PTPs mediate activation and inactivation of RhoA, respectively. How both RhoA activation and inactivation contributes to C/E cell movements remains to be determined definitively. We hypothesize that asymmetric distribution of RhoA-GTP and RhoA-GDP over the leading and trailing edge of the cell is required for proper polarity and migration. Over-activation of RhoA or over-inhibition of RhoA will both result in loss of polarity, explaining why both knockdown of upstream activators like RPTP α and PTP ϵ and inhibitors like PTP-BL and Ptpn20 lead to similar phenotypes (Fig. 7b). That inhibition and activation of a signaling pathway leads to similar phenotypes is not unprecedented. Noonan and LEOPARD mutations in Shp2 result in activation and inactivation of phosphatase activity, respectively, but both result in remarkably similar phenotypes in humans and zebrafish [44], [65]. Similarly, both inhibition and overexpression of Rok2 has been shown to induce similar phenotypes in zebrafish embryos [24]. Our data shows that RPTP α , PTP ϵ , PTP-BL and Ptpn20 function in pairs, where low dose co-knockdown of *ptpra* and *ptpn13* resulted in a severe phenotype and co-knockdown of *ptpra* and *ptpn20* did not. Similarly, *ptpre* and *ptpn20*, but not *ptpn13* cooperated. To explain these results we suggest a model as depicted in Fig. 7b. We propose that RPTP α and PTP ϵ act on one side of the cell as activators of RhoA, while PTP-BL and Ptpn20 act on the opposite side as inhibitors. Full knockdown of either one of the components, activating or inhibiting, will reduce RhoA-GTP or RhoA-GDP levels to such an extent that cell polarity will be lost (cf. Fig. S5). Low dose knockdown of a single component mildly reduces RhoA-GTP or RhoA-GDP levels, but does not result in loss of polarity and defective C/E cell movements, because of normal signaling on the opposing side. Combined low dose knockdown however, will lead to reduced activation of RhoA on one side and reduced inhibition of RhoA on the other side, resulting in loss of polarity and hence C/E cell movement defects (Fig. S5). We speculate that upstream activation of the different PTPs, subcellular localization of the PTPs and their target proteins, substrate specificity and cell

type specific expression may play a role in fine-tuning of the regulation of RhoA activity, possibly explaining the specificity of the combined knockdowns, i.e. why combined knockdown of *ptpra* and *ptpn13*, but not *ptpra* and *ptpn20*, induced C/E cell movement defects.

Methods

Ethics statement

Only wild type embryos up to 3 dpf were used for these experiments, which do not require approval of the animal experiments committee according to national and European law.

Zebrafish maintenance and in situ hybridization and microinjection

Zebrafish were kept and the embryos were staged as described before [66]. *In situ* hybridizations were done essentially as described [67] using probes specific for *dlx3* (currently known as *dlx3b*), *hgg1* (currently known as *ctsl1b*), *krox20* and *myod* as described earlier [44], [54]. Zebrafish were injected at the one cell stage in the cell with. Needles were calibrated to dispense 1 nanoliter volumes. Embryos were kept in E3 medium at 28.5°C. A considerable part of our results are based on measuring tail length as readout for the severity of observed phenotypes. To ensure correct interpretation of the results, we injected all morpholino and RNA constructs into the cell at the 1 cell stage, as opposed to the yolk, to ensure equal delivery of injected cargo. Since variation in volumes injected may affect the observed phenotype, special attention was paid to calibrating every needle used, and verifying amounts injected after each injection series. To minimize variation, injection conditions that were compared were injected in a single batch of embryos.

Morpholinos and RNA

Morpholinos for *ptpra*, *ptprea* and *ptpreb* have been described before [46]. Morpholinos targeting *ptpn13*, *ptpn20*, *arhgap29b* and *arhgap5* were designed as splice donor targeting, using the following sequences: MO *ptpn13*: 5'CTCTCTCTCACCTGGACGTCTTT'3; MO *ptpn20*: 5'AGAATAAGCTTACACAGAGGTGGGG'3; MO *arhgap29b*: 5'GTGCTATTGTACCTGTGCAGATGTG'3 and MO *arhgap5*: 5'GACGGGTCTCCTTATTCTTGGCCAT'3. *Ptpn13* RNA was transcribed from full length mouse cDNA kindly provided by Wiljan Hendriks (Department of Cell Biology, Radboud University Nijmegen Medical Centre, Nijmegen, The Netherlands).

Westernblot and IP

Zebrafish embryos were microinjected and raised in standard conditions. At 28hpf: whole embryos were lysed inside the chorion in buffer containing 50 mM Tris, pH 7.5, 150 mM NaCl, 1 mM EDTA, 1 mM sodium orthovanadate, 1% Nonidet P-40, 0.1% sodium deoxycholate, protease inhibitor mixture (Complete Mini, Roche Diagnostics) and vanadate, using a bioruptor and 30 μ l lysisbuffer for each embryo. Lysates were spun down and 4 \times sample buffer was added to supernatant; Samples were run on SDS-PAGE gel (15%) and transferred to PVDF membrane. After transfer the membrane was stained with Coomassie Blue stain to verify equal loading of the lysates. Subsequently the PVDF membrane was blocked with 5% BSA and then incubated with the corresponding antibodies targeting pY-87-ephexin1 (EP2841 rabbit polyclonal; ECM Biosciences - Versailles, KY, USA) or Actin (A5060 Anti-Actin 20–33 rabbit polyclonal; Sigma Aldrich - St. Louis, MO, USA) followed by the horseradish peroxidase conjugated secondary antibody. The membranes were subjected to detection by enhanced chemiluminescence.

Confocal microscopy

To achieve ubiquitous fluorescent membrane labeling, the embryos were injected at 1 cell stage with 20 pg of mRNA encoding membrane-citrine (an YFP variant with a C-terminal fusion of the Ras membrane-localization sequence [CAAX]). To visualize the cell shape in the presomitic mesoderm, membrane-citrine expressing live embryos were mounted in 0.75% soft agarose at the dorsal side in glass bottomed Petri dishes. Using a SP2 Leica confocal microscope the presomitic mesoderm was imaged using a 40 \times oil objective. Images were processed in ImageJ and, analysis of cell length-to-width ratio and angular deviation was performed by the Shape_Descriptor1u plugin [68].

Tail length assay and statistics

Embryos were microinjected at the one cell stage and grown under standard conditions to 3dpf. Pictures were taken at identical magnification and tail lengths were measured using ImageJ software. All tail lengths were calculated as percentage of non-injected control embryos from the same clutch. Comparisons were done between different injection conditions within the same clutch. Results of at least three individual experiments were pooled and tail lengths were plotted as percentages deviating from 100%. We compared tail lengths of 2 and 3 dpf embryos, measured from the border of the yolk-yolk extension to the tip of the tail and found that tail length increases about 6% from day 2 to day 3. In our experience, injection of morpholino or mRNA inducing phenotypes generally in-



duces a delay of approximately 1 hour maximum at the 1 somite stage. Error bars represent S.E.M. in all graphs. Two tailed student t-tests assuming unequal variance were performed to compare individual injection conditions. Total number of samples are indicated in figures, throughout figures, P-values are represented by no asterisk ($P>0.05$), * ($0.05>P>0.001$) or ** ($P<0.001$), individual P-values are indicated in the figure legends.

Footnotes

Competing Interests: The authors have declared that no competing interests exist.

Funding: This work was supported by a Marie Curie Research Training Network (PTPNET/MRTN-CT-2006-035830) and a grant from the Research Council for Earth and Life Sciences (ALW 815.02.007) with financial aid from the Netherlands Organisation for Scientific Research (NWO). The funders had no role in study design, data collection and analysis, decision to publish, or preparation of the manuscript.

Acknowledgments

We kindly thank Wiljan Hendriks (Department of Cell Biology, Radboud University Nijmegen Medical Centre, Nijmegen, The Netherlands) for providing PTP-BL constructs.

References

1. Keller R. Shaping the vertebrate body plan by polarized embryonic cell movements. *Science*. 2002;298:1950–1954.
2. Warga RM, Kimmel CB. Cell movements during epiboly and gastrulation in zebrafish. *Development*. 1990;108:569–580.
3. Heisenberg CP, Tada M, Rauch GJ, Saude L, Concha ML, et al. Silberblick/Wnt11 mediates convergent extension movements during zebrafish gastrulation. *Nature*. 2000;405:76–81.
4. Keys DN, Levine M, Harland RM, Wallingford JB. Control of intercalation is cell-autonomous in the notochord of *Ciona intestinalis*. *Dev Biol*. 2002;246:329–340.
5. Wallingford JB, Fraser SE, Harland RM. Convergent extension: the molecular control of polarized cell movement during embryonic development. *DevCell*. 2002;2:695–706.
6. Wallingford JB, Rowning BA, Vogeli KM, Rothbacher U, Fraser SE, et al. Dishevelled controls cell polarity during *Xenopus* gastrulation. *Nature*.

2000;405:81–85.

7. Ybot-Gonzalez P, Gaston-Massuet C, Girdler G, Klingensmith J, Arkell R, et al. Neural plate morphogenesis during mouse neurulation is regulated by antagonism of Bmp signalling. *Development*. 2007;134:3203–3211.
8. Wang Y, Nathans J. Tissue/planar cell polarity in vertebrates: new insights and new questions. *Development*. 2007;134:647–658.
9. Murdoch JN, Henderson DJ, Doudney K, Gaston-Massuet C, Phillips HM, et al. Disruption of scribble (*Scrb1*) causes severe neural tube defects in the circletail mouse. *Hum Mol Genet*. 2003;12:87–98.
10. Myers DC, Sepich DS, Solnica-Krezel L. Bmp activity gradient regulates convergent extension during zebrafish gastrulation. *Dev Biol*. 2002;243:81–98.
11. von der Hardt S, Bakkers J, Inbal A, Carvalho L, Solnica-Krezel L, et al. The Bmp gradient of the zebrafish gastrula guides migrating lateral cells by regulating cell-cell adhesion. *Curr Biol*. 2007;17:475–487.
12. Ataliotis P, Symes K, Chou MM, Ho L, Mercola M. PDGF signalling is required for gastrulation of *Xenopus laevis*. *Development*. 1995;121:3099–3110.
13. Ghil JS, Chung HM. Evidence that platelet derived growth factor (PDGF) action is required for mesoderm patterning in early amphibian (*Xenopus laevis*) embryogenesis. *Int J Dev Biol*. 1999;43:329–334.
14. Symes K, Mercola M. Embryonic mesoderm cells spread in response to platelet-derived growth factor and signaling by phosphatidylinositol 3-kinase. *Proc Natl Acad Sci U S A*. 1996;93:9641–9644.
15. Conway G, Margoliath A, Wong-Madden S, Roberts RJ, Gilbert W. Jak1 kinase is required for cell migrations and anterior specification in zebrafish embryos. *Proc Natl Acad Sci U S A*. 1997;94:3082–3087.
16. Miyagi C, Yamashita S, Ohba Y, Yoshizaki H, Matsuda M, et al. STAT3 noncell-autonomously controls planar cell polarity during zebrafish convergence and extension. *J Cell Biol*. 2004;166:975–981.
17. Chan J, Mably JD, Serluca FC, Chen JN, Goldstein NB, et al. Morphogenesis of prechordal plate and notochord requires intact Eph/ephrin B signaling. *Dev Biol*. 2001;234:470–482.
18. Jones TL, Chong LD, Kim J, Xu RH, Kung HF, et al. Loss of cell adhesion in *Xenopus laevis* embryos mediated by the cytoplasmic domain of XLerk, an erythropoietin-producing hepatocellular ligand. *Proc Natl Acad Sci U S A*. 1998;95:576–581.
19. Oates AC, Lackmann M, Power MA, Brennan C, Down LM, et al. An early developmental role for eph-ephrin interaction during vertebrate gastrulation. *Mech Dev*. 1999;83:77–94.
20. Hammerschmidt M, Pelegri F, Mullins MC, Kane DA, Brand M, et al. Mutations affecting morphogenesis during gastrulation and tail formation in the



- zebrafish, *Danio rerio*. *Development*. 1996;123:143–151.
21. Heisenberg CP, Brand M, Jiang YJ, Warga RM, Beuchle D, et al. Genes involved in forebrain development in the zebrafish, *Danio rerio*. *Development*. 1996;123:191–203.
 22. Jessen JR, Topczewski J, Bingham S, Sepich DS, Marlow F, et al. Zebrafish trilobite identifies new roles for *Strabismus* in gastrulation and neuronal movements. *Nat Cell Biol*. 2002;4:610–615.
 23. Kilian B, Mansukoski H, Barbosa FC, Ulrich F, Tada M, et al. The role of *Ppt/Wnt5* in regulating cell shape and movement during zebrafish gastrulation. *Mech Dev*. 2003;120:467–476.
 24. Marlow F, Topczewski J, Sepich D, Solnica-Krezel L. Zebrafish Rho kinase 2 acts downstream of *Wnt11* to mediate cell polarity and effective convergence and extension movements. *Curr Biol*. 2002;12:876–884.
 25. Sepich DS, Myers DC, Short R, Topczewski J, Marlow F, et al. Role of the zebrafish trilobite locus in gastrulation movements of convergence and extension. *Genesis*. 2000;27:159–173.
 26. Solnica-Krezel L, Stemple DL, Mountcastle-Shah E, Rangini Z, Neuhauss SC, et al. Mutations affecting cell fates and cellular rearrangements during gastrulation in zebrafish. *Development*. 1996;123:67–80.
 27. Topczewski J, Sepich DS, Myers DC, Walker C, Amores A, et al. The zebrafish glypican *knypek* controls cell polarity during gastrulation movements of convergent extension. *Dev Cell*. 2001;1:251–264.
 28. Chae J, Kim MJ, Goo JH, Collier S, Gubb D, et al. The *Drosophila* tissue polarity gene *starry night* encodes a member of the protocadherin family. *Development*. 1999;126:5421–5429.
 29. Feiguin F, Hannus M, Mlodzik M, Eaton S. The ankyrin repeat protein *Diogo* mediates *Frizzled*-dependent planar polarization. *Dev Cell*. 2001;1:93–101.
 30. Gubb D, Green C, Huen D, Coulson D, Johnson G, et al. The balance between isoforms of the prickle LIM domain protein is critical for planar polarity in *Drosophila* imaginal discs. *Genes Dev*. 1999;13:2315–2327.
 31. Klingensmith J, Noll E, Perrimon N. The segment polarity phenotype of *Drosophila* involves differential tendencies toward transformation and cell death. *Dev Biol*. 1989;134:130–145.
 32. Taylor J, Abramova N, Charlton J, Adler PN. *Van Gogh*: a new *Drosophila* tissue polarity gene. *Genetics*. 1998;150:199–210.
 33. Vinson CR, Conover S, Adler PN. A *Drosophila* tissue polarity locus encodes a protein containing seven potential transmembrane domains. *Nature*. 1989;338:263–264.
 34. Jenny A, Darken RS, Wilson PA, Mlodzik M. Prickle and *Strabismus* form a functional complex to generate a correct axis during planar cell polarity signaling. *EMBO J*. 2003;22:4409–4420.



35. Montcouquiol M, Kelley MW. Planar and vertical signals control cellular differentiation and patterning in the mammalian cochlea. *J Neurosci*. 2003;23:9469–9478.
36. Boutros M, Mlodzik M. Dishevelled: at the crossroads of divergent intracellular signaling pathways. *Mech Dev*. 1999;83:27–37.
37. Boutros M, Paricio N, Strutt DI, Mlodzik M. Dishevelled activates JNK and discriminates between JNK pathways in planar polarity and wingless signaling. *Cell*. 1998;94:109–118.
38. Strutt DI, Weber U, Mlodzik M. The role of RhoA in tissue polarity and Frizzled signalling. *Nature*. 1997;387:292–295.
39. Dunah AW, Hueske E, Wyszynski M, Hoogenraad CC, Jaworski J, et al. LAR receptor protein tyrosine phosphatases in the development and maintenance of excitatory synapses. *Nat Neurosci*. 2005;8:458–467.
40. Elchebly M, Wagner J, Kennedy TE, Lanctot C, Michaliszyn E, et al. Neuroendocrine dysplasia in mice lacking protein tyrosine phosphatase sigma. *Nat Genet*. 1999;21:330–333.
41. Wallace MJ, Batt J, Fladd CA, Henderson JT, Skarnes W, et al. Neuronal defects and posterior pituitary hypoplasia in mice lacking the receptor tyrosine phosphatase PTPsigma. *Nat Genet*. 1999;21:334–338.
42. Saunders AE, Johnson P. Modulation of immune cell signalling by the leukocyte common tyrosine phosphatase, CD45. *Cell Signal*. 2010;22:339–348.
43. Tartaglia M, Mehler EL, Goldberg R, Zampino G, Brunner HG, et al. Mutations in PTPN11, encoding the protein tyrosine phosphatase SHP-2, cause Noonan syndrome. *Nat Genet*. 2001;29:465–468.
44. Jopling C, van Geemen D, den Hertog J. Shp2 knockdown and Noonan/LEOPARD mutant Shp2-induced gastrulation defects. *PLoS Genet*. 2007;3:e225.
45. van Eekelen M, Runtuwene V, Overvoorde J, den Hertog J. RPTPalpha and PTPepsilon signaling via Fyn/Yes and RhoA is essential for zebrafish convergence and extension cell movements during gastrulation. *Dev Biol*. 2010;340:626–639.
46. van Eekelen M, Overvoorde J, van Rooijen C, den Hertog J. Identification and expression of the family of classical protein-tyrosine phosphatases in zebrafish. *PLoS One*. 2010;5:e12573.
47. Li Y, Kanki H, Hachiya T, Ohyama T, Irie S, et al. Negative regulation of Fas-mediated apoptosis by FAP-1 in human cancer cells. *Int J Cancer*. 2000;87:473–479.
48. Ungefroren H, Voss M, Jansen M, Roeder C, Henne-Bruns D, et al. Human pancreatic adenocarcinomas express Fas and Fas ligand yet are resistant to Fas-mediated apoptosis. *Cancer Res*. 1998;58:1741–1749.
49. Lin D, Gish GD, Songyang Z, Pawson T. The carboxyl terminus of

- B class ephrins constitutes a PDZ domain binding motif. *J Biol Chem.* 1999;274:3726–3733.
50. Palmer A, Zimmer M, Erdmann KS, Eulenburg V, Porthin A, et al. EphrinB phosphorylation and reverse signaling: regulation by Src kinases and PTP-BL phosphatase. *Mol Cell.* 2002;9:725–737.
51. Hatta K, Takahashi Y. Secondary axis induction by heterospecific organizers in zebrafish. *Developmental dynamics : an official publication of the American Association of Anatomists.* 1996;205:183–195.
52. Li H, Marijanovic I, Kronenberg MS, Erceg I, Stover ML, et al. Expression and function of Dlx genes in the osteoblast lineage. *Developmental biology.* 2008;316:458–470.
53. Jopling C, den Hertog J. Fyn/Yes and non-canonical Wnt signalling converge on RhoA in vertebrate gastrulation cell movements. *EMBO Rep.* 2005;6:426–431.
54. Jopling C, Hertog J. Essential role for Csk upstream of Fyn and Yes in zebrafish gastrulation. *Mech Dev.* 2007;124:129–136.
55. Saras J, Franzen P, Aspenstrom P, Hellman U, Gonez LJ, et al. A novel GTPase-activating protein for Rho interacts with a PDZ domain of the protein-tyrosine phosphatase PTPL1. *J Biol Chem.* 1997;272:24333–24338.
56. Zhang Y, Sawada T, Jing X, Yokote H, Yan X, et al. Regulation of ephexin1, a guanine nucleotide exchange factor of Rho family GTPases, by fibroblast growth factor receptor-mediated tyrosine phosphorylation. *J Biol Chem.* 2007;282:31103–31112.
57. Fodero-Tavoletti MT, Hardy MP, Cornell B, Katsis F, Sadek CM, et al. Protein tyrosine phosphatase hPTPN20a is targeted to sites of actin polymerization. *Biochem J.* 2005;389:343–354.
58. Stenzel N, Fetzer CP, Heumann R, Erdmann KS. PDZ-domain-directed basolateral targeting of the peripheral membrane protein FRMPD2 in epithelial cells. *J Cell Sci.* 2009;122:3374–3384.
59. Wansink DG, Peters W, Schaafsma I, Suttmuller RP, Oerlemans F, et al. Mild impairment of motor nerve repair in mice lacking PTP-BL tyrosine phosphatase activity. *Physiol Genomics.* 2004;19:50–60.
60. Egea J, Nissen UV, Dufour A, Sahin M, Greer P, et al. Regulation of EphA 4 kinase activity is required for a subset of axon guidance decisions suggesting a key role for receptor clustering in Eph function. *Neuron.* 2005;47:515–528.
61. Knoll B, Drescher U. Src family kinases are involved in EphA receptor-mediated retinal axon guidance. *J Neurosci.* 2004;24:6248–6257.
62. Sahin M, Greer PL, Lin MZ, Poucher H, Eberhart J, et al. Eph-dependent tyrosine phosphorylation of ephexin1 modulates growth cone collapse. *Neuron.* 2005;46:191–204.
63. Shamah SM, Lin MZ, Goldberg JL, Estrach S, Sahin M, et al. EphA recep-

- tors regulate growth cone dynamics through the novel guanine nucleotide exchange factor ephexin. *Cell*. 2001;105:233–244.
64. Jorgensen C, Sherman A, Chen GI, Pasculescu A, Poliakov A, et al. Cell-specific information processing in segregating populations of Eph receptor ephrin-expressing cells. *Science*. 2009;326:1502–1509.
65. Edouard T, Montagner A, Dance M, Conte F, Yart A, et al. How do Shp2 mutations that oppositely influence its biochemical activity result in syndromes with overlapping symptoms? *Cell Mol Life Sci*. 2007;64:1585–1590.
66. Westerfield M. *The Zebrafish Book*. Eugene, Oregon: University of Oregon Press; 1995.
67. Thisse C, Thisse B, Schilling TF, Postlethwait JH. Structure of the zebrafish *snail1* gene and its expression in wild-type, *spadetail* and *no tail* mutant embryos. *Development*. 1993;119:1203–1215.
68. Syverud K, Chinga G, Johnsen PO, Leirset I, Wiik K. Analysis of lint particles from full-scale printing trials. *APPITA*. 2007;60:286–290.



Supplementary figures

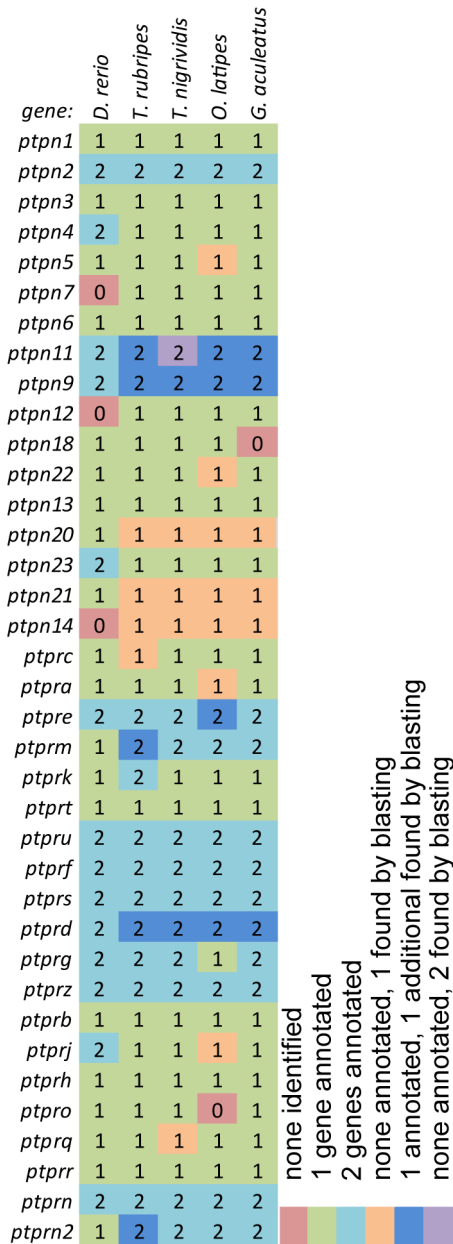


Figure S1. Protein tyrosine phosphatase genes in five fish species identified by blasting.

Fish orthologs of all PTP encoding genes were identified by BLASTing the PTP domains of every single human PTP gene against the 5 respective zebrafish genomes. Indicated are genes already annotated in Ensembl (green), or 2 genes already annotated (light blue), 1 gene annotated, 1 additional one found by blasting (dark blue), none annotated, 1 identified by blasting (orange), none annotated and 2 identified by blasting (purple) or none annotated and none identified (red).

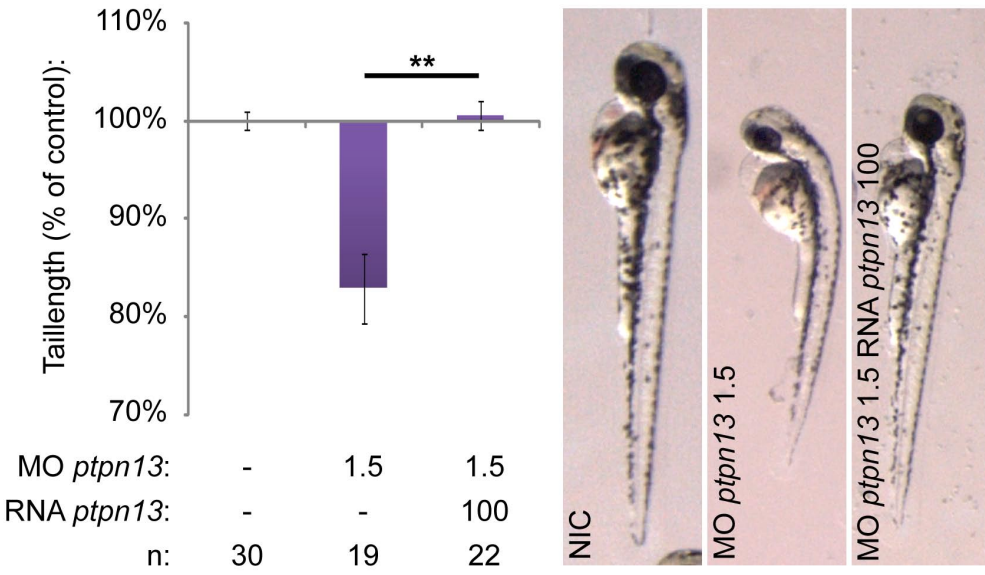


Figure S2. *Ptpn13* knockdown phenotype can be rescued by co-injection of *ptpn13* mRNA. Zebrafish embryos were microinjected at the one cell stage with MO *ptpn13* alone or in combination with mouse *ptpn13* mRNA. Fish were grown to 3dpf and tail lengths were measured. Average tail length relative to non-injected control is plotted. All error bars are standard error of the mean. Student t-test was performed where indicated; ** indicates $P < 0.001$.

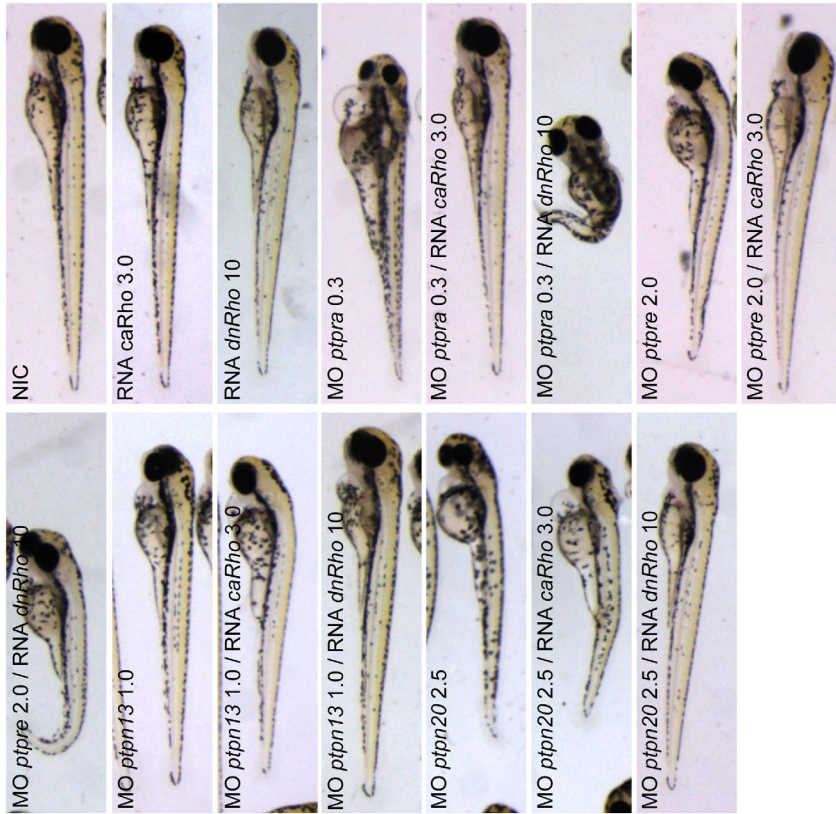


Figure S3. PTP knockdowns are rescued by active or dominant negative RhoA.

Embryos were micro-injected at the one cell stage using morpholinos (high concentration) targeting the indicated genes together with no RNA, RNA encoding constitutively active RhoA (3 pg/embryo) or RNA encoding dominant negative RhoA (20 pg/embryo). Fish were grown to 3dpf and pictures were taken; representative fish for each condition are shown.



Figure S4. Arhgap29 and NGEF act downstream of distinct PTPs.

Low dose combined knockdowns of *ptpn13*, *ptpn20*, *ptpra*, or *ptpre* and *arhgap29b* or *arhgef27* (*ngef*) were performed by injecting indicated amounts of morpholino at the one cell stage. Fish were grown to 3dpf and pictures were taken; representative embryos for each condition are shown. Co-knockdowns with *arhgap5* were included as a control.

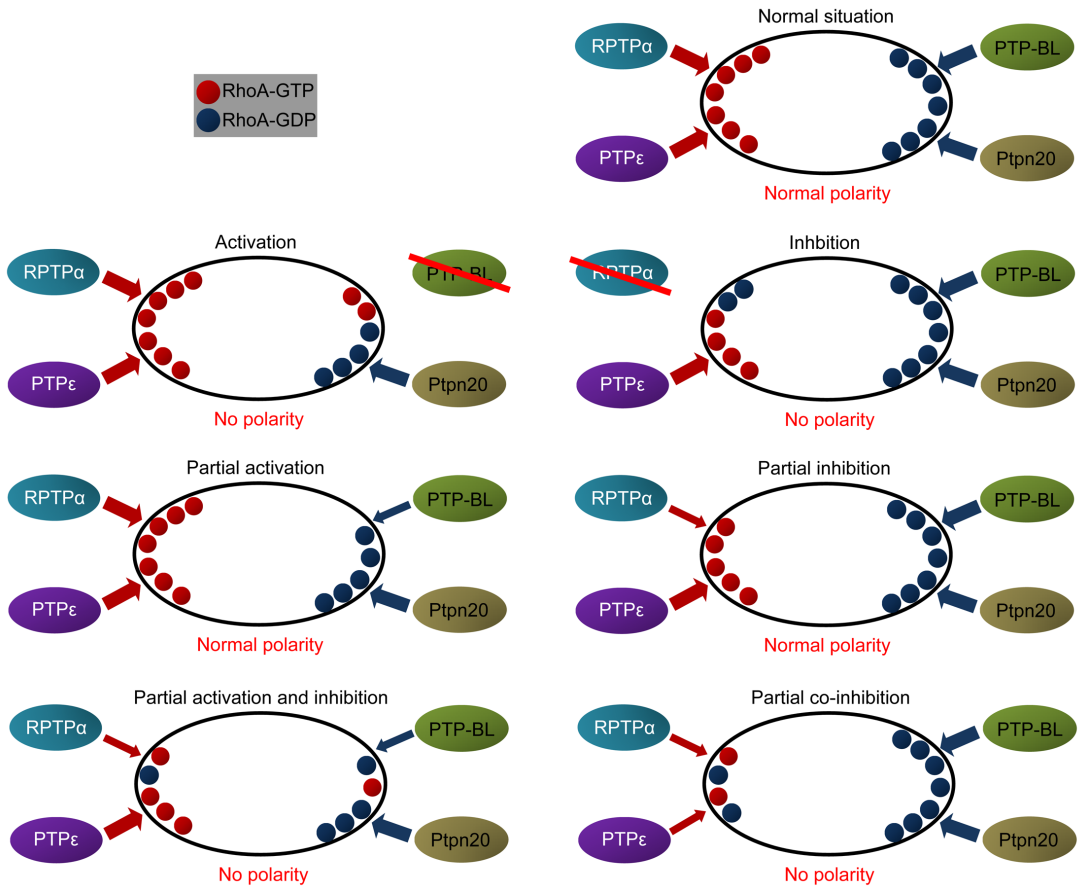


Figure S5. Model for low dose PTP co-knockdown-induced defects.

In the normal situation RPTP α and PTP ϵ activate RhoA one side of the cell and RhoA activity is inhibited on the opposing side by PTP-BL and Ptn20. Normal RhoA activation and inhibition of RhoA is indicated by thick red and blue arrows, respectively. RhoA-GTP is schematically indicated by red dot, Rho-GDP by blue dot. Deletion of an inactivator (PTP-BL) or activator (RPTP α) – indicated by strike-through – results in reduced RhoA-GDP or RhoA-GTP on one side of the cell, respectively, and hence loss of polarity. Low dose knockdown of one of the PTPs (thin arrows) results in small differences in RhoA-GTP/RhoA-GDP distribution that do not affect cell polarization. Partial knockdown of both activators (or both inactivators, not shown) will result in severe changes in RhoA activation on one side of the cell and hence disturb cell polarization. Partial activation and partial inhibition of RhoA may lead to reduction of RhoA-GTP on one side of the cell and reduction of RhoA-GDP on the other side of the cell, hence disturbing cell polarization. Together, this model explains how two pairs of PTPs with opposing effects on RhoA activation act in concert to maintain cell polarization that is at the basis of convergence and extension cell movements during zebrafish gastrulation.

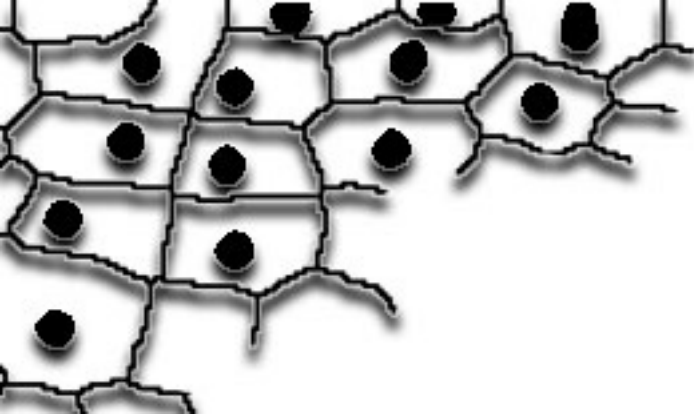
Table S1. Non-annotated PTP genes in four fish species identified by blasting.

The PTP domains of human phosphatases were blasted against the genomes of fugu, medaka, tetraodon and stickleback. All PTP encoding genes identified not previously annotated as being a PTP encoding gene are listed here with corresponding gene name appended with a or b in case of gene duplication.

Table S1. Non-annotated PTP genes in four fish species identified by blasting.

Species:	Gene:	Location:
<i>T. Rubripes</i>	pt-	ENSTRUG00000006764
	pn11b	
	ptpn9b	ENSTRUG00000004960
	ptpn20	ENSTRUG00000012682
	ptpn21	ENSTRUG00000013692
	ptpn14	ENSTRUG00000014100
	ptprc	NP_001027788.1
	ptprmb	scaffold_297: 283,607-287,768
	ptprdb	scaffold_11124
<i>T. Nigrividis</i>	ptprn2b	scaffold_9445
	ptpn11a	GSTENT10016339001
	pt-	ENSTNIG00000010883
	pn11b	
	ptpn9b	ENSTNIG00000017817
	ptpn20	ENSTNIG00000003885
	ptpn21	ENSTNIG00000017244
	ptpn14	ENSTNIG00000016380
	ptprdb	ENSTNIG00000004098
<i>O. Latipes</i>	ptprq	GSTENG10005433001
	pt-	ENSORLG00000000613
	pn11b	
	ptpn9b	ENSORLG00000005257
	ptpn22	scaffold12_contig11260
	ptpn20	FRMPD2
	ptpn21	ENSORLG00000012974
	ptpn14	ENSORLG00000014908
	ptpra	Q76K58_ORYLA
ptpreb	Q76K57_ORYLA	
<i>G. Aculeatus</i>	ptprdb	ENSORLG00000004685
	ptprj	ENSORLG00000017385
	pt-	ENSGACG00000004807
	pn11b	
	ptpn9b	ENSGACG00000016107
	ptpn20	ENSGACG00000007126
	ptpn21	ENSGACG00000010542
	ptpn14	ENSGACG00000010112
	ptprdb	ENSGACG00000015921





4

Noonan Syndrome Gain-of-Function Mutations in NRAS cause Zebrafish Gastrulation Defects

Vincent Runtuwene*, Mark van Eekelen*, John Overvoorde, Holger Rehmann, Helger G. Yntema, Willy M. Nillesen, Arie van Haeringen, Ineke van der Burgt, Boudewijn Burgering and Jeroen den Hertog

Dis Model Mech. 2011 May; 4(3): 393–399.

*=equal contribution

Abstract

Noonan syndrome is a relatively common developmental disorder that is characterized by reduced growth, wide-set eyes and congenital heart defects. Noonan syndrome is associated with dysregulation of the Ras-mitogen-activated-protein-kinase (MAPK) signaling pathway. Recently, two mutations in *NRAS* were reported to be associated with Noonan syndrome, T50I and G60E. Here, we report a mutation in *NRAS*, resulting in an I24N amino acid substitution, that we identified in an individual bearing typical Noonan syndrome features. The I24N mutation activates N-Ras, resulting in enhanced downstream signaling. Expression of N-Ras-I24N, N-Ras-G60E or the strongly activating mutant N-Ras-G12V, which we included as a positive control, results in developmental defects in zebrafish embryos, demonstrating that these activating N-Ras mutants are sufficient to induce developmental disorders. The defects in zebrafish embryos are reminiscent of symptoms in individuals with Noonan syndrome and phenocopy the defects that other Noonan-syndrome-associated genes induce in zebrafish embryos. MEK inhibition completely rescued the activated N-Ras-induced phenotypes, demonstrating that these defects are mediated exclusively by Ras-MAPK signaling. In conclusion, mutations in *NRAS* from individuals with Noonan syndrome activated N-Ras signaling and induced developmental defects in zebrafish embryos, indicating that activating mutations in *NRAS* cause Noonan syndrome.

Introduction

Activating mutations in genes encoding components of the Ras-MAPK pathway have not only been identified in various tumor types, but also in developmental disorders (Aoki et al., 2008; Karnoub and Weinberg, 2008; Schubert et al., 2007). Germline mutations in genes of the Ras-MAPK pathway have been found in a group of genetic syndromes that are collectively called RASopathies, including Noonan syndrome (OMIM 163950), LEOPARD syndrome (OMIM 151100), Costello syndrome (OMIM 218040) and cardio-facio-cutaneous (CFC) syndrome (OMIM 115150) (Denayer et al., 2008; Tidyman and Rauen, 2009). These syndromes are characterized by partially overlapping symptoms, including distinctive craniofacial features and cardiovascular anomalies, and they are genetically heterogeneous, with mutations in known disease genes accounting for 70–80% of the cases.

Noonan syndrome is a relatively common dominantly inherited genetic disorder characterized by congenital heart defects, reduced growth, facial dysmorphism and variable congenital defects (Gelb and Tartaglia, 2006). The syndrome is caused by activating mutations in genes encoding upstream factors of the Ras-MAPK pathway, including *PTPN11* (*Shp2*) (Tartaglia et al., 2001) and *SOS1* (Roberts et al., 2007; Tartaglia et al., 2007), as well as *KRAS* (Pandit et al.,



2007; Schubbert et al., 2006), *SHOC2* (Cordeddu et al., 2009) and the more downstream signal transducers *RAF1* and *BRAF* (Pandit et al., 2007; Razzaque et al., 2007; Tartaglia et al., 2007). The most recent addition to the group of genes that are associated with Noonan syndrome is *NRAS*. In a cohort of 917 individuals with typical features of Noonan syndrome, who were negative for mutations in previously known Noonan-syndrome-associated genes, two distinct mutations, T50I and G60E, were identified in *NRAS* in four individuals. Mutant N-Ras-G60E and, to a lesser extent, N-Ras-T50I activated MAPK signaling in cells (Cirstea et al., 2010). Activation of N-Ras was previously found to be associated with acute myeloid leukemia (AML) (Bos et al., 1985; Bos et al., 1987) and melanoma (van 't Veer et al., 1989), and a germline activating mutation in *NRAS* causes autoimmune lymphoproliferative syndrome (Oliveira et al., 2007).

Here, we report the identification of a new mutation in N-Ras in an individual with Noonan syndrome that results in an amino acid substitution, I24N. Mutant N-Ras-I24N activates downstream MAPK signaling. We used zebrafish embryos to assess the *in vivo* effects of dominant mutations in genes that are associated with Noonan syndrome, as we and others have done previously (Anastasaki et al., 2009; Jopling et al., 2007; Razzaque et al., 2007; Stewart et al., 2010). Expression of N-Ras-I24N or two other Noonan-syndrome-associated N-Ras mutants, T50I or G60E, in zebrafish embryos resulted in severe developmental defects during epiboly and gastrulation that resemble the defects observed in response to a known Noonan-associated gene. Interestingly, pharmacological inhibition of MEK rescued these activated N-Ras-induced developmental defects, demonstrating that the activated N-Ras-induced defects are caused by activation of MAPK signaling.

Results and Discussion

In search of the genetic cause of Noonan syndrome, we resequenced all exons of *NRAS* in a Dutch cohort of 56 Noonan syndrome patients lacking mutations in known Noonan-syndrome-associated genes. We found a single individual heterozygous for a nucleotide mutation in exon 2, c.71T>A, resulting in the amino acid substitution p.I24N (Fig. 1A). The 30-year-old patient had been diagnosed with Noonan syndrome and demonstrated the facial features, low posterior hairline, webbing of the neck, pectus excavatum, cryptorchism, mild learning difficulties and mild short stature characteristic of the syndrome. Assessment at birth and at age 15 revealed no heart abnormalities. His parents did not exhibit classical Noonan features and did not harbor the mutation in *NRAS* (Fig. 1Ab,c), demonstrating the *de novo* origin of the mutation. To exclude the possibility of somatic mosaicism, *NRAS* was resequenced in skin fibroblasts and buccal epithelial

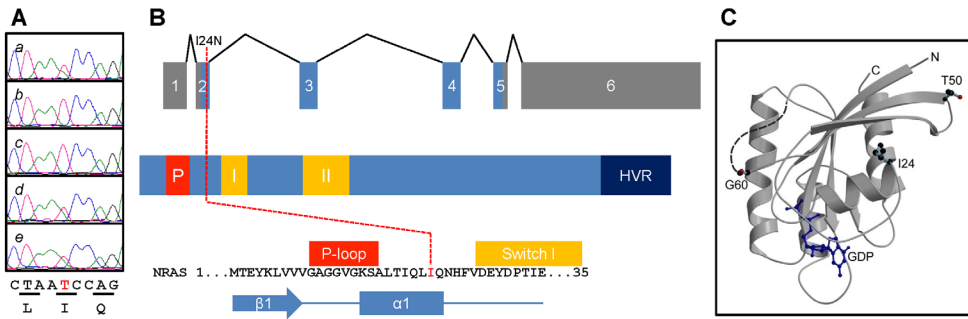


Figure 1. Identification and localization of an I24N amino acid substitution in N-Ras in an individual with typical features of Noonan syndrome.

(A) The heterozygous *c.71T>A* nucleotide substitution in exon 2 that was first identified in the patient (a) was not detected in the father (b) or the mother (c) and was detected in DNA isolated from fibroblasts (d) and sputum (e) of the patient. (B) Genomic organization (top), protein structure (middle) and sequence of N-Ras around Ile24 (bottom), which is encoded by exon 2, which is located on helix $\alpha 1$, between the P-loop (P) and switch I (I). Switch II (II) and the hypervariable region (HVR) are also indicated in the protein structure. (C) Ribbon representation of N-Ras•GDP (Protein Data Bank code: 3con), with GDP (blue) and residues Ile24, Thr50 and Gly60 highlighted as ball and stick representation. Missing connectivity for residues 61 to 71 is indicated by a dotted line.

cells from sputum from the patient, both of which showed the *c.71T>A* mutation heterozygously (Fig. 1Ad,e), which supports the conclusion that the patient has a germline *NRAS* mutation. The *c.71T>A* mutation was not found in 100 controls without Noonan syndrome.

The surrounding sequence of I24 is identical in N-Ras, K-Ras and H-Ras, and is localized between the P-loop, involved in nucleotide binding, and Switch I, involved in effector binding (Fig. 1B). Mutations in I24 have not previously been identified in any Ras isoform. Whereas efficient GTP hydrolysis is blocked in oncogenic Ras with G12V or Q61K mutations, resulting in activated Ras, such an effect of I24N is unlikely, given the location of I24 in N-Ras (Fig. 1B,C). Recently, H-Ras mutations in Gln22 (Q22) were described in three patients diagnosed with RASopathies, specifically Noonan syndrome (Q22R), CFC syndrome (Q22E) and Costello syndrome (Q22K) (van der Burgt et al., 2007; Zenker et al., 2007). Although biochemical data that the Q22 mutations activate H-Ras was not provided, other patients with similar symptoms contained well-known activating mutations in H-Ras, including G12V, G12S, G60R or E63K. Hence, it is likely that the Q22 mutations activate H-Ras, suggesting an important regulatory role for the region between the P-loop and Switch I, which includes N-Ras I24 (Fig. 1B).

Two mutations in *NRAS* were previously identified in Noonan syndrome patients, one of which (G60E) is characterized as highly GTP bound, whereas the other (T50I) showed normal GTP loading (Cirstea et al., 2010). To assess the activation state of N-Ras-I24N, GTP-bound Ras was selectively precipitated from cells stimulated with serum. We found that a higher proportion of N-Ras-I24N was precipitated relative to wild-type N-Ras (Fig. 2A). A similar effect was observed for N-Ras-G12V and N-Ras-G60E, but not for N-Ras-T50I. In the absence of serum, out of these mutants only oncogenic N-Ras-G12V was highly GTP bound. These results group N-Ras-I24N in the class of ‘mild activating’ mutations, the activation of which is dependent on upstream signaling. Mild activating mutations are commonly associated with Noonan and Noonan-related syndromes (Tidyman and Rauen, 2009). The side chain of Ile24 (I24) in the α 1-helix points towards the β 2-strand (Fig. 1C) and mutation to Asn (N) would probably result in repulsing forces between the α 1-helix and the β 2-strand, thereby destabilizing the fold of the G protein. Hence, the nucleotide affinity might be weakened, resulting in an increased exchange rate and therefore higher GTP loading under physiological conditions, because the GTP:GDP ratio is \sim 9:1 in cells. This would be in agreement with the ‘mild activation’ character of the I24N mutant.

We next investigated MAPK activation, a downstream consequence of N-Ras activation, in 293T cells expressing N-Ras-I24N and found robust MAPK

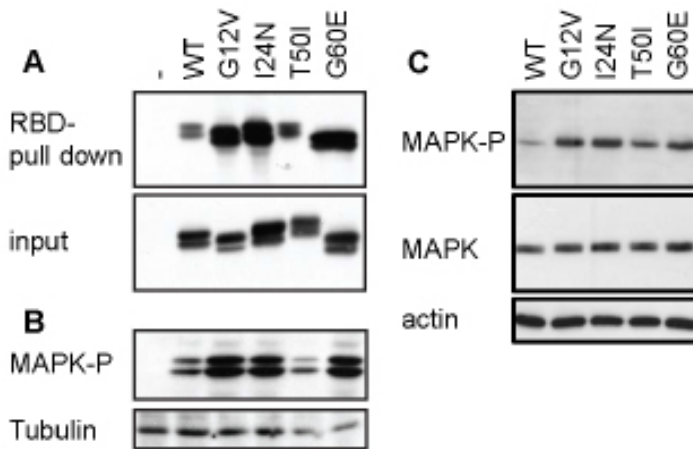


Figure 2. I24N mutation activates N-Ras and downstream signaling.

(A) Active, GTP-bound Ras was selectively precipitated from lysates of growing 293T cells transfected with RNA encoding N-Ras (wild type or mutants) with the Ras-binding domain (RBD) of Raf-1. Precipitated Ras was detected by immunoblotting using a Ras-specific antibody. The amount of Ras in the lysates was monitored by immunoblotting. (B) Transfected, growing

293T cells expressing N-Ras (mutants) were lysed and equal amounts of these lysates were loaded onto SDS-PAGE gels, blotted and probed with antibody against phospho-MAPK, or against Tubulin as a loading control. (C) Synthetic RNA (5 μ g) encoding wild-type or mutant N-Ras was injected into zebrafish embryos at the one-cell stage. Embryos were lysed at 24 hpf and loaded onto SDS-PAGE gels, blotted and probed with antibodies against phospho-MAPK, MAPK and, as a loading control, against actin.

phosphorylation in the presence of serum in comparison with wild-type N-Ras (Fig. 2B). N-Ras-G60E and the positive control, N-Ras-G12V, also enhanced MAPK activation, but N-Ras-T50I did not, which is in agreement with a weak or no increase in Ras-binding domain (RBD) binding (Fig. 2A). Together, these results demonstrate that the I24N amino acid substitution increases the fraction of active N-Ras and enhances MAPK activation, which might be due to enhanced GTP loading from subtle changes in the conformation of the GTP-binding pocket.

To evaluate the functional consequences of activating mutations in Noonan-syndrome-associated genes at the organismal level, we and others have used zebrafish as a model system (Anastasaki et al., 2009; Jopling et al., 2007; Razzaque et al., 2007; Stewart et al., 2010). Mutant N-Ras was expressed in zebrafish embryos at the one-cell stage by injection of synthetic RNA encoding wild-type or mutant N-Ras. We first established that MAPK phosphorylation is enhanced in response to N-Ras-I24N, N-Ras-G60E and N-Ras-G12V, relative to wild-type N-Ras in zebrafish embryos (Fig. 2C), which is consistent with our results in 293T cells (Fig. 2B). N-Ras-T50I only weakly activated MAPK phosphorylation in zebrafish embryos.

Morphological defects in embryos expressing mutant forms of N-Ras were apparent at 11 hours post-fertilization (hpf). The morphology of the *nras*-injected embryos was monitored by time-lapse imaging. Notably, N-Ras-I24N seemed to induce epiboly and gastrulation defects, as reflected in the reduced body axis extension at 14 hpf (supplementary material Fig. S1) and the oval shape of the embryos at epiboly (Fig. 3A). Severe morphological defects were not observed at 11 hpf or 24 hpf in embryos injected with RNA encoding wild-type N-Ras. The morphological phenotypes induced by N-Ras-I24N at 24 hpf ranged in severity from completely disorganized embryos to mildly affected shorter embryos (Fig. 3A).

The epiboly defects were quantified by analysis of the ratio of the major and minor embryonic axes (Fig. 3B). Non-injected control embryos were almost perfect spheres and the ratio of the major and minor embryonic axes was approximately 1. Injection of RNA encoding N-Ras-I24N resulted in a significant increase in the major:minor axis ratio, whereas the ratio with wild-type N-Ras was similar to non-injected controls. N-Ras-G12V from tumors and N-Ras-G60E from Noonan patients both strongly affected the major:minor axis ratio, whereas N-Ras-T50I only had mild effects (Fig. 3C). Activating mutants in B-Raf were recently reported to induce defects in epiboly (Anastasaki et al., 2009); thus, we included the robustly active B-Raf-V600E mutant as a positive control in our assay. As expected, this mutant exerted a strong effect on the major:minor axis ratio, whereas wild-type B-Raf had no effect (Fig. 3C).

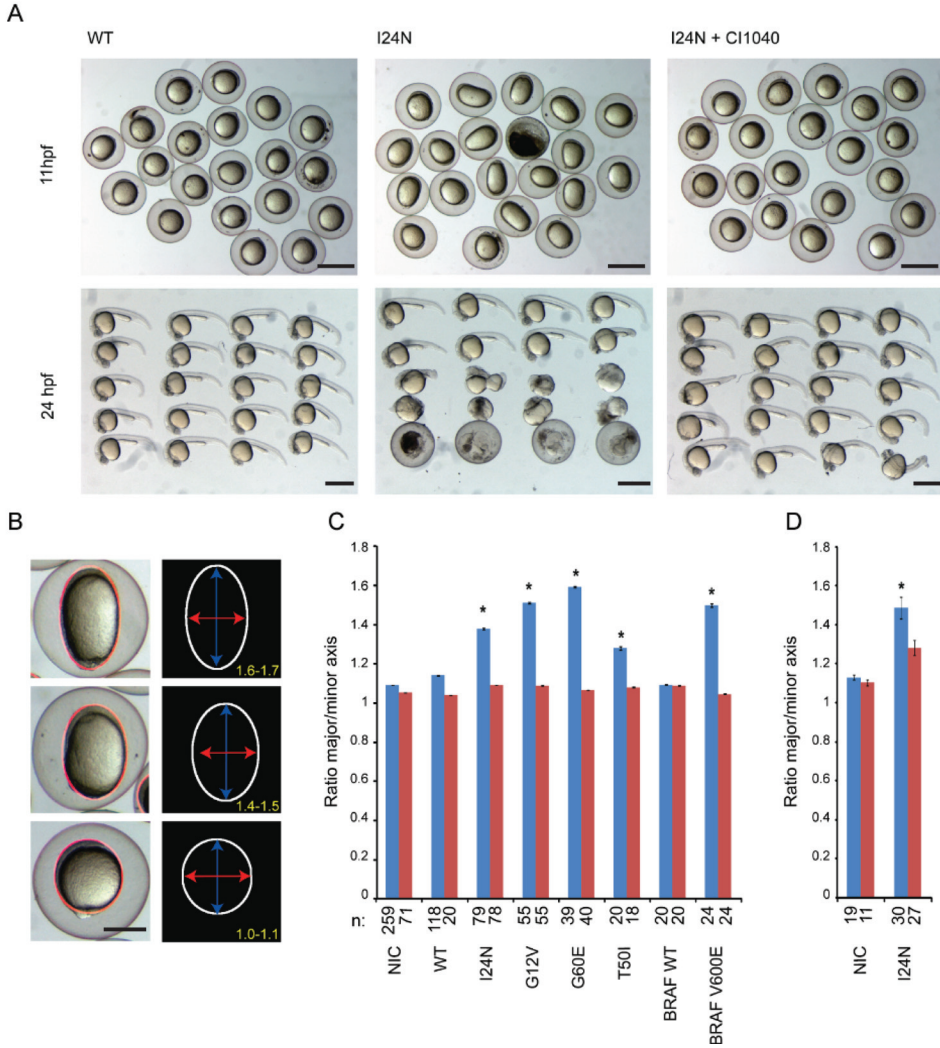


Figure 3. Active N-Ras-induced early developmental defects in zebrafish embryos.

(A) Embryos were injected at the one-cell stage with synthetic RNA (5 pg) encoding N-Ras (wild type or mutant), and morphology was assessed at 11 hpf and 24 hpf. Injected embryos were incubated with MEK inhibitor CI-1040 (1 μ M) from 4.5 hpf until 5.5 hpf. Representative batches of embryos are depicted here. Scale bars: 1 mm. (B) The severity of the phenotype was determined by assessment of the shape of the embryos at 11 hpf. The ratio of the length of the major and minor axes was determined, as indicated in examples of severely affected (top), mildly affected (middle) and a control (bottom) embryos. Scale bar: 500 μ m. (C) Quantification of the ratio of the major and minor axes upon injection of synthetic RNAs encoding wild-type (WT) or mutant N-Ras as indicated. As a negative control, the major:minor axis ratio was determined in non-injected control embryos (NIC). In addition, RNA encoding wild-type B-Raf or activated mutant B-Raf-V600E was injected. Blue bars: embryos were mock treated (0.1% DMSO); red bars: embryos were treated with MEK inhibitor CI-1040 (1 μ M). (D) Embryos were treated with the FGFR inhibitor SU5402 (5 μ M) from 4.5 hpf onwards and the phenotype was quantified as in C. Blue bars: mock-treated

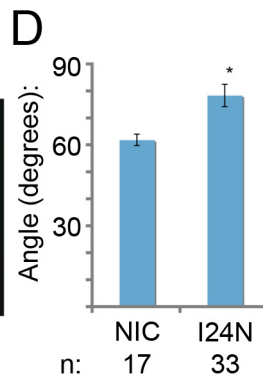
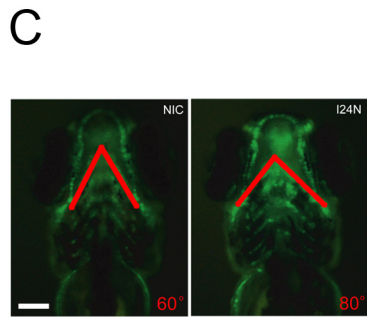
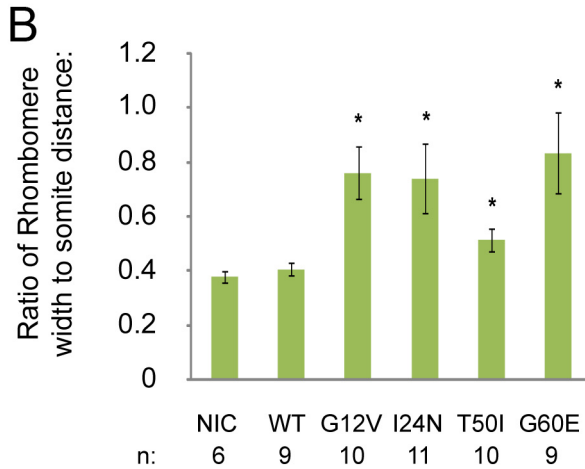
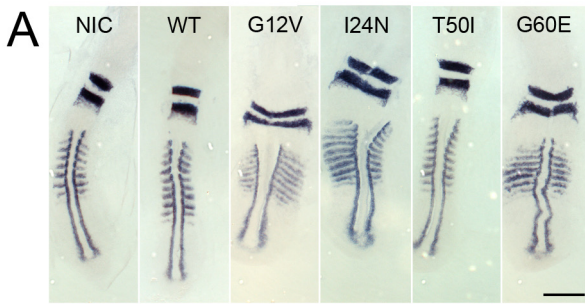


(0.1% DMSO); red bars: FGFR-inhibitor-treated. Averages of the major:minor axis ratio are depicted in panels C and D and the s.e.m. is indicated; Student's t-tests (two-tailed, assuming unequal variance) were performed between mutant and wild-type N-Ras-injected groups; *P<0.001. The total number of embryos from two to six independent experiments that were used per condition are indicated (n).

The effects of the N-Ras mutants on early zebrafish development were probably due to activation of the MAPK pathway. Using the MEK inhibitor CI-1040 to suppress downstream MAPK activation, we found that the deleterious effects of N-Ras-I24N on epiboly and later development were completely rescued by inhibition of MEK (Fig. 3A). Quantification of the epiboly defects confirmed the complete rescue of the N-Ras-I24N, N-Ras-G12V, N-Ras-G60E and N-Ras-T50I mutants, as well as B-Raf-V600E (Fig. 3C). Taken together, our data demonstrate that N-Ras-I24N is a functionally activated mutant of N-Ras that induces developmental defects, similar to those induced by N-Ras-G12V and N-Ras-G60E in a pathway requiring N-Ras-mediated activation of MAPK. It should be noted that the rescues were mediated by a pulse of MEK inhibitor between 4.5 and 5.5 hpf, whereas a more prolonged exposure to the inhibitor induced developmental defects on its own, consistent with a previous report (Anastasaki et al., 2009).

N-Ras-I24N is a mildly activating mutant of N-Ras, which requires serum to be present for activation of the Ras-MAPK pathway in 293T cells (Fig. 2B). Fibroblast growth factor receptor (FGFR) signaling is an upstream factor in convergence and extension cell movements during gastrulation. We assessed the effect of the FGFR inhibitor SU5402 on N-Ras-I24N-induced developmental defects. Interestingly, we observed that SU5402 partially rescued the gastrulation defects that were induced by N-Ras-I24N, whereas SU5402 at these concentrations had no effect on non-injected control embryos (Fig. 3D). We conclude that upstream FGFR signaling is required for the developmental defects that are induced by N-Ras-I24N.

To further characterize the activated N-Ras-induced epiboly and gastrulation cell-movement defects, we used classical molecular markers for *in situ* hybridization. Convergence and extension cell movements during gastrulation shape the embryos, making the embryo narrower (convergence) and longer (extension) (Solnica-Krezel, 2006). A well-known marker for convergence and extension cell movements during gastrulation is the ratio between the width of the *krox20*-positive rhombomeres 3 and 5 and the distance between somites 1 and 8, visualized by *myoD* staining at the eight-somite stage (12 hpf) (Li et al., 2008). Injection of N-Ras-I24N led to widening of the embryos at 12 hpf (Fig. 4A). N-Ras-G12V and N-Ras-G60E had extreme effects, whereas N-Ras-T50I resembled wild-type N-Ras (Fig. 4A). Quantification of the ratio of the width to the length



ceratohyal. The number of individuals used (n) is indicated. A Student's t-test was performed; asterisk indicates significant difference, $P < 0.005$.

revealed significant increases in this ratio in embryos injected with RNA encoding mutant N-Ras-G12V, N-Ras-I24N and N-Ras-G60E, compared with wild-type *nras*-injected and non-injected controls (Fig. 4B). N-Ras-T50I also induced a significant albeit small increase in the ratio, relative to wild-type N-Ras. Another marker for convergence and extension cell movements is *dlx3* and *hgg1* staining

Figure 4. Active N-Ras induced convergence and extension cell-movement defects and craniofacial defects.

(A) In situ hybridization was performed using embryos at the eight-somite stage (~12 hpf) using *krox20* and *myod*-specific probes: non-injected control (NIC) embryos or embryos injected with synthetic RNA encoding wild-type (WT) N-Ras or mutants, as indicated, were used. Dorsal views of flat-mounted embryos are depicted, anterior to the top. Scale bar: 250 μm . (B) The ratio of the width of the *krox20* staining and the length from the first to the eighth somite was determined using ImageJ software and is depicted here. Error bars indicate s.e.m.; Student's t-tests (two-tailed, assuming unequal variance) were performed between mutant and wild-type N-Ras-injected groups; $*P < 0.005$. Total numbers of embryos that were used for the analyses are indicated (n). (C) Embryos from the transgenic *Tg(-4.9sox10:EGFP)^{ba}* line, in which neural crest cells are marked, were injected at the one-cell stage with RNA encoding N-RAS-I24N. The ceratohyal is marked by GFP in the transgenic embryos at 4 dpf and lines (red) were drawn demarcating the ceratohyal, facilitating analysis of the angle in the ceratohyal, which is a direct marker for the width and bluntness of the heads of these embryos. Representative images of a non-injected control (NIC) and a N-RAS-I24N-injected embryo are depicted. Scale bar: 100 μm . (D) Quantification of the angle of the



at the one-somite stage (10 hpf) (Jopling and den Hertog, 2005; van Eekelen et al., 2010). These markers indicate that N-Ras-G12V, N-Ras-I24N and N-Ras-G60E induced significant defects in convergence and extension cell movements as well (supplementary material Fig. S2). Taken together, these results demonstrate that activating N-Ras mutants induce gastrulation cell-movement defects at severities that parallel the capacity to activate MAPK.

To monitor gastrulation cell movements directly, we have developed time-lapse fluorescent microscopy of zebrafish embryos injected with fluorescent Histone H1 protein, which labels all nuclei (van Eekelen et al., 2010). Using this cell tracking technology, we found that expression of N-Ras-I24N resulted in a 10% reduction in convergence and 6% reduction in extension of paraxial mesodermal cells, compared with embryos injected with RNA encoding wild-type N-Ras. These results are statistically significant ($P < 0.001$) because they are based on more than 1000 cell tracks each. One of the underlying mechanisms of convergence and extension is cell intercalation and mediolateral elongation (Concha and Adams, 1998; Myers et al., 2002). By cell membrane labeling and ratiometric analysis of cell shape and orientation, we found that cell polarization is reduced upon N-Ras-I24N expression (supplementary material Fig. S3), which is consistent with the observed convergence and extension cell-movement defects.

One of the hallmarks of Noonan syndrome is hypertelorism and we have demonstrated before that expression of mutant Shp2 leads to craniofacial defects, including wide-set eyes, in zebrafish embryos (Jopling et al., 2007). We assessed defects in craniofacial cartilage structures using the transgenic *Tg(-4.9sox10:EGFP)^{ba2}* zebrafish line, which expresses GFP in all neural crest cells (Carney et al., 2006). The angle of the ceratohyal is a direct measure for the width and the bluntness of the head (Fig. 4C), and is an excellent marker for hypertelorism. Expression of N-Ras-I24N led to a significant increase in the angle of the ceratohyal ($P < 0.05$; Student's *t*-test) (Fig. 4C,D) and hence we conclude that N-Ras-I24N expression induced craniofacial defects in zebrafish embryos that are reminiscent of the symptoms in individuals with Noonan syndrome.

In conclusion, we report an activating mutation in N-Ras, I24N, that is associated with Noonan syndrome. Interestingly, our *in vivo* data in zebrafish embryos (Figs 3, 4) demonstrate for the first time that the activating N-Ras mutants, I24N and G60E, are sufficient for inducing developmental defects that resemble the defects induced by active mutants of downstream factors, B-Raf, Raf-1 and MEK, from Noonan and related syndromes (Anastasaki et al., 2009), and hence firmly establish *NRAS* as a gene that causes Noonan syndrome upon activation. The observed craniofacial defects in zebrafish embryos (Fig. 4C,D) actually resemble symptoms in individuals with Noonan syndrome. Taken together, our *in*

vivo data demonstrate that *NRAS* is a bona fide Noonan-associated gene that has a causal role in the syndrome.

Ras mutations found in human cancer are thought to contribute to disease by activating at least three major downstream signaling pathways, i.e. the Raf-MAPK pathway, the PI3K-PKB/AKT pathway and the RalGDS-Ral pathway. In the case of Noonan N-Ras mutants, it becomes apparent that Raf-MAPK activation is sufficient. Mutational activation of B-Raf causes developmental defects in zebrafish that are identical to those in the activating N-Ras mutants, and pharmacological inhibition of MEK using CI-1040 completely rescues these developmental defects. MEK and/or MAPK inhibitors are currently in clinical trials for the treatment of cancers harboring active *RAS* mutations. This raises the interesting possibility that these inhibitors might also be appropriate for the treatment of developmental disorders that are caused by *RAS* mutations that depend exclusively on Raf-MAPK activation to convey their pathology.

Translational impact

Clinical issue

Noonan syndrome is a relatively common, dominantly inherited genetic disorder characterized by congenital heart defects, reduced growth, facial dysmorphism and other variable congenital defects. The syndrome is caused by activating mutations in genes encoding factors of the RAS-MAPK signaling pathway and hence belongs to a group of genetic syndromes that are collectively called RASopathies. Mutations in known disease-associated genes are found in 70–80% of patients with Noonan syndrome, and ~50% of patients have activating mutations in a gene encoding an upstream factor in the RAS-MAPK pathway [protein-tyrosine phosphatase, non-receptor type 11 (SHP2), encoded by *PTPN11*]. The most recent addition to the group of genes that are associated with Noonan syndrome is *NRAS*, which encodes a member of the Ras protein family.

Results

In this study, the authors report on a mutation in *NRAS* resulting in an I24N amino acid substitution that they identified in an individual bearing typical Noonan syndrome features. The I24N mutation mildly activates N-Ras, resulting in enhanced downstream signaling, similar to other activating N-Ras mutations that are associated with Noonan syndrome. By using zebrafish embryos as a model, they go on to show that expression of I24N or other disease-associated activat-



ing N-Ras mutants causes developmental defects, including cell migration defects during gastrulation. The craniofacial defects observed in the zebrafish embryos carrying disease-associated mutations in N-Ras resemble the defects observed in individuals with Noonan syndrome. Furthermore, developmental defects induced by activated N-Ras phenocopy the developmental defects that are induced by the expression of other genes known to be associated with Noonan syndrome, including *PTPN11*, in zebrafish embryos. Finally, they show that pharmacological inhibition of MEK, a downstream factor in the RAS-MAPK pathway, rescues the phenotype induced by activating N-Ras mutations, demonstrating that the observed defects are mediated exclusively by enhanced activation of the RAS-MAPK signaling pathway.

Implications and future directions

This study provides new evidence that *NRAS* is a bona fide Noonan-syndrome-associated gene and, moreover, that activation of N-Ras can cause the clinical phenotype. Hence, *NRAS* should be included in diagnostic screening for mutations in individuals with symptoms of Noonan syndrome. Notably, pharmacological inhibition of MEK rescues the developmental defects that are induced by activated N-Ras. Given that the RAS-MAPK pathway is also implicated in cancer, developing inhibitors of this pathway has been a major focus of many pharmaceutical companies, and clinical trials to test them in a subset of cancer patients are currently underway. Such inhibitors might also be effective for treating some RASopathies, including Noonan syndrome, that are caused by hyperactivation of the RAS-MAPK pathway.

Methods

Experimental subjects

Written informed consent was obtained from all subjects and/or their legal representatives, and the work was done according to the guidelines of the medical ethical committee of Radboud University, Nijmegen, The Netherlands.

All procedures involving experimental animals were performed in compliance with local animal welfare laws, guidelines and policies.

DNA isolation and sequencing

DNA was isolated from blood, fibroblasts or sputum. Mutational screening of *NRAS* (ENSG00000213281) was performed by PCR of all four exons, using the following primers: NRAS-1-F 5'-CGCCAATTAACCCTGATTAC-3'; NRAS-1-R 5'-AGAGAC-AGGATCAGGTCAGC-3'; NRAS-2-F 5'-ATAGCATTGCA-TTCCCTGTG-3'; NRAS-2-R 5'-CACAAAGATCATCCTT-TCAGAG-3'; NRAS-3-F 5'-CCACTGTACCCAGCCTAATC-3'; NRAS-3-R 5'-AAACTCTTGCACAAATGCTG-3'; NRAS-4-R 5'-CCTCCAAATTGCCCAATAC-3'; NRAS-4-F 5'-ATTTG-GATTGTGTCCGTTG-3'.

Bidirectional resequencing was performed using a commercial sequencing kit (ABI BigDye Terminator Sequencing kit V2.1; Applied Biosystems) and an automated capillary sequencer (ABI 3730; Applied Biosystems).

RBD assays and MAPK phosphorylation

Ras activation was determined with the minimal RBD of Raf-1 as an activation-specific probe, as described previously (de Rooij and Bos, 1997). Briefly, 293T cells [American Type Culture Collection (ATCC)] were transfected with CMV-promoter-driven expression vectors for N-Ras and mutants. The cells were lysed and active Ras was precipitated with glutathione-agarose beads coupled to GST-RBD. Precipitated N-Ras was detected by western blotting using an N-Ras-specific antibody (Santa Cruz). Zebrafish embryos (24 hpf) were lysed in boiling sample buffer and equal amounts of lysate were loaded onto SDS-PAGE gels. MAPK phosphorylation was established by western blotting using phospho-MAPK-specific mouse monoclonal antibody (mAb; Cell Signaling), and equal loading was monitored using tubulin-specific mouse mAb (Calbiochem), MAPK-specific rabbit mAb (Cell Signaling) and actin-specific rabbit polyclonal antibody (Sigma).

Zebrafish, injections and in situ hybridization

Zebrafish were kept and embryos were raised under standard conditions. Zebrafish were staged as described before (Westerfield, 1995). Constructs encoding human N-Ras and mutants were derived by PCR and verified by sequencing. The wild-type and mutant B-Raf-encoding constructs (Anastasaki et al., 2009) were a gift from Liz Patton. 5'-capped sense RNAs were synthesized using mMessage mMachine kit (Ambion). Synthetic RNA was injected at the one-cell stage. The amount of RNA encoding wild-type N-Ras was titrated down to an amount that did not induce morphological defects by itself (5 pg). Subsequently, 5 pg of all mutants was injected at the one-cell stage. 30 pg RNA encoding wild-type or mutant B-Raf was injected at the one-cell stage (Anastasaki et al., 2009). Phenotypes were assessed at the indicated stages. At 11 hpf, batches of embryos were photo-



graphed and the ratio of major:minor axis of each embryo was determined individually using ImageJ software. Pharmacological inhibitors were added directly to the embryo medium at 4.5 hpf. CI-1040 (Selleck Chemicals) was removed at 5.5 hpf to avoid inadvertent side effects of prolonged treatment, whereas SU5402 (Merck) was left on the embryos for the duration of the experiment. *In situ* hybridizations were performed essentially as described (Thisse et al., 1993) using probes specific for *myod* and *krox20* at the eight-somite stage (~12 hpf) (Li et al., 2008). Quantification of convergence and extension cell-movement defects by analysis of the ratio of the width of *krox20* staining and the length from somite-1 to somite-8 was done using ImageJ software as described before (van Eekelen et al., 2010).

Analysis of cell movement and polarization

Mesendodermal cell tracking was performed exactly as described before (van Eekelen et al., 2010). Briefly, embryos were injected at the one-cell stage with Histone-H1 tagged with Alexa Fluor 488 from Molecular Probes (H1). The embryos were dechorionated and mounted at shield stage in 1% low-melting-point agarose. A Leica SP2 confocal microscope with a 40× objective was used for live imaging and time points were recorded every 2 minutes from shield stage until the one-somite stage. Time-lapse images were analyzed using ImageJ (<http://rsbweb.nih.gov/ij/>). Following image processing, uniform objects were readily traced, and convergence and extension cell movements quantified. Statistical analysis was performed by the Microsoft Excel Student *t*-test assuming unequal variances with $\alpha=0.05$.

Craniofacial defects

Craniofacial defects were determined by measurement of the ceratohyal angle at 5 dpf. The *Tg(-4.9sox10:EGFP)^{ba2}* transgenic line, in which neural crest cells are marked (Carney et al., 2006), was used, facilitating detection of the ceratohyal. The angle was defined by two lines, one parallel to the left part of the ceratohyal and the other parallel to the right part (cf. Fig. 4C).

Acknowledgments

We thank Elizabeth E. Patton (Edinburgh University, UK) for the B-Raf-V600E construct and Linda A. Winston for critical reading of the manuscript. This work was supported in part by a Marie Curie Research Training Network (PTP-NET/MRTN-CT-2006-035830) and a grant from the Research Council for Earth and Life Sciences (ALW 815.02.007) with financial aid from the Netherlands Organisation for Scientific Research (NWO).

Footnotes

Competing interests

The authors declare that they do not have any competing or financial interests.

Author Contributions

V.R., M.v.E., B.B. and J.d.H. conceived and designed the experiments. V.R., M.v.E., J.O. and B.B. performed the experiments. V.R., M.v.E., H.R., B.B. and J.d.H. analyzed the data. H.G.Y., W.M.N., A.v.H. and I.v.d.B. provided samples. V.R., M.v.E. and J.d.H. wrote the paper.

References

Anastasaki C., Estep A. L., Marais R., Rauen K. A., Patton E. E. (2009). Kinase-activating and kinase-impaired cardio-facio-cutaneous syndrome alleles have activity during zebrafish development and are sensitive to small molecule inhibitors. *Hum. Mol. Genet.* 18, 2543–2554.

Aoki Y., Niihori T., Narumi Y., Kure S., Matsubara Y. (2008). The RAS/MAPK syndromes: novel roles of the RAS pathway in human genetic disorders. *Hum. Mutat.* 29, 992–1006.

Bos J. L., Toksoz D., Marshall C. J., Verlaan-de Vries M., Veeneman G. H., van der Eb A. J., van Boom J. H., Janssen J. W., Steenvoorden A. C. (1985). Amino-acid substitutions at codon 13 of the N-ras oncogene in human acute myeloid leukaemia. *Nature* 315, 726–730.

Bos J. L., Verlaan-de Vries M., van der Eb A. J., Janssen J. W., Delwel R., Lowenberg B., Colly L. P. (1987). Mutations in N-ras predominate in acute myeloid leukemia. *Blood* 69, 1237–1241.

Carney T. J., Dutton K. A., Greenhill E., Delfino-Machin M., Dufourcq P., Blader



- P, Kelsh R. N. (2006). A direct role for Sox10 in specification of neural crest-derived sensory neurons. *Development* 133, 4619–4630.
- Cirstea I. C., Kutsche K., Dvorsky R., Gremer L., Carta C., Horn D., Roberts A. E., Lepri F., Merbitz-Zahradnik T., Konig R., et al. (2010). A restricted spectrum of NRAS mutations causes Noonan syndrome. *Nat. Genet.* 42, 27–29.
- Concha M. L., Adams R. J. (1998). Oriented cell divisions and cellular morphogenesis in the zebrafish gastrula and neurula: a time-lapse analysis. *Development* 125, 983–994.
- Cordeddu V., Di Schiavi E., Pennacchio L. A., Ma'ayan A., Sarkozy A., Fodale V., Cecchetti S., Cardinale A., Martin J., Schackwitz W., et al. (2009). Mutation of SHOC2 promotes aberrant protein N-myristoylation and causes Noonan-like syndrome with loose anagen hair. *Nat. Genet.* 41, 1022–1026.
- de Rooij J., Bos J. L. (1997). Minimal Ras-binding domain of Raf1 can be used as an activation-specific probe for Ras. *Oncogene* 14, 623–625.
- Denayer E., de Ravel T., Legius E. (2008). Clinical and molecular aspects of RAS related disorders. *J. Med. Genet.* 45, 695–703.
- Gelb B. D., Tartaglia M. (2006). Noonan syndrome and related disorders: dysregulated RAS-mitogen activated protein kinase signal transduction. *Hum. Mol. Genet.* 15 Suppl 2, R220–R226.
- Jopling C., den Hertog J. (2005). Fyn/Yes and non-canonical Wnt signalling converge on RhoA in vertebrate gastrulation cell movements. *EMBO Rep.* 6, 426–431.
- Jopling C., van Geemen D., den Hertog J. (2007). Shp2 knockdown and Noonan/LEOPARD mutant Shp2-induced gastrulation defects. *PLoS Genet.* 3, e225.
- Karnoub A. E., Weinberg R. A. (2008). Ras oncogenes: split personalities. *Nat. Rev. Mol. Cell Biol.* 9, 517–531.
- Li C., Inglis P. N., Leitch C. C., Efimenko E., Zaghoul N. A., Mok C. A., Davis E. E., Bialas N. J., Healey M. P., Heon E., et al. (2008). An essential role for DYF-11/MIP-T3 in assembling functional intraflagellar transport complexes. *PLoS Genet.* 4, e1000044.
- Myers D. C., Sepich D. S., Solnica-Krezel L. (2002). Bmp activity gradient regulates convergent extension during zebrafish gastrulation. *Dev. Biol.* 243, 81–98.

Oliveira J. B., Bidere N., Niemela J. E., Zheng L., Sakai K., Nix C. P., Danner R. L., Barb J., Munson P. J., Puck J. M., et al. (2007). NRAS mutation causes a human autoimmune lymphoproliferative syndrome. *Proc. Natl. Acad. Sci. USA* 104, 8953–8958.

Pandit B., Sarkozy A., Pennacchio L. A., Carta C., Oishi K., Martinelli S., Pogna E. A., Schackwitz W., Ustaszewska A., Landstrom A., et al. (2007). Gain-of-function RAF1 mutations cause Noonan and LEOPARD syndromes with hypertrophic cardiomyopathy. *Nat. Genet.* 39, 1007–1012.

Razzaque M. A., Nishizawa T., Komoike Y., Yagi H., Furutani M., Amo R., Kamisago M., Momma K., Katayama H., Nakagawa M., et al. (2007). Germline gain-of-function mutations in RAF1 cause Noonan syndrome. *Nat. Genet.* 39, 1013–1017.

Roberts A. E., Araki T., Swanson K. D., Montgomery K. T., Schiripo T. A., Joshi V. A., Li L., Yassin Y., Tamburino A. M., Neel B. G., et al. (2007). Germline gain-of-function mutations in SOS1 cause Noonan syndrome. *Nat. Genet.* 39, 70–74.

Schubbert S., Zenker M., Rowe S. L., Boll S., Klein C., Bollag G., van der Burgt I., Musante L., Kalscheuer V., Wehner L. E., et al. (2006). Germline KRAS mutations cause Noonan syndrome. *Nat. Genet.* 38, 331–336.

Schubbert S., Shannon K., Bollag G. (2007). Hyperactive Ras in developmental disorders and cancer. *Nat. Rev. Cancer* 7, 295–308.

Solnica-Krezel L. (2006). Gastrulation in zebrafish – all just about adhesion? *Curr. Opin. Genet. Dev.* 16, 433–441.

Stewart R. A., Sanda T., Widlund H. R., Zhu S., Swanson K. D., Hurley A. D., Bentires-Alj M., Fisher D. E., Kontaridis M. I., Look A. T., et al. (2010). Phosphatase-dependent and -independent functions of Shp2 in neural crest cells underlie LEOPARD syndrome pathogenesis. *Dev. Cell* 18, 750–762.

Tartaglia M., Mehler E. L., Goldberg R., Zampino G., Brunner H. G., Kremer H., van der Burgt I., Crosby A. H., Ion A., Jeffery S., et al. (2001). Mutations in PTPN11, encoding the protein tyrosine phosphatase SHP-2, cause Noonan syndrome. *Nat. Genet.* 29, 465–468.

Tartaglia M., Pennacchio L. A., Zhao C., Yadav K. K., Fodale V., Sarkozy A., Pandit B., Oishi K., Martinelli S., Schackwitz W., et al. (2007). Gain-of-function SOS1 mutations cause a distinctive form of Noonan syndrome. *Nat. Genet.* 39, 75–79.



Thisse C., Thisse B., Schilling T. F., Postlethwait J. H. (1993). Structure of the zebrafish snail1 gene and its expression in wild-type, spadetail and no tail mutant embryos. *Development* 119, 1203–1215.

Tidyman W. E., Rauen K. A. (2009). The RASopathies: developmental syndromes of Ras/MAPK pathway dysregulation. *Curr. Opin. Genet. Dev.* 19, 230–236.

van 't Veer L. J., Burgering B. M., Versteeg R., Boot A. J., Ruiter D. J., Osanto S., Schrier P. I., Bos J. L. (1989). N-ras mutations in human cutaneous melanoma from sun-exposed body sites. *Mol. Cell Biol.* 9, 3114–3116.

van der Burgt I., Kupsky W., Stassou S., Nadroo A., Barroso C., Diem A., Kratz C. P., Dvorsky R., Ahmadian M. R., Zenker M. (2007). Myopathy caused by HRAS germline mutations: implications for disturbed myogenic differentiation in the presence of constitutive HRas activation. *J. Med. Genet.* 44, 459–462.

van Eekelen M., Runtuwene V., Overvoorde J., den Hertog J. (2010). RPTPalpha and PTPepsilon signaling via Fyn/Yes and RhoA is essential for zebrafish convergence and extension cell movements during gastrulation. *Dev. Biol.* 340, 626–639.

Westerfield M. (1995). *The Zebrafish Book*. Eugene, OR: University of Oregon Press.

Zenker M., Lehmann K., Schulz A. L., Barth H., Hansmann D., Koenig R., Korinthenberg R., Kreiss-Nachtsheim M., Meinecke P., Morlot S., et al. (2007). Expansion of the genotypic and phenotypic spectrum in patients with KRAS germline mutations. *J. Med. Genet.* 44, 131–135.

Supplementary Figures

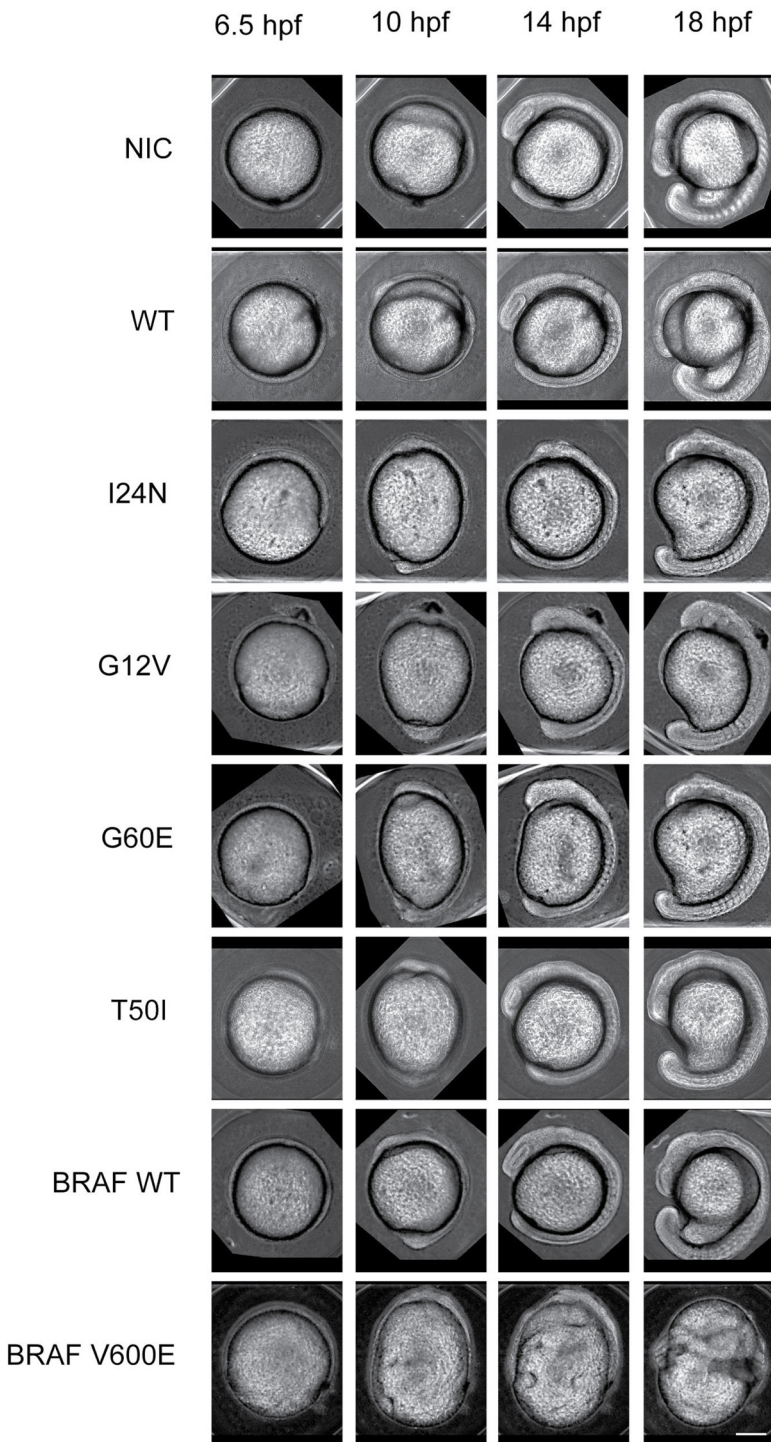


Figure S1. Active N-Ras expression in zebrafish embryos induced developmental defects.

Zebrafish embryos were not injected (NIC) or injected at the 1-cell stage with synthetic RNA encoding wild type (WT) or mutant N-Ras-I24N, N-Ras-G12V, N-Ras-G60E, N-Ras-T50I, wild type BRAf (BRAF WT) or mutant BRAf (BRAF V600E). Ten embryos of each group were mounted and their morphology was recorded by time-lapse microscopy from 0 till 18 hpf. Images from representative series are depicted here at 6.5, 10, 14 and 18 hpf. It is noteworthy that at 14 hpf the distance between the anterior-most and posterior-most part of the embryo is enhanced in mutant, active N-Ras injected embryos compared to wild type N-Ras-injected embryos. This is a hallmark of extension defects in gastrulation. The BRAf-V600E injected embryos were severely affected, whereas wild type BRAf injected embryos did not display significant phenotypes. Scale bar is 250 μ m.



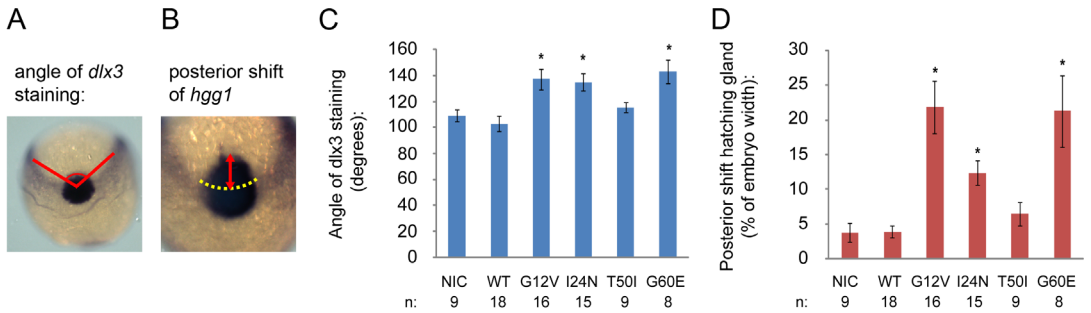


Figure S2. Active N-Ras induced convergence and extension cell movement defects.

(A,B) *In situ* hybridization was done using embryos at the 1-somite stage (~10 hpf) with the *dlx3* and *hgg1* probe. Dorsal views are shown with posterior to the top. Defects in convergence cause widening of the edges of the neural plate (*dlx3*) and hence the angle in (A) is directly proportional to convergence. The position of the precursor of the hatching gland (*hgg1*-staining) relative to the neural plate is directly proportional to extension. The *dlx3/hgg1* staining patterns were analyzed using ImageJ software and quantified. (C) The angle of *dlx3* staining and (D) the relative posterior shift of the hatching gland precursor as a proportion of the embryo width of non-injected control (NIC) and embryos injected with synthetic RNA (5 pg) encoding wild type (WT) N-Ras or mutants as indicated were determined. Error bars indicate standard errors of the mean; student's t-tests (2 tailed, assuming unequal variance) were performed between mutant and wild type N-Ras-injected groups, * indicates a P value<0.001. The total number of embryos that were used for the analyses are indicated.

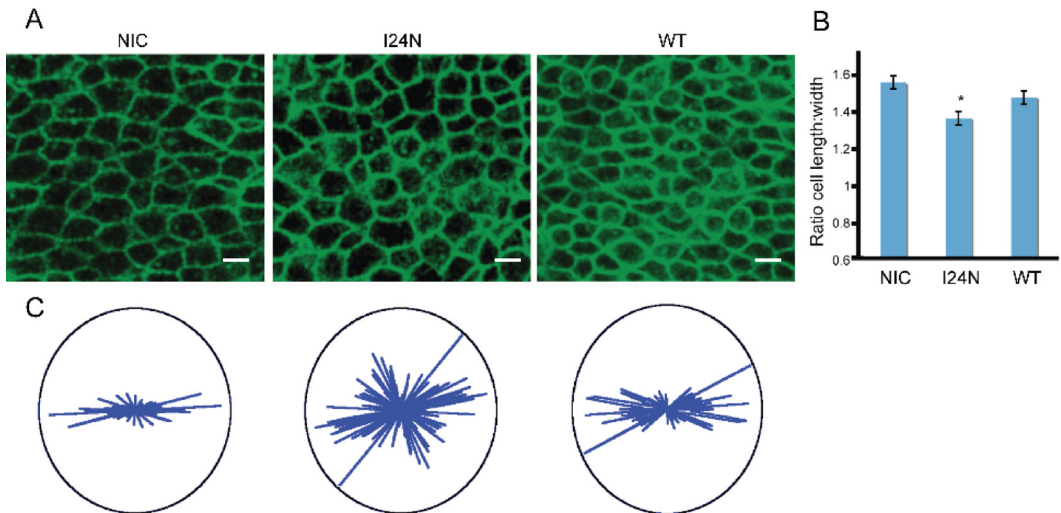
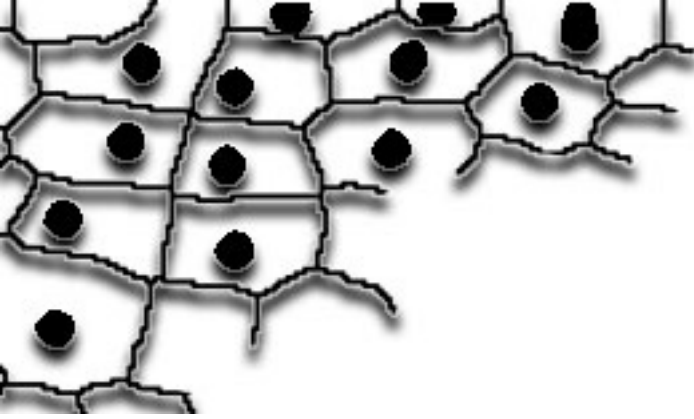


Figure S3. Impaired cell polarization in response to N-RAS-I24N.

Zebrafish embryos were injected with YFP-CAAX and N-RAS-I24N or wild type N-RAS (WT). Embryos were mounted and imaged at late gastrulation stage posterior of the future site of the first somite in the region next to the notochord. (A) Depicted are representative images of non-injected control (NIC), N-RAS-I24N-injected and wild type N-RAS-injected embryos. Scale bar is 10 μ m. (B) Length and width of the cells were determined and the ratios are plotted. Error bars represent standard deviation. A student's t-test was performed; asterisk indicates significant difference, P<0.001. (C) The angles of cells towards the notochord were determined using ImageJ software and are plotted in a rose diagram.



5

5



Cell Outliner and Cell Roses: New Tools for Automated Cell Membrane Detection and Determination of Cell Polarity

Vincent Runtuwene and Jeroen den Hertog

Abstract

Quantitative analysis and clear presentation of the data is essential for modern day biology. For instance, phenotypic analysis of convergence and extension cell movement defects involves quantitative analysis of defects in cell polarization. Cell polarization underlies convergence and extension cell movements during gastrulation, which are the driving forces behind the formation of the three germ layers and the shaping of an anterior-posterior axis from a radially symmetrical blastula stage embryo. The annotation of the cell membranes required for analysis of cell polarization is usually carried out manually, making it time consuming, tedious and subjective. Here we describe tools that we developed that enable radiometric analysis of cell shape and direction, “Cell Outliner” and an integrated method to present these data, “Cell Roses”. Cell Outliner is an automated image processing-based algorithm to detect membranes in 2D images. It performs a series of conversions of the original images, including adaptive thresholding, resulting in accurate detection and representation of fluorescent cell membranes. The algorithm is fast, objective and accurate. Cell Roses is a graphical application to depict cell shape and orientation in the same graph. As proof-of-principle, we successfully applied these new tools in the analysis of the presomitic mesoderm of a known zebrafish convergence and extension mutant.

The analysis of cell shape and orientation is widely used to assess differences in many biological processes. We emphasize that these tools are by no means restricted to analysis of gastrulation cell movements in zebrafish. To underline this, we have used these tools to model cell images from four distinct sources. We have made Cell Outliner and Cell Roses available for quantitative analysis of cell shape and direction in any 2D image.

Introduction

Cell polarization and directed cell migration are at the basis of many processes in embryonic development. For proper description of cell polarization and direction, and to be able to quantitatively determine differences in these parameters between (groups of) embryos, it is imperative to accurately measure the cell shape and direction of cells. For instance, the evolutionary conserved convergence and extension (CE) cell movements during zebrafish gastrulation are highly characteristic and remodel the evidently undiversified zebrafish blastula stage embryo into a complex elongated structure consisting of three germ layers, and clearly defined structures along the anterior posterior axis [1]. Medio-lateral cell elongation and orientation underlie these morphogenetic movements in the dorsal mesodermal and ectodermal cells [2,3,4,5,6]. Phenotypical analysis of cellular layers in CE phenotypes relies on quantitative information of individual cells within a tissue, collected from microscopic images. The detection of cell boundaries in these images is often carried out manually [2,5,7], which is labor intensive, error-prone, time-consuming and subjective. Therefore, great potential lies in automated image analysis for enhancing reproducibility, accuracy, speed and objectivity. Recently, efforts have been made to develop automated microscopy image analysis techniques focused on detection of cellular features [8,9]. While a growing number of studies report algorithms for localization, detection, and analysis of nuclei, only a few have been described for cell membranes. The reason for this lies in the inherent difference between detection of fluorescent nuclear markers compared to cell membrane markers. Fluorescent nuclear markers mark a volume within the cell. As a consequence, a signal from a three-dimensional source is generated upon laser-excitation which can be sufficiently sampled to create a relatively well-defined representation of the nucleus in the resulting image, making nuclei relatively straightforward to detect [10]. The sheet-like structure of the cell membrane is much thinner than the diameter of the nucleus. In fact, the cell membrane is thinner than the point spread function which marks the resolution of a standard scanning point confocal microscope [11]. Detection of a fluorescently tagged membrane can only result from sufficient sampling and interpolation of emitted light from neighboring markers, thus creating a more diffuse boundary in the confocal images. Consequently, the pixel intensities generated by the membrane signal fluctuate. As a result, the fluorescence intensity of the cell membrane that is detected is subject to the proximity of membrane junctions, adjacent cell membranes, and marker aggregations [10]. These characteristics make the detection of fluorescent membranes more cumbersome.

The problem of automated segmentation of cell membranes such as depicted in Fig. 1A has been addressed before. An anisotropic plate diffusion fil-



tering method has been proposed, which detects and enhances cell membranes using an image Hessian's eigensystem, followed by a diffusion tensor, applicable to confocal 3-D data sets [10]. Another method applies a series of artificial neural networks for the detection of neuronal membranes in 2D for electron microscopy images [12]. The use of both abovementioned methods requires intensive computation power, knowledge of computation, and in the case of artificial neural networks specialized hardware, making their use currently unfeasible for most standard biological research labs. The use of simple morphological operators has been described to detect and model cell geometries in early sea urchin embryos, which have the advantage of being less computationally intensive to execute [13]. The method takes advantage of the more conveniently detectable cell nuclei and extrapolates the location of the cell membrane by applying voronoi tessellation on the nuclear center positions [13]. This method performs accurately when applied to relatively circular cells in which the nucleus is, in fact, in the center of the cell cytoplasm (see yellow arrowhead in Fig. 1B). However, wildtype zebrafish dorsal mesodermal and ectodermal cells are elongated during CE movements and their nucleus is more often than not biased from the center of the cell cytoplasm. Applying this method on these cells results in a model in which cell elongation is underestimated, modeling elongated cells closer to a circular shape (see red arrowheads in Fig. 1B). The presence of cells in which the nucleus does not reside in the center of the cytoplasm causes an inaccurate shift in the estimated position of the cell membrane in the direction of the nucleus (see blue arrowhead in Fig. 1B).

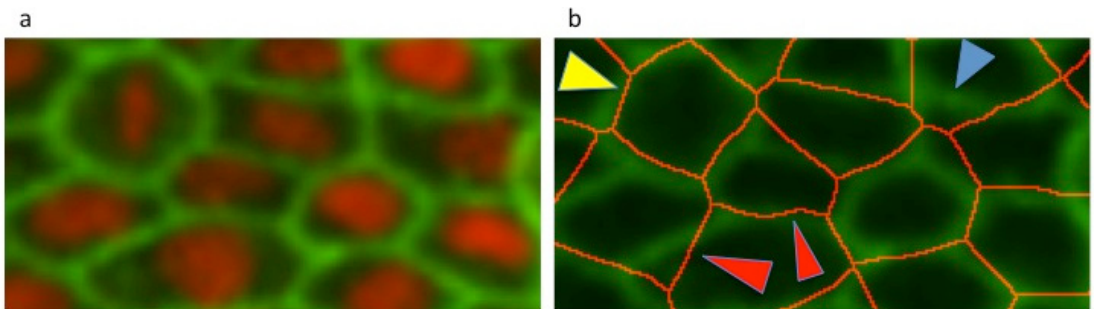


Figure 1: Application of voronoi tessellation membrane modelling method based on detection of nuclear center positions.

(A) Raw confocal image of presomitic mesoderm of an embryo micro-injected with 20 pg of YFP-CAAX mRNA, a membrane marker, and 20 pg of H2B-mCherry mRNA, a nuclear marker. (B) Voronoi diagram based on the nuclear fluorescence superimposed onto the raw membrane channel. The yellow arrowhead indicates a circular cell shape that was accurately segmented. The red arrowheads indicate 2 cells of which the modeled membranes result in an underestimation of the cell polarization. The blue arrowhead points at a cell in which the cell nucleus is offset from the center of the cytosol resulting in an inaccurate modeling of the membrane position.



Here, we report a new method for analyzing cell polarity during zebrafish CE movements. We created a new Cell Outliner algorithm as a plugin for ImageJ for automated detection and modeling of cell membranes, which employs image filtering and morphological operators in images acquired using a standard scanning point confocal microscope. The process is fast and accurate and utilizes voronoi tessellation based on the detection of cell cytoplasm rather than cell nuclei. Additionally, we employed Cell Roses to represent data on cell elongation and orientation in the same graph. This composite graph shows the correlation between cell elongation and orientation in a single view. We successfully analyzed the presomitic mesoderm in zebrafish mutants, that have a well-studied defect in CE movements, to validate the use of Cell Outliner and Cell Roses as a tool for phenotypical analysis. This tool can be adapted to any 2-D image of cells in which the cell membrane is highlighted to assess cell shape and direction in an automated manner and we have analyzed images from four distinct origins.

Materials and methods

Zebrafish maintenance, in vitro transcription of mRNA, and injection

Zebrafish were kept and the embryos were staged as described before [14]. Only wild type embryos up to 3 dpf were used for these experiments, which does not require approval of the animal experiments committee according to national and European law. Using the mMessage mMachine kit (Ambion), we synthesized 5'-capped sense mRNA encoding membrane-localized citrine (a YFP variant with a C-terminal fusion of the Ras membrane localization sequence [CAAX]) (kindly provided by Jeroen Bussman of the Hubrecht Institute) or memRFP (kindly provided by Jeroen Bakkers of the Hubrecht Institute). To achieve ubiquitous fluorescent membrane labeling, the embryos were injected at the one cell stage with 20 pg of YFP-CAAX mRNA or 30 pg of memRFP mRNA.

Confocal microscopy and positioning

To visualize the cell shape in the presomitic mesoderm, live embryos were mounted in 0.75% soft agarose at the dorsal side in glass bottomed petri dishes. Using an SP2 Leica Confocal microscope the presomitic mesoderm was imaged using a 40 X oil objective. 2-D images 512 X 512 were acquired during the 2 to 3 somite stage 100 μm posterior to the developing somites in the paraxial mesoderm, lateral to the notochord. Alternatively, the epiblast was imaged at 70% epiboly stage. All images analyzed by Cell Outliner were digitally enlarged to make the surface occupied by one cell approximately 2000 pixels, which is the optimal size for Cell Outliner.

Mice and immunostainings

All mice were in the C57Bl6j/CBA mixed background and were housed according to national and european law, under the licenses required in the Netherlands. Experiments were carried out under Hubrecht Institute license number HI10.01.05. Embryos were dissected and fixed according to [15]. Two distinct monoclonal rat E-cadherin antibodies (Uvomorulin/E-Cadherin from Sigma and ECCD-2 from Millipore) were used as primary antibodies for detection of the cell shapes both in 1:250 dilution. Appropriate secondary antibodies were obtained from Jackson Immunoresearch and used in 1:500 dilution. Before incubation with primary antibodies, embryos were treated with 0,1% Triton X-100 for 10-15 minutes and blocked in 1% BSA solution for 5 hours at room temperature. Incubation with primary antibodies was carried out for three days followed by 8 washes (30 minutes each, at 4°C) and overnight for secondary antibodies followed by washes. Embryos were analyzed by confocal laser scanning microscope.

Results

Cell Outliner: Automated segmentation workflow for cell membrane recognition

In order to quantitatively analyze the polarization properties of the cells making up the presomitic mesoderm it is necessary to acquire information of a large number of cells. Manual analysis is labor-intensive, error-prone and subjective. Quantitative analysis performed by mathematical algorithms is faster, more accurate and objective. However, the bottleneck in this approach lies in detection, i.e. segmentation, of the cell shape. The problem is caused by fluctuation in the intensity of the detected fluorescent signal due to mechanical noise inherent to the confocal technique and biological fluctuation, which includes background fluorescence, non-uniform distribution of marker, and fluctuations in signal due to the proximity to membrane junctions, adjacent cell membranes, and marker aggregations.

Cell Outliner was designed to compensate for intensity fluctuations, which often occur in biological samples, facilitating automatic detection of fluorescently marked cell membranes. The algorithm was optimized for images of cell populations closely compacted together marked by YFP-CAAX. More than 20 sample pictures of presomitic mesoderm of different embryos, each constituting between 40 and 60 cells were used to optimize the workflow of the algorithm. After segmentation the morphological information can be extracted.

The most important source of mechanical noise is shot noise, which can

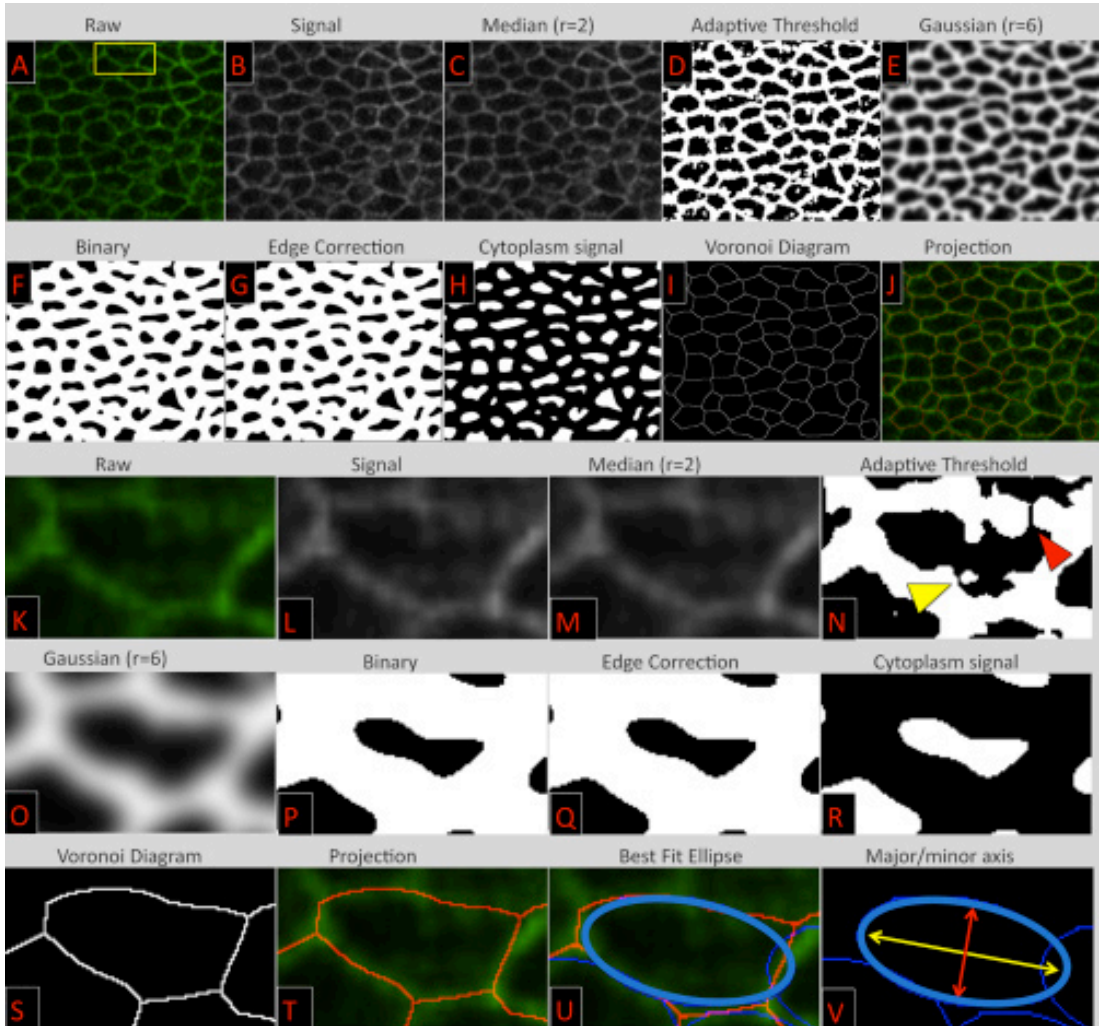


Figure 2: Workflow of the Cell Outliner Algorithm for detection and subsequent measurement of cell polarization.

Embryos were injected with 20 pg of YFP-CAAX mRNA and the presomitic mesoderm was imaged in late gastrulation stage. (A-J), Raw image and result of the Cell Outliner algorithm of a representative image of the presomitic mesoderm. (A), a raw confocal image in 8-bit colour version. (B), the signal of the YFP converted to 8-bit grayscale. (C), a median blur operation (radius=2 pixels) reduces shot noise, while preserving the edges of structures. (D), application of an adaptive thresholding procedure results in detection of the area of the cell membranes. (E), artefacts generated by the thresholding procedure are reduced greatly by applying a Gaussian blur (radius=6). (F), Binarization, using a threshold of gray value 60. (G), an Edge Correction step is applied, which converts all edge pixels to background, which is necessary for the detection of edge objects later in the procedure. (H), inversion of the signal from (G) generates an image, wherein the foreground objects represent cytosolic signals. (I), these cytosolic signals are now used to perform Voronoi tessellation, generating a Voronoi diagram, i.e. the modelled membranes. (J), the projection of the modelled membranes onto the raw confocal image. (K-T), an enlarged section of the image in (A, yellow box). N, the red arrowhead indicates a site in the thresholded image, where an abrupt change in intensity in the raw image resulted in a discontinuity in the detected membrane signal. The yellow arrowhead indicates the location of a round segmented object, caused by the presence

of a fluorescent vesicular structure present in the cytosol. (O), both these objects are eliminated by a Gaussian Blur (radius=6) and subsequent binarization (P), edge correction (Q), and Voronoi tessellation (S), based on the cytoplasmic signals (R), generate an accurate model of the cell membranes. (U), projection of the best fit ellipses, in blue, onto the projection (T). (V), representation of the major (yellow) and minor (red) axis of the best fit ellipse which were used to calculate the cell elongation (aspect ratio of the length of major and minor axes) and cell orientation (the angle of the major axis of the ellipse relative to the medio-lateral direction, which is in all these images the horizontal axis).

be minimized, although its presence is inherently linked to the physical principle used by confocal microscopes. It results from the statistical variation in the number of detected photons, which can be described as a Poisson distribution [16]. As an initial step for segmentation a **median filter** with radius of 2 pixels was implemented as it was found to reduce noise greatly without affecting borders (Fig. 2A-C).

Given the common occurrence of intensity gradients in confocal images, global thresholding techniques often give poor results in separating foreground pixels (cell membranes) from the background (cytosol). Global thresholding uses a fixed threshold for all pixels in the image. It therefore works only if the intensity histogram of the input image contains neatly separated peaks, corresponding to the objects of interest. Hence, it cannot deal with images containing a strong intensity gradient. **Adaptive thresholding** (Fig. 3) is a more sophisticated technique, which selects an individual threshold for each pixel based on the range of intensity values in its local neighborhood, rather than the entire image. This allows for thresholding of an image with an intensity gradient [17]. While complex formulas have been developed to determine these local thresholds [18,19,20], we found that implementing a threshold value based on the median of the intensity

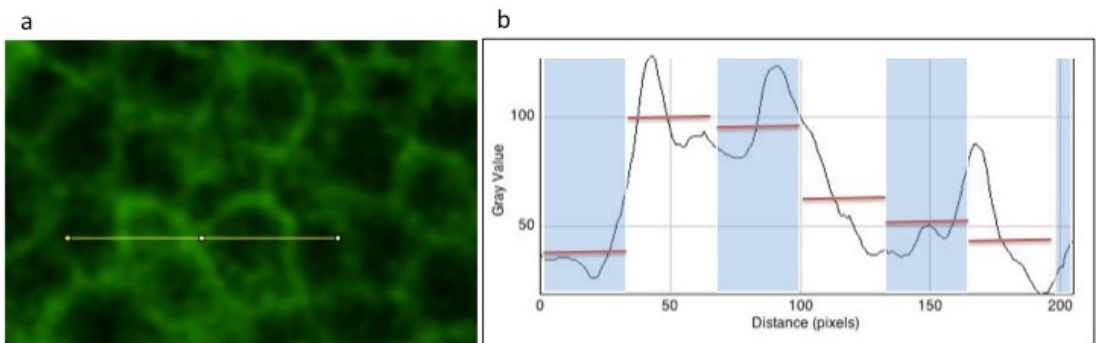


Figure 3: Adaptive Thresholding.

(A), Raw confocal image of cell membranes of an embryo injected with 20 pg of YFP-CAAX mRNA. (B), a profile plot along the region marked by the yellow line in (A). The peaks in the profile plot clearly show the regions of high membrane intensity compared to a lower cytosolic signal in between. The profile plot is subdivided in different regions, 30 pixels wide, marked by the alternating white and blue areas. Within each of these areas a separate threshold is calculated based on the median gray value of the area, which will be used for discerning the membrane signal from the local background.



of the pixels in the immediate surroundings gave the best results. A local environment of 30 X 30 pixel area around the analyzed pixel was found to be optimal (Fig. 2D).

While this method proved to be highly efficient in separating the membrane signal, two sources of error needed to be minimized. First, fluorescent vesicular structures within the cytosol occasionally create round, segmented objects (yellow arrowhead in Fig. 2N). Presence of these structures is unavoidable since these vesicles are part of the endomembrane system, which is used to traffic CAAX-tagged proteins to the plasma membrane [21]. Second, abrupt changes in membrane intensity which often occur in biological samples, can cause sites where the membrane is not detected (red arrowhead in Fig. 2N). We found a **Gaussian filter** (Fig. 2E) with a radius of six pixels followed by a **binarization**, which applied a global threshold of gray value 60 to be highly efficient in minimizing these sources of error (Fig. 2F).

The resulting image was further processed by an **edge correction** converting all pixels at the edge of the image to background (Fig. 2G). **Inversion** of this image resulted in a segmented image in which the edge of the image and the cytoplasm are foreground objects (Fig. 2H). The edge correction is needed to include cells of which the membrane is close to the edge of the image in the analysis. The reason for this lies in the next processing step: Generation of a **Voronoi diagram**. This divides an image into regions by drawing points at coordinates which are equidistant from the closest surrounding objects [22]. In other words, it subdivides the binary image into regions such that the Voronoi region of an object is the cluster of points (surface) located closest to this object. This operation is called Voronoi tessellation. By making the edge particles as well as the cytoplasm foreground, the cytoplasm close to the edge, which are in full view within the image (i.e. the ones from cells of which the plasma membrane is close to the edge of the image), are now also included in the analysis instead of being discarded as edge objects (Fig. 2I). The Voronoi diagram is used as a binary model of the cell membranes (Fig. 2J). Close-ups of the modeling process showing a single cell are depicted in Fig. 2K-T. From the images in Fig. 2 it is apparent that the cell membranes are accurately modelled by Cell Outliner.

Efficient segmentation of membranes

To determine the efficiency of Cell Outliner for membrane segmentation, the generated membrane models were verified by manual comparison to the raw confocal images. We used samples acquired from the presomitic mesoderm of 10 embryos and all images were analyzed automatically by Cell Outliner. The program creates a second image in which a model of the membranes is generated from the raw data, and a third image in which the detected cells are numbered

and superimposed on the original raw image. In order to validate the method used by Cell Outliner, the generated objects were verified one by one by comparison of the detected/generated cell membranes in the model to their complement in the raw images.

In total 661 cells of YFP-CAAX mRNA injected embryos were analyzed and validated. Since Cell Outliner is based on the indirect detection of cytosols, a false positive is defined as a single cytosol that has been detected as multiple cytosols. A false negative is defined as an undetected cytosol. Cell Outliner showed very high efficiency: 96,89 % of the cytosols was detected correctly. The error range consisted of 2.69 % false positives and 3.10 % false negatives. The main source of false positives are rows of small, fluorescent, vesicular structures which occur occasionally within the cytosol and high intensity cytosolic signals which result from cell membranes lying in and parallel to the confocal plane. False negatives occur when the visible cytosol is very narrow, i.e. only a small part of the cytosol of the cell was visible in the confocal plane while the bulk of the cell resided either closer to the surface or deeper within the tissue.

Cell Outliner was initially designed and optimized to detect YFP-CAAX in living zebrafish embryos. However, it was highly likely that it could also be applied to detect fluorescent cell membranes in different samples. To test this, we determined its efficiency when using data from live imaging of gastrula stage zebrafish embryos injected with mRNA of memRFP, a chimeric protein containing the 10 N-terminal amino acids of GAP43 fused to N-terminus of RFP. Moreover, we used images of lateral mesoderm from fixed 4-somite stage mouse embryos that were labeled with 2 different monoclonal rat antibodies for E-Cadherin, Uvomorulin/E-Cadherin antibody or ECCD-2 (Fig. 4). Cell Outliner was shown to have a very high efficiency for all markers and cell types (> 95 %) with a low incidence of both false positives (< 2,69 %) and negatives (< 4,06 %). Cell Outliner was able to correctly identify objects in images with intensity gradients and images with low intensity were also processed with high efficiency when the membranes within the images did not appear to be interrupted. Images with low intensity in which the cells were poorly defined were not processed well and should be discarded. Cell Outliner functions consistently as it always generates the same model for a given sample. Given the objectivity and consistency of this method, multiple samples can be analyzed and compared to each other directly. These results show that Cell Outliner is a broadly applicable, highly efficient, and consistent method to model cell membranes.

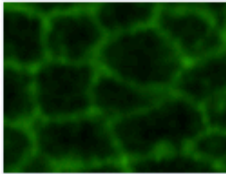
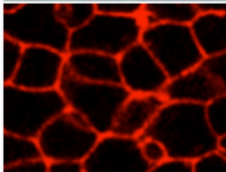
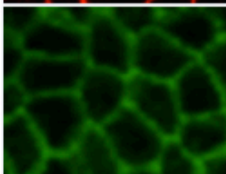
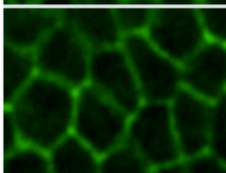
	Sample	Detected cytosols	Real total	False positives	False negatives	Efficiency
YFP-CAAX		625	645	2,69 %	3,10 %	96,89 %
memRFP		713	738	0,70 %	4,06 %	95,93 %
E-Cad		669	682	1,04 %	1,90 %	97,06 %
ECCD-2		1045	1042	0,19 %	0,47 %	99,52 %



Figure 4: Cell Outliner efficiently detects cell membranes in distinct images.

Zebrafish were injected with 20 pg of YFP-CAAX mRNA and were imaged at the 2-3 somite stage or 30 pg of membrane-RFP mRNA (memRFP) and were imaged at 70% epiboly. Mice were fixed at 4 somite stage and labeled with one of 2 monoclonal anti E-cadherin rat antibodies; Uvomorulin/ E-Cadherin or ECCD-2. Detection of both antibodies was done with a FITC labeled secondary antibody. Imaging was performed, focusing on mouse lateral mesoderm and zebrafish presomitic mesoderm. Confocal images were collected and analyzed by Cell Outliner, followed by manual comparison of the segment of cell membranes. A false positive is defined as a single cytosol, which is detected as (divided in) multiple cytosols. A false negative is defined as an undetected cytosol. Data from at least two independent experiments was analyzed and is presented here.

Using ImageJ, the cell shapes that were determined by Cell Outliner were analyzed by determining a best fit ellipse onto the segmented cell shapes (Fig. 2U). The length of the major and minor axis of these best fit ellipses were determined to calculate the elongation of cells, defined as the ratio of the length of major and minor axis. Additionally, the orientation of the major axis of the cells was determined as the angle this axis makes towards the medio-lateral direction (Fig. 2V). Data describing cell elongation and orientation in developing embryos is conventionally presented on separate plots [5,6,23]. Presenting these values on separate diagrams might obscure potentially valuable information regarding their correlation. Using the principle of a wind rose [24], both elongation and orientation are presented on a Cell Rose. This type of plot might reveal differences

in the correlation between cell orientation and elongation when analyzing phenotypes. To this end, we adjusted a windrose-plugin (<http://www.mathworks.com>) for matlab to generate Cell Roses representing both the distribution of polarization directions and intensities (here defined as aspect ratio of the best fit ellipse to the cell shape) in a colour coded radial histogram. Measurements of the direction of orientation were grouped into 10° bins and plotted as a radial histogram. Within this histogram, the area of each sector is proportional to its relative frequency (radius proportional to the square root of frequency). The length to width ratios of the best fit ellipses are calculated using Microsoft Excel and grouped into 0.2 unit bins. Each sector of the radial histogram is subdivided into smaller colour coded zones. The area of each colour coded zone is proportional to the relative frequency of elongation values within this sector. The colour code is indicated in the legend of Fig. 5. Statistical analysis of the length to width ratio was done by the student t-test assuming unequal variances. Statistical analysis of the cell orientation data was performed using Watson's U^2 square tests for significance in Matlab.

Cell Outliner and Cell Roses can be used to analyze cell polarization defects

In order to test the value of Cell Outliner and Cell Roses in the determination of cell polarization defects we analyzed wildtype and mutant embryos, with a known CE defect. *Ptpra* encodes a receptor like protein-tyrosine phosphatase which has an essential role in CE movements during gastrulation [23]. *Ptpra*^{-/-} mutant zebrafish embryos have defects in medio-lateral elongation and orientation of mesendodermal cells. Heterozygous *ptpra*^{+/-} fish were incrossed and the presomitic mesoderm of the embryos was imaged at late gastrulation. Subsequently, the images were analyzed using Cell Outliner and Cell Roses. We consistently found a significant loss of medio-lateral elongation and a more randomly distributed cell orientation for homozygous *ptpra*^{-/-} mutants compared to wildtype siblings (Fig. 5), consistent with cell polarization defects in the mutants. The embryos were sequenced following imaging in order to determine their genotype. In three independent experiments a clear defect in cell polarization and orientation in the medio-lateral direction was apparent, albeit some variation was evident from experiment to experiment (Fig. 5). Yet, there was no significant difference among the wildtype samples from three independent experiments following analysis using the student t-test with unequal variances for cell elongation and the Watson U^2 test for orientation. The colour code of the Cell Roses showed that the low percentage of wildtype cells of which the orientation deviates strongly from the medio-lateral direction did not show a strong elongation (Fig.5). This is caused in part by mitotic cells, which adopt a more spherical shape and display no strong preferential orientation. Taken together, these data show that Cell Outliner and Cell Roses are powerful tools to analyze cell polarization defects with respect to elongation and direction.

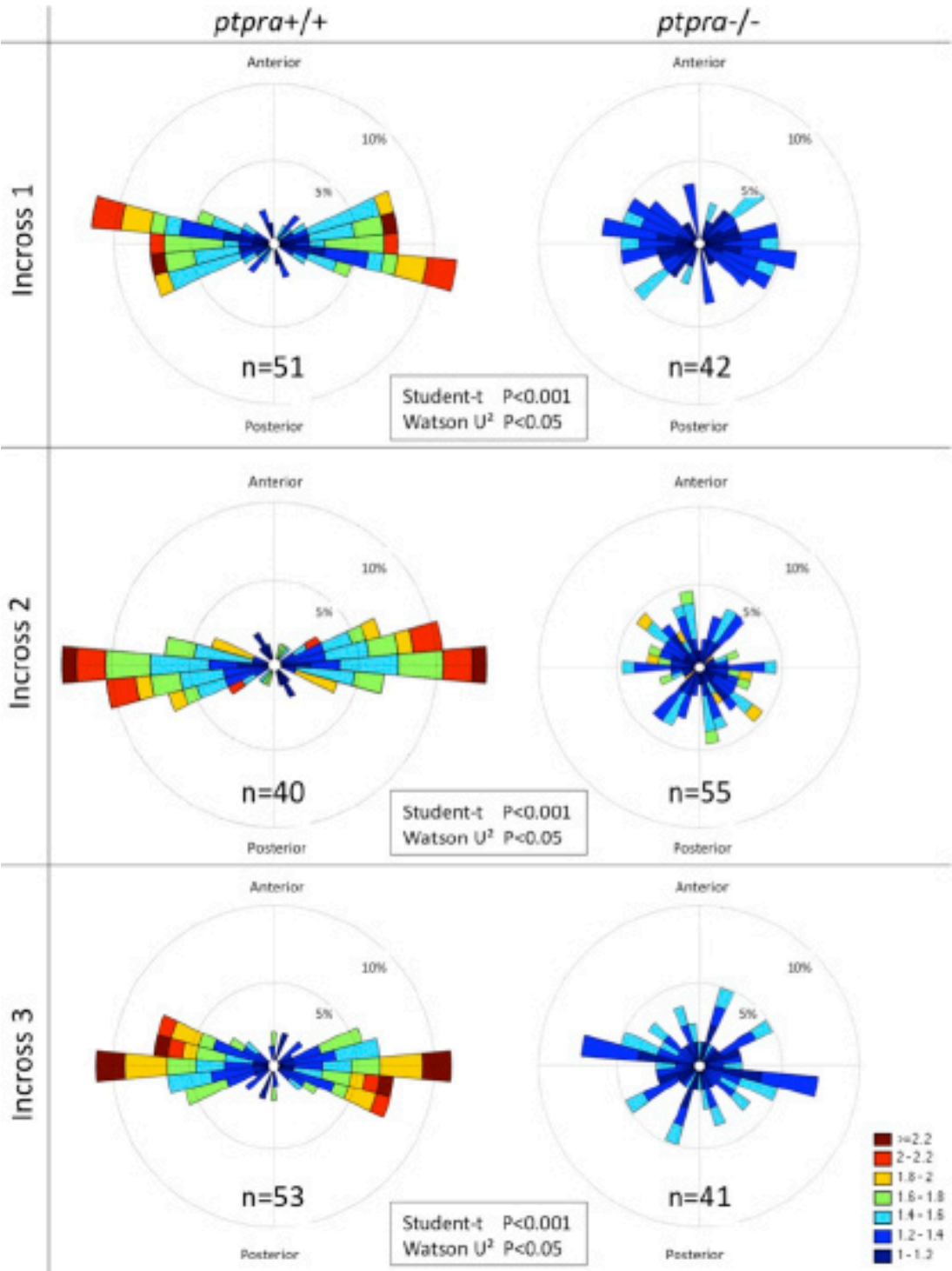


Figure 5: Cell Roses are effective tools to compare, analyze and determine cell polarization defects.

In 3 independent experiments heterozygous *ptpra*^{+/-} fish were incrossed and their offspring was injected with 20 pg YFP-CAAX mRNA. The embryos were imaged at the 2-3 somite stage and subsequently, genotyped by sequencing. The resulting images were processed by Cell Outliner and the resulting data was plotted using Cell Roses. These graphs show the distribution of the orientations of the cells in the presomitic mesoderm in radial histograms. Two circles on the graphs represent the 5% (inner circle) and 10% (outer circle) population fraction markers for the radial histogram. Within the bars of the histogram, a second subdivision is shown, indicating the frequencies (by surface area) and intensity of elongation (aspect ratio is indicated in colour code as indicated in the legend, bottom right) of cells within that particular population. Student-t statistics was used to compare the cell elongation values and Watson U2 statistic was used to compare the orientation data of the cells.

Discussion

Cell Outliner was designed to detect cell membranes in samples with high cell density, marked with fluorescent membrane markers, acquired through confocal imaging. It has been validated *in vivo* in zebrafish embryos for the membrane markers YFP-CAAX, in which the C-terminal CAAX-motif mediates association with the cell membrane [21], and memRFP, containing the N-terminal sequence of GAP43, which mediates association with the cell membrane [25,26]. Imaging of zebrafish embryos with ubiquitous expression of these markers yielded images of cell sheets with high density and a high fluorescence intensity signal at the cell membrane, and occasionally low intensity vesicular structures in the cytosol. Some images, used for analysis, contained fluctuation of signal intensity within a membrane segment or a global intensity gradient. The method has shown to be robust in handling gradual intensity changes and has shown to be able to compensate for small abrupt changes of intensity, producing very accurate results for these markers.

We also showed the method to be effective in fixed 4 somite stage mouse embryos labeled with 2 antibodies for E-cadherin, demonstrating a wide compatibility and applicability. Cell Outliner can in principle be used in other model organisms or any *in vivo* or *in vitro* model yielding images describing data in 2D array format in which the cell membranes are labeled. Cell Outliner may be applicable for alternative purposes as well. However, it is essential to confirm that the objects of interest are of comparable size (in pixels) to the cells it was designed to model since the numerical values used in the algorithm were optimized for this purpose.

The defining parameters for the determination of cell polarization defects are quantifications of cell elongation and medio-lateral orientation. Conventionally, these are analyzed and represented separately. In doing so, there is a potential loss of information about the correlation between the aforementioned param-

eters. By representing both on a Cell Rose, the well-studied correlation between medio-lateral elongation and orientation of the presomitic mesoderm was clear for the wildtype samples. We demonstrated the combined use of Cell Outliner and Cell Roses for analyzing the mutant phenotype of *rptpa* in the presomitic mesoderm of zebrafish embryos. The cell roses clearly showed the concomitant loss of elongation and medio-lateral orientation of the cells in the mutant.

Application and Conclusion

The necessity of determining and scoring individual cell behaviours and polarity as part of a population or tissue is not restricted to the study of gastrulation. In development alone numerous examples can be found in which polarity and tissue migration are key factors, like in angiogenesis [27] and the establishment of the highly organized structure of auditory and vestibular epithelia [28]. Collective tissue migration also underlies wound healing; the basal random individual movements of the endothelial cells are reoriented to collectively polarized migration by modular control, independent from growth factors, upon the appearance of cell free space [29]. Similar cell behaviors have also been observed in metastatic processes in mouse mammary tissue [30]. The advent of more sophisticated imaging technology, including hardware and a plethora of highly sensitive and specific fluorescent probes, allows the visualization of these biological processes in unprecedented detail. Data analysis of these huge data sets for morphological features can be greatly facilitated by the use of algorithms like Cell Outliner.

Cell Outliner is a freely available ImageJ plug-in (<http://rsbweb.nih.gov/ij/plugins/>), which works with ImageJ version 1.45h or higher. The application is very simple: install as an ImageJ plugin, and the application will appear in the scroll-down menu within the ImageJ program. Apply to an 8-bit image (or stack of images) representing the cell membranes: the output contains the original image, an image of the generated model, a projection of the detected objects onto the original image and a table with the data of the analyzed cells. The method eliminates the need for conventional, labor-intensive, manual annotation of the membranes and is extremely fast, objective, reliable, and reproducible. Since Cell Outliner facilitates the collection of information regarding a commonly used phenotypic parameter like cell shape, it can be applied to a wide range of phenotypes and is certainly not limited to the zebrafish or mouse model.

Cell Roses is a freely available plugin (upon request) for Matlab, which can be used to plot the output of Cell Outliner. The data generated by Cell Outliner, which is in an excel format, can be imported into Matlab and subsequently processed. This novel method of data representation not only combines the advantages of the conventional separate representation of cell elongation and medio-



lateral orientation, it also adds additional information regarding their correlation, potentially revealing vital information.

Acknowledgements

The authors would like to thank Monika Bialecka and Jacqueline Deschamps for kindly providing the images of mouse embryos stained with the different E-cadherin antibodies and Jeroen Bakkers and Jeroen Bussman for plasmids encoding fluorescent membrane markers. This work was supported by a Marie Curie Research Training Network (PTPNET / MRTN-CT-2006-035830). The funders had no role in study design, data collection and analysis, decision to publish, or preparation of the manuscript.

References

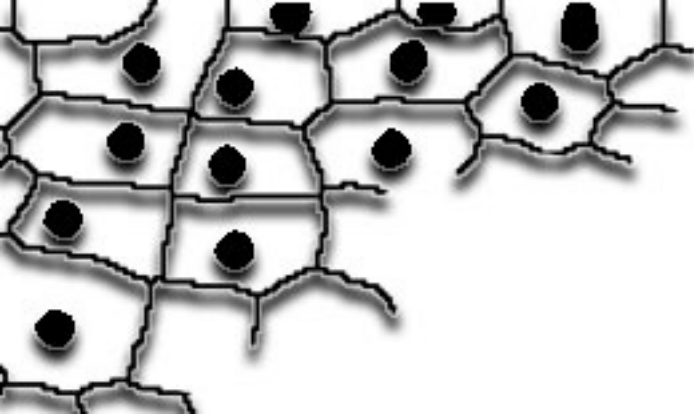
1. Roszko I, Sawada A, Solnica-Krezel L (2009) Regulation of convergence and extension movements during vertebrate gastrulation by the Wnt/PCP pathway. *Semin Cell Dev Biol* 20: 986-997.
2. Myers DC, Sepich DS, Solnica-Krezel L (2002) Bmp activity gradient regulates convergent extension during zebrafish gastrulation. *Dev Biol* 243: 81-98.
3. Myers DC, Sepich DS, Solnica-Krezel L (2002) Convergence and extension in vertebrate gastrulae: cell movements according to or in search of identity? *Trends Genet* 18: 447-455.
4. Topczewski J, Sepich DS, Myers DC, Walker C, Amores A, et al. (2001) The zebrafish glypican knypek controls cell polarity during gastrulation movements of convergent extension. *Dev Cell* 1: 251-264.
5. Jessen JR, Topczewski J, Bingham S, Sepich DS, Marlow F, et al. (2002) Zebrafish trilobite identifies new roles for Strabismus in gastrulation and neuronal movements. *Nat Cell Biol* 4: 610-615.
6. Concha ML, Adams RJ (1998) Oriented cell divisions and cellular morphogenesis in the zebrafish gastrula and neurula: a time-lapse analysis. *Development* 125: 983-994.
7. Lin F, Sepich DS, Chen S, Topczewski J, Yin C, et al. (2005) Essential roles of G α 12/13 signaling in distinct cell behaviors driving zebrafish convergence and extension gastrulation movements. *J Cell Biol* 169: 777-787.
8. Keller PJ, Schmidt AD, Wittbrodt J, Stelzer EH (2008) Reconstruction of zebrafish early embryonic development by scanned light sheet microscopy. *Science* 322: 1065-1069.
9. Megason SG (2009) In toto imaging of embryogenesis with confocal time-lapse microscopy. *Methods Mol Biol* 546: 317-332.
10. Mosaliganti K, Janoos F, Gelas A, Noche R, Obholzer N, et al. (2010) Anisotropic Plate Diffusion Filtering for Detection of Cell Membranes in 3d Microscopy Images. *Proc IEEE Int Symp Biomed Imag-*
ing: 588-591.
11. Megason SG, Fraser SE (2007) Imaging in systems biology. *Cell* 130: 784-795.



12. Jurrus E, Paiva AR, Watanabe S, Anderson JR, Jones BW, et al. (2010) Detection of neuron membranes in electron microscopy images using a serial neural network architecture. *Med Image Anal* 14: 770-783.
13. M.A.Luengo-Oroz LD, C.Castrcfi, T.SavyK E.Faure, B.Lombardo,, P.Bourgine NPaAS (2008) Can voronoi diagram model cell geometries in early sea urchin embryogenesis? *ISBI*: 504-507.
14. Westerfield (1995) *The zebrafish book*: University of Oregon press, Eugene, Oregon.
15. Lawson KA (1999) Fate mapping the mouse embryo. *Int J Dev Biol* 43: 773-775.
16. Pawley JB (2006) *Handbook of biological confocal microscopy*.
17. Davies E (1990) *Machine vision: theory, algorithms and practicalities*: Academic press.
18. Bernsen J. *Dynamic Thresholding of Grey-Level Images*; 1986.
19. Niblack W (1986) *An introduction to Digital Image Processing*: Prentice-Hall.
20. Sauvola J, Pietaksinen M (2000) Adaptive Document Image Binarization. *Pattern Recognition* 33: 225-236.
21. Choy E, Chiu VK, Silletti J, Feoktistov M, Morimoto T, et al. (1999) Endomembrane trafficking of ras: the CAAX motif targets proteins to the ER and Golgi. *Cell* 98: 69-80.
22. Aurenhammer F (1991) Voronoi Diagrams - A Survey of a Fundamental Geometric Data Structure. *ACM Computing Surveys* 23: 345-405.
23. van Eekelen M, Runtuwene V, Overvoorde J, den Hertog J (2010) RPTAlpha and PTPepsilon signaling via Fyn/Yes and RhoA is essential for zebrafish convergence and extension cell movements during gastrulation. *Dev Biol* 340: 626-639.
24. Slade DH (1968) *Meteorology and atomic energy*: US Atomic Energy Commission. 28-30 p.
25. Greaves J, Prescott GR, Fukata Y, Fukata M, Salaun C, et al. (2009) The hydrophobic cysteine-rich domain of SNAP25 couples with downstream residues to mediate membrane interactions and recognition by DHHC palmitoyl transferases. *Mol Biol Cell* 20: 1845-1854.

26. Greaves J, Salaun C, Fukata Y, Fukata M, Chamberlain LH (2008) Palmitoylation and membrane interactions of the neuroprotective chaperone cysteine-string protein. *J Biol Chem* 283: 25014-25026.
27. Cirone P, Lin S, Griesbach HL, Zhang Y, Slusarski DC, et al. (2008) A role for planar cell polarity signaling in angiogenesis. *Angiogenesis* 11: 347-360.
28. Kelly M, Chen P (2007) Shaping the mammalian auditory sensory organ by the planar cell polarity pathway. *Int J Dev Biol* 51: 535-547.
29. Vitorino P, Meyer T (2008) Modular control of endothelial sheet migration. *Genes Dev* 22: 3268-3281.
30. Wyckoff JB, Wang Y, Lin EY, Li JF, Goswami S, et al. (2007) Direct visualization of macrophage-assisted tumor cell intravasation in mammary tumors. *Cancer Res* 67: 2649-2656.





6

The Protein-Tyrosine Phosphatase Family in Gastrulation Cell Movements in Zebrafish

Vincent Runtuwene, Mark van Eekelen and Jeroen den Hertog

Abstract

The zebrafish model ideally lends itself to large scale morpholino screens due to its high fecundity and ease of morpholino injection. Moreover, zebrafish embryos are optically transparent, facilitating morphological analysis of developmental defects. We took advantage of the zebrafish system to screen the entire family of classical protein-tyrosine phosphatases. Despite the fact that this family of proteins has been studied intensively, still relatively little is known about its function *in vivo*. We designed 2 splice site morpholinos for each of the 48 genes, encoding protein-tyrosine phosphatases. In the first round all embryos were analyzed morphologically, which resulted in the identification of four candidate genes with a potential role in convergence and extension. These positive hits were analyzed in detail for convergence and extension defects in the second round by *in situ* hybridization and confocal microscopy-based cell shape analysis, yielding one *bona fide* novel PTP with a role in convergence and extension cell movements.

Introduction

Reversible tyrosine phosphorylation of proteins is a key mechanism for transducing inter- and intracellular stimuli, and acts as a highly dynamic molecular switch between different activation states of signaling molecules [1-3]. Given its elemental role it is not surprising that disruption of the synergy between protein-tyrosine kinases (PTKs) and phosphatases (PTPs) underlies many human diseases and developmental defects [4-9]. While much work has been done in the characterization of PTKs, the function of many PTPs remains to be elucidated.

During gastrulation, the zebrafish morphology undergoes a drastic change from an apparent homogeneous, 'inverted cup'- shape to a bilaterally symmetric, narrow and long body frame. This impressive remodeling is due in great part to the evolutionary conserved convergence and extension (CE) cell movements [10]. Together with epiboly and internalization, the CE movements form the germ layers, ectoderm, mesoderm and endoderm. Additionally, they are crucial for proper organ anlage positioning and as a consequence are essential for normal development [11]. Collective polarization of the cells in the mediolateral direction is essential for both the convergence towards the midline as well as intercalation, which is needed for extension in the antero-posterior direction. Cell polarization is in part regulated by the non-canonical Wnt/PCP pathway [12-15]. Cell adhesion has also been implied to be a key factor in zebrafish CE movements [16].

We are interested in the role of PTPs in CE cell movements. Previously, we have identified all members of the family of classical PTPs in the zebrafish genome and provided a detailed analysis of the spatio-temporal expression patterns of these 48 PTPs during early embryonic development. Many PTPs are maternally contributed and most PTPs are ubiquitously expressed at shield stage [17]. We and others have shown that knockdown or knockout of several members of the family of classical PTPs, including *ptpra*, *ptprea*, *ptpreb*, *ptpn11*, and *ptprua* affect the CE cell movements during zebrafish gastrulation [18-20]. Moreover, we have recently found that *ptpn13* and *ptpn20* are required for normal gastrulation cell movements as well (Chapter 3, this thesis). These morphant and mutant embryos show a common shorter and broader phenotype. For *ptprea* and *ptpreb*, simultaneous knockdown was necessary to produce a phenotype, suggesting redundant functions of these ohnologs [19]. Given the role of some PTPs in CE cell movements and given that the majority of transmembrane PTPs encode components of cell adhesion molecules in their extracellular domain, including immunoglobulin-like domains and Fibronectin type III repeats, which may mediate cell-cell contacts and thus play a role in CE cell movements during gastrulation, we were interested to investigate the function of all classical PTPs in CE.



We set out to perform a functional screen on the role of the entire family of classical PTPs in gastrulation CE movements, using morpholino (MO) based gene knockdown. For each PTP, two independent splice site MOs were used. Initially, knockdown was assessed on a morphological basis. A gene was considered positive when both MOs generated a significant reduction in tail length at 72 hpf. In total 41 PTPs with unknown function in CE movements were analyzed and four of these genes were considered to be positive based on this principle. In the second round, the four positives were scored more directly for defects in CE movements using two independent methods: *in situ* hybridization with CE specific probes and analysis of the polarization of the presomitic mesoderm using confocal microscopy. Based on these tests, we found that one of these genes had a role in CE cell movements, namely *ptprda*. To our knowledge this is the first MO screen in which an entire protein family was systematically knocked down.

Results

Screening for PTPs that affect CE cell movements

In the present study we aim to identify PTPs which have a role in CE movements during gastrulation. Previously, we have identified all members of the classical PTP family in the zebrafish genome. Here, we designed a functional screen to assess the role of each PTP in early development (Fig. 1). Briefly, we designed two independent splice site MOs for all PTPs. Each MO was injected into zebrafish embryos at the one-cell stage and phenotypes were assessed at 24, 48 and 72 h post fertilization (hpf). Embryos with shorter body axis were selected and the tail length was determined at 72 hpf as a first indication of potential CE cell movement defects. Subsequently, p53-MO was co-injected with each of the PTP-MOs to rule out that the observed defects were caused by non-specific p53-dependent DNA damage responses. Finally, candidate hits where the two MOs induced similar developmental defects in a p53-independent manner were selected and subjected to specific analysis of defects in CE cell movements.

Design of the MOs

Using the previously identified PTP sequences in the almost completely sequenced zebrafish genome, version Zv8, we designed splice site MOs [17, 22]. Several human PTP encoding genes like *PTPRC*, *PTPRD*, *PTPRE*, *PTPRS*, *PTPRF* and *PTPRO* have been shown to generate multiple isoforms, usually differing in the N-terminal extracellular domain in receptor-like PTPs, which are assumed to be formed by alternative splicing [23-25]. Yet, expression of *PTPRE* and *PTPRO* isoforms is driven by alternative promoters, resulting in transmembranal and cytosolic isoforms, respectively [26, 27]. It is highly likely that other PTP genes

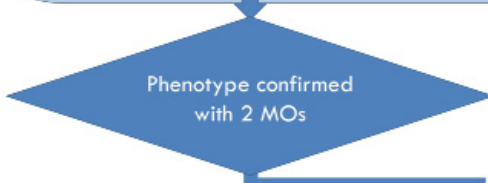
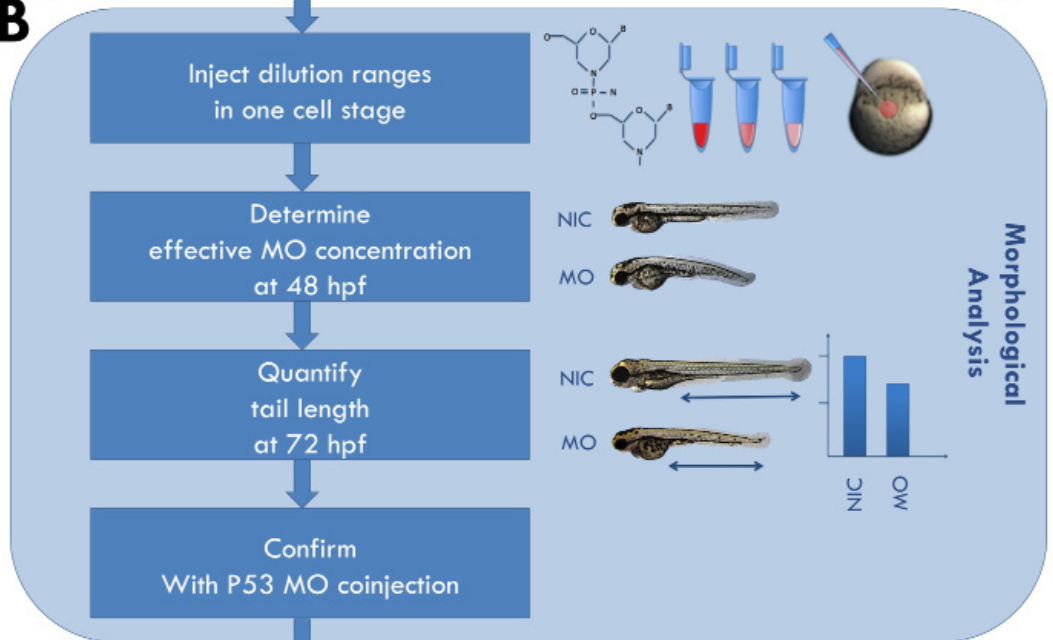
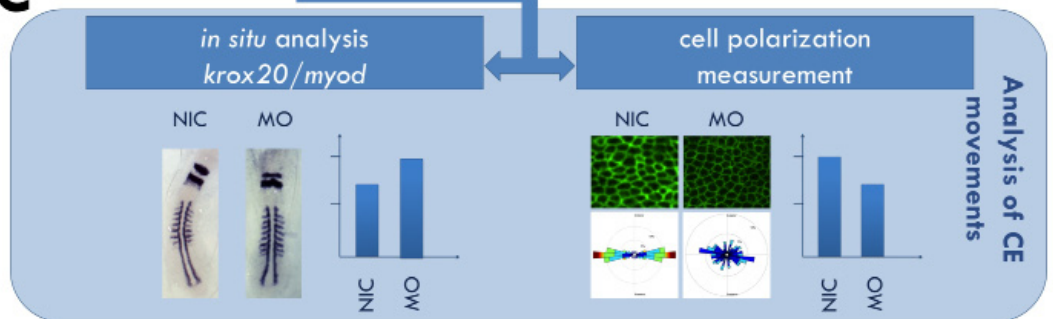
A**B****C****6**

Figure 1. Schematic overview of the screen for PTPs with a role in CE movements.

(A) Splice site MOs were designed based on the identified PTP sequences in the zebrafish genome (version ZV8). (B) Dilution ranges of MOs (0.3 – 5.0 ng/nl) were injected to determine an efficient MO concentration, defined as the lowest concentration that induced morphological defects at 48 hpf. The tail lengths of embryos were quantified at 72 hpf. The embryo phenotypes were confirmed by coinjection of p53 MO. (C) When 2 MOs cause a significant reduction in tail length and both are confirmed by coinjection of p53 MO, we proceeded with quantitative tests for the analysis of specific aspects of CE. In situ hybridization was done with well characterized markers for CE movements. Analysis of cell polarity in the presomitic mesoderm was done by confocal microscopy and automated scoring of cell shape.

generate different isoforms through similar mechanisms. The use of ATG MOs would only suppress the expression of certain isoforms of a PTP gene. Therefore, we designed splice site MOs targeted at the exon-intron boundaries within the PTP domain, immediately upstream of the catalytic site to ensure that the MOs disrupt the phosphatase activity of all isoforms of the respective PTPs. For all PTP genes, two splice site MOs (25-mers) were designed in accordance with the criteria provided by the manufacturer (<http://www.gene-tools.com/>) (Table 1).

Gene	MO name	sequence
ptprc	MO1*	ACAAAGCACAAACCTTATTTCCCTTC
	MO2	CCCTATCTGTACCTGCAGTGGACCA
ptprm	MO1*	TTGATGCTGCACCTTCTCCACAGCG
	MO2	ATTCTCCTGTACCTGCAGTGCACCA
ptprk	MO1*	AAAATAATCTCACCCCTCTCCAGAGT
	MO2	GGCCACACACACCTCGGTCTGTACC
ptprt	MO1	AAAGAGATTTTACCTTCTGTACAGT
	MO2	ATAGCAGCATACTGCAGTGAACCA
ptprua	MO1*	AGTCATCTCGTACCCGCTCCAGGGC
	MO2*	GAAGCTCCATACCTGCAGTGCACCA
ptprub	MO1	TAACACACTTACCCGCTCCATGGCA
	MO2	AGTAATTTCTACCTGCAGTGGACAA
ptprfa	MO1	GGAACCTTTTACCTTGTAAGGGCA
	MO2*	AACCGTACTCACCTGCAGTGCACCTA
ptprfb	MO1*	GAACACACACACCTTGTAGAGAGCG
	MO2	GTCACGCTGTACCTGCAGTGCACCA
ptprsa	MO1	TTGAAATCTTACCTTGTGCAAGGAG

ptprsb MO2 CAGATTTTCAGACCTGCAGTGGGCGA
 MO1* GCACACACTCACCCCTGGCGTCGGTG
 MO2* GTCGTGTTTTACCTCAGTCTGCACC
 ptprda MO1* CTGTTTGGTTACCTTAAAGAGGGCA
 MO2* GGTAATAGCTACCTGCAGTGGACCA
 ptprdb MO1 CACCGCTCGTACCCTGGACCGCTCC
 MO2 TGAGAGTCAGACCTGCAGTGCACCA
 ptprb MO1 GACTCCACTTACGCATGATATTTTG
 MO2 TGTGACTCTTACCTCGGTTTGTACC
 ptprja MO1 TGAGGTTCTTACATGGCAGCACATT
 MO2 TGAGGTTCTTACATGGCAGCACATT
 ptprh MO1 ACATTGCCTTACCCTTCCACCCTCA
 MO2 GAAATGGCTTACATTTTTGACATTA
 ptprq MO1 GCATTGGTTTACCCGCTCCACTTTG
 MO2 GCGTCTGTGTACCTGCAGTGGACCA
 ptpro MO1* TGTTTTCCCTCACGTATGCGAGTCTG
 MO2* GTTAGCACTGACCCTGCGGCGCTCG
 ptpra MO1* TTGCGGCGTTTACCTCTTTCCGCTC
 MO2* TGCCCTGGAGAAACGAAACCTGCAT
 ptprea MO1* AAGGGATGCTAACCTCTTTTCTCTC
 MO2* ATTAAGACTTACATATTGCACACAG
 ptpreb MO1* TATCTTATCTCACCTCTTTTCTCTC
 MO2* CTGCAGTCTTACCTACAGTGCACCTA
 ptprga MO1 AAACATTGTGTACCTTCTTTACTTT
 MO2 TGTGGGTTTTACCTGCAGTGTACAA
 ptprgb MO1* ATGGATACTCACCCCTGCCTTTCTCC
 MO2* GCTTTAACGCACCTTTTTTCAGTTTG
 ptprza MO1* CTCAAAGCCTTACCCGGCCCTTCTC
 MO2 GTAAGTACTTACCTGCAGTGCACCA
 ptprzb MO1 AAAATGTCTTACCCTTCTTTCTCC
 MO2 AAATATTGATACCTTTTTTATGCTG
 ptprrr MO1 ATCAGGACTTACTCGTATGTAGTTG
 MO2* TCAGATACTGACTTGGCAAATGGT
 ptprna MO1 GGTTTTCAGTAGGTGCGGAAGTCCA
 MO2 AAGTTTGCTTACCTTTGGCCATGCG
 ptprnb MO1 ATGTATGCAGTACCTGCGAAAGTCC
 MO2 TGAAGTGCTGACCTTTAGCCATGCG



ptprn2	MO1	TGTGGACACATACCTGCGGAAGTCC
	MO2*	TGTGGTACTTGCCTGCAATGAACAA
ptpn1	MO1	CAAGAGCCTCACCGACAGATTTTCC
	MO2	CCGTCATCTACCAATAGAAGGCAG
ptpn2	MO1*	AATGTGACTCACCGTGCCTTTCTCT
	MO2	TTACATTACACCTTGCCATTTTGA
ptpn6	MO1	ACTCATTCCTTACCCGATGCGGAGC
	MO2*	TTATTAAGTACCTGCAGTGAATGA
ptpn11a	MO1*	GAAACCCTTTACCTTTCCCGTTCC
	MO2*	GGTGAACCACCTTCGGGATGTCAT
ptpn11b	MO1	GCATTGCTCTTACCCTGTCTAGACG
	MO2	CCTGGACCTTACCCGTCTCTCTCC
ptpn9a	MO1	TATGATGTCGTACCTTGTTATCATG
	MO2	TTAGAAATGTACCTCAGTGTTGTGC
ptpn9b	MO1	TAACGAAACTAACCTTGTAGTCATA
	MO2*	TAAGAAACTAACCTGAGTGTTGAAC
ptpn18	MO1	TGAAACAGCTCACCTTAACATTATG
	MO2	GAAAACACTTACAGTTGAGACAGTA
ptpn3	MO1	TGTTGTTGTTACCTGAGTGTTAGTG
	MO2*	ACGAAGTTGTACCGATGTCTGAACC
ptpn4a	MO1	GTGATAAGCTCACCTCAATGTGAGT
	MO2	ATGTGGACTTACAGGCGTCTGAATC
ptpn4b	MO1*	ATGCTTTTCATACCCGGCCCCGCTC
	MO2	TCCAGGCCTGACCTGCAGTGAACCA
ptpn21	MO1	GTGCTGTACTTACAGAGAAAGCCTT
	MO2*	TGCAGTGCATACCTCATTGTGTTCC
ptpn13	MO1*	CTCTCTCTCTCACCTGGACGTCTTT
	MO2*	TGTGACACTTACATCTGCGTCTTTG
ptpn23a	MO1	AAAAGTCCCTTACAGTTCAGGCCAT
	MO2	TAAGTGGTTTACCTTTAGTGTAATG
ptpn20	MO1*	CATGCTCCTAACCTTTTTTTCCACC
	MO2	TAAATGACTCACACTGAGGTCTTTC
ptpn5	MO1	AACTCAGACAGACCTTCACAGTGAA
	MO2*	TAAAAATGTTACCTGCAGTGGACGA

Table 1. PTP genes and Morpholino sequences.

All splice site MOs were designed to target one (marked MO1) or two (marked MO2) exons upstream of the catalytic site and manufactured by Genetools (Pilomath, OR, USA). MOs, that caused a CE defect based on morphological analysis are marked with an asterisk (*).

PTP-MO induced tail length defects

Gene knockdown was achieved by injection of MOs at the one cell stage. In at least two independent experiments we injected dilution ranges from 0.3 to 5.0 ng/nl per embryo, using 50 embryos per condition (n= 50). Effective concentrations for each MO were determined as the lowest concentration at which defects in morphology were clearly visible at 48 hpf in at least 80% of the injected embryos (Fig. 2A). As a quantitative read-out for body axis extension, a hallmark of CE defects, we determined the tail length at 72 hpf (Fig. 2B). A hit was considered positive when both MOs generated a significant reduction in tail length at 72 hpf. Of 41 PTPs with unknown function in convergence and extension movements, four genes were considered to be positive based on these criteria: *ptprsb*, *ptprda*, *ptpro* and *ptprgb*. As positive controls, we included *ptprua*, *ptpra* and *ptprea/b* (combined *ptprea* and *ptpreb*) that are known to have a role in CE cell movements. Genes of which only one MO caused a significant reduction in tail length were considered tentatively negative and were excluded from further analysis.

Previous studies reported a shortened AP-axis, neural toxicity, widespread cell death, and defects in epiboly as possible off-target or non-specific effects [28-30]. The risk of observing these effects increases significantly when using MO concentrations higher than 5 ng/nl [31-33]. Indeed, in our hands neural toxicity, cell death, defects in epiboly, and shortened AP-axes were occasionally observed upon injection of high concentrations of MO. However, for all four positive hits effective MO concentrations were below 5 ng/nl. Furthermore, the replication of the phenotype using a second sequence-independent MO, reduces the probability that the observed phenotype is an off-target effect to great extent and in fact two independent morpholinos are considered as the standard for MO specificity. To ascertain that the observed phenotypes were not caused by a mere non-specific DNA damage response, all hits that were positive for both MOs were subsequently coinjected with a p53-specific MO, which has been shown to alleviate non-specific MO phenotypes by blocking p53-dependent apoptosis [34]. None of the four positive hits were affected by co-injection of p53-MO. Whereas all four candidate genes caused a reduction in tail length, the knockdowns induced clearly different overall morphological defects (Fig. 2A), warranting specific analysis of the effects on CE cell movements in response to knockdown of these four PTPs.

Analysis of CE movements

CE cell movements during gastrulation are characterized by mesendodermal cells that migrate towards the dorsal midline, intercalate and consequently contribute to body axis extension. These critical cellular rearrangements are largely driven by highly coordinated shape changes, *i.e.* collective polarization and elongation in the mediolateral direction [11]. Therefore, overall CE cell move-



ment defects are characterized by shorter and broader embryos. At the cellular level, CE cell movement defects are characterized by defective polarization, reduced cell elongation and defective cell orientation.

To investigate whether the shortened body axis was caused by defective CE cell movements, we performed *in situ* hybridization experiments on embryos fixed at 8-10 somite stage using the *krox20* and *myod* probes, well-established markers for CE cell movements [19, 35, 36] (Fig. 3A). The *krox20* probe stains rhombomeres 3 and 5. The width of these structures is used as a measurement for convergence. The *myod* probe stains the somites. The distance from the first to the eighth somite is used to analyze extension. Defects in CE movements will cause a wider *krox20* staining and a shorter distance between the first and eighth

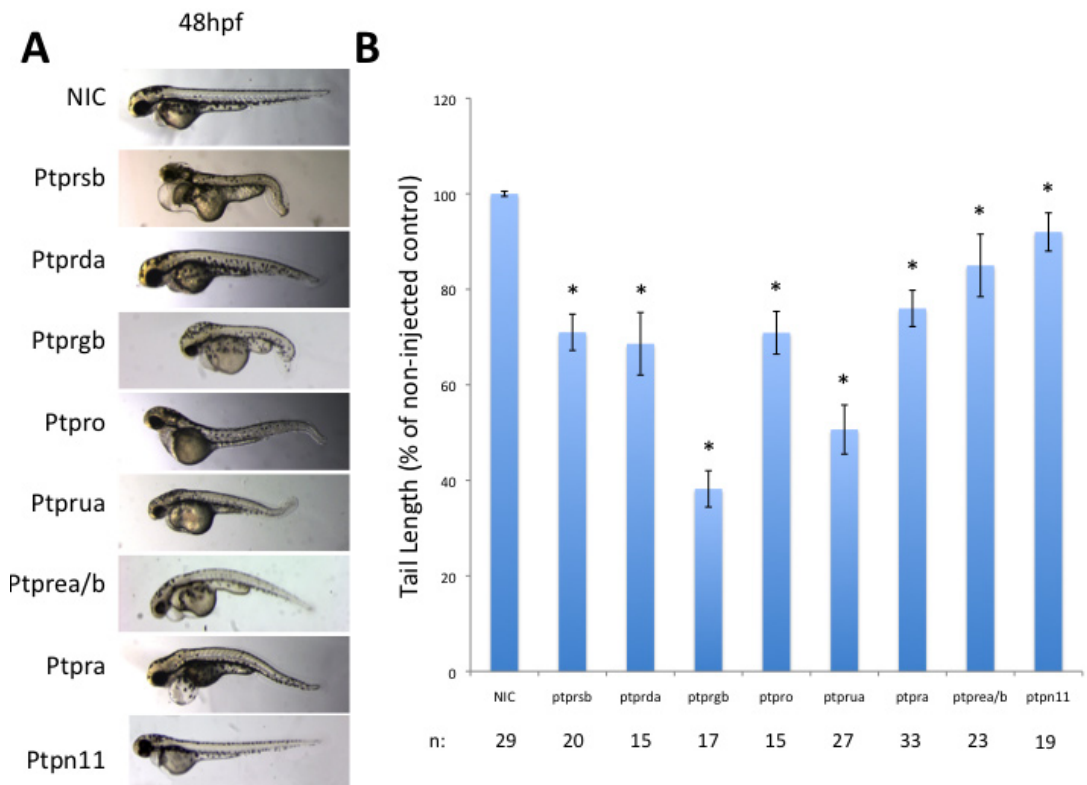


Figure 2. Knockdown of Ptps causes a shorter antero-posterior axis.

(A) Representative phenotypes at 48 hpf after injection at 1-cell stage with a MO targeting *ptprsb* (1,25 ng), *ptprda* (1,25 ng), *ptprgb* (1,25 ng), *ptpro* (1 ng), *ptprua* (1,25 ng), *ptpra* (0,3 ng), *ptprea/b* (mix of 2,5 ng *ptprea* and 2,5 ng *ptpreb*), *ptpra* (0,3 ng) or *pnpn11* (1 ng). Injections were done at least twice for each MO. (B) Quantification of the phenotypes shown in panel (A). Individual tail lengths, i.e. the distance between the beginning of the yolk extension and the tip of the tail, of embryos at 72 hpf from each group were measured using ImageJ software and the data were analyzed statistically in excel using a 2-tailed student t-test assuming unequal variances. Significant differences were determined using $\alpha=0,05$ upon comparison to the ratio of the non-injected control (NIC). Significant differences are indicated with an asterisk.

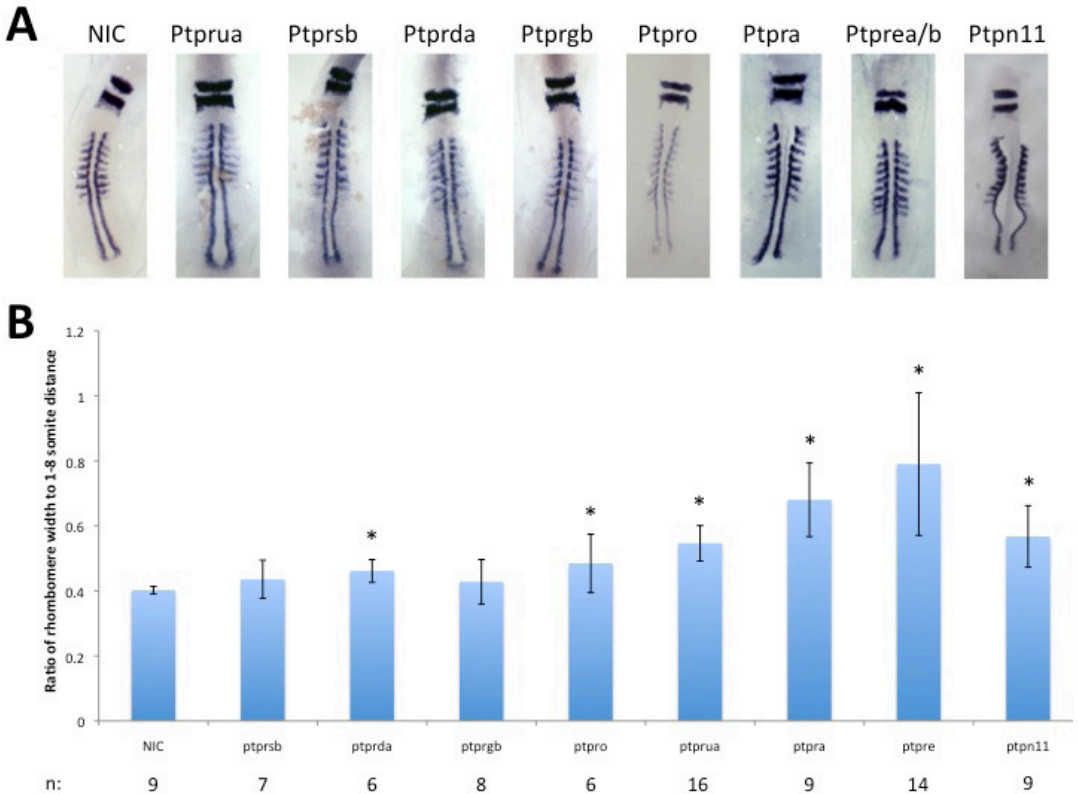


Figure 3. CE defects in PTP knockdowns.

(A) Embryos were injected at 1-cell stage with a MO targeting *ptprua* (1,25 ng), *ptprsb* (1,25 ng), *ptprda* (1,25 ng), *ptprgb* (0,625 ng), *ptpro* (1 ng), *ptpra* (0,3 ng), *ptprea/b* (mix of 2,5 ng *ptprea* and 2,5 ng *ptpreb*), and *ptpn11* (1 ng). The embryos were fixed at the 8-10 somite stage and in situ hybridisation was done using *krox20*- and *myod*-specific probes. The *krox20* probe stains rhombomere 3 and 5 and the *myod* probe stains the somites. The ratio between the width of the rhombomeres and the distance between the 1st and 8th somite was determined as a direct measure for CE cell movements. A representative embryo from each group is shown. (B) The resulting ratios for all MOs from (A). The data was statistically analyzed in excel using a 2-tailed student t-test assuming unequal variances. Significant differences were determined using $\alpha=0,05$ upon comparison to the ratio of the non-injected control. Significant differences are indicated with an asterisk.

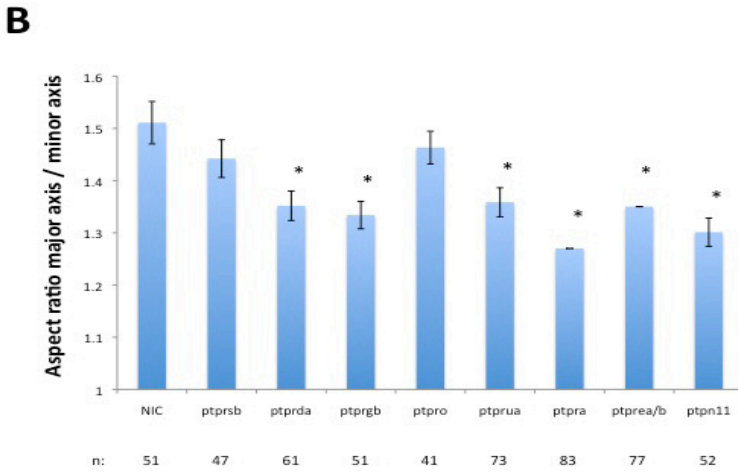
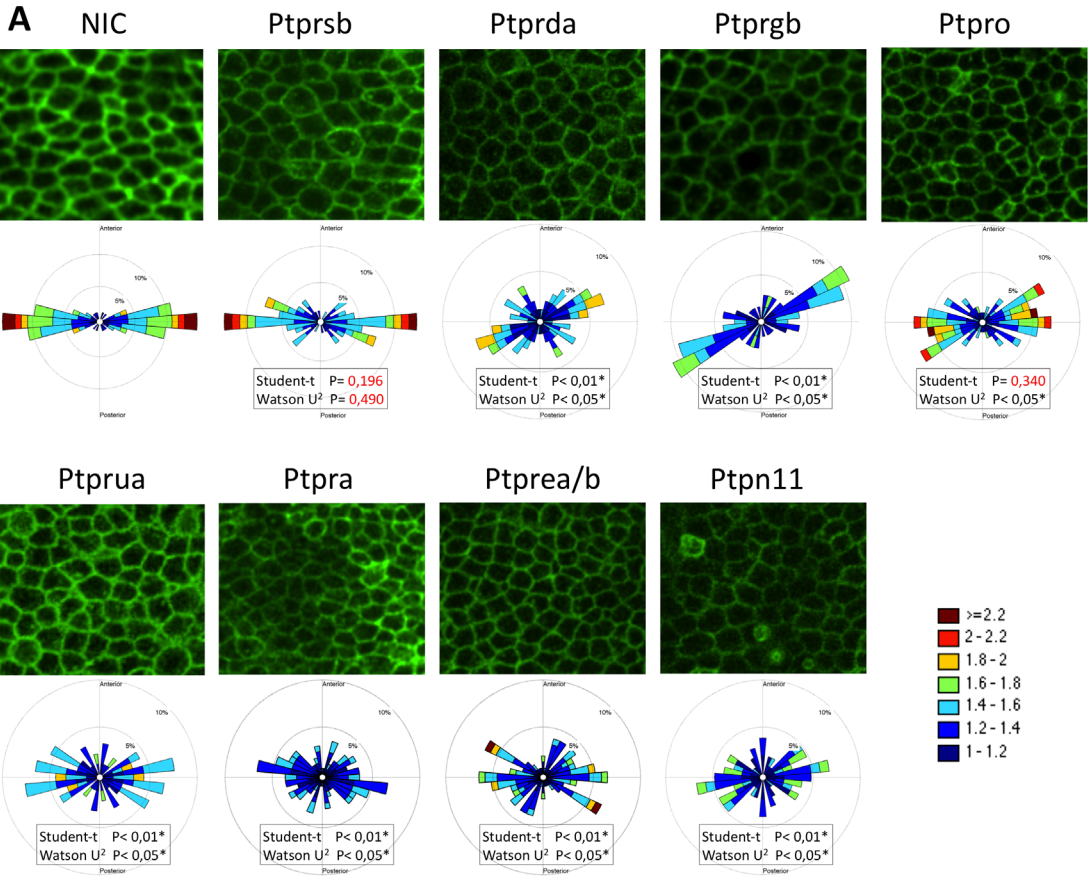
somite. Defects can readily be quantified by comparing the ratio of rhombomere width to somite distance between MO injected embryos and NIC embryos (Fig. 3B). Knockdowns of PTPs with a known role in CE cell movement defects resulted in a significant increase in this ratio for each of these genes (Fig. 3B). *Krox20/myod* in situ patterns showed that knockdown of *ptprda* and *ptpro* caused a significant increase of the rhombomere width to somite distance ratio at 8-10 somite stage, in contrast to *ptprsb* or *ptprgb* (Fig. 3B).

To assess defects in cell polarization, we determined the elongation and polarization angle of the presomitic mesendodermal cells. We used confocal micros-

copy to visualize the cellular membranes in the presomitic mesoderm at the 2 to 3 somite stage. In order to fluorescently mark the membranes, the embryos were injected with 20 pg of YFP-CAAX mRNA. The presomitic mesoderm was imaged 100 μm posterior to the developing somites in the paraxial mesoderm, lateral to the notochord. All cells within a region of 14000 μm^2 were analyzed in each sample by an automated algorithm. In order to get a more machine-interpretable representation of the cell shapes, we used a custom-made ImageJ plug-in, Cell Outliner, to convert the raw confocal images to binary representations, wherein the fluorescent membranes were segmented into a model with uniform intensity and line thickness (Chapter 5, this thesis). This was necessary because the inherent fluctuation in fluorescence intensity in raw confocal images causes artefacts. Subsequently, the cell shapes were analyzed regarding aspect ratios of length and width, i.e. cell elongation, and orientation of the long axis in relation to the mediolateral direction, i.e. cell polarization angle. Further, using an adapted windrose plug-in in Matlab, radial color-coded histograms were made showing the relationship between the distribution of the cell polarization angle and cell elongation, henceforth referred to as Cell Roses (Fig. 4A) (Chapter 5, this thesis). Additionally, the cell aspect ratios were compared separately between MO injected embryos and NIC (Fig. 4B). Using this method we observed for *ptpra*, *ptprea/b*,

Figure 4. *Ptprda* is required for normal gastrulation cell movements.

(A) Embryos were injected at 1-cell stage with a MO targeting *ptprua* (1,25 ng), *ptprsb* (1,25 ng), *ptprda* (1,25 ng), *ptprgb* (1,25 ng), *ptpro* (1 ng) *ptpra* (0,3 ng), *ptprea/b* (mix of 2,5 ng *ptprea* MO and 2,5 ng *ptpreb* MO), and *ptpn11* (1 ng). All embryos were coinjected with YFP-CAAX mRNA (25 pg) a fluorescent marker for the cell membranes. The embryos were mounted at shield stage on the dorsal side, approximately 100 μm posterior to shield position. (A) Imaging of the presomitic mesoderm was performed at 2-3 somite stage. The cell shape segmentation was performed using a custom made plugin, Cell Outliner, in ImageJ and the resulting data was plotted using a Cell Rose (an adapted windrose plot plugin in Matlab). ImageJ determines the angles of the major axes of the cells within the PSM to the notochord (the orientation of the notochord is parallel to the vertical axis, marked on top “anterior” and at the bottom “posterior”). In addition, ImageJ measures the length to width ratios of the cells. The graphs in (A) show the distribution of the orientations of the cells in the presomitic mesoderm in radial histograms. Two circles on the graphs represent the 5% (inner circle) and 10% (outer circle) population fraction markers for the radial histogram. Within the bars of the histogram, a second subdivision is shown, indicating the frequencies (by surface area) and intensity of elongation (aspect ratio is indicated in colour code as indicated in the legend, bottom right) of cells within that particular population. Student-t statistics was used to compare the cell elongation values and Watson U2 statistic was used to compare the orientation data of the cells. As such, the resulting Matlab windrose graphs in (A) show both the polar distribution of all cell angles and shows in color code (see legend) the extent of polarization of the cells within a certain orientation. Statistical comparison data displayed, resulted from comparison of a MO-injected embryos to NIC siblings within the same experiment. (B) Bar graph of the polarization of the PSM solely based on the major/minor axes ratios. The data was statistically analyzed in excel using a 2-tailed student t-test assuming unequal variances. Significant differences were determined using $\alpha=0,05$ upon comparison to the ratio of the non-injected control. Significant differences are indicated with an asterisk.



ptprua, and *ptpn11* morphants a strikingly similar pattern. The Cell Roses show a randomization of cell orientations as well as a clear loss of cell elongation indicated by a blue shift in the color code in comparison to the wild-type (Fig. 4A). The quantitative comparison of cell elongation reaffirms this significant decrease (Fig. 4 A,B). Of note, while the role for *ptprua* and *ptpn11* in CE movements has already been established, to our knowledge, this is the first study to provide direct evidence for the loss of cell polarization in the presomitic mesoderm of *ptprua* and *ptpn11* morphants.

Targeting *ptprsb* did not reveal a significant cell elongation defect in *ptprsb* knockdown embryos (Fig. 4 A,B). The Cell Roses showed a very slight randomization in the distribution of the polarization angles, yet a clear preference for the polarization angles in the mediolateral direction remained showing no significant difference to the positive controls (Fig. 4A). We conclude that the shortened body axis which is apparent at 72 hpf in *ptprsb* knockdown embryos is unlikely to be caused by defective CE movements.

Knockdown of *ptprda* caused a statistically significant difference in cell elongation (Fig. 4 A,B). Moreover, the Cell Rose showed a significant difference in the distribution of the polarization angles, demonstrated by a clear randomization, reminiscent of the pattern seen upon knockdown of PTPs known to play a role in CE movements (Fig. 4A). These results are consistent with a role for *ptprda* in CE movements.

Injection of **Ptpro**-specific MOs did not result in a statistically significant loss of cell elongation (Fig. 4 A,B). However, the Cell Rose showed a statistically significant randomization in the distribution of the polarization angles (Fig. 4A). This retaining of the cell elongation along with some randomization of the polarization angles is also indicated as red and brown areas on the cell rose (Fig. 4A). Given the retaining of cell elongation and the lower randomization of the polarization angles in comparison to the positive controls, we conclude that the shortened body axis which is apparent at 72 hpf upon knockdown of *ptpro* is unlikely to be caused by defective CE movements.

We found that knocking down *ptprgb* resulted in a significant loss of cell elongation (Fig. 4 A,B). Additionally, the cell rose showed a significant difference in the distribution of the polarization angles, yet a clear preference of direction was apparent, albeit deviating from the mediolateral direction (Fig. 4A). We conclude that the shortened body axis, which was apparent at 72 hpf in *ptprgb* knockdown embryos was more likely to be caused by mechanisms other than defective CE movements, because *bona fide* CE defects are characterized not only by defective cell elongation, but also by randomized distribution of the polarization angles.

Discussion

Identification of a putative effector of CE movements

We have performed a knockdown screen of the family of classical protein-tyrosine phosphatases. To our knowledge, this is the first time a MO- screen has been performed of an entire family of proteins. Our main goal was to identify PTPs with a role in CE movements. The workflow of the screen was subdivided into two main parts: morphological analysis and analysis of CE cell movements. 48 genes, which included seven PTPs with a known role in CE cell movements (*ptpra*, *ptprea*, *ptpreb*, *ptpn11*, *ptprua*, *ptpn13* and *ptpn20*), were systematically knocked down during zebrafish development and four genes with previously unknown function in zebrafish development were selected based on morphological parameters. Further analysis using *in situ* hybridization with known markers for CE movements and confocal microscopy-based cell polarity measurements, narrowed the number of putative hits to one *bona fide* novel PTP that acts in CE cell movements. For the other three hits from the morphological analysis, a different mechanism seems to underlie the observed phenotypes.

Evaluation of the screen

The MO screen described here has its pitfalls. One obvious problem is that the phenotype, which is considered positive in the morphological analysis, i.e. shorter body axis, is a known non-specific MO-induced artefact [32]. We used several controls to prevent false positives: (1) we never injected more than 5 ng MO and in general used the lowest amount which generates a phenotype [31]; (2) we injected a second sequence-independent MO to confirm the phenotype, which is generally established as the standard to assess specificity of MOs; (3) we coinjected both MOs with a p53-specific MO to establish that the observed defects were not due to a mere non-specific p53-dependent DNA-damage response [34]. A draw-back of the first control is that since we are using the lowest concentration of MO possible, it is not unlikely that the phenotype analyzed is a hypomorph and hence, we may miss MO-induced phenotypes (false negatives). In particular the genes for which only one of the MOs induced a phenotype are candidate false negatives.

*Lack of functional redundancy between *ptprsb*, *ptprda* and *ptprgb* and their ohnologs*

As mentioned above, there is functional redundancy between *ptprea* and *ptpreb*. Both genes need to be knocked down for a phenotype to become apparent. For *ptprsa/ptprsb*, *ptprda/ptprdb* and *ptprga/ptprgb* this is clearly not the case, indicating a functional divergence between these ohnologs. Moreover, for *ptprsa*, *ptprdb* and *ptprga* both MOs did not induce a phenotype, indicating that it



is unlikely that these genes have an essential function in early development. Apparently, the functions of these ohnologs have diverged.

The ohnologs *ptprsa/ptprsb* and *ptprga/ptprgb* have very similar expression patterns, especially during early development [17]. Interestingly, the expression patterns of *ptprda* and *ptprdb* differ greatly. While *ptprda* is maternally contributed and is expressed ubiquitously at the start of gastrulation, *ptprdb* seems not to be maternally contributed or expressed at the start of gastrulation [17]. This is consistent with a role for *ptprda* in early development. The functional divergence between *ptprda* and *ptprdb* may be explained by the difference in expression patterns, whereas *ptprsa/b* and *ptprga/b* presumably have different functions.

It should be noted for *ptprsa/ptprsb* and *ptprga/ptprgb* which show a similar expression pattern, that this screen did not include tests for partial redundancy between these gene couples, in that we did not include coinjection of MOs targeting both ohnologs. It is possible that the loss of *ptprsa* or *ptprga* was compensated by *ptprsb* or *ptprgb*, respectively, but not *vice versa*. It would be interesting to explore these possibilities.

Evolutionary conservation of PTP function

Gene functions of orthologs in distantly related species are often conserved. Here we compare the developmental defects in zebrafish morphants to the corresponding mouse knockout phenotypes.

Ptprsb is the ortholog of *Ptprs* in the mouse and it encodes a classical type IIb subfamily receptor-like PTP [17, 23]. *Ptprsb* knockdown in zebrafish caused small heads and eyes, and a severe cardiac edema. The *Ptprs* knock-out mouse displays early developmental defects, particularly in the nervous system [37]. These mice also display retarded growth, increased neonatal mortality, hyposmia, hypofecundity, and showed a decrease in overall brain size [38]. We conclude that zebrafish *Ptprsb* and mouse *Ptprs* have similar functions in early development.

Ptprda is a classical type IIb subfamily receptor-like PTP, the ortholog of mouse *Ptprd* [17, 39]. Knockdown of *ptprda* generated zebrafish embryos with only slight heart edema and bent tails. Like *Ptprs*, *Ptprd* has been shown to have an early developmental function in nervous system development in mouse [37]. Later phenotypes include semi-lethality due to insufficient food intake and learning impairment [40]. The zebrafish *ptprda* knockdown and mouse *ptprd* knock-out are consistent, but because the mouse knock-outs predominantly display late defects and we analyzed only early developmental defects in zebrafish embryos, the phenotypes are hard to compare definitively.



Zebrafish **Ptpro**, ortholog of mouse Ptpro, encodes a classical type III subfamily receptor-like PTP, characterized by a cytoplasmic region with a single PTP domain and an extracellular region comprising 8 Fibronectin type III repeats [17, 41, 42]. The Zebrafish *ptpro* morphants had smaller heads and heart edemas. Two distinct *ptpro*-deficient mouse models have been generated. The first Ptpro knock-out model displays an altered podocyte structure associated with hypertension and low glomerular filtration rate [43]. The second Ptpro knock-out displays defects in the development and function of the sensory nervous system [44]. Given the discrepancy in developmental defects in the two mouse knock-out models, it remains to be determined definitively whether zebrafish and mouse Ptpro have orthologous functions.

Ptprgb is the ortholog of Ptprg, a classical type V subfamily receptor-like PTP [17, 45]. MOs targeting *ptprgb* induced severe shortening of embryos, heart edemas and a slight hindbrain edema. Mouse Ptprg is expressed in pyramidal cells and sensory neurons in the nervous system. Ptprg knock-out mice develop normally and it appears that Ptprg is not required for normal development [46]. Apparently, Ptprgb is not dispensable for normal embryonic development in zebrafish and hence the function of Ptprgb differs from mouse Ptprg.

Conclusion

We conclude that a MO screen on an entire gene family with 48 members is feasible in zebrafish. Next to the seven known PTPs with a role in CE cell movements, we have identified one additional PTP that is essential for normal gastrulation cell movements, Ptprda. It will be interesting to investigate how Ptprda affects gastrulation cell movements and whether it interacts with the signaling pathway that is well-known to regulate CE movements, the non-canonical Wnt pathway. In addition, it will be interesting to investigate cross-talk among all PTPs that have been identified to play a role in CE cell movements.

Materials and methods

Zebrafish maintenance and in situ hybridization

Zebrafish were kept and the embryos were staged as described before [47]. *In situ* hybridizations were done essentially as described [48] -- using probes specific for *krox20* and *myod*.

Morpholinos, in vitro transcription of mRNA and injection

Antisense splice site MOs were designed to target one or two exons upstream of the phosphatase catalytic site and manufactured by GeneTools (Pilo-

math, OR, USA). Using the mMessage mMachine kit (Ambion), we synthesized 5' sense mRNA encoding membrane citrine (a YFP variant with a C-terminal fusion of the Ras membrane localization sequence [CAAX]). The embryos were injected at one cell stage.

Confocal microscopy, positioning and analysis

To visualize the cell shape in the presomitic mesoderm, membrane citrine expressing live embryos were mounted in 0.75% soft agarose at the dorsal side in glass bottomed petri dishes. Using SP2 Leica Confocal microscope the presomitic mesoderm was imaged using a 40 X oil objective. 2-D images were acquired during the 2 to 3 somite stage 100 μ m posterior to the developing somites in the paraxial mesoderm, lateral to the notochord. Automated segmentation of cell membranes using Cell Outliner and Cell rose based analysis was performed as described before in Chapter 5 of this thesis.

References

1. Hunter, T., *Protein kinases and phosphatases: the yin and yang of protein phosphorylation and signaling*. Cell, 1995. **80**(2): p. 225-36.
2. van der Geer, P., T. Hunter, and R.A. Lindberg, *Receptor protein-tyrosine kinases and their signal transduction pathways*. Annu Rev Cell Biol, 1994. **10**: p. 251-337.
3. Van Vactor, D., A.M. O'Reilly, and B.G. Neel, *Genetic analysis of protein tyrosine phosphatases*. Curr Opin Genet Dev, 1998. **8**(1): p. 112-26.
4. den Hertog, J., *Protein-tyrosine phosphatases in development*. Mech Dev, 1999. **85**(1-2): p. 3-14.
5. Alonso, A., et al., *Protein tyrosine phosphatases in the human genome*. Cell, 2004. **117**(6): p. 699-711.
6. Hendriks, W.J., et al., *Protein tyrosine phosphatases: functional inferences from mouse models and human diseases*. FEBS J, 2008. **275**(5): p. 816-30.
7. LaForgia, S., et al., *Receptor protein-tyrosine phosphatase gamma is a candidate tumor suppressor gene at human chromosome region 3p21*. Proc Natl Acad Sci U S A, 1991. **88**(11): p. 5036-40.
8. Tartaglia, M., et al., *Mutations in PTPN11, encoding the protein tyrosine phosphatase SHP-2, cause Noonan syndrome*. Nat Genet, 2001. **29**(4):

p. 465-8.

9. Wang, Z., et al., *Mutational analysis of the tyrosine phosphatome in colorectal cancers*. Science, 2004. **304**(5674): p. 1164-6.
10. Roszko, I., A. Sawada, and L. Solnica-Krezel, *Regulation of convergence and extension movements during vertebrate gastrulation by the Wnt/PCP pathway*. Semin Cell Dev Biol, 2009. **20**(8): p. 986-97.
11. Warga, R.M. and C.B. Kimmel, *Cell movements during epiboly and gastrulation in zebrafish*. Development, 1990. **108**(4): p. 569-80.
12. Heisenberg, C.P., et al., *Silberblick/Wnt11 mediates convergent extension movements during zebrafish gastrulation*. Nature, 2000. **405**(6782): p. 76-81.
13. Jessen, J.R., et al., *Zebrafish trilobite identifies new roles for Strabismus in gastrulation and neuronal movements*. Nat Cell Biol, 2002. **4**(8): p. 610-5.
14. Sepich, D.S., et al., *Role of the zebrafish trilobite locus in gastrulation movements of convergence and extension*. Genesis, 2000. **27**(4): p. 159-73.
15. Topczewski, J., et al., *The zebrafish glypican knypek controls cell polarity during gastrulation movements of convergent extension*. Dev Cell, 2001. **1**(2): p. 251-64.
16. Solnica-Krezel, L., *Gastrulation in zebrafish -- all just about adhesion?* Curr Opin Genet Dev, 2006. **16**(4): p. 433-41.
17. van Eekelen, M., et al., *Identification and expression of the family of classical protein-tyrosine phosphatases in zebrafish*. PLoS One, 2010. **5**(9): p. e12573.
18. Jopling, C., D. van Geemen, and J. den Hertog, *Shp2 knockdown and Noonan/LEOPARD mutant Shp2-induced gastrulation defects*. PLoS Genet, 2007. **3**(12): p. e225.
19. van Eekelen, M., et al., *RPTPalpha and PTPepsilon signaling via Fyn/Yes and RhoA is essential for zebrafish convergence and extension cell movements during gastrulation*. Dev Biol, 2010. **340**(2): p. 626-39.
20. Aerne, B. and D. Ish-Horowicz, *Receptor tyrosine phosphatase psi is required for Delta/Notch signalling and cyclic gene expression in the presomitic mesoderm*. Development, 2004. **131**(14): p. 3391-9.

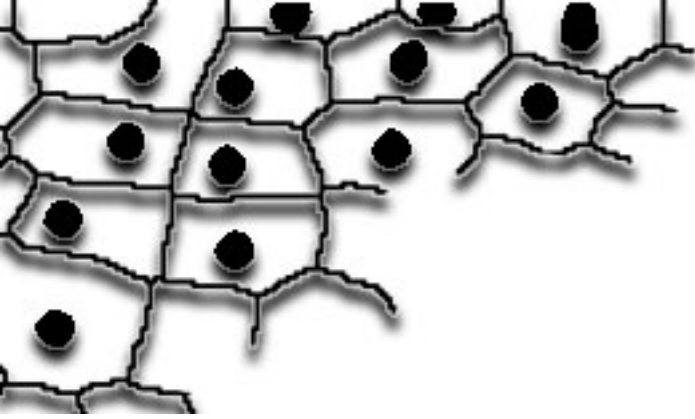


21. van eekelen, M., runtuwene, V., masselink, W., den Hertog, J., *Pairwise regulation of convergence and extension cell movements by four phosphatases via RhoA*. submitted.
22. Flicek, P., et al., *Ensembl's 10th year*. Nucleic Acids Res, 2010. **38**(Database issue): p. D557-62.
23. Pulido, R., et al., *The LAR/PTP delta/PTP sigma subfamily of transmembrane protein-tyrosine-phosphatases: multiple human LAR, PTP delta, and PTP sigma isoforms are expressed in a tissue-specific manner and associate with the LAR-interacting protein LIP.1*. Proc Natl Acad Sci U S A, 1995. **92**(25): p. 11686-90.
24. Saunders, A.E. and P. Johnson, *Modulation of immune cell signalling by the leukocyte common tyrosine phosphatase, CD45*. Cell Signal, 2010. **22**(3): p. 339-48.
25. Aguiar, R.C., et al., *PTPROt: an alternatively spliced and developmentally regulated B-lymphoid phosphatase that promotes G0/G1 arrest*. Blood, 1999. **94**(7): p. 2403-13.
26. Elson, A. and P. Leder, *Protein-tyrosine phosphatase epsilon. An isoform specifically expressed in mouse mammary tumors initiated by v-Ha-ras OR neu*. J Biol Chem, 1995. **270**(44): p. 26116-22.
27. Amoui, M., et al., *Expression of a structurally unique osteoclastic protein-tyrosine phosphatase is driven by an alternative intronic, cell type-specific promoter*. J Biol Chem, 2003. **278**(45): p. 44273-80.
28. Imai, Y. and W.S. Talbot, *Morpholino phenocopies of the bmp2b/swirl and bmp7/snailhouse mutations*. Genesis, 2001. **30**(3): p. 160-3.
29. Braat, A.K., et al., *A zebrafish vasa morphant abolishes vasa protein but does not affect the establishment of the germline*. Genesis, 2001. **30**(3): p. 183-5.
30. Lele, Z., J. Bakkers, and M. Hammerschmidt, *Morpholino phenocopies of the swirl, snailhouse, somitabun, minifin, silberblick, and pipetail mutations*. Genesis, 2001. **30**(3): p. 190-4.
31. Ekker, S.C. and J.D. Larson, *Morphant technology in model developmental systems*. Genesis, 2001. **30**(3): p. 89-93.
32. Heasman, J., *Morpholino oligos: making sense of antisense?* Dev Biol, 2002. **243**(2): p. 209-14.

33. Ekker, S.C., *Nonconventional antisense in zebrafish for functional genomics applications*. *Methods Cell Biol*, 2004. **77**: p. 121-36.
34. Robu, M.E., et al., *p53 activation by knockdown technologies*. *PLoS Genet*, 2007. **3**(5): p. e78.
35. Li, C., et al., *An essential role for DYF-11/MIP-T3 in assembling functional intraflagellar transport complexes*. *PLoS Genet*, 2008. **4**(3): p. e1000044.
36. Runtuwene, V., et al., *Noonan syndrome gain-of-function mutations in NRAS cause zebrafish gastrulation defects*. *Dis Model Mech*, 2011. **4**(3): p. 393-9.
37. Chagnon, M.J., N. Uetani, and M.L. Tremblay, *Functional significance of the LAR receptor protein tyrosine phosphatase family in development and diseases*. *Biochem Cell Biol*, 2004. **82**(6): p. 664-75.
38. Elchebly, M., et al., *Neuroendocrine dysplasia in mice lacking protein tyrosine phosphatase sigma*. *Nat Genet*, 1999. **21**(3): p. 330-3.
39. Pulido, R., et al., *Molecular characterization of the human transmembrane protein-tyrosine phosphatase delta. Evidence for tissue-specific expression of alternative human transmembrane protein-tyrosine phosphatase delta isoforms*. *J Biol Chem*, 1995. **270**(12): p. 6722-8.
40. Uetani, N., et al., *Impaired learning with enhanced hippocampal long-term potentiation in PTPdelta-deficient mice*. *EMBO J*, 2000. **19**(12): p. 2775-85.
41. Seimiya, H., et al., *Cloning, expression and chromosomal localization of a novel gene for protein tyrosine phosphatase (PTP-U2) induced by various differentiation-inducing agents*. *Oncogene*, 1995. **10**(9): p. 1731-8.
42. Wiggins, R.C., et al., *Molecular cloning of cDNAs encoding human GLEPP1, a membrane protein tyrosine phosphatase: characterization of the GLEPP1 protein distribution in human kidney and assignment of the GLEPP1 gene to human chromosome 12p12-p13*. *Genomics*, 1995. **27**(1): p. 174-81.
43. Wharram, B.L., et al., *Altered podocyte structure in GLEPP1 (Ptpro)-deficient mice associated with hypertension and low glomerular filtration rate*. *J Clin Invest*, 2000. **106**(10): p. 1281-90.



44. Gonzalez-Brito, M.R. and J.L. Bixby, *Protein tyrosine phosphatase receptor type O regulates development and function of the sensory nervous system*. Mol Cell Neurosci, 2009. **42**(4): p. 458-65.
45. Barnea, G., et al., *Identification of a carbonic anhydrase-like domain in the extracellular region of RPTP gamma defines a new subfamily of receptor tyrosine phosphatases*. Mol Cell Biol, 1993. **13**(3): p. 1497-506.
46. Lamprianou, S., et al., *Receptor protein tyrosine phosphatase gamma is a marker for pyramidal cells and sensory neurons in the nervous system and is not necessary for normal development*. Mol Cell Biol, 2006. **26**(13): p. 5106-19.
47. Westerfield, *The zebrafish book*. 1995: University of Oregon press, Eugene, Oregon.
48. Thisse, C., et al., *Structure of the zebrafish snail1 gene and its expression in wild-type, spadetail and no tail mutant embryos*. Development, 1993. **119**(4): p. 1203-15.



7

Summarizing Discussion

During gastrulation the zebrafish morphology undergoes a drastic change from an ‘inverted cup’- shape to a narrow and long body frame. This impressive remodeling is due in great part to the evolutionary conserved CE movements, which are crucial for proper organ anlage positioning and as a consequence are essential for normal development. The cells collectively polarize, *i.e.* elongate and orient their longest axis in mediolateral direction, and migrate towards the dorsal midline, where cell intercalation occurs. Many genes have been identified regulating CE movements, although the exact mechanism remains unclear. However, mutants and morphant phenotypes have shown that a loss of the cell polarization is a key factor underlying the resulting, characteristic, shorter and broader embryo phenotypes.

Previously, we have identified all members of the family of classical PTPs in the zebrafish genome and provided a detailed analysis of the spatio-temporal expression patterns of these 48 PTPs during early embryonic development. In this thesis, we focus on the role of PTPs in gastrulation convergence and extension (CE) cell movements.

Functional screening of the family of classical PTPs using MOs in the zebrafish system

Using the remarkably efficient morpholino micro-injection knockdown techniques in zebrafish, we investigated the function of four zebrafish PTP genes (*ptpra*, *ptprea/b*, *ptpn13*, and *ptpn20*) in zebrafish CE cell movements. In **Chapter 2** it is shown that *ptpra*, *ptprea* and *ptpreb* not only play a role in the polarization which underlies the gastrulation morphogenetic movements, we also speculate that they operate in a pathway which regulates cell polarity through Src family kinases Fyn and Yes, and RhoA in parallel to the non-canonical Wnt pathway. Both *ptpra* and *ptprea/b* morphants and *ptpra* *-/-* mutants show the characteristic shorter phenotypes apparent at 48 hpf (quantified by taillength) and loss of cell polarity associated with CE defects. It was shown that the knockdown could be alleviated by coinjection with constitutively active Fyn and Yes and RhoA, a well-known downstream effector of non-canonical Wnt signaling. Co-injection of mRNA of *ptpra* or *ptpre* with Wnt11 MO or vice versa did not result in alleviation of the phenotype, indicating a parallel pathway to the non-canonical Wnt signaling leading to RhoA activation.

An automated cell tracing algorithm was developed to determine the migration speeds of individual cells and was used to demonstrate a significant difference between the average convergence and extension rate of the gastrulation cell movements of *ptpra* *-/-* homozygous mutant embryos and wildtype (wt) siblings. For the determination of cell polarization of the presomitic mesoderm, a method was devised to more efficiently quantify the shapes of cells within a tissue

based on confocal images. In contrast to the conventional method, which relies on manual annotation of the cell outline, this method applies user determined image processing steps to filter out the outline of the cells in the images (an automated algorithm for this has been developed and presented in **Chapter 5**).

In **chapter 3**, we identified PTP-BL and Ptpn20 as structural paralogues and determined both to be critical to CE cell movements as components of a system regulating cell polarity in concert with RPTP α and RPTP ϵ . We demonstrate that full knockdown of PTP-BL and Ptpn20 results in CE defects reminiscent of the phenotypes resulting from RPTP α and RPTP ϵ knockdown. While knockdowns of RPTP α and RPTP ϵ were rescued by co-injection of activated RhoA, knockdowns of PTP-BL and Ptpn20 were rescued by co-injection of dominant negative RhoA. Next, using co-injection of suboptimal amounts of MOs, genetic interactions were established between *ngef* (identified as a Rho-GEF) and *ptpra/ptpre* and between *ahrgap29* (identified as a Rho-GAP) and *ptpn13* and *ptpn20*. Our data shows that PTP-BL, Ptpn20, RPTP α and RPTP ϵ function in pairs, where low dose co-knockdown of *ptpra* and *ptpn13* resulted in a severe phenotype and co-knockdown of *ptpra* and *ptpn20* did not. Similarly, *ptpre* and *ptpn20*, but not *ptpn13* resulted in synergistic effects. We hypothesize that asymmetric distribution of RhoA-GTP and RhoA-GDP over the leading and trailing edge of the cell is required for proper polarity and migration. We propose that RPTP α and RPTP ϵ act on one side of the cell as activators of RhoA, while PTP-BL and Ptpn20 exert their function on the opposite side as inhibitors. Full knockdown of either one of the components will reduce RhoA-GTP/RhoA-GDP levels to such an extent that cell polarity will be lost. Low-dose knockdown of the single components only mildly reduces RhoA-GTP/RhoA-GDP levels, but does not result in loss of polarity because of normal signaling on the opposing side. Combining low-dose knockdown on the other hand, leads to reduced activation of RhoA on one side and reduced inhibition of RhoA on the other side, resulting in loss of polarity, and as a consequence CE defects. It remains to be determined which mechanism of differential upstream activation of PTPs, subcellular localization, substrate specificity or cell type specific expression may underly the specificity of the combined knockdowns.

In **chapter 6**, we performed a screen of the family of classical PTPs to identify genes with a role in gastrulation cell movements in zebrafish. To our knowledge, this is the first time a MO-screen has been performed on an entire family of proteins. We designed 2 independent splice site morpholinos for each of the 48 genes, encoding PTPs. In the first round all embryos were analyzed morphologically, by quantifying the tail length at 72hpf, as a measurement for body axis extension, a hallmark of CE defects. Positive hits were identified based on both MOs causing similar phenotypes. This resulted in the identification of four candidate genes with a potential role in CE. These positive hits were analyzed in detail for CE defects in the second round by in situ hybridization using well-established



markers for CE cell movements. The tools described in **Chapter 5** were used to assess defects in cell polarization of the presomitic mesoderm. Based on the comparative analysis of the results with four positive controls, i.e. PTPs with a known role in CE cell movements (*ptpra*, *ptprea/b*, *ptpn11*, *ptprua*), one additional PTP, *ptprda*, was identified as essential for normal gastrulation cell movements.

The relative ease of combining MOs by co-injection allows for an efficient method for simultaneous knockdown of multiple genes and has proven to be a valuable technique in identifying genes operating in the same signaling pathway and identifying redundancy between ohnologs (**chapter 2 and 3**). One obvious setback in their use for screening for CE phenotypes is the fact that the phenotype, which is considered positive in the morphological analysis, i.e. a shorter body axis, is also a known non-specific morpholino induced artefact, making the use of controls for morpholino specificity warranted [1].

Identification and characterization of NRas-I24N, a novel Noonan-associated mutation

Noonan syndrome is a relatively common dominantly inherited genetic developmental disorder that is characterized by reduced growth, orbital hypertelorism, and congenital heart defects. It is classified as a RASopathy, a group of genetic disorders in which the underlying cause is associated with dysregulation of the Ras-mitogen-activated-protein-kinase (RAS-MAPK) signaling pathway. ~50% of Noonan patients present with activating mutations in *PTPN11*, a gene encoding SHP2, a PTP which regulates signaling upstream in the RAS-MAPK pathway [2]. Other mutations associated with Noonan syndrome are also found in this pathway, namely SOS1 [3, 4], KRAS [5, 6], SHOC2[7], RAF1 and BRAF [3, 5, 8]. Earlier work has also shown that Noonan associated mutations in *Shp2*, the zebrafish ortholog of *SHP2* induce gastrulation defects in zebrafish [9].

Recently two mutations in *NRAS* were reported to be associated with Noonan syndrome, T50I and G60E [10]. In **chapter 4**, we report a mutation in *NRAS*, resulting in an I24N amino acid substitution, that we identified in individual bearing typical Noonan syndrome features. The I24N mutation activates N-Ras, resulting in enhanced downstream signaling. This is the first report of an I24 mutation in any RAS isoform. The surrounding region of the mutation, which is localized between the P-loop, involved in nucleotide binding, and Switch I, involved in effector binding, is highly conserved between N-RAS, K-RAS, and H-RAS. This together with the fact that mutations in Q22 have been found in patients diagnosed with Noonan (Q22R) and other Rasopathies (Q22E and Q22K) [11, 12], suggests a regulatory role for this region of which the mechanism remains to be elucidated.

Expression of N-Ras-I24N, N-Ras G60E or the strongly activating mutant

N-Ras G12V, which we included as a positive control, resulted in the developmental defects in zebrafish embryos, demonstrating for the first time that these activating N-Ras mutants are sufficient to induce developmental disorders that resemble the defects induced by active mutants of downstream factors, B-RAF, RAF-1 and MEK, from Noonan and related syndromes [13]. These defects in zebrafish embryos are reminiscent of symptoms in individuals with Noonan syndrome. We were able to show that these symptoms appear to be a result of defective cell polarization and resulting aberrant gastrulation CE cell movements. MEK inhibition, using the small molecular inhibitor CI-1040, completely rescued the activated N-Ras-induced phenotypes, demonstrating that these defects are mediated exclusively by Ras-MAPK signaling. This finding also raises the possibility of using pharmacological inhibitors in the treatment of RASopathies or other developmental disorders caused by overactivation of the RAS-MAPK pathway.

In conclusion, mutations in *NRAS* from individuals with Noonan syndrome activated N-Ras signaling and induced developmental defects in zebrafish embryos, indicating that activating mutations in *NRAS* cause Noonan syndrome.

Image processing and automated algorithms

Quantitative analysis and clear representation of the data is essential to modern day biology. Studying collective cell migrations, for instance during gastrulation CE cell movements requires the analysis of the net effect of cell polarization and/or displacements of a large number of cells within a tissue rather than measurements of a few individuals [14].

For analyzing CE defects in zebrafish, quantifying the coordinated orientation, or randomization evidently requires the analysis of quite a number of cells in order to obtain reliable data. The annotation of the cell membranes required for analysis of cell polarization is usually carried out manually, making it time consuming, tedious, and subjective. In **Chapter 5** we describe the development of an automated algorithm Cell Outliner for the detection of cell membranes, to facilitate data collection for polarization analysis. The method was proven to be effective using different fluorescent markers and on data sets both from zebrafish and mice. Additionally, a novel method of graphical data representation is introduced called Cell Roses, which adds the advantage of showing the correlation between both defining quantitative parameters of cell polarization, cell elongation and medio-lateral orientation, by plotting them on one comprehensive graph rather than separate ones. As a proof-of-principle this method was used to analyze the presomitic mesoderm of *ptpra*^{-/-} mutant zebrafish, a well-described CE phenotype. The Cell Roses clearly showed the concomitant loss of elongation and mediolateral orientation of the cells in the mutant tissues in comparison to wt siblings.



Several automated image processing algorithms were also developed for the detection and tracking of nucleus center positions, the latest version named Sugar Rush (available upon request). In **Chapter 2** automated cell tracing is used to determine and compare the average extension and convergence speeds of zebrafish *ptpra*^{-/-} to wt sibling samples. While multiple programs are available for standard object tracing tasks, none of the available (online or in house) programs were able to trace efficiently or accurately, the large numbers of cells needed for estimating these average migrating speeds, when applied on a standard laptop computer (in this instance defined as a Apple® MacBook Pro 2.7 GHz Intel® core i7 early-2011). Sugar Rush proved to be a very efficient and accurate cell tracer.

The most critical aspect in developing automated algorithms for image analysis is efficient segmentation, the separation of foreground objects from the background, i.e. detection. Typically, confocal images contain fluctuations (biological noise) in signal intensity and occasionally contain intensity gradients on top of mechanical shot noise, inherently linked to the physical principle used by confocal microscopes. The efficiency of both Sugar Rush and Cell Outliner lies in series of simple non-computationally-intense image processing steps used for segmentation, designed to efficiently eliminate the noise (biological or mechanical) in the image. As a result the original image is converted to a binary version containing white objects on a black background. This format immensely facilitates computational analysis of the objects, whether they need to be traced in a time series or scored for shape parameters.

The necessity of determining and scoring cell parameters such as collective migration speed or cell polarity is not restricted to the study of gastrulation. Angiogenesis [17], the establishment of the highly organized structures of auditory and vestibular epithelia [18], neurogenesis [19], metastatic processes [20], wound healing [15, 16] and numerous more examples can be found in which the determination of tissue migration and cell polarization is critical in a quantitative analysis. The advent more sophisticated imaging technology, and the continuous development of more sensitive and specific fluorescent probes, allows the visualization of biological processes in unprecedented detail. Data analysis can be greatly facilitated by the use of algorithms like Cell Outliner and Sugar Rush.

Conclusion

In this thesis 6 PTP genes (*ptpra*, *ptprea*, *ptpreb*, *ptpn13*, *ptpn20*, and *ptprda*) were identified as having a role in zebrafish CE cell movements. Five of these (*ptpra*, *ptprea*, *ptpreb*, *ptpn13*, *ptpn20*) have been further characterized and shown to function within signaling pathways which converge on downstream effectors of the non-canonical Wnt pathway, a pathway well-known to regulate CE cell movements, like RhoA. Additionally, for 2 PTPs (*ptpn11* and *ptprua*), which

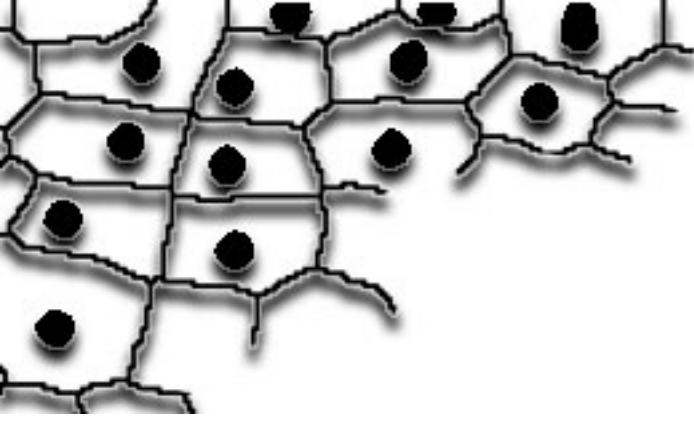
were already indicated to have a role in CE cell movements, direct evidence was generated for their function in cell polarization. It will be interesting to investigate whether and, if so, how *ptprda* interacts with the non-canonical Wnt pathway. Additionally, it will also be interesting to investigate crosstalk among the PTPs that have been identified to play a role in CE cell movements. Further, a novel Noonan-associated mutation was reported and shown to hyperactivate FGFR-RAS-MAPK signaling, causing developmental defects. Finally, new tools were generated to quantify gastrulation cell movements and cell polarization which also could be useful outside of the domain of zebrafish gastrulation.

References

1. Heasman, J., *Morpholino oligos: making sense of antisense?* Dev Biol, 2002. **243**(2): p. 209-14.
2. Tartaglia, M., et al., *Mutations in PTPN11, encoding the protein tyrosine phosphatase SHP-2, cause Noonan syndrome.* Nat Genet, 2001. **29**(4): p. 465-8.
3. Tartaglia, M., et al., *Gain-of-function SOS1 mutations cause a distinctive form of Noonan syndrome.* Nat Genet, 2007. **39**(1): p. 75-9.
4. Roberts, A.E., et al., *Germline gain-of-function mutations in SOS1 cause Noonan syndrome.* Nat Genet, 2007. **39**(1): p. 70-4.
5. Pandit, B., et al., *Gain-of-function RAF1 mutations cause Noonan and LEOPARD syndromes with hypertrophic cardiomyopathy.* Nat Genet, 2007. **39**(8): p. 1007-12.
6. Schubbert, S., et al., *Germline KRAS mutations cause Noonan syndrome.* Nat Genet, 2006. **38**(3): p. 331-6.
7. Cordeddu, V., et al., *Mutation of SHOC2 promotes aberrant protein N-myristoylation and causes Noonan-like syndrome with loose anagen hair.* Nat Genet, 2009. **41**(9): p. 1022-6.
8. Razzaque, M.A., et al., *Germline gain-of-function mutations in RAF1 cause Noonan syndrome.* Nat Genet, 2007. **39**(8): p. 1013-7.
9. Jopling, C., D. van Geemen, and J. den Hertog, *Shp2 knockdown and Noonan/LEOPARD mutant Shp2-induced gastrulation defects.* PLoS Genet, 2007. **3**(12): p. e225.



10. Cirstea, I.C., et al., *A restricted spectrum of NRAS mutations causes Noonan syndrome*. Nat Genet, 2010. **42**(1): p. 27-9.
11. Zenker, M., et al., *Expansion of the genotypic and phenotypic spectrum in patients with KRAS germline mutations*. J Med Genet, 2007. **44**(2): p. 131-5.
12. van der Burgt, I., et al., *Myopathy caused by HRAS germline mutations: implications for disturbed myogenic differentiation in the presence of constitutive HRas activation*. J Med Genet, 2007. **44**(7): p. 459-62.
13. Anastasaki, C., et al., *Kinase-activating and kinase-impaired cardio-facio-cutaneous syndrome alleles have activity during zebrafish development and are sensitive to small molecule inhibitors*. Hum Mol Genet, 2009. **18**(14): p. 2543-54.
14. Roszko, I., A. Sawada, and L. Solnica-Krezel, *Regulation of convergence and extension movements during vertebrate gastrulation by the Wnt/PCP pathway*. Semin Cell Dev Biol, 2009. **20**(8): p. 986-97.
15. Vitorino, P. and T. Meyer, *Modular control of endothelial sheet migration*. Genes Dev, 2008. **22**(23): p. 3268-81.
16. Caddy, J., et al., *Epidermal wound repair is regulated by the planar cell polarity signaling pathway*. Dev Cell, 2010. **19**(1): p. 138-47.
17. Cirone, P., et al., *A role for planar cell polarity signaling in angiogenesis*. Angiogenesis, 2008. **11**(4): p. 347-60.
18. Kelly, M. and P. Chen, *Shaping the mammalian auditory sensory organ by the planar cell polarity pathway*. Int J Dev Biol, 2007. **51**(6-7): p. 535-47.
19. Rieger, S., F. Wang, and A. Sagasti, *Time-lapse imaging of neural development: zebrafish lead the way into the fourth dimension*. Genesis, 2011. **49**(7): p. 534-45.
20. Wyckoff, J.B., et al., *Direct visualization of macrophage-assisted tumor cell intravasation in mammary tumors*. Cancer Res, 2007. **67**(6): p. 2649-56.



Addendum

Samenvatting in het Nederlands

Vroege morfogenese is heel vergelijkbaar in alle vertebraten. Zoals in elke vertebraat, resulteert de bevruchting van de zebravis oocyt in een 1-cel -stadium zygote. Deze wordt vervolgens getransformeerd door mitotische delingen tot een massa van cellen bovenop een dooier. De onverschillend lijkende cellen in deze massa zijn de voorlopers van alle celtypes van het organisme.

Tijdens gastrulatie wordt het embryo gereorganiseerd tot een verlengde structuur die duidelijk te onderscheiden delen bevat. De doorheen evolutie geconserveerde convergentie en extensie (CE) celbewegingen zijn voor een groot stuk verantwoordelijk voor deze reorganisatie. Samen met epibolie en internalisatie gaan de CE celbewegingen de kiemlagen vormen, nl. ectoderm, endoderm en mesoderm. De cellen, en daarmee ook de orgaan primordia, worden gerepositioneerd volgens hun toekomstige rangschikking langs de antero-posterieure as. De CE celbewegingen zijn cruciaal voor een normale ontwikkeling en defecten in het mechanisme zijn de onderliggende oorzaak van menselijke pathologiën zoals spina bifida en Noonan syndroom. In hoofdstuk 4 rapporteren we een mutatie in *NRAS* die resulteert in een I24N aminozuur substitutie, die we geïdentificeerd hebben in een individu met typische kenmerken van Noonan syndroom. In tegenstelling tot de wildtype versie, veroorzaakt deze mutatie gastrulatie defecten in zebravissen wanneer deze tot expressie wordt gebracht via mRNA injectie.

Collectieve polarisatie van de cellen in de medio-laterale richting zijn essentieel voor de convergentie naar de middenlijn. De gepolariseerde cellen intercaleren bij de middenlijn. Dit intercalatieproces, welke ook polarisatie vereist, resulteert in de extensie van de antero-posterieure as. De coordinatie en regulatie van de CE celbewegingen worden gestuurd door fijn gereguleerde signalisatie mechanismen. Tyrosine fosforylatie is een van deze mechanismen. Door fosforylatie door proteïne-tyrosine kinasen ofwel door defosforylatie door proteïne-tyrosine fosfatasen (PTPs) van tyrosine residues, kunnen een groot aantal signaalmoleculen van een actieve naar een inactieve staat worden geschakeld. Fosforylatie gebeurt heel dynamisch en reguleert veel cellulaire processen zoals proliferatie, migratie en differentiatie. De PTP superfamilie is onderverdeeld in de 'klassieke' (fosfo-tyrosine-specifiek) fosfatasen en de duale specifieke fosfatasen (welke fosfo-tyrosine, fosfo-serine en fosfo-threonine kunnen defosforyleren). In deze thesis focussen we op de rol van 'klassieke' PTPs in zebravis gastrulatie.

In **hoofdstuk 3** hebben we PTP-BL en Ptpn20 als structurele paralogen geïdentificeerd en hebben we bepaald dat beide van kritiek belang zijn voor de CE celbewegingen als onderdelen van een systeem dat cel polarisatie reguleert



samen met RPTP α en RPTP ϵ (welke ook beschreven worden in **hoofdstuk 2**). We tonen aan dat deze 4 PTPs de activatiestaat van RhoA reguleren. Activatie van RhoA is nodig voor de polarisatie van cellen en daardoor van cruciaal belang voor CE celbewegingen.

In **hoofdstuk 6** beschrijven we een screen van de familie van 'klassieke' PTPs om genen te identificeren die een rol spelen in gastrulatie celbewegingen in zebrafissen. We ontwierpen 2 onafhankelijke splice-site morfolino's voor elk van de 48 genen, die coderen voor PTPs. In de eerste ronde werden alle embryos morfologisch geanalyseerd. In een tweede ronden werden positieven tot in het detail geanalyseerd voor CE defecten gebruik makend van *in situ* hybridisatie met welgekende merkers voor CE celbewegingen. De algoritmes beschreven in hoofdstuk 5 werden gebruikt om de defecten te meten die zich voordeden in het presomitisch mesoderm. Gebaseerd op de vergelijkende analyse tussen vier positieve controles, werd een bijkomende PTP, *ptprda* geïdentificeerd als essentieel voor normale gastrulatie celbewegingen.

Kwantitatieve analyse en duidelijke representatie van de data zijn essentieel in de moderne biologie. Wanneer men bijvoorbeeld collectieve celbewegingen analyseert, wordt de analyse vereist van het netto effect van cell polarisatie en/of verplaatsing van een groot aantal cellen en niet de metingen van enkel een paar. We hebben hulpmiddelen voor de kwantificatie van celbewegingen en polarisatiedefecten ontwikkeld. In **hoofdstuk 2** is een ge-automatiseerde cel tracer ontwikkeld om de migratiesnelheden te determineren van individuele cellen, welke vervolgens gebruikt werden om een verschil aan te tonen tussen de gemiddelde convergentie en extentie snelheden tijdens de CE celbewegingen van de *ptpra*^{-/-} homozygote mutante embryos en wildtype broers en zussen. In **Hoofdstuk 5** beschrijven we de ontwikkeling van een automatisch algoritme Cell Outliner voor de detectie van celmembranen. Dit dient om de verzameling van data rond celpolarisatie te vergemakkelijken. Bijkomend hebben we een nieuwe methode geïntroduceerd, Cell Roses, om grafisch de data te representeren. Deze methode biedt het voordeel dat de twee termen die polarisatie bepalen, cel elongatie en de medio-laterale orientatie, op eenzelfde grafiek kunnen worden gebracht waardoor ook hun correlatie duidelijk wordt. Als proof-of-principle werd deze methode gebruikt om de polarisatie te analyseren van het mesoderm van *ptpra*^{-/-} homozygote mutante embryos, een welbestudeerd CE defect fenotype. Cell Roses toonde duidelijk het verlies van elongatie en mediolaterale orientatie van de cellen in het mutante weefsel in vergelijking met de wildtype broers en zussen.

Summary

Early morphogenesis is very similar in all vertebrates. As in every vertebrate, fertilization of the zebrafish oocyte results in a one cell stage zygote, which is then transformed via mitotic divisions into a mass of cells on top of the yolk. The evidently undiversified cells within this mass, are the progenitors of all cell types of the organism.

During gastrulation, the embryo is reorganized to an elongated framework containing clearly defined structures. The evolutionary conserved convergence and extension (CE) cell movements are largely responsible for this rearrangement. Together with epiboly and internalization, the CE cell movements form the germ layers, ectoderm, mesoderm and endoderm. The cells, and consequently the organ anlagen, are repositioned according to their future arrangement along the antero-posterior axis. These movements are crucial for normal development and defects in their mechanism underlie human pathologies like spina bifida and Noonan syndrome. In **chapter 4**, we report a mutation in *NRAS*, resulting in an I24N amino acid substitution, that we identified in individual bearing typical Noonan syndrome features. In contrary to the wildtype form, the mutation causes gastrulation defects when expressed via mRNA injection in zebrafish.

Collective polarization of the cells in the mediolateral direction is essential for the convergence towards the midline. The polarized cells intercalate at the midline. This intercalation process, which also requires polarization, results in the extension of the antero-posterior body axis. The coordination and regulation of the CE cell movements are governed by intricate signaling mechanisms. Tyrosine phosphorylation is one of such mechanisms. By either phosphorylation by protein-tyrosine kinases or dephosphorylation by protein-tyrosine phosphatases (PTPs) of tyrosine residues, a large number of signaling proteins can be switched from active to inactive states. Phosphorylation is highly dynamic and regulates many cellular processes like cell migration, proliferation and differentiation. The PTP superfamily is subdivided in 'classical' (phospho-tyrosine-specific) phosphatases and dual specificity phosphatases (which dephosphorylate phospho-tyrosine, phospho-serine and phospho-threonine). In this thesis, we focus on the role of 'classical' PTPs in zebrafish gastrulation.

In **chapter 3**, we identified PTP-BL and Ptpn20 as structural paralogues and determined both to be critical to CE cell movements as components of a system regulating cell polarity in concert with RPTP α and RPTP ϵ (which are also described in **chapter 2**). We show that these 4 PTPs regulate the activation state of RhoA. Activation of RhoA is required for the polarization of cells and as a



consequence crucial for CE cell movements.

In **chapter 6**, we performed a screen of the family of ‘classical’ PTPs to identify genes with a role in gastrulation cell movements in zebrafish. We designed 2 independent splice site morpholinos for each of the 48 genes, encoding PTPs. In the first round all embryos were analyzed morphologically. Positive hits were analyzed in detail for CE defects in the second round by *in situ* hybridization using well-established markers for CE cell movements. The tools described in **chapter 5** were used to assess defects in cell polarization of the presomitic mesoderm. Based on the comparative analysis of the results with four positive controls, one additional PTP, *ptprda*, was identified as essential for normal gastrulation cell movements.

Quantitative analysis and clear representation of the data is essential to modern day biology. Studying collective cell migrations requires the analysis of the net effect of cell polarization and/or displacements of a large number of cells within a tissue rather than measurements of a few individuals. In **chapter 2**, an automated cell tracing algorithm was developed to determine the migration speeds of individual cells and was used to demonstrate a significant difference between the average convergence and extension rate of the gastrulation cell movements of *ptpra* *-/-* homozygous mutant embryos and wt siblings. In **chapter 5** we describe the development of an automated algorithm Cell Outliner for the detection of cell membranes, to facilitate data collection for polarization analysis. Additionally, a novel method of graphical data representation is introduced called Cell Roses, which adds the advantage of showing the correlation between both defining quantitative parameters of cell polarization, cell elongation and medio-lateral orientation, by plotting them on one comprehensive graph rather than separate ones. As a proof-of-principle this method was used to analyze the presomitic mesoderm of *ptpra* *-/-* mutant zebrafish, a well-described CE phenotype. The Cell Roses clearly showed the concomitant loss of elongation and mediolateral orientation of the cells in the mutant tissues in comparison to wildtype siblings.

List of publications

RPTPalpha and PTPepsilon Signaling via Fyn/Yes and RhoA is Essential for Zebrafish Convergence and Extension Cell Movements during Gastrulation.

van Eekelen M*, Runtuwene V*, Overvoorde J, den Hertog J.
Dev Biol. 2010 Apr 15;340(2):626-39. Epub 2010 Feb 24.

Noonan Syndrome Gain-of- Function Mutations in NRAS Cause Zebrafish Gastrulation Defects.

Vincent Runtuwene*, Mark van Eekelen*, John Overvoorde, Holger Rehmann, Helger G. Yntema, Willy M. Nillesen, Arie van Haeringen, Ineke van der Burgt, Boudewijn Burgering and Jeroen den Hertog
Dis. Model. Mech. dmm.007112; Published online ahead of print January 24, 2011,
doi:10.1242/dmm.007112

Essential role for the d-Asb11 cul5 Box Domain for Proper Notch signaling and Neural Cell Fate Decisions in Vivo

Maria A. Sartori da Silva, Jin-Ming Tee, Judith Paridaen, Anke Brouwers, Sander H. Diks, Vincent Runtuwene, Danica Zivkovic, Daniele Guardavaccaro, Maikel P. Peppelenbosch
PLoS One. 2010 Nov 19;5(11):e14023.

Pair-Wise Regulation of Convergence and Extension Cell Movements by Four Phosphatases via RhoA

Mark van Eekelen, Vincent Runtuwene, Wouter Masselink and Jeroen den Hertog
PLoS One. 2012; 7(4): e35913

*=equal contribution



Curriculum Vitae

Vincent Jimmy Runtuwene was born on the 25th Juli 1982 in Leuven. He completed his secondary education in 2000 in Latin and Sciences. In that same year he started his Bio-engineering studies in Leuven. Vincent did an internship in the Centre of Microbial and Plant Genetics under Prof. Dr. Jan Michiels, where he worked on the interaction between symbionts *Rhizobium etli* CNPAF512 and *Phaseolus vulgaris*. He graduated in 2006 with distinction from the Catholic University of Leuven as a Bio-engineer in cell and gene biotechnology (MSc). In 2007, he began as a PhD student at the Hubrecht Institute in Utrecht as a member of the group of Prof. Dr. Jeroen den Hertog. The work described in this thesis was carried out under the supervision of Prof. Dr. Jeroen den Hertog. Vincent is now a clinical data manager at SGS in Mechelen.